European Doctorate in Indium Phosphide PIC Fabrication Technology

Deliverable D7.6

Comprehensive Education Programme Report

Lead Beneficiary	UNIVERSITY OF VIGO
Delivery date	2022-12-21
Dissemination	Public
Status	Approved
Version	1.0
Keywords	Website, Open Access,Training, Education

This project has received funding from the European Union's Horizon 2020 research and innovation programme under Marie Skłodowska-Curie grant agreement No 813467

Document Information

Grant Agreement Number	813467
Project Acronym	EDIFY
Work Package	WP 7
Deliverable	D7.6
Title	Comprehensive Education Programme Report
Author(s)	Francisco Javier Diaz Otero
File Name	EDIFY_D7.6_Website_20221221_v1.0.docx

Abstract

Through the Doc-TIC PhD Programme a number of course modules in canonical areas related to photonics (active and passive devices), quantum mechanics, solid-state physics and integrated photonics are given to the ESRs. Moreover, other collateral as transferable skills training courses were given to the students. Besides, some other extra training was accesible to students. In this report, the overall collection of these trainings and final comments are exposed.

Keywords: Open Access, Media, Events, Training, Education

Change Record

Revision	Date	Description	Reviewer
0.1	01-10-2022	Outline proposal	Francisco J. Diaz Otero
0.5	15-12-2022	Partial contents developed	WP7 partners
0.7	20-12-2022	Version for peer review	Anxo Moreira (UVIGO)
0.9	21-12-2022	Reviewed	Steven Grijseels (SP)
1.0	09-01-2023	Final deliverable for the EC	EC

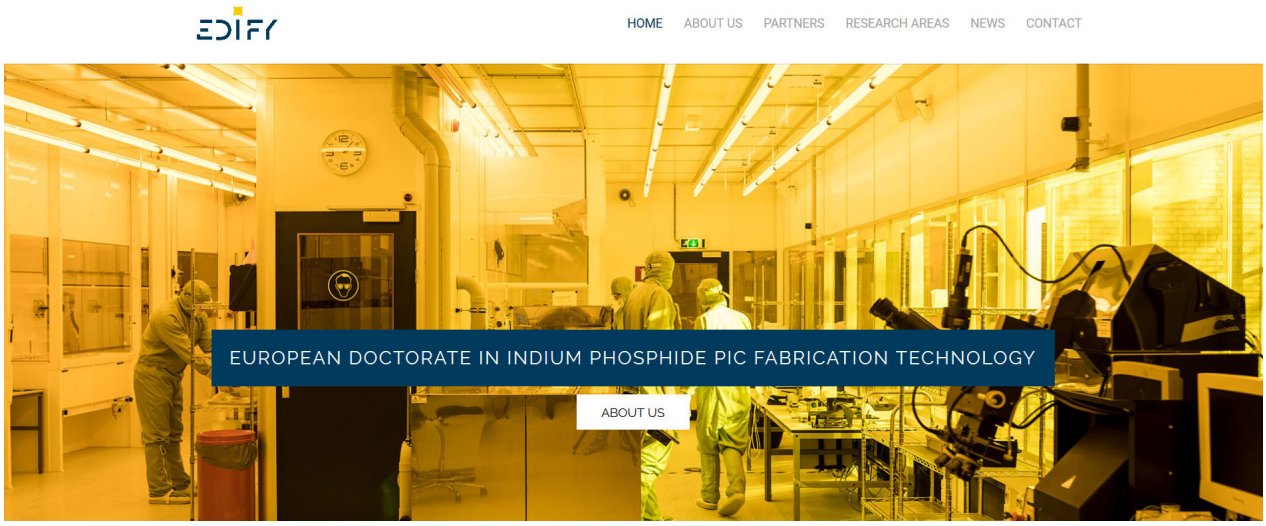
HOME
ABOUT US
PARTNERS
RESEARCH AREAS
NEWS
CONTACT
EUROPEAN DOCTORATE IN INDIUM PHOSPHIDE PIC FABRICATION TECHNOLOGY
ABOUT US


EDIFY

TABLE OF CONTENTS

1. INTRODUCTION

The challenge for the EDIFY Training Network was to develop new fundamental skills on simulation, design, measurement automation, fabrication and validation, and organization in an integrated photonics foundry. To achieve this, EDIFY training strategy aimed to combine ***scientific advanced training (Scientific Courses 1-5), technical hands-on courses (TC1-3), Winter School and regular EID meetings and networking events. Furthermore, all ESRs have been equipped with a range of transferable skills, as defined in the proposal, as well as with extra training provided by the network of partners.***

The following specific training objectives (TOs) were defined to fulfill these goals:

- TO1: To enhance the attractiveness of a career in the front-line area of research in integrated photonics InP design, fabrication, characterization and modelling. To provide the opportunity for the fellows to be involved in the creation of a new line of industrial automation and organization of tasks in the InP foundry.
- TO2: To provide academic and industrial sector employers with researchers skilled in a wide range of techniques and methods, and direct experience of interaction across disciplines and sectors.
- TO3: To produce researchers with excellent transferable skills and the ability to transform abstract and challenging ideas into influential and practical outcomes.
- TO4: To create an active, long-term network of young researchers whose personal contacts, support and expertise will help Europe shape the future of research in active/passive devices and enhance/optimize the process of automated integrated photonics fabrication to enable the future of photonics industry in Europe in the next years.
- TO5: To cascade expertise and spread good practice throughout Europe by personnel exchange, and delivering European researchers able to become leaders in the fields of integrated photonics design, fabrication and characterization and industrial organization and automation in photonics industry in the near and mid-term future.

Furthermore, the four ESRs **have been enrolled (07/10/2019) in the PhD program from the UVigo (Doc-TIC)**. Doc-TIC is the PhD Program promoted by the School of Telecommunications Engineering and atlanTTic. Its mission is to train the best professionals and researchers to generate quality research with international impact and to provide the industry with professionals with advanced knowledge to improve its competitiveness at global level. Doc-TIC involves the merging and expansion of the previous PhD Programmes in Signal Theory and Communications (TSC) and Telematics Engineering, both with Mention of Excellence awarded by the Spanish Ministry of Education. Each ESR has been required to accumulate at least 30 ECTS (European Credit

Transfer and Accumulation System) credits, among the pool of scientific- and transferable skills-based courses at UVigo and TUe **to obtain their PhD title**.

In the next sections we describe the contents of the Education Programme provided in EDIFY, the number of attendants, main topics covered by each Course or training and relevant aspects of each of them.

1.1 SCIENTIFIC COURSES

The first group of scientific courses were ***SC1a and SC1b***, focused ***on basic physics and photonics*** topics:

ESR1 and 4	Title	*Photonics, quantum mechanics, solid-state physics (SC1a)*	Month: 8	Duration: 1 Month
Lead		UVigo		
Contents: This group of courses covers the latest research of optical communications and optical devices, semiconductors and quantum mechanics. Concepts on physical foundations of the optical transmission systems and optical information processes, in particular, those that deviate most from the classical technics such as the optical generation and photonic detection; Basic theory of optical devices and optical subsystems like, for example, LEDs and lasers, photodetectors, modulators, fibre amplifiers and optical filters.				
Skills for ESR1: To understand the origin and reasons for the use of optical transmission systems. To be able to specify the type of optical fibres and other necessary opto-electronical components that are needed for a certain optical link. Also, to understand their physical and technological limitations; To understand the physical concepts underlying semiconductor physics, band gaps, electrical and optical properties and their application to physical devices like optical Lasers and LEDs; To apply deep concepts related to quantum mechanics to interfaces with semiconductor materials.				
ESR2 and 3	**Title**	***Classical and Modern Physics (SC1b)***	**Month: 8**	**Duration:1 Month**
Lead		UVigo		
Contents: Fundamental concepts from classical and modern physics form the basis for the design and behaviour of materials and devices as well as provide an understanding of natural phenomena. This course will provide a basis for the specialization courses that deal with physical processes in devices such as telecom systems, electric motors, power plants, lasers, electronics or detectors and sensing systems. Basic concepts in mechanics, thermodynamics, special relativity, quantum mechanics and atomic and solid state structure are introduced.				
Skills for ESR2 and 3: Resolve problems applying the laws of Ampère, Gauss and Faraday and the Maxwell Equations; Calculate the main parameters of the electromagnetic waves: frequency, wavelength, propagation constant, polarization, Poynting vector, phase constant, attenuation constant; Analyze the propagation of waves in media with and without losses; Understanding and mastering of the basic concepts on the general laws of Mechanics and Thermodynamics; Ability to use the basic instrumentation to measure physical quantities.				

Although these courses were divided and tailored for each ESRs needs (ESR1 and 4 to SC1a; and ESR2 and 3 to SC1b), mainly due to their different background and skills, after the recruitment process it was clear that they could attend all the courses. Moreover, they wanted to attend these courses not only for refreshment purposes but to interact with other teammates and for group working.

The outline of these courses is described below.

Photonics, quantum mechanics, solid-state physics (SC1a) Prof. Francisco Javier Fraile-Pelaez

1. Basic Concepts of Photonics and Optical Communications
2. Electromagnetic Formalism of the Propagation and Amplification of Light
3. Laser Oscillation
4. Basic Nonlinear Optics
5. Direct and Coherent Optical Detection. Noise
6. Fundamentals of Quantum Mechanics
7. Fundamentals of Semiconductor Physics
8. Semiconductor Optical Sources and Amplifiers

Classical and Modern Physics (SC1b) Prof. Angel Paredes Galan

1. Introduction: from electromagnetism to optics
2. Laser physics
    Laser oscillation: basic concepts.
    Interaction of radiation with matter and line broadening.
    Passive optical resonators.
    Pumping.
    Rate equations.
    Pulsed lasers.
    Types of lasers.
3. Nonlinear optics
    The nonlinear wave equation.
    Frequency mixing.
    The Kerr effect and nonlinear effects on beam propagation. Numerical simulation.
4. Quantum optics
    Photon statistics.
    Coherent states and squeezed light.
    Cold atoms.
    Quantum information processing.

APPENDIX: Extra topics

Relativistic / ultrafast optics

Optical tweezers

Optical clocks

Topological photonics

Prof. Francisco Javier Fraile Pelaez has more than 25 years of experience in research areas like optoelectronic devices, optical communications, nonlinear optics and quantum optics. He has supervised more than 10 PhD. students and 3 postdocs. He is national evaluator from the Spanish Ministry of Education and ANEP auditor. He has more than 50 articles and has written two internationally recognized books on optical communications.

Prof. Angel Paredes Galán is Ph. D. in Particle Physics from the University of Santiago de Compostela in 2004. Postdoctoral stays at École Polytechnique (France) - as a Marie Curie fellow - , University of Utrecht (the Netherlands) and University of Barcelona (Spain). His current research interests lie at the intersection of particle physics, many body quantum physics and laser-driven optical technologies.

In the same month of the EDIFY chronogram, M8, a new scientific intensive course was given, ***SC2, related to optoelectronic devices design***. In the following Table we describe the fundamentals of this scientific-based course and corresponding skills and the topics covered.

Title	***Photonic Integrated Devices Design (SC2)***	**Month: 8**	**Duration: 1 Month**
Lead	UVigo		
Contents: Covered is the theory of optical waveguiding: propagation in free space, reflection and refraction, three layer waveguides. Guided optical modes and modal fields are treated. Three dimensional wave guides and curved waveguides are described. Waveguiding devices such as splitters/combiners arrayed waveguide gratings. Optoelectronic devices such as lasers (FP, DBR, DFB, VCSEL), semiconductor optical amplifiers and photodiodes will be explained. The steady state and dynamic behaviour of lasers is discussed using rate equation models.			
Skills for ESRs: To understand the basic concepts of photonic integration; to understand the physics and behaviour of semiconductor optoelectronic devices such as waveguiding devices, (de)multiplexers, diode lasers, detectors and their applications.			

Photonic Integrated Devices Design (SC2) Prof. Jose Ramon Salgueiro

1.Introduction

Optics for communications. Integrated optics. Waveguides. Types of waveguides. Fabrication technologies.

2. The step-index planar waveguide

Geometrical analysis. Propagation and radiation modes. TE and TM modes. Electromagnetic analysis. Energy carried by the modes. Mode excitation and coupling. Experimental techniques.

3.Graded-index planar waveguides
Parabolic profile. Variational method. WKB method.
4.Channel waveguides
Introduction and examples. Modal equations. Scalar approximation. Marcatilli's method. Effective index method.
5.Modal coupling theory
Coupled modal equations. Parallel waveguides. Symmetric waveguides. Proximity couplers. Y-junctions.
6.Numerical methods
Modal analysis in the frequency domain. Beam propagation methods. Time-domain simulation methods.
7.Optical fibers
Types of fibers. Propagation modes. Step-index fibers. Weak-guiding approximation. LP modes. Dispersion phenomena in optical fibers. Attenuation in optical fibers.
8.Photonic crystals and metamaterials
Miscellaneous topics

Prof. Jose Ramon Salgueiro, PhD in Physics from University of Santiago de Compostela (Spain) in 2001 working with the Group of Integrated Optics and Optical Fibers. After his PhD he became assistant professor at the University of Vigo in Ourense (Spain) working in nonlinaear optics with the Physical Optics Group. In 2002, he joined for two years the Nonlinear Physics Group at the The Australian National University in Canberra (Australia). Then, he had a tenure track contract of the Ramón y Cajal program in 2005 at the University of Vigo, where he is currently Professor and researchs on the fields of photonic crystals, nonlinear optics and quantum optics.

A new set of skills and competencies were acquired by the ESRs in M30 through a new course, ***SC3, in this case devoted to technology and fabrication.***

Title	***Photonic integration: technology and characterization (SC3)***	**Month: 30**	**Duration: 1 Month**
Lead	TUe		
Contents: In the technology part the following subjects are covered: Crystal properties of semiconductors, Substrate manufacturing, Vacuum technology, Epitaxy, Lithography, wet and dry etching, Plasma deposition, Metallization. The characterization part will explain how the basic parameters of a realized device can be determined. For electrical properties diode characteristics, contact and sheet resistances based on IV measurements will be explained, including the interpretation of the results. Optical characterization focusses on waveguide propagation loss (Fabry-Perot measurement), electrooptic phase shifting (interferometric measurement), gain measurement (Thomson method), laser emission (LI curves and spectral analysis), and photodetection (responsivity and dynamics). Also here proper interpretation of the results is included.			
Skills for ESRs: To understand the process steps needed for fabrication of devices and photonic integrated circuits. To learn which process steps and technologies are needed to fabricate a device or photonic integrated circuit. To understand how devices and photonic integrated circuits are measured and tested including electrical and optical characterization.			

Scientific Course SC4: Technology, fabrication and characterization (Dr. Francisco Soares)

Basics of this course: To understand the process steps needed for fabrication of devices and photonic integrated circuits. To learn which process steps and technologies are needed to fabricate a device or photonic integrated circuit. To understand how devices and photonic integrated circuits are measured and tested including electrical and optical characterization.

Syllabus

1. Technologies, materials and properties.
2. Foundry platforms and fabrication technologies: Group IV and III-V.
3. Applications depending on the technologies.
4. Introduction to characterization: the characterization part explains how the basic parameters of a realized device can be determined.
5. Electrical properties: diode characteristics, contact and sheet resistances based on IV measurements have been explained, including the interpretation of the results.
6. Optical characterization:
    a. Waveguide propagation loss (Fabry-Perot measurement).
    b. Electrooptic phase shifting (interferometric measurement).
    c. Gain measurement (Thomson method).
    d. Laser emission (LI curves and spectral analysis) .
    e. Photodetection (responsivity and dynamics). Proper interpretation of the results is included.

Dr. Francisco Soares has more than 20 years experience in the design, fabrication, and characterization of photonic integrated circuits (PICs). His main expertise is in PICs based on Indium-Phosphide technology, but he is also experienced in several other technologies as well, such as silica waveguide technology, Silicon-On-Insulator technology, and the polymer technology. He has worked in four different cleanrooms (in Europe and the US) developing fabrication processes for realizing PICs. He was one of the first researchers to implement the generic foundry model in the InP technology for realizing highly-integrated PICs containing DFB lasers, optical amplifiers, high-speed Mach-Zehnder modulators, high-bandwidth photodetectors, and all kinds of passive devices. He has supervised one PhD Student, and around five MSc Students. He has authored and co-authored more than 50 publications, and co-authored one chapter in a book.

Scientific Course 5 was also devoted to fabrication, but in this case to Silicon Photonics technology, covering Group IV skills. In the following Table we describe the fundamentals of this scientific-based course and corresponding skills acquired by the ESRs.

Title	*Systems on Silicon (SC5)*	Month: 31	Duration: 1 Month
Lead	TUe		
Contents: This course presents the student with the design trajectory to implement complex Systems on a Chip. Emphasis lies on design approaches to improve the overall system performance in terms of robustness, power-delay product, and hands-on experience to design an integrated circuit using commercial EDA tools. At the end of the course, the student will understand the various trade-offs between area, time, power, cost, and design effort, and also have the basic knowledge and hands on experience to carry out both the front and back end stages needed to implement circuits on silicon.			
Skills for ESRs: To understand SoC design complexity and performance/power trade-offs as well as manufacturing costs. To learn Physical design using EDA tools, logic simulation and synthesis and to learn technology trends in nanometer technologies.			

Topics covered in the course were: waveguiding, coupling, passive devices, resonant structures, sources, heterogeneous sources, detectors and packaging.

Scientific Course SC5: Systems on Silicon (Dr. Francisco Soares)

Basics of this course: < comprehensive repository of information, starting from the theoretical fundamentals to outlining the technical and practical issues in producing optical devices in silicon. We start with a solid theoretical analysis on the properties of guided waves, optical modes and optical dispersion. Then it takes this theory and describes how to translate it into designing waveguides in silicon using a basic rib structure and the parameters required to make these waveguides single-mode. Then we went through the processing steps that are needed to produce optical waveguides and photonic devices in silicon and is exposed to some of the processing tolerances and techniques that affect optical device performance. A very thorough and detailed analysis for producing an active device is taught and we showed the various parameters that can be varied to improve device performance. Finally, there is a technical review of the silicon-based light emitters, as well as concepts on silicon packaging.

Syllabus

7. Fundamentals.
8. The basics of waveguides. Reflection coefficients. Modes. Confinement factor.
9. Silicon-on-insulator (SOI) photonics. Effective index and refractive index. Loss and coupling. Optical modulation mechanisms.
10. Concepts on fabrication. Oxidation and doping. Metallization.
11. SOI devices: phase modulators; variable attenuators. Modelling, parametric variation, switching and performance.
12. SOI devices (II): bends, Mach-Zehnder interferometer, couplers, array waveguide gratings (AWGs).
13. Light emitting devices: erbium doping, low-dimensional geometries, Raman excitation.
14. Packaging concepts.
15. Hybrid integration with InP

Scientific Course 4 was the first of a series, including Transferable Skills Training, related to Integrated Photonics Design, using a specific set of commercial tools available through the partners of the network:

Title	*Phoenix and Photon Design intensive training (SC4)*	Month: 9	Duration: 1 Week
Lead	UVigo		
Contents: Training seminars and hands on session on Photonic Design Automation for core and metro WDM systems, optical access networks, lasers as well as active devices and circuits. Experts in the field of photonic modelling lead guided tours, provide lectures on various application topics, and are available for questions and support during individual lab exercises. Design topics include: Graphical User Interface features; Overview of signal models and simulation techniques; Parameter sweeps and optimizations; Visualization and post-processing of simulation results; Scripted simulations and automated system design.			
Skills for ESRs: Active/Passive photonic integrated circuits; Semiconductor lasers and other active photonic devices; Integrated photonic waveguides; Doped-fiber lasers and amplifiers; Hybrid (EDF/Raman) amplification and Raman pump optimization; Co-simulation (integration of third-party code).			

The outline of the course is described below.

Optodesigner and Photon Design Intensive Training

1. PICWave: an advanced laser diode and SOA model, a powerful photonic integrated circuit (PIC) design and simulation tool, a flexible design flow environment.
    a. Introduction. How to design PICs using pre-defined design kits.
    b. The calculation engine of PICWave. A powerful and flexible time-domain travelling wave (TDTW) model, from which almost all other results are derived.
    c. PICWave devices. Any number of passive elements like waveguides, Y-junctions, directional couplers, mirrors, plus active components like an SOA or an electro-absorption modulator. LRC electrical circuits can then be connected to drive the circuit.
2. FIMMWave: Waveguide Mode solvers. FIMMWAVE is a suite of robust and fully vectorial mode solvers for 2D+Z waveguide structures.
    a. Study of complementary algorithms, which allows to solve a large variety of waveguides which may be made of any material and of almost any geometry.
    b. How to model propagation in 2D and 3D structures thanks to its propagation module FIMMPROP.
3. Harold: Advance Heterostructure model.
4. Optodesigner:
    a. Photonic chip and mask layout
    b. OptoDesigner advanced connectors and autorouting
    c. OptoDesigner simulation modules
    d. Photonic design verification

All these Courses were related to photonics and physics and introductory techniques for technology, fabrication and design. All of them were awarded between 1 and 5 ECTS, as described in respective 6.X Deliverables, required for the Doctoral Degree award. The competences acquired by the ESRs were:

- Ability to project, calculate and design products, processes and facilities in photonics areas.
- Capacity for mathematical modeling, calculation and simulation in engineering companies, particularly in research, development and innovation tasks in areas related to photonics and associated multidisciplinary fields.
- Ability to apply acquired knowledge and to solve problems in new or unfamiliar environments within broader and multidiscipline contexts, being able to integrate knowledge.
- Ability to apply advanced knowledge of photonics, optoelectronics and high-frequency electronics.

As well as proposed learning outcomes:
1. Functional knowledge of the essential photonic devices for optical communications: LEDs and lasers, photodetectors, optical modulators, couplers, circulators, AWG, fibre amplifiers, semiconductor optical amplifiers, optical filters, single-mode fibres, multi-mode fibres and multicore fibres.
2. Knowledge of the noise models used to characterise the optical transmitter subsystems, optical amplifiers and receivers, and capacity to calculate its impact in terms of the signal to noise ratio and error probability.
3. Knowledge of the physical concepts underlying semiconductor physics, band gaps, electrical and optical properties and their application to physical devices.
4. Understanding and mastering of the basic concepts on the general laws of Mechanics and Thermodynamics; Ability to use the basic instrumentation to measure physical quantities.

The methodology applied was based in:
Lectures: The professor introduces the main contents of each chapter to the students. These lectures did not cover all the contents of each subject. For that reason, the students had to review the supplementary notes provided in class. It is also expected that the students reviewed the concepts introduced in the classroom and expand on their contents using the guide of each chapter, together with the recommended bibliography, as a reference.
Laboratory: The lectures included some exercises in the lab involving different optical devices and optical communication systems.

Case studies: It consisted on activities that complement the master sessions and allow a better understanding of the theoretical concepts.

In addition to the scientific-based training, EDIFY offerED to all ESR specific short-term hand-on training which provided the ESRs with skills in highly experienced organizations, receiving cutting-edge technological knowledge and skills. These hands-on training have been provided at the same time the ESRs are seconded to Partner Organizations providing the courses, i.e. BP, and were aimed to explore knowledge in circuit simulation and packaging.

In the following Table we describe the fundamentals of these technical hands-on courses and corresponding skills acquired by the ESRs.

Title	***Hands-on Optodesigner training (TC1)***	**Month: 22**	**Duration: 1 Week**
Lead	PBV		
Contents: To get an overview of the latest status of the integrated photonics eco-system for the three major photonics technologies: InP, silicon photonics and TriPleX (SiN). This overview will include the available design tools today and the importance of considering test and packaging in an early stage. The unique combination of lectures and hands- on training exercises will teach how to perform circuit simulations, including fabrication tolerances, how to use and develop a design library (PDK) and how to set-up libraries in a structured way. PhoeniX Software tools will be used for this purpose.			
Skills for ESRs: Get introduced to Integrated Photonics Design Flow Automation. Learn the use of photonic integrated circuit simulation tools. Obtain in-depth knowledge of integrated design from mask to photonic and process flow simulations. Exchange experiences and ideas with other participants.			
Title	***Hands-on Fimmwave, PICWave and Harold (TC2)***	**Month: 23**	**Duration: 2 Weeks**
Lead	PDesign		
Contents: To learn a suite of robust and fully vectorial mode solvers for 2D+Z waveguide structures. It supports a complementary algorithms which allows it to solve a large variety of waveguides which may be made of any material and of almost any geometry.			
Skills for ESRs: to learn how to model InP related waveguides; buried, etched (rib, ridge) and geometries commonly used in opto-electronics; , slanted-wall and graded structures; and waveguides; simulation of gain and absorption spectra of active material.			
Title	***Bright Photonics (TC3)***	**Month: 22**	**Duration: 1 Week**
Lead	BP		
Contents: PIC design flow and design training; How to develop a PIC from user specification to packaging. This reaches across PIC technologies (SOI, InP, SiN, glass) and across multiple packages. The training will be hands-on on the newly in-house developed open source Nazcad design flow tool, covering mode solving, foundry and technology definition, layout design and verification, and data processing.			
Skills for ESRs: An introduction towards becoming an all-round PIC engineer and exposure to the latest software developments in the open source Python language to empower the engineer to customize a design flow to evolving needs.			

The first of these **Technical courses, TC1 – Hands-on Optodesigner Training**, had the following syllabus:

Technical Hands-on Course TC1: Hands-on Optodesigner Training

1. Installation. Windows, Linux. Installing PDKs. Codemeter
2. Create your first Mask Layout.

3. Connecting elements.
4. Elastic connectors.
5. Elastic ruler.
6. Asymmetric Mach-Zehnder interferometer.
7. Mode solver simulation.
8. Refractive index target for frequency domain.
9. Introduction to Phoenix script engine
10. Mask layout. GDS layers. Design rule checking. Autorouting.
11. Introduction: developing a PDK.

EXAMPLES

Simulations: Mode solver. FMM-FD. Thermo optics.

Simulations: Propagation. Beam propagation. Bidirectional eigenmode.

The second of these **Technical courses, TC2 – Hands-on Fimmwave, PICWave and Harold Training**, was related to two different solvers:

Fimmwave is a vectorial 3D mode solver including a variety of calculation engines each optimized for different geometries. Suitable for all types of waveguides including multi-mode waveguides & fibers, high index structures (E.g SOI), metals, Graded Index, photonic crystal fibers and more.
PICWave is a bidirectional time-domain modeling of photonic ICs capable of modeling the interaction between both passive and active components using the TWTD (Travelling Wave Time Domain) method. Suitable for studying the interaction of optical components in a larger circuit as well as the design of individual active components such as Laser Diodes, SOAs, TWAs, DFB & DBR lasers. PICWave can model gain switching, mode-locking, time resolved spectra and more.
Harold is a detailed hetero-structure laser diode modeling. Including bandgap narrowing, quantum wells - capture/escape, recombination, strain, drift-diffusion, power dissipation effects. Can be used as a stand-alone product or complementary to PICWave.

Technical Hands-on Course TC2: Hands-on Fimmwave, PICWave and Harold Training (Dr. Nathan Soper)

1. **Fimmwave:**
    a. **The FMM Solver:** This solver, based on the Film Mode Matching method, is optimized for rectangular waveguide structures commonly seen in integrated optics. It is fully

vectorial capable of solving structures with complex refractive index such as metallic components, or even radius of curvature.

b. **The FDM Solver:** The FDM Solver brings the Finite Difference method to FIMMWAVE. It can model both real and lossy materials, supports PML absorbing boundary conditions, and anisotropic dielectric tensors (diagonal tensor).
c. **Effective Index Solver:** This well known approximate method is both a fast and reliable way of finding estimates for 3D modes for near 2D waveguides (many ridge structures fit into this category). This home grown solver is extremely robust; in particular it can deal with structures with completely decoupled cores.
d. **The FEM Solver:** The FEM Solver brings the Finite Element method to FIMMWAVE and is offered as an optional add-on to the base module. Ideal for structures with curved interfaces or unusual shapes such as holey fibers.
e. **Vectorial Fibre Solver:** This option houses two vectorial engines for solving generic circular waveguides with arbitrary refractive index. The first is based on a rigorous solution to the vectorial wave equation in cylindrical co-ordinates. It will find all the modes of such structures using metallic or transparent boundaries. Although it is a fully vectorial solver it exploits the circular symmetry, thus making it an almost instant calculation.
f. **Stress Solver:** The Stress Solver for FIMMWAVE allows the user to calculate the stress fields in a waveguide and the consequential perturbation of the waveguide modes. This Finite Element method based solver supports thermally induced stress fields – typically generated during cooling of a device constructed from materials with different thermal expansion coefficients.
g. **Thermal Profiler and EO module:** This option allows the user to study the thermal or electro-optic response of the waveguides. The change in refractive index profile of the structure is calculated by a 2D Poisson Solver before the subsequent modes are calculated.
h. Design utilities and optimization.

2. PICWave:

a. **Active module:** Lorentzian optical phase and intensity noise model; Electrical noise model; Travelling wave electrode model; Longitudinal hole burning; Lateral hole burning; Carrier diffusion; Non-linear gain; Auger processes; Thermal effects.

b. **Features:** PI and PV curves; MQWs; Quantum efficiency; Chirp simulation; RIN spectra; Material database system; Import gain tables; Electro-absorb modulator model.
c. **Applications:** Photonic integrated circuits (PICs); Tunable laser diodes; Large ring resonators; Mach-Zehnder modulators; Travelling wave SOAs; Electro-absorption modulators.

EXAMPLES

Large ring resonator.

Mode hopping in a Fabry-Perot laser.

3. **Harold:**
    a. **Electrical model**: Self consistent solution of Poisson Equation, drift-diffusion, and capture/escape for both holes and electrons.
    b. **Thermal model**: Full vertical-longitudinal solution of the heat flow equation, including the substrate, the metal contacts and the heat sinks.
    c. **Optical model**: Photon distribution according to the optical mode of the laser cavity. The total photon density is determined considering the gain/loss balance in the full cavity.
    d. **Capture/escape**: In QW regions, thermal equilibrium between confined and unconfined carriers is not assumed, but described by means of appropriate capture/escape balance equations.
    e. **Quaternary alloys**: Utilization of quaternary alloys is fully supported through the material database.
    f. **Gain model**: Material gain for quantum well lasers is computed as a function of the wavelength and carrier concentration, using a parabolic band approximation.
    g. **Recombination:** Shockley-Read-Hall, Auger, stimulated and spontaneous recombination processes are included.
    h. **Surface recombination:** Recombination at the facets is included via deep trap levels at the mirror.
    i. **Quantum well:** The program will determine the energy levels by solving Schrödinger's equation; this data is then used in the gain computations.

And finally, the last one of these courses specifically designed to acquire master practice in integrated photonics design was **TC3 – Bright Photonics Training**.
Topics covered in the TC3 were: PIC layout design, cells and layer, interconnect, building block and PDK creation, GDS introduction and advanced manipulation, connection DRC, circuit level path-tracing and compact models.

Technical Hands-on Course TC3: Bright Photonics Training (Dr. Katarzyna Lawniczuk)

1. **Introduction**: PIC requirements and specifications depending on the specific application. Technology selection.
2. **PIC technologies (SOI, InP, SiN, glass).** PIC design constraints related to technology and across multiple packages. How the PIC specifications and technology selection influence the circuit design. How to carefully design your PIC to accommodate the circuit into the mask layout.
3. To learn to use **PIC design with Nazca Design in Python**:
    a. To **get started and directions** into the more advanted features of circuit integrity validation, GDS manipulation and PDK development.
    b. **The role of Nazca** in the PIC development chain and how an open source design tool with community and commercial support provide long term security, flexibility and innovation.
4. **Hands-on through an example: A PIC transceiver**. Design flow tool. Foundry and technology definition. Layout design and verification. Mode solving. Data processing.

With these contents, the ESRs have acquired a set of **competences**:

- Capacity for mathematical modeling, calculation and simulation in engineering companies, particularly in research, development and innovation tasks in areas related to photonics and associated multidisciplinary fields.
- Ability to apply acquired knowledge and to solve problems in new or unfamiliar environments within broader and multidiscipline contexts, being able to integrate knowledge.
- Ability to apply advanced knowledge of photonics, optoelectronics and high-frequency electronics.

The **methodology** applied was based in:

Lectures: The lecturer introduced the main contents of each chapter to the students. These lectures did not cover all the contents of each subject. For that reason, the students had to review the supplementary notes provided in the Nazca Design manuals. It is also expected that the ESRs reviewed the concepts introduced in the webinars and expand on their contents using the guide of each chapter, together with the recommended bibliography, as a reference.
Laboratory: The lectures included some exercises in the lab involving different optical devices and optical communication systems.

1.2 TRANSFERABLE SKILLS TRAINING

Sometimes it's difficult for PhD students to identify what skills they have since the academic experience is not necessarily focused on articulating skill sets. We also often find that PhD students struggle, understandably, to present the transferability of their academic experiences to non-academic contexts. In the EDIFY project we provided the ESRs with a set of Transferable Skill Courses that help them solve some of these problems. Specifically, we have designed some courses on these areas:

Entrepreneurship Skills

- Facilitate group discussions or conduct meetings
- Motivate others to complete projects (group or individual)
- Respond appropriately to positive or negative feedback
- Effectively mentor subordinates and/or peers
- Collaborate on projects
- Teach skills or concepts to others
- Navigate complex bureaucratic environments

Project Management & Organization

- Manage a project or projects from beginning to end
- Identify goals and/or tasks to be accomplished and a realistic timeline for completion
- Prioritize tasks while anticipating potential problems
- Maintain flexibility in the face of changing circumstances

Written & Oral Communication

- Prepare concise and logically-written materials
- Organize and communicate ideas effectively in oral presentations to small and large groups
- Write at all levels — brief abstract to book-length manuscript
- Debate issues in a collegial manner and participate in group discussions
- Use logical argument to persuade others
- Explain complex or difficult concepts in basic terms and language
- Write effective grant proposals

1.2 TRANSFERABLE SKILL COURSES

The Transferable Skill Courses included in the EDIFY program were:

Title	*Project management (TSC 1)*	Month: 40	Duration: 1 Week
Lead	UVigo		
Contents: This course will give an introduction into the basics of project management in particular to the notions of project life cycle, milestones, deliverables, special requirements of complex R&D projects, work breakdown structure and work packages, cost projection and risk assessment, communication, etc. Exercises will be provided from the many years of experiences with coordinating projects funded by the European Commission.			
Skills for ESRs: The ESRs learn to properly set-up and plan a project with new approaches to time management.			
Title	***Scientific writing and dissemination (TSC2)***	**Month: 40**	**Duration: 2 Weeks**
Lead	UVigo		
Contents: The purpose of this seminar is the improvement of written English skills specifically e vocabulary and styles required for scientific writing. Resource materials and strategies for verifying the specificity and correctness of specialty vocabulary for scientific papers and publications will be made available to the participants and discussed. These materials can be used by the participants to continue improvement of writing skills after the seminar.			
Skills for ESRs: The ESRs learn how to use written language effectively to present scientific data for scientific publishing. To learn how to deal and manage innovation processes in company, to understand the workflow of innovation and research in a company department, to learn how to manage the ESR´s scientific career, to evaluate and develop a proposal for an European project.			
Title	***Entrepreneurship (TSC3)***	**Month: 42**	**Duration: 1 Week**
Lead	UVigo		
Contents: The course covers the essentials on:- ***Day 1*** - Business Models and Business plan construction; Business mission statement, vision, products & services; Definition of the target markets using the Value Proposition Canvas; Understanding the target industry;- ***Day 2*** **-** The basics of marketing and marketing for different Products or Service types: The internet side of marketing; Developing a market communications plan including how to communicate benefits and competitive advantages; Promotional components to help reach target customers including estimated costs - ***Day 3*** **-** Legal and Operations Understanding the different legal entities and pros and cons of each; Basics of employment law, workers' compensation & unemployment compensation - the difference between independent contractors and employees; Basics of patents, copyright, trademarks & trade secrets - Buying a business or franchise - An overview of business operations (Technology needs, Location, Risk Management); Human Resource Management and Operations - Management/personnel regulations and job descriptions - Hiring the first employee, including recruiting & interviewing - Operations Continued; Accounting and Record Keeping; Financing- crowdfunding, angel and venture capital - Importance factors including credit for bank financing - Steps for applying for a loan - Different reasons for borrowing money (start-up, cash flow, capital equipment, expansion, etc.			
Skills for ESRs: Analyse customer value creation; Conduct an initial novelty screening and draft a patent application; Draft a business plan on a selected subject; Analyse team member skills, competencies and experience Identify business opportunities in industrial challenges.			

TSC2- SCIENTIFIC WRITING AND DISSEMINATION (40 HOURS)

Scientific writing and publishing

- Develop writing skills and confidence writing for journals
- Understand editorial processes and what editors look for
- Learn best practices for submitting a paper and peer review

Effective collaboration in research

- Understand the different forms, benefits, and challenges of collaborative research
- Develop key collaborative skills such as communication and teamwork
- Learn how to initiate and run a successful collaboration
- Learn how to maximize the value of, and conclude, a collaborative project

Data Management & Narrative Tools for Researchers

- Understand the benefits of managing research data effectively
- Learn the steps required to create and maintain a data management plan
- Learn how to apply best practices to organise, store, archive and check the quality of your data
- Evaluate the different options for sharing research data
- The importance of conducting effective data analysis
- The best tools for exploring various datasets
- The range of analytic methods available and understand which is most suited to your data
- Strategies for obtaining feedback, troubleshooting and expressing the limitations of your analysis

Grant Writing, Networking, Communications and Experimental Design

- Understand how narrative tools can improve the quality of your grant applications
- Learn to align your grant proposal with the requirements and objectives of your chosen funder
- Learn how to apply narrative tools when writing their grant proposal to make it more informative, persuasive and engaging

- Identify techniques that can help to overcome the challenges that researchers commonly experience when delivering oral presentations
- Learn how to build compelling research stories to use as the foundation for your presentations
- Learn how to create professional slide decks that effectively communicate research findings to your audience
- Learn how to apply strategies to help you deliver your presentation effectively on the day, in both virtual and face-to-face environments

- Understand the theory behind and the importance of networking, and how to use your research and career goals to guide you to find appropriate networking opportunities
- Learn how to research and prepare key resources to help you build an effective network
- Learn strategies to approach and connect with potential contacts, and how to follow up – both in person and online
- Learn strategies for nurturing your networking contacts, and how to leverage them to advance your research and career

TSC1- PROJECT MANAGEMENT (150 HOURS)

Upon completion of the Nature Masterclass Course, ESRs are able to:

- Understand project management design, development, and deployment
- Use project management tools, techniques, and skills
- Employ strategies to address the ubiquitous issue of resistance to change
- Align critical resources for effective project implementation
- Understand the implications, challenges, and opportunities of organizational dynamics in project management
- Identify and use key performance metrics for project success
- Understand how to manage project cost, quality, and delivery
- Engage and lead effective project management teams in your organization
- Impart project management knowledge, tools, and processes to your colleagues
- Recognize and mitigate the early seeds of failure in the project life cycle

The syllabus of the course is:

The Right Start: Preparing people and organizations for the challenge of change: Identify and link the three essential elements of true innovation

- Examine insights into the antecedents and consequences of project failure
- Summarize the characteristics of a change-adverse workforce
- Identify the driving force in establishing individual readiness for change
- Define three domains required to create organizational readiness for change
- Discuss, interpret, and ascribe meaning to a typology for change initiatives
- Examine seven critical success factors for launching change initiatives
- Understand the structure and expectations of MGMT 5030 Project Management

Strategic Excellence in Project Management: Project Activation Management System (PAMS) Process for Project Management

- Consider the definition and common attributes of a project
- Understand stakeholders' key to the early development of a project

Phase II: The Start-Up Process. Introduction to Green-Lighted Projects PAMS Process for Project Management

- Review the steps in the Start-Up process
- Understand how to build a strong project foundation
- Discuss the challenges and opportunities of working in a team
- Discuss the team expectations document that teams created
- Consider strategies to influence without authority

Phase III: "Develop" – Preparing Projects for Launch PAMS Process for Project Management

- Explore elements of key project management tools including WBS, schedule, budget
- Understand risk mitigation strategies
- Consider key performance metrics
- Discuss scope and scope statements

Phase IV: "Implement" PAMS Process for Project Management

- Construct the final project implementation plan
- Manage plan revisions and change control

- Conduct problem solving and stakeholder management
- Discuss strategies for monitoring the project implementation plan

Phase V: "Close" PAMS Process for Project Management

- Explore the process for closing out the project
- Capture Lessons Learned
- Highlight the importance of project team recognition

Tales and tips from the Field: Enable East Case Studies

Project Presentations, assignments

<u>TSC 3 – ENTREPRENEURSHIP (120 HOURS)</u>

The ESRS received an additional online training on Entrepreneurship in a seven modules training:

Strategic Innovation: Building and Sustaining Innovative Organizations

- Understand key ideas about innovation and product strategy
- Strategize for value capture in a business model
- Critically examine the roles of various players in a business ecosystem

Strategic Innovation: Managing Innovation Initiatives

- Analyze innovations and their impact on organizations
- Articulate a research-informed perspective on innovation
- Utilize frameworks, tools, and concepts to address challenges that arise in innovation

Creativity Toolkit I: Changing Perspectives

Design pitches for innovative ideas to build excitement and clarity
-Evaluate the pitches of others to identify great new ideas
-Lead groups to foster effective collaboration for innovation

Entrepreneurship I: Laying the Foundation

- Develop a foundational understanding of the entrepreneurial process
- Consider the relationship between growth and error
- Understand how particular opportunities influence entrepreneurial phenomena

Entrepreneurship II: Preparing for Launch

- Develop an understanding of what is required in a new venture
- Create a plan to identify and approach your first customers
- Build financial projections for the new venture
- Understand how to raise equity capital for the new venture
- Monitor the health and scalability of a new venture

Innovation: From Creativity to Entrepreneurship Capstone

- A venture of one's own or within a larger organization
- To develop the current business model and compare against alternative business models so as to identify potential opportunities and challenges.

1.3 OTHER COURSES

Finally, other courses were offered as part of the education program of the ESRs:

- Winter School training:
  The four ESRs have been enrolled in a Winter School (28th of October - 08th of November 2019) taking advantage of the annual JePPIX Design Course. JePPIX (http://www.jeppix.eu/) is the joint European platform for photonic integrated components and circuits, established in 2006, and committed to driving the industrialisation and use of high performance indium phosphide, silicon nitride and hybrid photonic integration. JePPIX Partners representing all Photonics Supply chain work together to stimulate the evolution of integrated Photonics by defining standards, and optimising work flow to ensure the best insight into the technology. JePPIX also shares insights on the evolution of technology, emerging markets and applications, and future customer demands in the JePPIX Roadmap.

This two weeks flagship immersion Winter School has been held at the Eindhoven University of Technology between 28th of October, 2019 and 08th of November, 2019. Our ESRs have been enrolled in this training, that is designed for students/researchers/professionals who have a good background in photonics and who wish to understand how to get the best out of design tools and the PIC technology. Experts from the Institute of Photonic Integration (formerly known as the COBRA Institute) are joined by specialist trainers from the Photonic CAD community, professional designers and experts from foundries to share insights and knowhow.
Participants gain first hand clean room experience and a detailed insight into the steps in designing and creating PICs. The Winter School covers the theory and practice of integrated photonic component and circuit design using the powerful JePPIX building blocks. Hands on training with lab tools and design tools are complemented with clean room tours to develop insights into design rules. Layout and simulation methods are developed with JePPIX CAD tool developers and professional designers.

In the first week of the Winter School, our ESRs have developed insights into mode analysis to better understand the design space for waveguide based integrated optics, how best to construct interferometers and filters. Active building blocks including semiconductor optical amplifiers, modulators and detectors have been introduced in terms of physical principles and practical implementation as components and circuit elements. Methods for laying out circuits have been developed. Hybrid and monolithic integration schemes have been described.

In the second week, the emphasis turned to practical skills, with the opportunity to trial commercial CAD tools, process design kits (PDKs) and develop insights with expert designers and leading academic instructors. Representatives from the foundries have also been available to talk through the latest platform capabilities. Visits to clean room facilities and measurements laboratories were included to provide insights into the role of fabrication tolerances and testing methods on design methods. Packaging have also been reviewed to ensure package, test and manufacture aware design.

The technical program of this Winter School was:

JePPIX PIC Design Course 2019. Week 1					
Time	**Monday (28.10)**	**Tuesday (29.10)**	**Wednesday (30.10)**	**Thursday (31.10)**	**Friday (1.11)**
09:00-10:00	Welcome / JePPIX Ecosystem *Kevin Williams*	MMI couplers *Xaveer Leijtens*	Active components. Part I: SOA, lasers *Erwin Bente*	Processing Introduction, Lithography, epitaxy, COBRA Flow *Yuqing Jiao*	Active components. Part II: SOA, lasers *Erwin Bente*
10:15-11:15	Dielectric waveguide basics *Xaveer Leijtens*	Arrayed Waveguide Gratings *Xaveer Leijtens*	Simulation methods: Mode, BPM, FDTD *Victor Calzadilla*		RF components: MZI, EAM, Detectors - Part 1 *Weiming Yao*
11:30-12:30		Mode analysis *Xaveer Leijtens*	What is a mask? GDS, cell, PDK, DRC *Ronald Broeke*		Why InP? Application examples *Meint Smit*
Lunch break					
			Parallel sessions	**Parallel sessions**	**Parallel sessions**
13:30-14:30	2D confinement, propagation Xaveer Leijtens	Overview of software tools	**Measurement Lab 2 groups** / **Software Hands-on NAZCA or Photon Design or Luceda***	**Cleanroom 2 groups** / **Software Hands-on NAZCA or Photon Design or Luceda or Synopsys***	**Cleanroom 2 groups** / **Software Hands-on NAZCA or Photon Design* or Luceda**
14:45-15:45	Curved waveguides, junctions Xaveer Leijtens	Participants' presentations			
16:00-17:00	Couplers and splitters Xaveer Leijtens	Mode analysis *Xaveer Leijtens*			
		Social dinner		**Het Walhalla**	

JePPIX PIC Design Course 2019. Week 2					
Time	**Monday (4.11)**	**Tuesday (5.11)**	**Wednesday (6.11)**	**Thursday (7.11)**	**Friday (8.11)**
09:00-10:00	Process tolerances and device design *Victor Calzadilla*	Characterization of Optical chips *Weiming Yao*	Fraunhofer HHI *Moritz Baier*	Klayout	Evaluation 9:-9:30
10:15-11:15	SMART Photonics *Luc Augustin*	Lasers in InP technology *Erwin Bente*	LioniX International *Douwe Geuzebroek*	Practical hands-on worked example	Design with Experts
11:30-12:30	Standardization and packaging. Part I *Sylwester Latkowski*	Speed workshop on rate equations solver *Erwin Bente*	From system specs to PIC design Iñigo Artundo	JePPIX MPW workflow and DRC	
Lunch break					
		Parallel sessions	**Parallel sessions**	**Parallel sessions**	
13:30-14:30	Standardization and packaging. Part II *Sylwester Latkowski*	**Measurement Lab 2 groups** / **Software Hands-on Lumerical* or Synopsys or VPIphotonics**	**Cleanroom 2 groups** / **Software Hands-on Lumerical or Synopsys or VPIphotonics**	**Measurement Lab 2 groups** / **Software Hands-on Lumerical or VPIphotonics***	
14:45-15:45	RF components: MZI, EAM, Detectors - Part 2 *Weiming Yao*				
16:00-17:00	Hybrid integration Kevin Williams				
				Het Walhalla	

- Additional complementary skills training not included in the original proposal (all ESRs attended in virtual mode):
  - Nanophotonics and nanoelectronics. May 2020 – webinar
  - Structures for near field enhancement for detection and spectroscopy. May 2020 - webinar.

- VLC Photonics Webinars - Photonic Integration Technology – Sep/Dec 2020
- UVigo - How to manage a research project. Mar 2021
- Synopsys workshop – How to simulate LiDAR systems. Mar 2021
- From Waveguides to Optical Transmission Systems VPI training-Oct 2021

Finally, find below the ESRs PhD thesis submitted (ESR1 and ESR2) and drafts (ESR3 and ESR4). ESR1 will defend on 27/02/23, ESR2 on 13/02/23 while ESR3 will wait until April 23 and ESR4 in March 2023.

Universidade Vigo

Universidade Vigo

Integrated indium phosphide quantum key distribution and coherent transmitter – Damiano Massella

TESE DE DOUTORAMENTO

QKD and QPSK integrated optical transmitters.

Damiano Massella

Ano: 2022

Universidade Vigo

EIDO
Escola Internacional
de Doutoramento

Universidade Vigo

Escola Internacional de Doutoramento

Damiano Massella

TESE DE DOUTORAMENTO

QKD and QPSK integrated optical transmitters.

Dirixida polos doutore:

Dr. Francisco Javier Díaz Otero

Ano: 2022

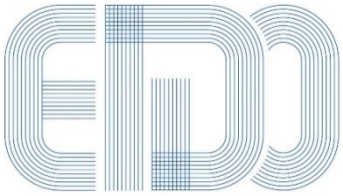

International Doctoral School

Universidade Vigo

Escola Internacional de Doutoramento

Francisco Javier Díaz Otero

FAI CONSTAR que o presente traballo, titulado "*QKD and QPSK integrated optical transmitters*.", que presenta Damiano Massella para a obtención do título de Doutor, foi elaborado baixo a súa dirección no programa de doutoramento "Tecnoloxías da Información e as Comunicacións".

Vigo, 30 de Diciembre de 2022.

Os Directores da tese de doutoramento

Dr. Francisco Javier Díaz Otero

DAMIANO MASSELLA

QKD AND QPSK INTEGRATED OPTICAL TRANSMITTERS

QKD AND QPSK INTEGRATED OPTICAL TRANSMITTERS

DAMIANO MASSELLA

Design and Characterization of photonic integrated chips

Damiano Massella: *QKD and QPSK integrated optical transmitters,*
Design and Characterization of photonic integrated chips, © June 2022

Damiano, lo sai perche le cose cadono?

— my dad

You either die a physicis or you live long enough to see yourself become the engeneer.

–Batman

Dedicated to all those that try their best.

ABSTRACT

Secure communications of the future will need to implement Quantum Key Distribution systems in order to coop with the growing computational power of quantum computers. For mass adoption of these systems we will need to integrate different optical components into small chips. In this work we present the design and experimental verification of photonic integrated circuits able to, not only implement Quantum key distribution protocols, but also classical coherent communications. The possibility of using these designs for either type of communication with state-of-the-art performances makes them ideal for future mass adoption.

Focusing isn't just an optical activity,
it is also a mental one.

— Bridget Riley

ACKNOWLEDGMENTS

This thesis project has been founded by the European Union under the Marie Sladowska Curie action with the name of European Doctorate on Indium Phosphate Technologies(EDIFY).

For the incredible support and help that I received in the making of this project I would like to thank the following people:
Francisco Diaz, for his help in the organization of the project and for being my supervisor during the entire three year of this PhD.
The entire Bright Photonics team, Ronald, Katarzyna, Marco, Stef, Michael, Lodovico and Gido, for the help in the design of the chips, the programming of the interface and the incredible learning experience during my internship in Bright.
Smart photonics and Fraunhofer Heinrich-Hertz-Institute for the fabrication of the chips and in case of Smart photonics for allowing me to experience first hand the environment of a foundry.
Steven Grijseels, for being my supervisor during my internship in Smart photonic and for teaching and guiding me during that period.
David Alvarez Outerelo, for building the experimental setup in Vigo and helping me with the experimental characterization of my chips.
My adventure's colleagues, Andrea and Marcin, for the nice time spent together and the good scientific (and not) discussions.
Rachel, for her support in both my scientific and personal life, I ultimately own to her for keeping me mentally healthy during different moments of this journey.

In fine vorrei ringraziare la mia famiglia senza la quale sarebbe stato impossibile per me arrivare a questo importante traguardo:
A Gli zii di Mantova che hanno sempre portato una boccata di allegria nella mia vita.
A mia zia Nadia, per avermi insegnato il bello della letteratura e

del pensiero umanistico e per aver condiviso insieme un viaggo dall'inferno fino al paradiso.
A mia sorella Giulia che, anche se lei non lo sa, é sempre stata un modello di riferimento per coraggio e dolcezza, due doti apparentemente opposte che in lei si fondono perfettamente.
A mia madre Mirella, che piu di ogni altro mi ha insegnato a comprendere le persone e il valore dei sentimenti propri ed altrui.
A mio padre Lucio, il cui contributo puo essere riassunto nella domanda che apre questa tesi: "perche le cose cadono?". Questa domanda, rivolta a un me di 8 anni o poco piu, ha sempre rappresentato per me l'inizio della mia carriera da studente della natura, insegnandomi anche le domande piu semplici posso nascondere risposte complesse.

CONTENTS

LIST OF FIGURES

LIST OF TABLES

ACRONYMS

AWG Arreyed Waveguide Gratings

BB Building Block

BB84 BennetBrassard1984 Bennett and Brassard [1]

CCW counter clockwise

CV-QKD Continuous Variable Quantum Key Distribution

CW clockwise

DFB Distributed FeedBack laser

DBR Distributed Bragg Reflector

DRC Design rule check

DV-QKD Discrete Variable Quantum Key Distribution

FP Fabry-Perot

HHI Fraunhofer Heinrich-Hertz-Institute

MDI-QKD Measurement device independent Quantum Key Distribution

MMI Multi Mode Interferometer

MUB Mutually Unbiased Base

MPW Multi-project Wafer

MZI Mach-Zender interferometer

OIL Optical injection Locking

OTP One-time-pad

PDK Process design kit

PIC Photonic integrated Circuit

PNS photon number splitting

QBER Quantum Bit Error Rate

QKD Quantum Key Distribution

QPSK Quadrature Phase Shift Keying

RF Radio Frequency

SNR Signal to Noise ratio

SOA Semiconductor Optical Amplifier

SOI Silicon on Insulator

SSC Spot Size Converter

SUMMARY

PHOTONIC INTEGRATED CIRCUITS

Similar to the process that underwent microelectronics in the past, optical devices see an increase interest in the miniaturization of components and circuits. In this context Photonic integration has been developed, first with application oriented processes but recently leaving space to a generic integration model. Generic photonic integration aims at lowering the barrier to enter the market of photonic integration and it does so implementing a series of processes and procedures that are unified across the production and design chain.
In this thesis the generic integrated photonic approach will be presented and discussed in each step that goes from the circuit idea to the packaged chip.

Photonic integrated Circuits (PICs) are devices that include multiple photonic components into a single chip. The first Idea of photonic integration was suggested in 1969 by S.Miller [2]. Since then, the Advances in the field lead to the first commercialized PIC by the company Infinera in 2005. Nowadays, the commercial offer of integrated photonics has widened with several companies offering different range of products and materials.

Overview of integrated photonic technology

The variety of integrable components depends on the materials and processes used for fabrication, but it ranges from passive components: waveguides, splitters, multiplexers and others, to active components like SOAs and photodiodes [3]. Although the main domain of photonic integration has been mainly telecommunications in recent years a series of application in different fields as bio-photonics, tomography and quantum technologies have emerged [4, 5].
The performances and possibilities of designed circuits strongly depend on the material platform used in the fabrication:

- III-V based platforms, are the only ones that allow the integration of gain components due to the direct bandgap of the crystalline structures. Usually these platforms have lower performances in passive building blocks such as

waveguides due to the high absorption of the surrounding material needed electrical conduction.

- Silicon on Insulator (SOI) platforms, offer great performances of passive components and lower costs thanks to the use of fabrication technologies taken borrowed from the electronic industry. They can integrate modulators and photodetectors. Respect to III-V platforms the absence of a gain module limits the application or requires the bonding of the SOI chip to a III-V chip.

- SiN platforms, offers a wider range of wavelengths operation due to the larger transparency window respect to other platform. Similar to the SOI case the absence of a gain section require the co-integration with other platforms to have light emitting components

The above list comprehends only the main materials and technologies, but different types are being developed and commercialized in recent years including glass based materials and polymers.
We will limit the discussion of this thesis to InP based integrated photonics and all the chips discussed here have been fabricated, or are still under fabrication, in the InP material platform.

QUANTUM KEY DISTRIBUTION

QKD is a rapidly evolving field of quantum information, new protocols and security proofs are developed regularly, and experimental demonstrations are moving from labs to in-field implementations. In this thesis we will cover the basic aspects of the technology in order to give the user the basic knowledge and reference to approach the QKD world. In the first introductory part we will cover the basic protocol BB84[1] discussing the basic theoretical aspects and the most common implementations. The second part is dedicated to the state of the art of experimental research and will discuss the recent advances in free space photonics QKD and integrated photonics.

Theoretical-secure communication

In Secure Communications two parties, conventionally named Alice and Bob, want to communicate privately using a common channel. The presence of an eavesdropper Eve, undermines the privacy of this communication. The best way for Alice and Bob to ensure that their information remains private is to use an

information-theoretical secure communication, meaning a communication that is fundamental secure by theory and even if Eve has a far superior technological advantage over Alice and Bob she can not decrypt the message. This type of communication can be achieved using a One-time-pad (OTP) method [6]. The OTP consists of a long key of random character that is ideally as long as the message and is kept secret from Eve. As long as the key remains secret and is used only once [7], the communication between Alice and Bob can be considered information-theoretical secure.
This communication procedure leaves us with a different problem, how can Alice and Bob share the key?
This is known as the key distribution problem.
The current solution to the key distribution problem is public key cryptography, in this concept Bob has a pair of keys. One of these two keys is public and Alice can use it to encrypt the message. The encrypted message can be decrypted only using Bob's private key. This type of cryptographic system is used extensively nowadays but is not information-theoretical secure. In fact the security is based on the fact that given the public key there is no efficient algorithm to calculate the private key. For instance the RSA [8] system is based on the factoring of large integer number, this task is extremely time-consuming for a classical computer. This kind of cryptography is clearly not resistent to advances in technology. It has been even more evident since the invention of the Shor algorithm[9] that creates an efficient way of calculating integer factorization using quantum computers.
Although the Shor algorithm requires a high number of qbit to execute and nowadays is not feasible, recent progresses in quantum computers technology are getting closer to the required specification.
QKD promises to solve the problem using fundamental laws of nature like the uncertainty principle and the entanglement of quantum particles. The idea from a communication perspective is to implement a OTP communication and use quantum key distribution to continuously share the cryptographic key realizing an information-theoretical secure communication.

Solutions to the key distribution problem.

The ideal realization of QKD is a complete encryption of a communication channel, in a realistic environment instead the devices used by the parties for the QKD protocol might be hackable or vulnerable to side channel attacks [10].

Measurement device independent Quantum Key Distribution (MDI-QKD) protocols [11] represent the safest possible implementation, the price to pay for the high security level is a low secret key rate. More practical QKD protocols, assume some level of trust in the devices used, and they can achieve reasonable key rates with lower security.
Another trade-off to consider is the one between key-rate and distance, in fact as proved in [12] the key rate distribution can not be higher that $-\log_2(1-\mu)$ where μ is the transmittivity of the channel.
This fundamental limit of QKD has been overcome using trusted repeaters in a number of metropolitan size networks: the DARPA Quantum Network[13] , the Vienna QKD network [14], the Chinese hierarchical metropolitan network [15], the Tokyo QKD network [16]. A better option would be to base the network on untrusted nodes as has been theoretically idealized using different systems [11, 17].

DEVELOPED TOOLS

This thesis' chapter expands the concepts and demonstrations that have been presented at the Photonic Benelux 2021 annual symposium.
Typically, PICs designers are forced to work in two separate environments, one for the laser/circuit simulation and one for the mask layout.
The disconnection between the two environments can easily lead to errors and mismatch between the two circuits. Typical errors range from laser designs that fail to comply with manufacturing constrains to errors in translating physical parameters between the two environments, e.g. optical path lengths.
In this chapter, we present and dig into the details of the integration between two open source software programs: the layout tool Nazca-design [18] and PHIsim traveling wave simulation software. First, We will dig into the working principles of the individual software[19]. After we will present our interface that bridges the two programs creating a single layout and simulation environments. We will demonstrate the use of the interface and compare it with experimental results.

Figure 1 is a schematic representation of the usual workflow. The designer starts in the simulation space and reproduces a schematic of the circuit in this environment. In this environment is not possible to set the final geometry of the circuit but only a

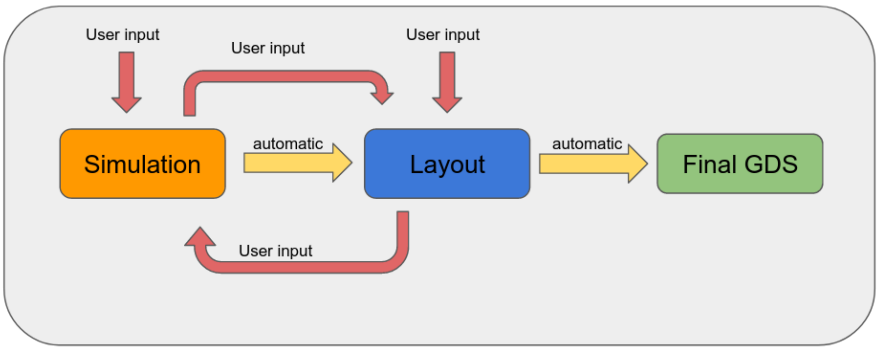

Figure 1: Schematic description of the typical workflow used in integrated photonics design. The user input (red arrows) is required in multiple parts of the design and creates a loop of back and forth between the layout design space and the simulation space.

list of elements and the connection between them. The designer have to translate the circuit into a layout that will be used by the foundry to build the masks. In this step some commercial tools provide an automatic export features, but this requires the use of complex auto-routing algorithms that usually result in unpredictable and inconvenient shapes.
In fact, the simulation schematic does not contain the information about position of the elements but only their connections, leaving to the automatic exporting tool the task to figure them out. Another underestimated factor, that is not taken into account in the simulation space, is the circuit footprint, this is often a critical information.
The result of the separation between the environments is that designers find them self going back and forth between environments to check parameters. This can easily lead in some cases to errors and mismatches between the simulated circuit and the mask layout or, in other cases, to mask layouts that due to time constrains are not simulated at all.

Figure 2 visualizes the workflow proposed and used in this thesis. In this case the designer inputs the circuit layout in the Nazca design framework. Since the circuit layout contains all the information to build the connectivity between the elements, an automatic exporting to simulation tool is always going to represent the designer's idea completely.
The designer can now import a series of simple parameters that are necessary only for the simulation, that can range from simulation length to gain of the active section. This working

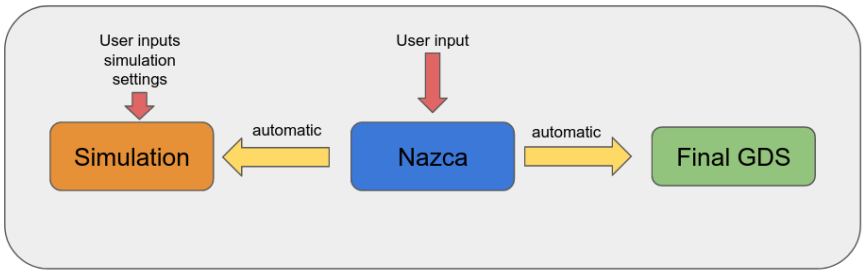

Figure 2: Unified workflow, the user input is required only two times and only once the user has to input the circuit, the second input is necessary only to set up the simulation parameters like duration, time step etc.

method saves the designer valuable time, since they don't have to translate the circuit manually anymore. The automatic procedure of translation ensures the agreement between the layout and the simulated circuit, reducing the possible error sources in the final submission.

DESIGNED CIRCUITS: QKD-QPSK INTEGRATED TRANSMITTER

Every QKD protocol is composed of two fundamental phases: a first phase when the photons are exchanged using a quantum channel and a second phase, where using a classical channel, information on the selected quantum basis for encoding is transmitted [20]. We have designed and fabricated a photonic integrated chip that can be used both as a Discrete Variable Quantum Key Distribution (DV-QKD) and as coherent transmitter with 10GHz modulation speed.
This chip allows not only to have a single chip for the QKD protocol but also to use the same channel for transmission of the encrypted data.

The basic principle of coherent optical comunication is to enchode the bit steam into the phase and amplitude of a carrier optical wave. This approach guarantees a better Signal to Noise ratio (SNR)/bit, when transmitter throught fiber and a better sensitivity of the receiver side resulting in longer reach for the signal [21, 22].

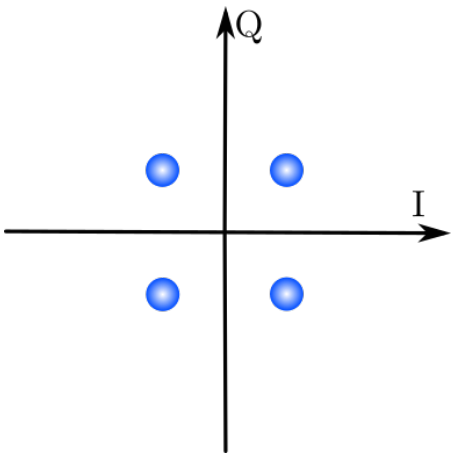

Figure 3: Constellation diagram of a QPSK modulation format, the blue dots represent possible phases that can be used to encode the signal. The I axis is the inphase signal, effectively representing the Real part of the electric field. The Q axis is the Quadrature signal that represent the imaginary part of the electric field.

We have decided to use QPSK as method of coherent transmission in our chip. This method transmits the information bits in the phase of a wave, it is already widely employed in telecomunications [23]. A conventional way of representing a coherent scheme modulation is the constellation diagram. In this diagram the possible amplitudes and phases allowed by the scheme are represented in the complex plane, in the case of a QPSK modulation we can see 4 point equidistant from the origin and located at $\frac{\pi}{4}, \frac{3\pi}{4}, -\frac{3\pi}{4}, -\frac{\pi}{4}$. Different modulation schemes have lower or higher number of points in this diagram, since the final representation is a binary the total number of point in a constellation diagram is usually a power of 2. In the case of QPSK we use a 4 point constellation meaning that we will encode 2 bits of infomation for each carrier modulation. Phase modulation is a popular choice in wireless communication, but it has been investigated extensively also in optical fiber communication, given the easy implementation and the increased data rate. A transmitter for QPSK basic schematic is presented in figure4 [24]. For the QKD part we have decided to use the scheme realized by Paraiso et al in [25] based on optically injected lasers,

Both the circuit for QKD and the one for QPSK contain a MZI interferometer, we decided to use one of them as a selector between the two operation modes. Figure5 represent a simplified diagram of the circuit. A DBR laser is used as main source, this

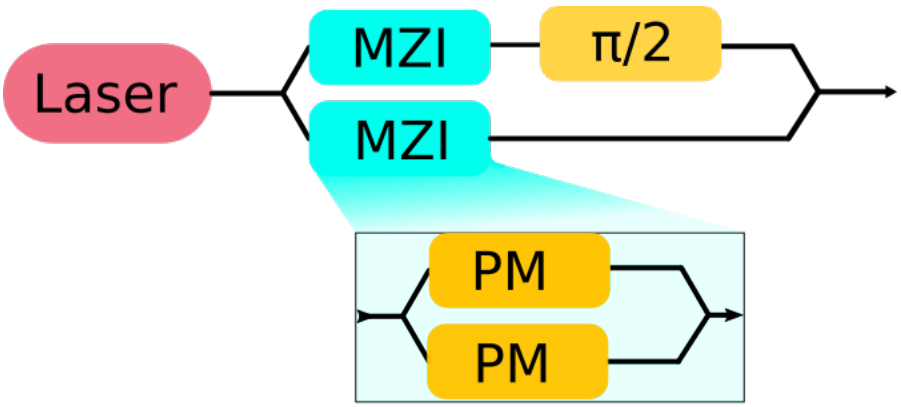

Figure 4: Basic schematic of a QPSK transmitter, the laser light is splited in two arms, each of them contains a MZI interferometer these are used to modulate the signal, an additional $\pi/2$ phase shift on one of the arms allow for full QPSK functionality.

is then divided and directed to two identical MZIs. The top interferometer is used both to modulate the signal in the QPSK modulation scheme and also in the selection of power reaching the DFB laser for QKD. An additional phase shifter is used to add the π half for QPSK modulation.

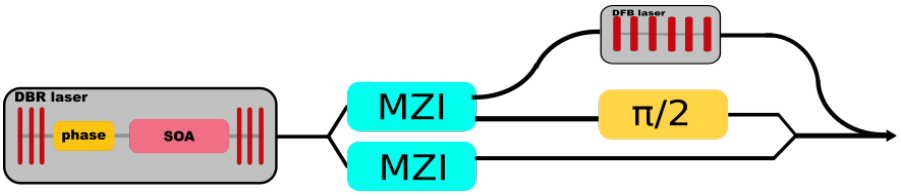

Figure 5: Schematic of the designed circuit. The output of a DBR laser is splitted in two paths going to two different MZI. The top MZI can be used to direct the light in the two different paths or to modulate the path in case the device is used as QPSK. The top path is then used to select a DFB laser to optically inject, recreating the QKD scheme proposed by [25].

DESIGNED CIRCUIT: RING LASER QKD-QPSK TRANSMITTER.

The technique that is used in the paper from Paraïso et al. is commonly refereed as Optical injection Locking (OIL). It is a technique to synchronize two lasers that can be used in various context and field, in this case is used in QKD.
In this chapter we are going to present two circuit based on OIL of ring lasers, this represent a first in our knowledge experimental demonstration of this technique on ring lasers in

monolitically integrated photonics. As we saw in the previous chapter OIL of DFB lasers can be difficult to obtain since it needs precise frequency matching conditions.
In this chapter we will discuss and experimentally demonstrate Optical injection of ring lasers. This system respect to the DFB has more resonances leading to an easy injection locking.
We have designed, fabricated and measured two circuit in an HHI MPW run.
The first circuit is composed of a simple DFB laser that is used to inject a slave ring laser. We will use this system to characterize the basic behavior of such systems, noticing that this simple circuit is already capable of QKD and QPSK.
The second circuit presented is composed by three lasers: a central DBR laser that is feed into two slave ring lasers. This system is capable of both QKD and high speed QPSK, being de facto and alternative design to the circuit presented in chapter 4.

In this chapter we are going to design two different circuit that are integrated in the same mask design.
Each of them is used to demonstrate the possibility of OIL ring lasers in integrated photonics and subsequently use it for QKD.
The first circuit is presented in figure 6. In this circuit we use a simple DFB laser to inject the ring laser. The simplicity of this circuit is its main advantage respect to other QKD circuits. In the schematic we have omitted the Multi Mode Interferometers (MMIs) blocks and the photodiodes used to monitor the state of the laser. A more extensive description of the circuit will be presented in the following sections. It is worth notice that this circuit is both capable of QKD and QPSK but both have quite limited bandwidth since it requires modulation of the DFB laser. This type of modulation in fact does not benefit from the characteristic mentioned above that can be applied only to the slave laser, in this case the ring laser.

A second circuit has been realized in the same mask design and is schematized in figure 7.
In this case we decided to exploit the two outputs of a DBR laser to OIL two ring lasers. The two rings output is then combined to a single output. This schematic can be used for both QKD and QPSK.
The main advantage respect to the first circuit is the possibility to use the modulation of the rings for encoding the bits of the QPSK scheme. For the use as QPSK transmitter we have added a phase modulator in the output of one of the ring laser, this allow

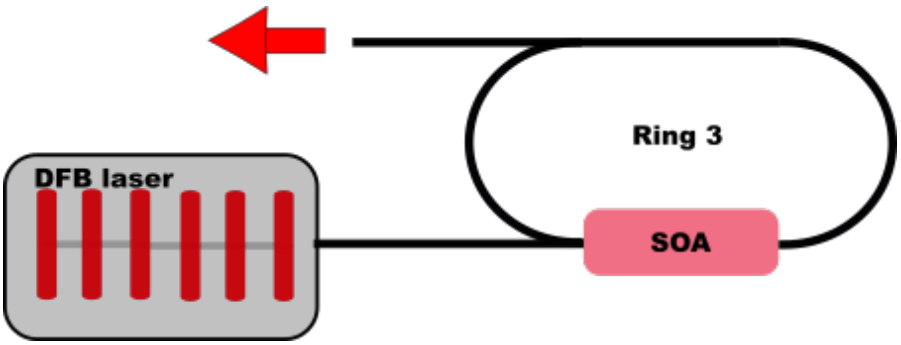

Figure 6: This schematic represent the first design of OIL ring laser. The ring laser is injected using a DFB laser.

to have the $\pi/2$ phase shift for QPSK. The modulation bandwidth in this case is enhanced by the OIL since we are going to modulate the two slave lasers and not the master laser. Also in this case we have omitted components that are not core parts of the circuit.
The ring lasers used for the two circuit are identical in dimensions and components used.

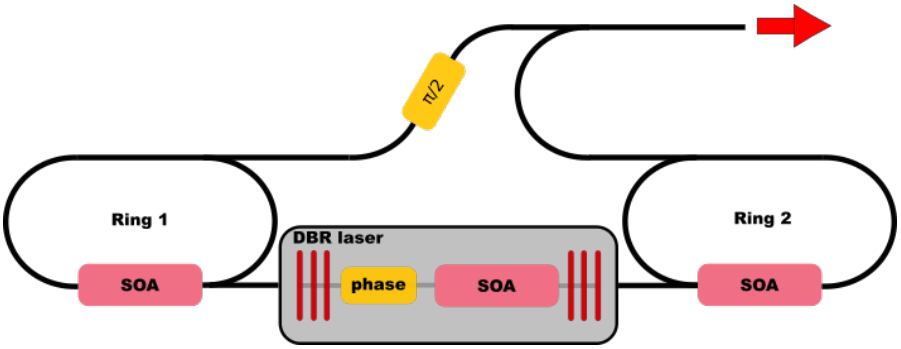

Figure 7: This schematic represent the second design of OIL ring laser. The two ring lasers are injected using a DBR laser.

DESIGNED CIRCUITS: TIME-BIN QKD TRANSMITTER

In this chapter we are going to discuss a different design for QKD.
The main objective in this case is to design a combination of transmitter and receiver that do not require long delay lines. As can be noted in the discussion in chapter 2 the receiver side in particular requires long delay lines to interfere the two photons. In the design that we are presenting in this chapter this is not required, a delay line is still present but it is only centimeter long

compared to the tents of centimeters long in more traditional approaches [26].
The working principle of this design is pretty straight forward. In time-bin encoding QKD the key is encoded in the phase difference between two pulses. In the traditional approaches the two pulses are transmitted with 1GHz clocking speed, resulting in long delay lines to recombine the two pulses.
Here we propose a different approach, we create a short pulse of few ps time width and use a short delay line to split it. This create two entangled pulses with short time separation. At the receiver side the two pulses can be recombined using the same delay line of few millimeters.
The our design has a small footprint and the short lenght of the delay made it possibel to be fabricated in an InP platform. We have submitted for fabrication in a SMART photonics MPW run.
Another advantage of this design is the symmetry between the transmitter and the receiver circuits. They, in fact, need to have the same identical delay line, resulting in a transmitter circuit that can be easily adapted to become a receiver.
In this Chapter we will present both a receiver and a transmitter and we will discuss the advantages and the difficulties respect to the common implementation until now. Both design are under fabrication and they are integrated in the same chip together with other test structures and a novel tunable mode-lock-laser design.
The design is still under fabrication at the moment so we will focus our attention to the simulation results and the theoretical framework of this design.

The main schematic of the circuit is presented in Figure 8, in this figure we have omitted the MMI splitters and combiners.
We use a DBR laser as a main source of our circuit.
A critical requirement for time bin encoded QKD is the randomization of the absolute phase of the pulses. In our circuit this is achieved using a phase modulator right after the laser.
After the phase randomization stage we need to create the pulses that we will use to encode our signal. To do so we use an MZI with fast electro-optical modulators, allowing us to obtain short pulse of few ps.
The structure that follows the MZI can be seen as an unbalanced MZI, in fact in this case the arms of the interferometer are not equal and a delay line is present on one of them. This structure will split the pulse in two separate pulses, the phase section in

the shortest arm is used to tune the phase difference between the output pulses. It is worth notice that this structure has two inputs and two outputs. one of the inputs is connected to the MZI and the second input is instead coupled off chip. The two outputs are instead both coupled off chip. This characteristic of double input/output allows the circuit to be both used as a transmitter and as a receiver.

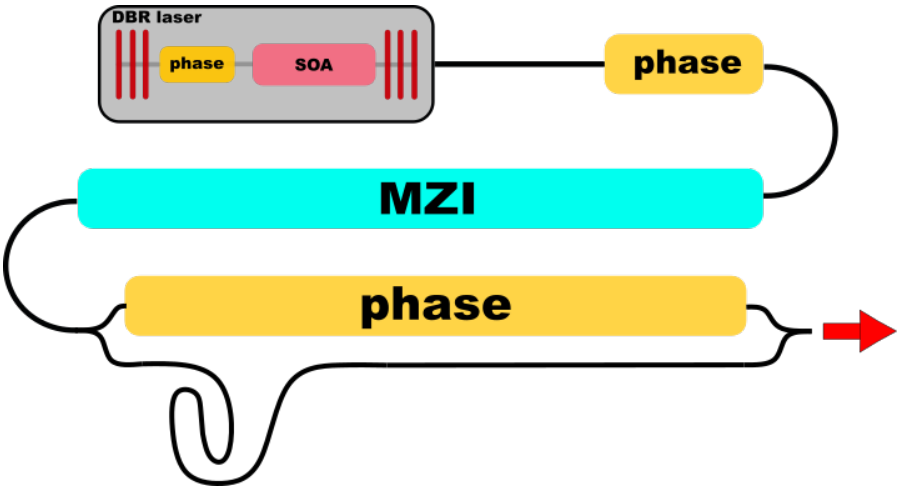

Figure 8: This schematic represent transmitter design presented in this chapter. The the top DBR laser is phase randomized using the first phase shifter. Using a MZI the laser output is then pulse shaped in short pulses. The final structure splits the pulse in two and adds a phase to the pulse in the short arm.

RESUMEN

INTEGRACIÓN FOTÓNICA GENÉRICA

De forma similar al proceso que sufrió la microelectrónica en el pasado, los dispositivos ópticos ven aumentar el interés por la miniaturización de componentes y circuitos. En este contexto, en la fotónica se ha desarrollado la integración, primero con la aplicación orientada a procesos pero recientemente dejando espacio a una integración genérica modelo. La integración fotónica genérica pretende reducir la barrera para entrar en el mercado de la integración fotónica y lo hace aplicar una serie de procesos y procedimientos unificados en toda la cadena de producción y diseño.

En esta tesis el enfoque fotónico integrado genérico será presentado y discutido en cada paso que va desde el circuito idea al chip empaquetado. Los circuitos integrados fotónicos (PIC) son dispositivos que incluyen múltiples componentes fotónicos en un solo chip. La primera idea de la integración fotónica fue sugerida en 1969 por S. Miller [2].

Desde entonces, los avances en este campo han llevado a la primera comercialización de PIC por la empresa Infinera en 2005. En la actualidad, la oferta comercial de la fotónica integrada se ha ampliado con varias empresas que ofrecen diferentes gamas de productos y materiales.

La variedad de componentes integrables depende de los materiales y los procesos utilizados para la fabricación, sino que va desde el pasivo componentes: guías de onda, divisores, multiplexores y otros, para componentes activos como SOAs y fotodiodos [3]. Aunque el dominio principal de la integración fotónica ha sido principalmente en las telecomunicaciones, en los últimos años una serie de aplicaciones en diferentes campos como la biofotónica, la tomografía y las tecnologías cuánticas han surgido [4, 5].

Las prestaciones y posibilidades de los circuitos diseñados dependen de la plataforma de materiales utilizada en la fabricación:

- plataformas basadas en III-V, son las únicas que permiten la integración de los componentes de ganancia debido

al bandgap directo de las estructuras cristalinas. Normalmente estas plataformas tienen menor rendimiento en los bloques de construcción pasivos, como las guías de ondas, debido a la alta absorción del entorno material necesario para la conducción eléctrica.

- Las plataformas de silicio sobre aislante (SOI), ofrecen grandes prestaciones de los componentes pasivos y menores costes gracias al luso de tecnologías de fabricación tomadas prestadas de la industria electrónica. Pueden integrar moduladores y fotodetectores. Con respecto a las plataformas III-V, la ausencia de un módulo de ganancia limita la aplicación o requiere la unión el chip SOI a un chip III-V.

- plataformas SiN, ofrece una gama más amplia de funcionamiento de las longitudes de onda debido a la mayor ventana de transparencia respecto a otra plataforma. Al igual que en el caso del SOI, la ausencia de una ganancia sección requieren la cointegración con otras plataformas que tienen componentes emisores de luz

La lista anterior comprende sólo los principales materiales, pero se están desarrollando y comercializando diferentes tipos de tecnologías en los últimos años, incluidos los materiales a base de vidrio y polímeros.
Limitaremos la discusión de esta tesis a los integrados basados en InP fotónica. Se han fabricado todos los chips de los que se habla en esta tesis, o están todavía en fase de fabricación, en la plataforma de materiales InP.

DISTRIBUCIÓN DE CLAVES CUÁNTICAS

La QKD es un campo de la información cuántica que evoluciona rápidamente, nuevos Los protocolos y las pruebas de seguridad se desarrollan con regularidad, y los experimentos y las demostraciones se trasladan de los laboratorios al terreno de las implementaciones. En esta tesis cubriremos los aspectos básicos de la tecnología para dar al usuario los conocimientos básicos y referencias para acercarse al mundo del QKD. En la primera parte de la introducción cubriremos el protocolo básico BB84[1] discutiendo la aspectos teóricos y las implementaciones más comunes. La segunda parte está dedicada al estado del arte de la experimentación y discutirá los recientes avances de la fotónica QKD en el espacio libre y la fotónica integrada.

En las comunicaciones seguras dos partes, denominadas convencionalmente Alice y Bob, quieren comunicarse en privado utilizando un canal. La presencia de un espía, Eva, socava la privacidad de esta comunicación. La mejor manera de que Alice y Bob puedan garantizar la privacidad de su información es utilizar una comunicación segura desde el punto de vista de la información, es decir, una comunicación que es fundamentalmente segura por la teoría, incluso si Eva tiene una ventaja tecnológica muy superior a Alice y Bob no puede desencriptar el mensaje. Este tipo de comunicación puede conseguirse mediante el método de la almohadilla de un solo uso (OTP) [6]. La OTP consiste en una clave larga de carácter aleatorio que es idealmente tan larga como el mensaje y se mantiene en secreto para Eva. Siempre que la clave sea secreta y se utilice una sola vez [7], la comunicación entre Alice y Bob puede considerarse información-teóricamente segura. Este procedimiento de comunicación nos deja un problema diferente, ¿cómo pueden Alice y Bob compartir la clave?
Esto se conoce como el problema de la distribución de claves.
La solución actual al problema de la distribución de claves es la criptografía pública de claves. En este concepto Bob tiene un par de claves. Una de estas dos claves es pública y Alice puede utilizarla para cifrar el mensaje. El mensaje encriptado sólo puede ser descifrado utilizando la clave privada de Bob. Este tipo de sistema criptográfico se utiliza ampliamente hoy en día, pero no es seguro desde el punto de vista de la información. De hecho, la seguridad se basa en el hecho de que dado la clave pública no hay un algoritmo eficiente para calcular la clave privada.
Por ejemplo, el sistema RSA [8] se basa en la factorización de un número entero grande y esta tarea requiere mucho tiempo para un ordenador clásico. Este tipo de criptografía no puede resistir a los avances de la tecnología. Ha sido aún más evidente desde la invención del algoritmo Shor [9] que crea una manera eficiente de calcular la factorización de números enteros utilizando ordenadores. Aunque el algoritmo Shor requiere un elevado número de qbit para ejecutarse y hoy en día no es factible, los recientes avances en la tecnología de los ordenadores se acercan a dicha especificación.
La QKD promete resolver el problema utilizando las leyes fundamentales de naturaleza como el principio de incertidumbre y el entrelazamiento de partículas cuánticas. La idea desde la perspectiva de la comunicación es implementar una comunicación OTP y utilizar la distribución de la clave cuántica para

compartir continuamente la clave criptográfica realizando una comunicación segura desde el punto de vista de la información. El método de distribución de claves cuánticas independiente del dispositivo de medición (MDI-QKD) [11] representa la implementación más segura posible. El precio a pagar por el alto nivel de seguridad es un baja tasa secreta de claves. Los protocolos QKD más prácticos asumen algún nivel de confianza en los dispositivos utilizados y pueden lograr una tasa de clave razonable con menor seguridad.
Otro compromiso que hay que tener en cuenta es el que se da entre la tasa de claves y distancia, de hecho como se ha demostrado en [12] la distribución de la tasa clave puede no sea mayor que $-\log_2(1-\mu)$ donde μ es la transmitancia del canal. Este límite fundamental de la QKD se ha superado con el uso de repetidores en una serie de redes de tamaño metropolitano: la DARPA Quantum Network[13] , la red QKD de Viena [14], la red china metropolitana jerárquica [15], la red QKD de Tokio [16]. Una mejor opción sería basar la red en nodos no confiables como se ha idealizado teóricamente utilizando diferentes sistemas [11, 17].

HERRAMIENTAS DESARROLLADAS

Este capítulo de la tesis amplía los conceptos y las demostraciones que se han presentado en la edición anual del simposio Photonic Benelux 2021.
Normalmente los diseñadores de PICs se ven obligados a trabajar en dos entornos distintos, una para la simulación del láser/circuito y otra para la diseño de la máscara.
La desconexión entre los dos entornos puede llevar fácilmente a errores y desajustes entre los dos circuitos. Errores típicos van desde diseños de láser que no cumplen con la fabricación y que limita la traducción de los parámetros físicos entre los dos entornos, por ejemplo, las longitudes de los trayectos ópticos.
En este capítulo, presentamos y profundizamos en los detalles de la integración entre dos programas de software de código abierto: el diseño herramienta Nazca-design [18] y el software de simulación de ondas viajeras PHIsim. En primer lugar profundizaremos en los principios de funcionamiento del software individual [19]. Después presentaremos nuestra interfaz que une los dos programas creando un único diseño y entorno de simulación. Demostraremos el uso de la interfaz y pasaremos a

compararlo con los resultados experimentales.
La figura 1 es una representación esquemática del flujo de trabajo habitual. El diseñador comienza en el espacio de simulación y reproduce un esquema del circuito en este entorno. En este entorno no es posible establecer la geometría final del circuito, sino sólo una lista de elementos y la conexión entre ellos. El diseñador tiene que traducir el circuito a un diseño que será utilizado por la fábrica para construir las máscaras. En este paso algunos módulos comerciales proporcionan una función de exportación automática, pero esto requiere el uso de complejos algoritmos de enrutamiento automático que suelen dar lugar a situaciones imprevisibles e inconvenientes.
De hecho, el esquema de simulación no contiene la información sobre la posición de los elementos, sino sólo sobre sus conexiones, dejando a la herramienta de exportación automática la tarea de calcularlos fuera. Otro factor subestimado, que no se tiene en cuenta en el espacio de simulación, es la huella del circuito, esto es a menudo una información crítica.
El resultado de la separación entre los entornos es que los diseñadores se encuentran yendo y viniendo de un entorno a otro para comprobar los parámetros. Esto puede llevar fácilmente en algunos casos a errores y desajustes entre el circuito simulado y el de la máscara o, en otros casos, para enmascarar diseños que debido a restricciones de tiempo las no se simulan en absoluto.
La figura 2 visualiza el flujo de trabajo propuesto y utilizado en esta tesis. En este caso, el diseñador introduce el diseño del circuito en el marco de diseño de Nazca. Dado que el diseño del circuito contiene toda la información para construir la conectividad entre los elementos, una herramienta de exportación automática a la simulación siempre va a representar completamente la idea del diseñador.
El diseñador puede ahora importar una serie de parámetros simples que son necesarios sólo para la simulación, que pueden ir desde la longitud de la simulación a la ganancia de la sección activa. Este método de trabajo ahorra al diseñador un tiempo valioso, ya que no tiene para traducir el circuito manualmente. El procedimiento automático de la traducción garantiza la concordancia entre el trazado y el circuito simulado, reduciendo las posibles fuentes de error en la presentación final.

CIRCUITOS DISEÑADOS: TRANSMISOR INTEGRADO QKD-QPSK

Todo protocolo QKD se compone de dos fases fundamentales: una primera fase en la que los fotones se intercambian mediante un canal cuántico y una segunda fase, en la que se utiliza un canal clásico en el que la información sobre la base cuántica seleccionada para la codificación es transmitida [20]. Hemos diseñado y fabricado un sistema fotónico en chip integrado que puede utilizarse tanto como Distribución de claves cuánticas (DV-QKD) de variable continua y como transmisor coherente con una velocidad de modulación de 10 GHz.
Este chip permite no sólo tener un único chip para el protocolo QKD, sino también para utilizar el mismo canal para la transmisión de los datos encriptados. Este enfoque garantiza una mejor relación señal/ruido (SNR)/bit, cuando se transmite por fibra y una mejor sensibilidad del lado del receptor, lo que da lugar a un mayor alcance de la señal [21, 22]. Hemos decidido utilizar QPSK como método de transmisión coherenteen nuestro chip. Este método transmite la información de los bits en la fase de una onda y ya se emplea ampliamente en telecomunicaciones [23]. Una forma convencional de representar una modulación de esquema coherente es el diagrama de constelación. En este diagrama las posibles amplitudes y fases permitidas se representan en el plano complejo, en el caso de un modulación QPSK podemos ver 4 puntos equidistantes del origen y situados en $\frac{\pi}{4}, \frac{3\pi}{4}, -\frac{3\pi}{4}, -\frac{\pi}{4}$. Diferentes esquemas de modulación tienen menor o mayor número de puntos en este diagrama, ya que la representación final es en binario el número total de puntos en un diagrama de constelación en una potencia de 2. En el caso de QPSK utilizamos una constelación de 4 puntos, lo que significa que codificaremos 2 bits de información para cada modulación de la portadora. La modulación de fase es una opción popular en la comunicación inalámbrica, pero ha sido investigada ampliamente también en la comunicación por fibra óptica, dada la facilidad de implantación y el aumento de la velocidad de datos.
El esquema básico del transmisor para QPSK se presenta en la figura 4 [24]. Para la parte QKD hemos decidido utilizar el esquema realizado por Paraiso et al en [25] basado en láseres inyectados ópticamente, Tanto el circuito para QKD como el de QPSK contienen un MZI como interferómetro y decidimos utilizar uno de ellos como selector entre los dos modos de funcionamiento.

La figura 5 representa un modelo simplificado de diagrama del circuito. Se utiliza un láser DBR como fuente principal, que se divide y dirige a dos MZI idénticos. La parte superior del interferómetro se utiliza tanto para modular la señal en el esquema de modulación QPSK y también en la selección de la potencia que alcanza el láser DFB para QKD. Se utiliza un desfasador adicional para añadir la mitad π para la modulación QPSK. La técnica que se utiliza en el trabajo de Paraïso et al. es comúnmente denominado OIL. Es una técnica para sincronizar dos láseres que pueden utilizarse en diversos contextos y campos, en este se utiliza en QKD. En este capítulo vamos a presentar dos circuitos basados en Bloqueo por inyección óptica (OIL) de los láseres de anillo, esto representa una demostración experimental, por primera vez según nuestro conocimiento, de esta técnica en láseres de anillo en fotónica integrada monolíticamente.
Como vimos en el capítulo anterior el OIL de los láseres DFB puede ser difícil de obtener, ya que necesita una adaptación precisa de la frecuencia.
En este capítulo discutiremos y demostraremos experimentalmente la inyección óptica de láseres de anillo. Este sistema respecto al DFB tiene más resonancias que conducen a un fácil bloqueo de la inyección. Hemos diseñado, fabricado y medido dos circuitos en una ronda de fabricación de HHI MPW. El primer circuito está compuesto por un simple láser DFB que se utiliza para inyectar a un láser de un anillo esclavo. Utilizaremos este sistema para caracterizar el comportamiento básico de estos sistemas, observando que este modelo simple ya es capaz de realizar QKD y QPSK. El segundo circuito presentado está compuesto por tres láseres: un láser DBR central que se alimenta de dos láseres anulares esclavos. Este sistema es capaz tanto de QKD como de QPSK de alta velocidad, siendo de diseño de facto y alternativo al circuito presentado en el capítulo 4.

En este capítulo vamos a diseñar dos circuitos diferentes que se integran en el mismo diseño de la máscara.
Cada uno de ellos se utiliza para demostrar la posibilidad de funcionamiento dual del anillo OIL en la fotónica integrada y posteriormente utilizarlo para la QKD.
El primer circuito se presenta en la figura 6. En este circuito utilizamos un láser DFB simple para inyectar al láser del anillo. La simplicidad de este es su principal ventaja respecto a otros circuitos QKD. En el esquema hemos omitido los interferómetros multimodales (MMIs) y los fotodiodos utilizados para controlar el estado del láser. Una descripción más amplia del circuito se

presentará en las siguientes secciones. Cabe destacar que este circuito es capaz tanto de QKD como de QPSK pero ambos tienen un ancho de banda bastante limitado, ya que requiere la modulación del láser DFB.
Se ha realizado un segundo circuito con el mismo diseño de máscara y se esquematiza en la figura 7. En este caso decidimos aprovechar las dos salidas de un láser DBR a los dos láseres de anillo OIL. La salida de los dos anillos se combina para una sola salida. Este esquema puede utilizarse tanto para QKD como para QPSK.
La principal ventaja respecto al primer circuito es la posibilidad de utilizar la modulación de los anillos para codificar los bits del esquema QPSK. Para el uso como transmisor QPSK hemos añadido un modulador de fase en la salida de uno de los láseres de anillo, esto permite tener el desplazamiento de fase $\pi/2$ para QPSK. El ancho de banda de modulación en este caso es potenciado por el OIL ya que vamos a modular los dos láseres esclavos y no el láser maestro. También en este hemos omitido los componentes que no son parte fundamental del circuito. Los láseres de anillo utilizados para los dos circuitos son idénticos en dimensiones y componentes utilizados.

CIRCUITOS DISEÑADOS: TRANSMISOR QKD CON BARRERA DE TIEMPO

En este capítulo vamos a hablar de un diseño diferente para QKD.
El objetivo principal en este caso es diseñar una combinación de transmisor y receptor que no requieran largas líneas de retardo. Como puede observarse en la discusión del capítulo 2, el lado del receptor en particular requiere largas líneas de retardo para interferir los dos fotones. En el diseño que presentamos en este capítulo esto no es necesario, sigue habiendo una línea de retardo, pero sólo tiene un centímetro de longitud en comparación con las de centímetros de longitud alternativas [26].
El principio de funcionamiento de este diseño es bastante sencillo. En la codificación QKD por intervalos de tiempo, la clave se codifica en la diferencia de fase entre dos pulsos. En los enfoques tradicionales los dos pulsos se transmiten con una velocidad de reloj de 1GHz, lo que resulta en líneas de retardo largas para recombinar los dos pulsos.
Aquí proponemos un enfoque diferente, creamos un pulso corto de pocos ps de ancho de tiempo y utilizamos una línea de re-

tardo corta para dividirlo. Este crear dos pulsos entrelazados con una corta separación de tiempo. En el lado del receptor los dos pulsos pueden recombinarse utilizando la misma línea de retardo de pocos milímetros.
Nuestro diseño ocupa poco espacio y la corta longitud del retardo hizo posible su fabricación en una plataforma InP. El diseño se fabricó en una ronda de SMART Photonics MPW.
Otra ventaja de este diseño es la simetría entre el transmisor y los circuitos del receptor. De hecho, necesitan tener una misma línea de retardo idéntica, lo que resulta en un circuito transmisor que puede adaptarse fácilmente para convertirse en un receptor.
En este capítulo presentaremos un receptor y un transmisor y discutiremos las ventajas y las dificultades respecto a la implementación común hasta ahora. Ambos diseños están bajo fabricación y se integran en el mismo chip junto a otras estructuras de prueba y un novedoso láser de modo sintonizable. El diseño está todavía en fase de fabricación por lo que centramos nuestra atención en los resultados de la simulación y en la teoría marco de este diseño.
El esquema principal del circuito se presenta en la figura 8; en esta figura hemos omitido los divisores y combinadores MMI. Utilizamos un láser DBR como fuente principal de nuestro circuito.
Un requisito crítico para la QKD codificada en bins de tiempo es la aleatorización de la fase absoluta de los pulsos. En nuestro circuito esto se consigue utilizando un modulador de fase justo después del láser.
Después de la etapa de aleatorización de la fase tenemos que crear los pulsos que utilizaremos para codificar nuestra señal. Para ello utilizamos un MZI con moduladores electro-ópticos rápidos, lo que nos permite obtener pulsos de pocos ps. La estructura que sigue a la MZI puede verse como un MZI desequilibrado, De hecho en este caso los brazos del interferómetro no son iguales y en uno de ellos hay una línea de retardo. Esta estructura dividirá el pulso en dos pulsos separados, la sección de fase en el brazo más corto se utiliza para sintonizar la diferencia de fase entre los pulsos de salida. Cabe destacar que esta estructura tiene dos entradas y dos salidas. Una de las entradas está conectada al MZI y la segunda entrada se acopla en cambio fuera del chip. Los dos Las salidas están acopladas fuera del chip. Esta característica de doble entrada/salida permite que el circuito se utilice tanto como transmisor y como receptor.

RESUMO

CIRCUÍTOS FOTÓNICOS INTEGRADOS

De xeito semellante ao proceso que sufriu a microelectrónica no pasado, os dispositivos ópticos ven cada vez máis interesados na miniaturización de compoñentes e circuítos. Neste contexto, a integración desenvolveuse en fotónica, primeiro coa aplicación orientada a procesos pero recentemente deixando espazo para un modelo xenérico de integración. A integración fotónica xenérica ten como obxectivo reducir a barreira para entrar no mercado da integración fotónica e faino aplicando unha serie de procesos e procedementos unificados ao longo da cadea de produción e deseño.
Nesta tese presentarase e discutirá o enfoque fotónico integrado xenérico en cada paso desde o circuíto idea ata o chip empaquetado.
Os circuítos fotónicos integrados (PIC) son dispositivos que inclúen varios compoñentes fotónicos nun único chip. A primeira idea de integración de fotóns foi suxerida en 1969 por S.Miller [2].
Desde entón, os avances neste campo propiciaron a primeira comercialización de PIC por parte da empresa Infinera en 2005. Na actualidade, a oferta comercial de fotónica integrada ampliouse con varias empresas que ofrecen diferentes gamas de produtos e materiais.
A variedade de compoñentes integrables depende dos materiais e procesos utilizados para a fabricación, pero abarca desde compoñentes pasivos: guías de ondas, divisores, multiplexores e outros, ata compoñentes activos como SOA e fotodiodos [3].
Aínda que o dominio principal da integración fotónica foi principalmente nas telecomunicacións, nos últimos anos xurdiron unha serie de aplicacións en diferentes campos como a biofotónica, a tomografía e as tecnoloxías cuánticas [4, 5].
As características e posibilidades dos circuítos deseñados dependen da plataforma de material empregada na fabricación:

- Plataformas baseadas en III-V, son as únicas que permiten a integración dos compoñentes de ganancia debido ao bandgap directo das estruturas cristalinas. Estas platafor-

mas adoitan ter un rendemento inferior en bloques de construción pasivos, como guías de ondas, debido á alta absorción do ambiente material necesario para a condución eléctrica.

- As plataformas de silicio sobre illante (SOI) ofrecen un alto rendemento dos compoñentes pasivos e uns custos máis baixos grazas ao uso de tecnoloxías de fabricación tomadas da industria electrónica. Poden integrar moduladores e fotodetectores. Con respecto ás plataformas III-V, a ausencia dun módulo de ganancia limita a aplicación ou require unir o chip SOI a un chip III-V.

- Plataformas SiN, ofrece unha gama máis ampla de lonxitudes de onda de operación debido á maior ventá de transparencia en comparación con outras plataformas. Como no caso de SOI, a ausencia dunha sección de ganancia require a cointegración con outras plataformas que teñan compoñentes emisores de luz.

A lista anterior inclúe só os materiais principais, pero nos últimos anos estanse a desenvolver e comercializar diferentes tipos de tecnoloxías, incluíndo materiais a base de vidro e polímeros. Limitaremos a discusión desta tese aos IC fotónicos baseados en InP. Todos os chips tratados nesta tese foron fabricados, ou aínda están en fase de fabricación, na plataforma de materiais InP.

DISTRIBUCIÓN DE CLAVES CUÁNTICAS

QKD é un campo de información cuántica en rápida evolución, novos protocolos e probas de seguridade desenvólvense regularmente e os experimentos e demostracións móvense dos laboratorios ao ámbito das implementacións. Nesta tese abordaremos os aspectos básicos da tecnoloxía para dotar ao usuario dos coñecementos básicos e referencias para achegarse ao mundo do QKD. Na primeira parte da introdución cubriremos o protocolo básico BB84[1] discutindo os aspectos teóricos e as implantacións máis habituais. A segunda parte está dedicada ao estado da arte da experimentación e analizará os avances recentes da fotónica QKD no espazo libre e a fotónica integrada.

Nas comunicacións seguras, dúas partes, chamadas convencionalmente Alice e Bob, queren comunicarse en privado me-

diante unha canle. A presenza dunha espía, Eva, socava a privacidade desta comunicación. A mellor forma de que Alice e Bob garantan a privacidade da súa información é empregar unha comunicación segura a nivel informativo, é dicir, unha comunicación fundamentalmente segura en teoría, aínda que Eva teña unha vantaxe tecnolóxica moi forte, superior a Alice e Bob non poden descifrar o mensaxe. Este tipo de comunicación pódese conseguir mediante o método de almofada de uso único (OTP) [6]. O OTP consiste nunha chave aleatoria longa que o ideal é sempre que a mensaxe e se manteña en segredo para Eva. Sempre que a chave sexa secreta e se use só unha vez [7], a comunicación entre Alice e Bob pode considerarse información teoricamente segura.

Este procedemento de comunicación déixanos un problema diferente, como poden Alice e Bob compartir a chave?

Isto coñécese como o problema de distribución de chaves.

A solución actual ao problema da distribución de claves é a criptografía de chave pública. Neste concepto Bob ten un par de chaves. Unha destas dúas claves é pública e Alice pode usala para cifrar mensaxe. A mensaxe cifrada só se pode descifrar usando a clave privada de Bob. Utilízase este tipo de sistema criptográfico amplamente hoxe en día, pero non é informadamente seguro. De feito, a seguridade baséase no feito de que dada a clave pública non existe un algoritmo eficiente para calcular a clave privada.

Por exemplo, o sistema RSA [8] baséase na factorización dun número enteiro grande e esta tarefa leva moito tempo para un ordenador clásico. Este tipo de criptografía non pode resistir os avances da tecnoloxía. Foi aínda máis evidente dende a invención do algoritmo Shor[9] que crea a forma eficiente de calcular a factorización de números enteiros mediante ordenadores.

Aínda que o algoritmo de Shor require un gran número de qbits para executalo e actualmente non é viable, os últimos avances en tecnoloxía informática achegáronse a tal especificación. QKD promete resolver o problema utilizando leis fundamentais da natureza, como o principio de incerteza e o enredo de partículas cuánticas. A idea desde a perspectiva da comunicación consiste en implementar unha comunicación OTP e utilizar a distribución de claves cuánticas para compartir continuamente a clave criptográfica realizando comunicación segura desde o punto de vista da información.

O método de distribución de claves cuánticas independente do dispositivo de medida (MDI-QKD) [11] representa a imple-

mentación máis segura posible. O prezo a pagar polo alto nivel de seguridade é unha baixa taxa de chave secreta. Os protocolos QKD máis prácticos asumen certo nivel de confianza nos dispositivos utilizados e poden acadar unha taxa de clave razoable con menos seguridade.
Outro compromiso que hai que ter en conta é o entre a taxa clave e a distancia, de feito, como se mostrou en [12], a distribución da taxa clave pode non ser maior que $-\log_2(1-\mu)$onde μ é a transmitancia da canle.
Este límite fundamental de QKD superouse co uso de repetidores en varias redes do tamaño dun metro: a rede cuántica DARPA [13] , a rede QKD de Viena [14], a rede metropolitana xerárquica chinesa [15] e a QKD de Tokio rede [16]. Unha mellor opción sería basear a rede en nodos pouco fiables como foi teoricamente idealizado usando diferentes sistemas [11, 17].

FERRAMENTAS DESENVOLVIDAS

Este capítulo da tese amplía os conceptos e demostracións que se presentaron na edición anual do simposio Photonic Benelux 2021.
Normalmente os deseñadores de PIC vense obrigados a traballar en dous ambientes diferentes, un para a simulación de láser/circuíto e outro para o deseño de máscaras.
A desconexión entre os dous ambientes pode provocar facilmente erros e desaxustes entre os dous circuítos. Os erros típicos van desde deseños con láser que non son conformes coa fabricación e que limitan a tradución de parámetros físicos entre os dous ambientes, por exemplo, as lonxitudes dos camiños ópticos.
Neste capítulo, introducimos e afondamos nos detalles da integración entre dous programas de software de código aberto: a ferramenta de deseño Nazca [18] e o software de simulación de ondas viaxeiras PHIsim. En primeiro lugar afondaremos nos principios de funcionamento do software individual [19]. Despois presentaremos a nosa interface que une os dous programas creando un único contorno de deseño e simulación. Demostraremos o uso da interface e compararémolo cos resultados experimentais.
A figura 1 é unha representación esquemática do fluxo de traballo típico. O deseñador comeza no espazo de simulación e reproduce a esquema de circuíto neste entorno. neste ambiente non é posible establecer a xeometría final do circuíto, senón só

unha lista de elementos e a conexión entre eles. O deseñador tes que traducir o circuíto nun deseño que será utilizado por a fábrica para construír as máscaras. Neste paso, algúns módulos empresariais proporcionan unha función de exportación automática, pero isto require o uso de algoritmos de enrutamento automático complexos que adoitan levar a situacións imprevisibles e inconvenientes.

A figura 2 visualiza o fluxo de traballo proposto e utilizado nesta tese. Neste caso, o deseñador introduce o deseño do circuíto no Marco de deseño Nazca. Dado que o deseño do circuíto contén toda a información para construír a conectividade entre os elementos, unha ferramenta de exportación de simulación automática sempre representará plenamente a idea do deseñador. O deseñador agora pode importar unha serie de parámetros sinxelos que son necesarios só para a simulación, que poden ir desde o lonxitude de simulación á ganancia da sección activa. Este método de traballo aforra ao deseñador un tempo valioso, xa que non ten que facelo para traducir o circuíto manualmente. O procedemento de tradución automática garante a concordancia entre o debuxo e o circuíto simulado, reducindo as posibles fontes de erro na presentación final.

CIRCUÍTOS DESEÑADOS: TRANSMISOR QKD-QPSK INCORPORADO

Cada protocolo QKD está formado por dúas fases fundamentais: unha primeira fase na que se intercambian os fotóns a través dunha canle cuántica e unha segunda fase, na que se utiliza unha canle clásica na que se transmite a información sobre a base cuántica seleccionada para a codificación [20]. Deseñamos e fabricamos un sistema fotónico integrado en chip que se pode utilizar tanto como distribución de claves cuánticas variables continuas (DV-QKD) como como transmisor coherente cunha taxa de modulación de 10GHz.
Este chip permite non só ter un único chip para o protocolo QKD, senón tamén utilizar a mesma canle para a transmisión dos datos cifrados.
Este enfoque garante unha mellor relación sinal-ruído (SNR)/bit, cando se transmite a través de fibra, e un mellor sensibilidade do lado do receptor, o que resulta nun rango de sinal máis longo [21, 22]. Decidimos utilizar QPSK como método de trans-

misión coherente nas nosas fichas. Este método transmite a información dos bits en fase de onda e xa é moi utilizado nas telecomunicacións [23]. Unha forma convencional de representar unha modulación de esquema coherente é o diagrama de constelación. Neste diagrama represéntanse no plano complexo as posibles amplitudes e fases permitidas, no caso dunha modulación QPSK podemos ver 4 puntos equidistantes da orixe e situados en $\frac{\pi}{4}, \frac{3\pi}{4}, -\frac{3\pi}{4}, -\frac{\pi}{4}$. Diferentes esquemas de modulación ten menor ou maior número de puntos neste diagrama, xa que a representación final é en binario o número total de puntos nun diagrama de constelación a unha potencia de 2. No caso de QPSK utilizamos unha constelación de 4 puntos, o que significa que codificaremos 2 bits de información por cada modulación de portadora. modulación de fase é unha opción popular na comunicación sen fíos, pero tamén se investigou amplamente na comunicación por fibra óptica, dada a facilidade de implementación e o aumento da taxa de datos.
O esquema básico do transmisor para QPSK preséntase na figura 4 [24]. Para a parte QKD decidimos utilizar o esquema feito por Paraiso et al en [25] baseado en láseres inxectados ópticamente, Tanto os circuítos QKD como QPSK conteñen un MZI como interferómetro e decidimos utilizar un deles como selector entre os dous modos de funcionamento. A figura 5 representa un modelo simplificado de diagrama de circuíto. Utilízase un láser DBR como fonte principal, que se divide e dirixe a dous MZI idénticos. A parte superior do interferómetro utilízase tanto para modular o sinal no esquema de modulación QPSK como para seleccionar a potencia que consegue o láser DFB para QKD. Utilízase un cambiador de fase adicional para engadir a metade π para a modulación QPSK.

A técnica utilizada no traballo de Paraïso et al. Chámase comunmente OIL. É unha técnica para sincronizar dous láseres que se poden empregar en diversos contextos e campos, sendo este usado en QKD. Neste capítulo imos presentar dous circuítos baseados en Bloqueo de inxección óptica (OIL) de láseres anulares, isto representa unha demostración experimental, por primeira vez que coñecemos, desta técnica en láseres anulares en fotónica integrada monolíticamente.
Como vimos no capítulo anterior, o OIL dos láseres DFB pode ser difícil de obter, xa que precisa dunha adaptación precisa da frecuencia. Neste capítulo discutiremos e demostraremos experimentalmente a inxección óptica de láseres anulares. Este sistema

con respecto ao DFB ten máis resonancias que conducen a un fácil bloqueo da inxección. Deseñamos, fabricamos e medimos dous circuítos nunha quenda de fabricación HHI MPW.
O primeiro circuíto está composto por un simple láser DFB que se usa para inxectar un láser de anel escravo. Utilizaremos este sistema para caracterizar o comportamento básico destes sistemas, sinalando que este modelo sinxelo xa é capaz de realizar QKD e QPSK. O segundo circuíto presentado está formado por tres láseres: o láser DBR central que se alimenta de dous láseres de anel escravos. Este sistema é capaz tanto de QKD como de QPSK de alta velocidade, sendo un deseño de facto e unha alternativa ao circuíto presentado no capítulo 4.
Neste capítulo imos deseñar dous circuítos diferentes que se integran no mesmo deseño de máscara. Cada un deles utilízase para demostrar a posibilidade de funcionamento dual do anel OIL en fotónica integrada e posteriormente utilízase para QKD.

O primeiro circuíto preséntase na figura 6. Neste circuíto utilizamos un simple láser DFB para inxectar o láser de anel. A simplicidade deste é a súa principal vantaxe sobre outros circuítos QKD. No esquema omitimos os interferómetros multimodo (MMI) e os fotodiodos utilizados para controlar o estado do láser. Nas seguintes seccións presentarase unha descrición máis ampla do circuíto. Salientable que este circuíto é capaz tanto de QKD como de QPSK pero ambos teñen un ancho de banda bastante limitado xa que require modulación láser DFB.
Realizouse un segundo circuíto co mesmo deseño de máscara e está descrito na figura 7. Neste caso decidimos aproveitar as dúas saídas dun láser DBR aos dous láseres de anel OIL. A saída dos dous aneis combínase para unha única saída. Este esquema pódese usar tanto para QKD como para QPSK.
A principal vantaxe sobre o primeiro circuíto é a posibilidade de utilizar a modulación en anel para codificar os bits do esquema QPSK. Para o seu uso como transmisor QPSK, engadimos un modulador de fase na saída dun dos láseres en anel, isto permite ter o desprazamento de fase $\pi/2$ para QPSK. O ancho de banda de modulación neste caso é potenciado polo OIL xa que imos modular os dous láseres escravos e non o láser mestre. Tamén nisto omitimos os compoñentes que non son parte fundamental do circuíto. Os láseres anulares utilizados para os dous circuítos son idénticos en dimensións e compoñentes utilizados.

CIRCUÍTOS DESEÑADOS: TRANSMISOR QKD CON BARREIRA DE TEMPO

Neste capítulo imos falar dun deseño diferente para QKD.
O obxectivo principal neste caso é deseñar unha combinación de transmisor e receptor que non requira longas liñas de atraso. Como se pode ver na discusión no capítulo 2, o lado do receptor en particular require longas liñas de retardo para interferir cos dous fotóns. No deseño presentado neste capítulo isto non é necesario, aínda hai unha liña de atraso, pero só ten un centímetro de longo en comparación coas alternativas de centímetros de lonxitude [26].
O principio de funcionamento deste deseño é bastante sinxelo. Na codificación de intervalos de tempo QKD, a clave está codificada na diferenza de fase entre dous pulsos. En enfoques tradicionais transmítense dous pulsos cunha frecuencia de reloxo de 1 GHz, o que resulta en longas liñas de retardo para recombinar os dous pulsos. Aquí propoñemos un enfoque diferente, creamos un pulso curto duns poucos ps de ancho de tempo e use unha liña de atraso curta para dividilo. Isto crea dous pulsos entrelazados cunha separación de tempo breve. No extremo do receptor os dous pulsos pódense recombinar usando a mesma liña de atraso duns poucos milímetros. O noso deseño ocupa pouco espazo e a curta lonxitude do atraso permitiu fabricalo nunha plataforma InP. O deseño foi fabricado nunha rolda SMART Photonics MPW.
Outra vantaxe deste deseño é a simetría entre o circuíto transmisor e receptor. De feito, precisan ter mesma liña de retardo idéntica, o que resulta nun circuíto transmisor que se pode adaptar facilmente para converterse nun receptor. Neste capítulo presentaremos un receptor e un transmisor e comentaremos as vantaxes e inconvenientes de ambos na implementación común ata o momento. Ambos os deseños están en fase de fabricación e están integrados no mesmo chip xunto con outras estruturas de proba e un novo modo láser sintonizable.
O deseño aínda está en fase de fabricación polo que centramos a nosa atención nos resultados da simulación e na teoría do marco deste deseño. O esquema principal do circuíto preséntase na figura 8; nesta figura omitimos os divisores e combinadores MMI. Usamos un láser DBR como fonte principal do noso circuíto. Un requisito crítico para QKD codificado en bins de tempo é a aleatorización da fase absoluta dos pulsos. No noso circuíto isto conséguese empregando un modulador de

fase xusto despois do láser. Despois da fase de aleatorización de fases temos que crear os pulsos que usaremos para codificar o noso sinal. Para iso usamos un MZI con moduladores electro-ópticos rápidos, o que nos permite obter pulsos de poucas ps. A estrutura que segue ao MZI pódese ver como unha MZI desequilibrada.De feito, neste caso os brazos do interferómetro non son iguais e nun deles hai unha liña de retardo. Esta estrutura dividirá o pulso en dous pulsos separados, a sección de fase do brazo máis curto úsase para axustar a diferenza de fase entre os pulsos de saída. Cómpre sinalar que esta estrutura ten dúas entradas e dúas saídas. Unha das entradas está conectada ao MZI e a segunda está acoplada fóra do chip. As dúas saídas están acopladas fóra do chip. Esta función de entrada/saída dual permite que o circuíto se utilice tanto como transmisor como como receptor.

THESIS OUTLINE

- In Chapter 1 the concept of generic photonic integration. The Process design kit (PDK) and the design workflow are decomposed in their basic elements and presented.
- In Chapter 2 contains basic concepts of Quantum Key Distribution. An overview of the experimental realizations in bulk optics and in integrated photonics is included.
- In Chapter 3, contains an extensive discussion of the main simulation an layout tool used in the thesis, with focus on the interface between the two. The interface allows the designers to have a single environment for design and for simulation, cutting on time and human errors. The chapter also contains two examples of simulation using the interface to demonstrate the easiness of use and the reliability of the tool.
- In Chapter 4 the design of a Quantum Key Distribution and coherent transmitter is discussed. The proposed design has been realized in a commercial foundry and here we present the results of the characterization of the main parts.
- In Chapter 5 presents the design of two Quantum Key Distribution circuits based on optical injection of ring lasers. One of this circuit is also capable of coherent transmission taking advantage of the increased modulation bandwidth in injected laser systems. The circuits have been realized in a commercial foundry and the results of the characterization of the main components is presented.
- In Chapter 6 contains the design and idea of a third circuit for Quantum Key Distribution, in this case the circuit implements a time-bin- encoding format. The circuit has been sent for fabrication but at the moment has not been delivered jet.

Part I

INTRODUCTION

This introductory part that covers the basic concept of integrated photonics and quantum key distribution.

1

GENERIC INTEGRATED PHOTONICS

Similar to the process that underwent microelectronics in the past, optical devices see an increase interest in the miniaturization of components and circuits. In this context, Photonic integration has been developed, first with application oriented processes but recently leaving space to a generic integration model. Generic photonic integration aims at lowering the barrier to enter the market of photonic integration and it does so implementing a series of processes and procedures that are unified across the production and design chain.
In this chapter the generic integrated photonic approach will be presented and discussed in steps that go from the circuit idea to the packaged chip.

1.1 PHOTONIC INTEGRATED CIRCUITS

Brief history of integrated photonics.

PICs are devices that include multiple photonic components into a single chip. The first Idea of photonic integration was suggested in 1969 by S.Miller [2]. Since then the Advances in the field lead to the first commercialized PIC by the company Infinera in 2005. Nowadays, the commercial offer of integrated photonics has widened with several companies offering different range of products and materials.

Overview of PICs technologies

The variety of integrable components depends on the materials and processes used for fabrication, but it ranges from passive components: waveguides, splitters, multiplexers and others, to active components like SOAs and photodiodes [3]. Although the main domain of photonic integration has been mainly telecommunications in recent years a series of application in different fields as bio-photonics, tomography and quantum technologies have emerged [4, 5].
The performances and possibilities of designed circuits strongly depend on the material platform used in the fabrication:

- III-V based platforms, are the only ones that allow the integration of gain components due to the direct bandgap of the crystalline structures. Usually these platforms have lower performances in passive building blocks such as waveguides due to the high absorption of the surrounding material needed electrical conduction.

- SOI platforms, offer great performances of passive components and lower costs thanks to the use of fabrication technologies borrowed from the electronic industry. They can integrate modulators and photodetectors. Respect to III-V platforms the absence of a gain module limits the application or requires the bonding of the SOI chip to a III-V chip.

- SiN platforms, offers a wider range of wavelengths operation due to the larger transparency window respect to other platform. Similar to the SOI case the absence of a gain section require the co-integration with other platforms to have light emitting components.

The above list comprehends only the main materials and technologies, but different platforms have been developed and commercialized in recent years including glass based materials and polymers.
We will limit the discussion of this thesis to InP based integrated photonics and all the chips discussed here have been fabricated, or are still under fabrication, in the InP material platform.

1.2 GENERIC PHOTONIC INTEGRATION TECHNOLOGY

Moor's law for integrated photonics

The amount of components in PICs is constantly growing and it follows a similar trend to the Moor's law. In the case of photonics the doubling of components per chip happens every 2.5 years [27].
The slower rate of growth respect to electronic circuits can be explained by different factors:
The bigger footprint of photonic components respect to electrical components that is due to the wavelength requirements limits the ability to integrate a high number of components into a single chip.
Photonic integration requires a broader and more diverse set of basic building blocks than electronic, and each of these blocks has to be optimized and tested, rising the investment necessary

to set up an integrated photonic foundry.
In the early days of integrated photonics, chips were developed

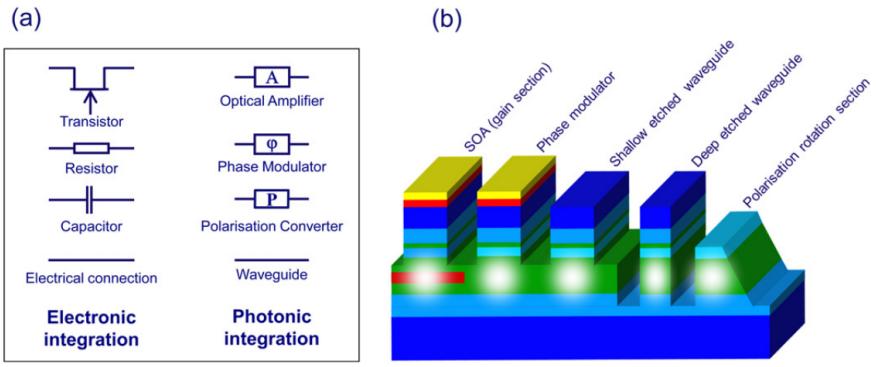

Figure 1.1: (a) comparison between electronic building blocks and photonic ones, (b) cross-section schema of the photonic basic building blocks that can be found in a typical InP generic integrate photonic platform [3]

for specific applications in mind and the set of processes for fabrication was custom. This approach lead to high costs of Research and Development and only big institutions could afford a similar technology.

Generic integration like in electronics

To reduce the costs of research and cleanroom per chip an approach equal to the electronic one has been developed. This consists in a standardized production process that uses basic building blocks. The available Building blocks can be connected and placed forming different structures based on specific circuit specifications. This approach is known as generic integration and allows a higher number of small users to enter the integrated photonic market.
The generic integration technology is already popular in electronics with big electronic companies like Nvidia or Qualcomm, to be "fabless". This means that they do not have their own chip making facilities, but they use the services of third companies aka foundries for the chip manufacturing.
In photonics a similar fabless ecosystem is being developed with different foundries developing their indipendent processes and allowing different customers to design circuits using a library of building blocks provided by the foundry itself.

Photonics foundries provide open access to their standardized fabrication process and a low-cost service for prototyping that consists in a small space in a wafer shared with other users,

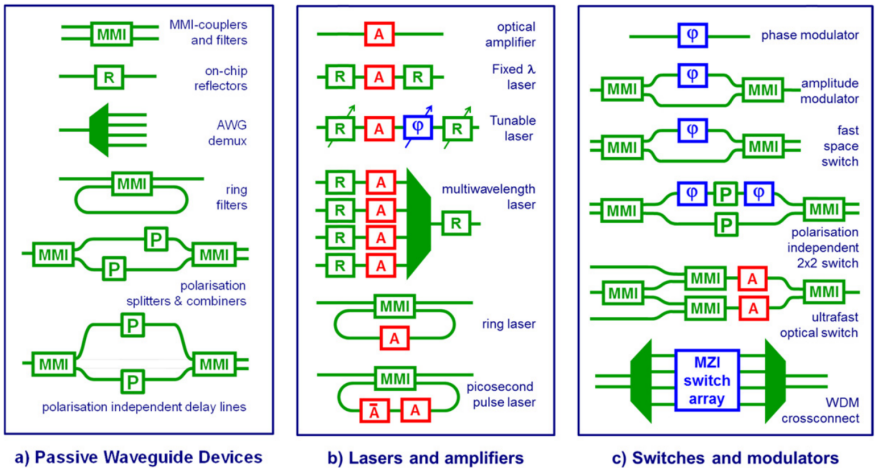

Figure 1.2: Examples of possible circuit topologies that can be obtained using (a) only passive devices, (b) amplifiers and lasers and (c) phase modulation sections [3].

usually referred as MPW.

The PDK elements

They also provide the users with a series of information for the design that are contained in the PDK. PDKs contain a wide variety of information that can be useful for the design of the chip like:

- Building Block (BB) library: is the set of elementary blocks that can be used to build the PIC.
- Simulation models often refereed as compact models: is a set of models that describes the behaviour of the BB. This allows the user and the software parties to simulate the BB or the full circuit.
- Experimental measurements of BB: all available experimental characterization of the single BB or of common combination of them eg. DBR laser.
- Mask assembly rules: They are used to assembly the mask layout coherently between different users.
- Design rules: have to be followed by the designer to have a design in line with expected performances. Not following these rules can lead in some cases to a circuit with unexpected performances drops e.g. bending waveguides more than the suggested radius can lead to extra losses. In other cases the design is not accepted by the foundry, and it has to be modified, e.g. not respecting the minimum distance between elements, it can lead to problems in the

fabrication that can affect other users of the MPW and for this reason it is not allowed.

- Packaging solutions: the suggested topology of some elements of the circuit that will make it easy to find a standardized packaging.
- Testing solutions: similar to the packaging solution this is a set of suggestions to follow to have a design that is easily tested.

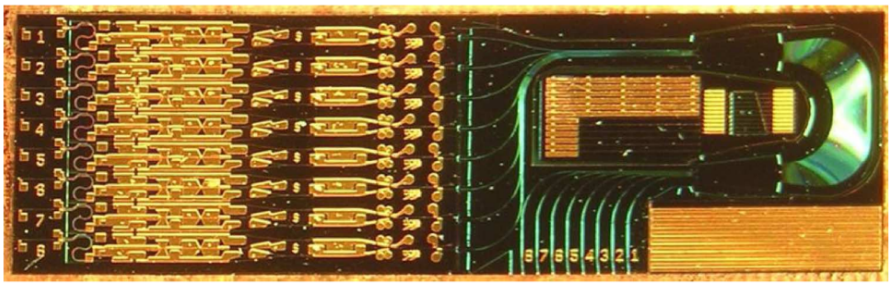

Figure 1.3: 8x8 InP integrated tunable optical router [28], A good example of the complexity of integration that can be achieved.

PDK contributors.

The information contained in the PDK not necessarily come from the foundry. The packaging information usually come from the packaging company that will suggest an easy to assemble design. The experimental measurements can come directly from the foundry or from the institutions that have agreements with them like universities of research centres. Finally, the compact models can be developed by the software partners based on information from the foundry and from the experimental measurements. The big number of contributors to the PDK brought the final product to be in different formats and requiring the end users to have different software and inconveniences to have full access to the information contained. Only recently a collection of open standard has been proposed with the aim of unifying the description of the PDK [29]

1.3 GENERIC PHOTONIC INTEGRATION WORKFLOW

The generic foundry model lowers the entry barrier since it does not need costly proprietary BB designs and fabrications to be owned by the users.
The typical work flow in generic photonics goes as:

PDK development

1. Foundries develop the fabrication process and the BB associated with it. The available information regarding the BB are then collected in the PDK. It is worth noticing that the BBcan separated in two distinct groups, basic BB and composite BB. Basic BB are the smallest and irreducible units that have a specific functionality in a circuit [3], e.g. waveguides and SOA. Composite BB are instead obtained combining multiple basic BB in structures that are of popular use between designers, e.g. DBR laser or MZI.

User enters the ecosystem.

2. The user that wants to develop a PIC chooses a foundry or a broker based on the specific needs of their circuit. The foundry or broker will then provide the user with the PDK in order to start them to start designing. In Europe there are two main brokers for integrated photonics: ePIXfab [30] is a broker for silicon fabs and gives access to different SOI Silicon Nitride foundries in Europe. JeppiX [31] instead provides access to InP and Triplex platforms. In this thesis the chips have been manufactured in Fraunhofer HHI and Smart Photonics thought the JePPIX MPW service.

Simulation of the circuit

3. Since the BB are standardized a lot of information and testing results can be predicted by the foundry and communicated to the user. All the elements of the PDK allow the user to design the circuit with specific performances expectancies. The circuit performances can also be simulated using various circuit simulators available on the market. In this thesis we will use mainly the open source simulation tool PHIsim.

Mask assembly

4. When the circuit is selected the designer can proceed with the mask assembly. The precise position of the BB inside the cell has to be decided, this will create a mask of the circuit. At this level also a series of fabrication checks are implemented in order fabricate the design with sufficient quality. This fase is called Design rule check (DRC) and is usually implemented inside the mask assembly software. In the case of an MPW run the individual design are combined by the foundry on a single wafer. In this thesis all the mask layouts have been made with the open source software Nazca-design [32].

PIC fabrication

5. The fabrication can be now carried out by the foundry at the wafer level without knowing the final application of the circuits under fabrication. This ensures all the user's

privacy in the sense that they don't need to share with the foundry the specific reason/applications of their circuits. On the foundry side is easier to guarantee the quality of the final products given the extensive testing that has been carried out on the single BB and the repeatedly used process. At the end of the fabrication each wafer is cleaved and the chips are delivered to the users.

6. In order to test the circuit foundries usually include into the fabricated wafer also a test cell that will be used to measure basic qualification parameters of the produced BB. An example of these parameters are waveguide losses and Fabry-Perot (FP) lasers. Using these parameters a test of the fabrication quality is produced. The user at this point can consider the BB that form the circuit as fully functional, and they can carry out the final tests based on the circuit necessary specifications.

PIC testing

1.4 CONCLUSIONS

In This chapter we have summarized the development of the generic integrated photonics platforms. We have discussed the main photonic platforms and material. The concept of PDK has been presented, and the main components have been described. Finally, a description of all the design workflow of an integrated photonic chip from the design to the packaging and testing has been discussed.

2

QUANTUM KEY DISTRIBUTION

QKD is a rapidly evolving field of quantum information, new protocols and security proofs are developed regularly, and experimental demonstrations are moving from labs to in-field implementations. In this introduction we will cover the basic aspects of the technology in order to give the user the basic knowledge and reference to approach the QKD world. In the first part we will cover the basic protocol BB84[1] discussing the basic theoretical aspects and the most common implementations. The second part covers the state of the art of experimental research and will discuss the recent advances in free space photonics QKD and integrated photonics.

2.1 MOTIVATIONS

Theoretical-secure communication

In Secure Communications two parties, conventionally named Alice and Bob, want to communicate privately using a common channel. The presence of an eavesdropper Eve, undermines the privacy of this communication. The best way for Alice and Bob to ensure that their information remains private is to use an information-theoretical secure communication. Meaning A communication that is fundamental secure by theory and even if Eve has a far superior technological advantage over Alice and Bob she can not decrypt the message. This type of communication can be achieved using a OTP method [6]. The OTP consists of a long key of random character that is ideally as long as the message and is kept secret from Eve. As long as the key remains secret and is used only once [7], the communication between Alice and Bob can be considered information-theoretical secure. This communication procedure leaves us with a different problem, how can Alice and Bob share the key?
This is known as the key distribution problem.

The current solution to the key distribution problem is public key cryptography, in this concept Bob has a pair of keys. One

of these two keys is public and Alice can use it to encrypt the message. The encrypted message can be decrypted only using Bob's private key.

Solutions to the key distribution problem.

This type of cryptographic system is used extensively nowadays but is not information-theoretical secure. In fact the security is based on the fact that given the public key there is no efficient algorithm to calculate the private key. For instance the RSA [8] system is based on the factoring of large integer number, this task is extremely time-consuming for a classical computer. This kind of cryptography is clearly not resistant to advances in technology. It has been even more evident since the invention of the Shor algorithm[9] that creates an efficient way of calculating integer factorization using quantum computers.
Although the Shor algorithm requires a high number of qbit to execute and nowadays is not feasible, recent progresses in quantum computers technology are getting closer to the required specification.
QKD promises to solve the problem using fundamental laws of nature like the uncertainty principle and the entanglement of quantum particles. The idea from a communication perspective is to implement a OTP communication and use quantum key distribution to continuously share the cryptographic key realizing an information-theoretical secure communication.

real life QKD

The ideal realization of QKD is a complete encryption of a communication channel, in a realistic environment instead the devices used by the parties for the QKD protocol might be hackable or vulnerable to side channel attacks [10].
MDI-QKD protocols [11] represent the safest possible implementation, the price to pay for the high security level is a low secret key rate. More practical QKD protocols, assume some level of trust in the devices used, and they can achieve reasonable key rates with lower security.
Another trade-off to consider is the one between key-rate and distance, in fact as proved in [12] the key rate distribution can not be higher that $-\log_2(1-\mu)$ where μ is the transmittivity of the channel.
This fundamental limit of QKD has been overcome using trusted repeaters in a number of metropolitan size networks: the DARPA Quantum Network[13], the Vienna QKD network [14], the Chinese hierarchical metropolitan network [15], the Tokyo QKD network [16]. A better option would be to base the network

on untrusted nodes as has been theoretically idealized using different systems [11, 17].

2.2 BASICS CONCEPTS OF QKD

In the last years a great number of different protocols for QKD have been discussed and analysed [33]. The two main categories of them are DV-QKD and Continuous Variable Quantum Key Distribution (CV-QKD).
In both cases the basic communication proceed as follows:

Basic communication procedure.

Alice (the sender) encodes the value of a random variable α into a selection of non-orthogonal quantum states. The sequence is then transmitted through a channel controlled by an eavesdropper (Eve). The amount of information that Eve can get from intercepting the communication is limited by the linearity of quantum mechanics that forbids perfect cloning [34].
At the other end of the channel the receiver (Bob) measures the incoming signal and obtains a new random variable β. Alice and Bob open a classical communication channel and share information of their preparation or measurement sequence. This is enough to agree on an identical common sequence.
If Eve sniffed the channel, the error introduced in the system will be detected my Alice and Bob who can discard the sequence and restart the protocol.
Notice that if a key is aborted it does not represent any security threat since it is just a random string. Eve doesn't get any advantage in this case, she just slows down the communication. From the security point of view QKD has the significant advantage that Eve has to break the security in real time since she can not clone and store a copy of the key.
In the following of this thesis I will limit the discussion to the case of DV-QKD.
With Discrete variable we are referring to the group of protocols based on Hilbert spaces with finite-dimensions of bases, whereas with Continuous Variable we are considering a Hilbert space with infinite dimensional bases.
To better understand the key principles let's recall some fundamental quantum physics concepts.

QKD quantum mechanics basics

A state in a bidimensional Hilbert space can be represented by a vector in the following basis:

$$|0\rangle = \begin{pmatrix} 1 \\ 0 \end{pmatrix}, \; |1\rangle = \begin{pmatrix} 0 \\ 1 \end{pmatrix} \tag{2.1}$$

and the generic state will be:

$$|\Psi\rangle = \alpha|0\rangle + \beta|1\rangle = \cos(\theta/2) + e^{i\phi}\sin(\theta/2)|1\rangle \tag{2.2}$$

Having $\theta \in (0, \pi)$, $\phi \in (0, 2\pi)$, the vector Ψ can be represented in the "Bloch-sphere". We can find the combination of θ and ϕ that correspond to the vectors aligned with the axes.

$$|\theta = 0, \phi = 0\rangle = \begin{pmatrix} 1 \\ 0 \end{pmatrix} = |0\rangle \tag{2.3}$$

$$|\theta = \pi, \phi = 0\rangle = \begin{pmatrix} 0 \\ 1 \end{pmatrix} = |1\rangle \tag{2.4}$$

these are the eigenstates of the Pauli operator σ_z and are usually refereed as the Z basis.

$$|\theta = \pi/2, \phi = 0\rangle = \frac{1}{\sqrt{2}}\begin{pmatrix} 1 \\ 1 \end{pmatrix} = |+\rangle \tag{2.5}$$

$$|\theta = \pi/2, \phi = \pi\rangle = \frac{1}{\sqrt{2}}\begin{pmatrix} 1 \\ -1 \end{pmatrix} = |-\rangle \tag{2.6}$$

are the eigenvector of the operator σ_x.

$$|\theta = \pi/2, \phi = \pi/2\rangle = \frac{1}{\sqrt{2}}\begin{pmatrix} 1 \\ i \end{pmatrix} = |+i\rangle \tag{2.7}$$

$$|\theta = \pi/2, \phi = 3\pi/2\rangle = \frac{1}{\sqrt{2}}\begin{pmatrix} 1 \\ -i \end{pmatrix} = |-i\rangle \tag{2.8}$$

for the operator σ_y. These eigenstates form what are a good example of MUBs, formally it means that given a d-dimensional Hilbert space: $\{|\psi_1\rangle ... |\psi_d\rangle$ and $\{|\phi_1\rangle ... |\phi_d\rangle$ are mutually unbiased if $|\langle\psi_i|\phi_i\rangle|^2 = 1/d$. In practical terms, measuring an eigenstate of one of the MUBs in a different basis will result in a random number.

2.2.1 *BB84 protocol*

The most used and known protocol is the BB84 [1]. At the beginning of the protocol Alice encodes a binary digit in one of

the MUBs, for example the polarization state of a photon. The two basis are associated with the vertical-horizontal oscillation of the electromagnetic field ($|H\rangle = |0\rangle$ and $|V\rangle = |1\rangle$ Z basis) and the diagonal-antidiagonal oscillation of the field ($|D\rangle = |+\rangle$ and $|A\rangle = |-\rangle$, X basis), the classical bits are encoded for example as $0 = |0\rangle = |+\rangle$ and $1 = |1\rangle = |-\rangle$. The non-orthogonality of the states secure protection against cloning from Eve. This condition implies that Eve cannot retrieve the full information transmitted by Alice and every action of Eve on the signal will result in a disturbance that can be detected by the legitimate users.

The photons are then transmitted to Bob that measures them in one of the two basis choosing X or Z randomly. Note that, if Bob uses the same measurement basis as Alice he will be able to retrieve the bit exactly and completely, in case he uses the other one the resulting bit will be random. To discard the bit that are randomly generated, at the end of the quatum transmission, Bob opens a classical channel to inform Alice of his basis choice. Alice will also share with Bob her basis choice. At this point both Alice and Bob are able to discard the events when they did not use the same basis, leaving them with a common sequence of bits. This string of bits is called "shifted-key", an example of the protocol implementation can be seen in Figure 2.1.

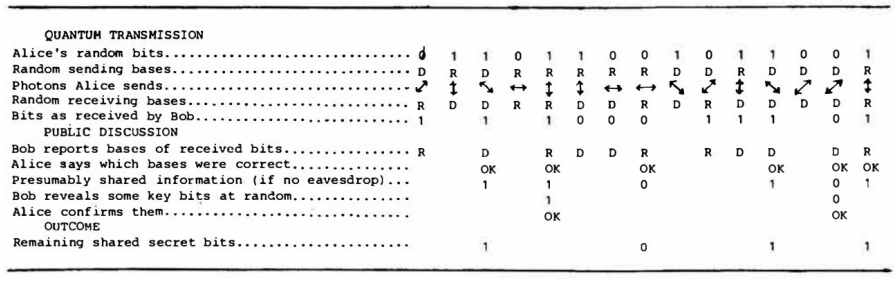

Figure 2.1: Visual example of the BB84 implementation take from the original manuscript of Bennet-Brassard [1]. Alice encrypts the random bit in one of the MUBs basis set, Bob has to choose a measurement basis without any information on Alice's basis choice. A final public discussion is used to extract the shifted key

The final stage of the protocol is to estimate the Quantum Bit Error Rate (QBER) this can be due to various noise source in the communication channel but in the worst case scenario is due to Eve. We define QBER the probability that a bit in Bob's shifted key is different from Alice's one. In order to estimate

this quantity Alice and Bob can decide to disclose part of the sequence and compare them. Knowing the used protocol there is a threshold for the QBER (11% for the BB84 [35]) to consider the communication secure. if the measured QBER one is above the threshold value Alice and Bob restart the protocol from the beginning.

BB84 using different encoding formats

It is worth mentioning that the BB84 protocol, although originally developed with polarized photon, is a completely general protocol that can be applied to any couple of MUBs. A common experimental setup for the BB84 protocol uses the phase of photons to encode the key. . This consists in using two subsequent time bins: one base is constituted in a photon inside bin 0 or bin 1, the second base is determined using the phase difference between the photons in the two bins. It is easy to see that Bob has to decide whether he wants to try to detect a single bin or interfere them to retrieve the phase difference, fulfilling the requirement of the BB84 protocol. The absolute phase of the photons must be random, and only the differential one encodes information.

2.2.2 *Weak coherent pulses*

In practical application of QKD there are two ways of obtaining the single photons used in the protocols: single photon sources[36] and laser attenuation, also refereed to as weak coherent pulses. The later one is the more used in practical QKD given the higher repetition rate and easy usability.

An alternative to single photon sources.

To better understand the use of weak coherent pulses, that will be used later in the thesis, it is worth recalling that a Laser pulse follows the Poisson distribution:

$$P(n) = \frac{\mu^n e^{-\mu}}{n!} \tag{2.9}$$

Where $P(n)$ is the probability of having n photons in the pulse and μ is the photon flux.

In Tab2.1 the probability of pulses with different number of photon is reported. Minimizing the flux leads to lower probability of multiphoton pulses, noticing that the probability of multiphoton pulses still remains finite. A multi-photon pulse during the key exchange can lead to a security treat and the probability of it has to be minimized.

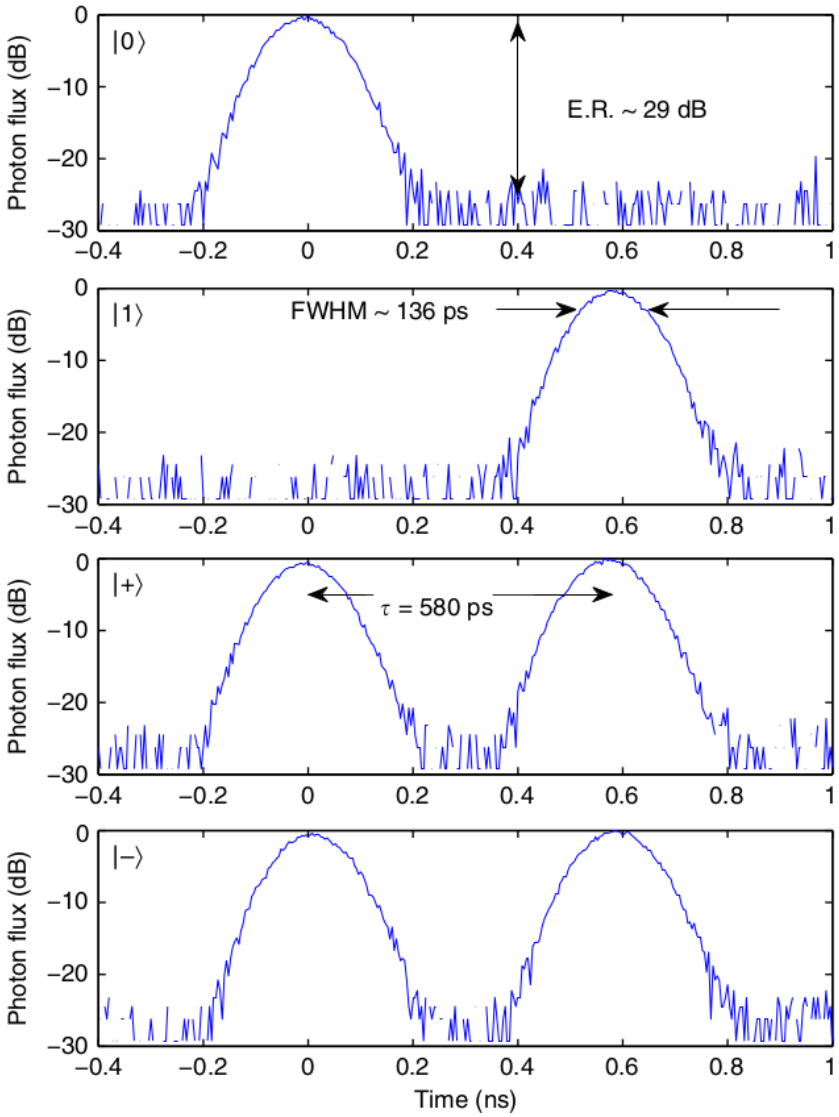

Figure 2.2: Example of time bin encoding from [26], the two bases are: X basis photon in bin 0 or bin 1, Z basis phase difference between photons of 0 or π.

Multiphoton attack

Eve can in fact use a multi-photon pulse for a photon number splitting (PNS) attack [37, 38]. This consists in doing a quantum non-demolition measurement on the channel to determine the number of photons per pulses, when Eve detects a multiphoton pulse she splits it and keep one or more photons, the remaining ones arrive to Bob that can proceed with the protocol without noticing any anomaly. Protocols different from the BB84 have been developed to be PNS resistant like the SARG04 [39] but in the practical implementation a solution to the PNS attack has been found using the Decoy-state method.

	P(0)	P(1)	P(2)	P(3)	P(4)
$\mu = 1$	0.3679	0.3689	0.1839	0.0613	0.0153
$\mu = 0.5$	0.6065	0.3032	0.0758	0.0126	0.0015
$\mu = 0.05$	0.9512	0.0475	0.0011	2e-5	2e-7

Table 2.1: Poisson probability with different photon fluxes.

On practical terms this solution is relevant since not only Alice's single photon source are expensive and not widely available, but also Bob suffers a similar problem with single photon detectors, in fact in most cases Bob uses threshold detectors.

2.2.3 *Decoy state method*

To fully understand the Decoy state method let's start with what Bob can actually measure. Bob's gain is in fact the sum of Bob's probability of detecting an i-photon pulse(Y_i) multiplied by the probability of Alice sending it $P(i)$ (equation 2.9):

$$Q_m = \sum_{i=0}^{\infty} Y_i P(i) \tag{2.10}$$

The QBER of can be now calculated similarly, using e_i the probability of error:

$$E_m = \frac{1}{Q_m} \sum_{i=0}^{\infty} Y_i e_i P(i) \tag{2.11}$$

It is not possible to measure Y_i and e_i in practice give that Bob can only measure Q_m and E_m.

Decoy state method principles.

However, if Alice sends different values of μ, corresponding a different value of $P(i)$ Eq 2.9 Bob can build a set of linear equation and estimate $[Y_0, ...Y_n]$ and $[e_0, ...e_n]$.
The set of equation of Bob will never be infinitely precise in fact to obtain that the number of different μ values that Alice sends should be infinite. However, the probability $P(i)$ approaches 0 for high number of photons so for Bob and Alice is sufficient to calculate only the first coefficients. In practical implementation has been shown that two photon flux states are sufficient to detect the presence of Eve [40].
In Practical terms the Decoy state method is implemented modulating the intensity of the pulses.
A base intensity is chosen for the key transmission, in some

random moments Alice changes the intensity to a decoy state one.
The decoy state are then used by Alice and Bob during the final phase of the protocol to establish the losses of the channel (Y_i and E_i). In case Eve is sniffing the channel she can not distinguish between the decoy states or the legitimate key carrying states. The interference of Eve leads to excess losses that now can be measured and Alice and Bob can abort the communication in this case.

2.3 EXPERIMENTAL IMPLEMENTATIONS

2.3.1 *free space optics QKD*

As analysed in the previous sections the main requirement for QKD is to prepare photon is states corresponding to the eigenstates of two or more MUBs. Once this is obtained the protocol can be chosen based on required security and key rates.

Achivements of QKD

The first implementation of a BB84 protocol with Decoy-state has been done using a commercial two-way idQuantique system [41] in 2006. In a two-way system, Bob produces laser pulses that are then sent to Alice who attenuates them, applies a phase shift and send them back to Bob. This first attempt and the sequent one implementing vacuum pulses for the estimation of background and dark count noise, achieved low-key rates of 422.5 bps on a maximum distance of 60 km .
More recently, mostly thanks to the improvement of single photon detectors, it has been possible to achieve high Key rates of 13.7Mbps after a 2dB attenuation, corresponding to 10km of standard fiber($\sim 0.2\text{dB/km}$) [42]. Boaron et al. [43] managed to achieve the highest reported distance for fiber QKD at 421km with the trade of a low keyrate of 6.5bps

Table2.2 summarizes the main achievements in experimental decoy-state QKD. It is noticeable the progression in the clock rates of the communication, this has been possible thanks to the new generation of detectors and transmitters, achieving a considerable increase in the key rate at the same distance. The majority of the experiments uses phase encoding to transmit the qbit, this is due to the easiness of this kind of encoding respect to polarization.

REFERENCE	CLOCK RATE	DISTANCE[KM]	KEY RATE [BPS]	notes
Zhao et al. [41]	5MHz	60	422.5	commercial QKD, phase encoding
Peng et al. [44]	2.5MHz	102	8.1	polarization encoding
Rosenberg et al. [45]	2.5MHz	107	14.5	phase encoded
Yuan, Sharpe, and Shields [46]	7.1MHz	25.3	5.5k	phase encoding
Zhen-Qiang et al. [47]	1MHz	123.6	1.0	phase encoding
Wang et al. [48]	0.65MHz	25	0.9	phase encoding
Dixon et al. [49]	1GHz	100.8	10.1k	phase encoding
Rosenberg et al. [50]	10MHz	135	0.2	phase encoding
Yuan et al. [51]	1.036GHz	100	10.1k	phase encoding
Liu et al. [52]	320MHz	200	15.0	polarization encoding
Lucamarini et al. [53]	1GHz	80	120k	phase encoding
Fröhlich et al. [54]	1GHz	240	8.4	phase encoding
Yuan et al. [42]	1GHz	2dB	13.7M	phase encoding
Boaron et al. [43]	2.5GHz	421	6.5	time-bin encoding

Table 2.2: Main experimental realizations of decoy state QKD experiments in chronological order, it is noticeable the progress in the clock rate.

QKD with optical injected lasers.

A scheme for QKD has been proposed by Yuan et al. [55] that takes advantage of optical injected lasers, and it is particularly suitable for integration.
Figure 2.3 shows the setup, a phase preparation laser is directly modulated in order to produce pulses from quasi steady-state emission. Using a circulator the phase preparation laser is then feed into the pulse generation laser, for each pulse of the phase preparation laser one or more short pulses of the generation laser are produced by gain switching. Let's now focus on the phase between pulses, the absolute phase of each pulse of the phase preparation laser is random since the lasing action is triggered by spontaneous emission, on the other hand the phase of the pulse generation laser is the same as the feed pulse.
This property allows the control of the relative phase between two consecutive laser pulses produced by the pulse generation laser, it can be obtained modulating the signal of the phase preparation laser. The pulse generation laser is gain switched off during the phase modulation to avoid fluctuation in the intensity and frequency. This leads to the creation of two subsequent pulses with random absolute phase but with deterministic differential phase.
The described scheme has been used to obtain QBER of 2.4% at 20 dB loss and 10 kbit/s secure key rates, that is similar to what has been in other experimental realizations[53] showing excellent stability over time. The modulator free design also allows the easy implementation of different protocols, an example of this is reported by Comandar et al. [56].

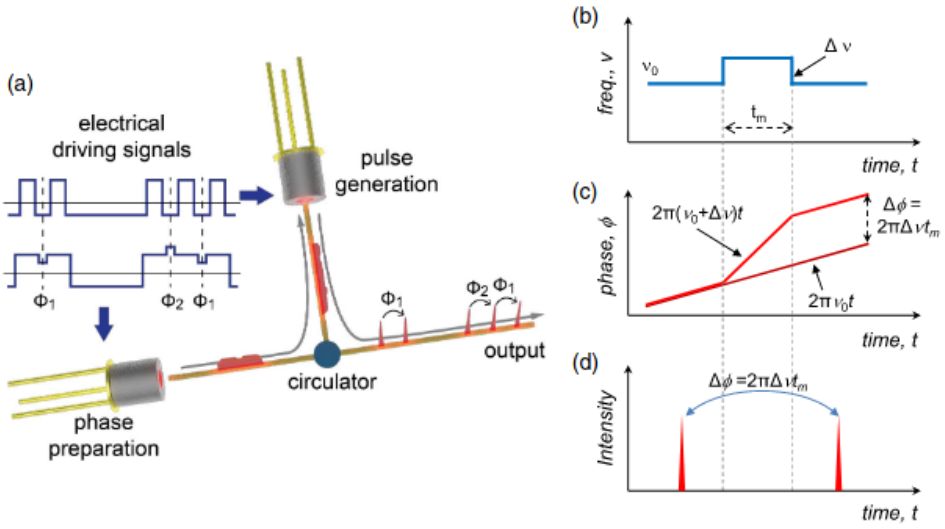

Figure 2.3: Optical laser injection scheme from [55]. The master laser is in this case refereed as the phase preparation laser, it is driven to produce nanosecond scale pulses and biased according to figure (b). This in order to modify the phase injected into the slave laser (pulse generation laser) according to graph (c). The pulse generation laser is then driven by a faster pulse train, the resulting emission is shown in (d).

2.3.2 *Integrated photonics QKD*

Integrated Photonics offers a compact platform for monolithic integration of photonic circuit. Various materials platforms have been used exploring the different capabilities and increasing the complexity.
Silicon photonics platform have recently gained traction as one of the main platform for quantum technologies due to the promise of integration of both photonics and electronics components. An implementation example is shown in Figure 2.5, although the achieved key rate is far from being impressive ~ 0.95 kbps with 5.4% QBER, the experiment of Ma et al. [40] was a first proof of the possibility of realizing QKD in integrated photonics.

InP QKD

A full integrated photonic QKD system has been developed by Paraïso et al. [25]. In this case the Transmitter is realized in Indium phosphide to take advantage of the gain section present in the platform. The receiver is instead realized in silicon Oxinitride, that allows low loss waveguides. The chips are also

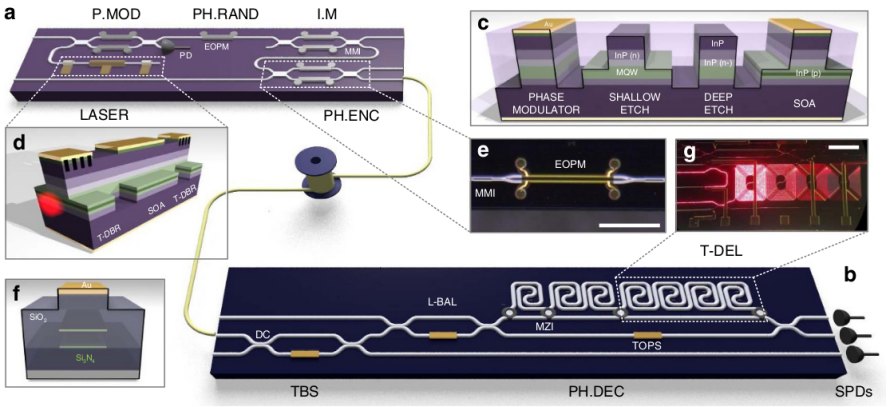

Figure 2.4: Complete QKD system in integrated photonics from [26],(a) transmitter chip realized in InP platform, capable of GHz clock rates and multiprotocol QKD. The Circuit is composed of a Laser, a pulse Modulation section (P.MOD) that create short pulses from the CW laser. A phase randomization section necessary for security in every time-bin encoded protocol. Intensity modulation (I.M) section to obtain signal-decoy and vacuum states. A final Phase encoding section (PH. ENC) to finally encode bits in the desired base. (b) Receiver chip based on SiO_xN_y platform, the photodiodes are off chip (SPDs), MZI and directional couplers allow the creation of loss balancing (L-BAL) and tunable delay lines(T-DEL) resulting in multiprotocol possibilities. (c) InP platform cross-section of different elements. (d) representation of a tunable CW laser using Tunable DBR (T-DBR). (e-g) photo of different elements of the integrated PICs (f) SiO_xN_y platform waveguide cross-section.

REFERENCE	CLOCK RATE	DISTANCE/LOSS	KEY RATE [BPS]	notes
Ma et al. [57]	10MHz	5km	0.95k	Silicon chip, decoy-BB84
Sibson et al. [26]	1.72GHz	4dB	565k	InP chip, DPS and BB84
Sibson et al. [58]	1.72GHz	20km	916k	silicon chip, coherent one way protocol
Bunandar et al. [59]	625MHZ	43km	157k	metropolitan network
Ding et al. [60]	5KHz	4dB	7.5	silicon high dimension
Zhang et al. [61]	1MHz	16dB	0.14k	silicon cv-qkd
Paraïso et al. [25]	1GHz	20dB	270k	inP, modulator free
Wei et al. [62]	1.25GHz	140km	497	silicon,mdi-qkd

Table 2.3: table of main QKD experiments based on integrated photonics chips.

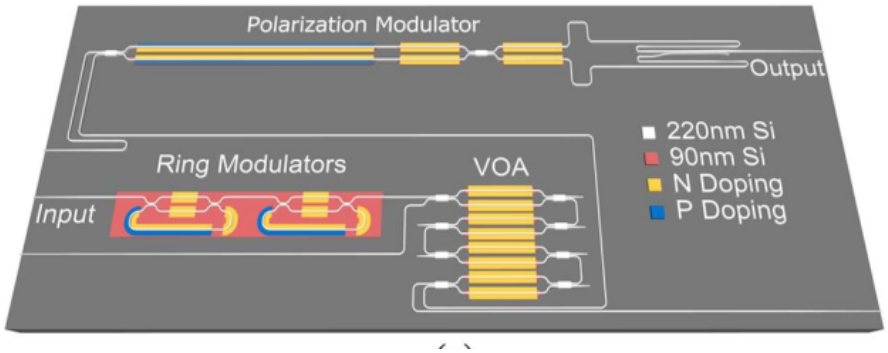

Figure 2.5: Scheme from [40] of Si based PIC for polarization encoded QKD, the ring modulators are used to obtain short pulses, Variable optical attenuators are used to reach QKD power levels and a final polarization modulator is used before output of the signal.

capable of multiprotocol transmission and are demonstrated to work with BB84[1], coherent one way (COW)[37] and DPS .
In this case the key rates achieved with different protocols are still below the state of the art but are of interest given the advantages offered by PIC. For the BB84 protocol a key rate of 345 ± 15 kbps with 1.17% QBER at 20 km of standard fiber is achieved, with the key rate lower that the 1.06 Mbps but with improved key rate respect to the 4% respect to [53]. The performance is similar instead to the optical injected laser QKD.

A chip implementing the circuit of Yuan et all[55] based on optical injected laser has been developed by Paraïso et al. [25]. This design is particularly advantageous since it doesn't require high speed modulators. The performance are also comparable or even better than state of the art QKD reaching 840 kb/s @ 50 km of standard fiber with a QBER of 3.2%. The chip implemented by Paraiso et al. is displayed in figure 2.6.

2.4 CONCLUSIONS

In this Chapter we have presented some basic concepts and the state of the art quantum cryptography. The technology is still facing numerous challenges in both the theoretical and experimental work. Current experimental work goes in multiple directions exploring solutions both in bulk photonics and integrated photonics. The later one is representing an avail-

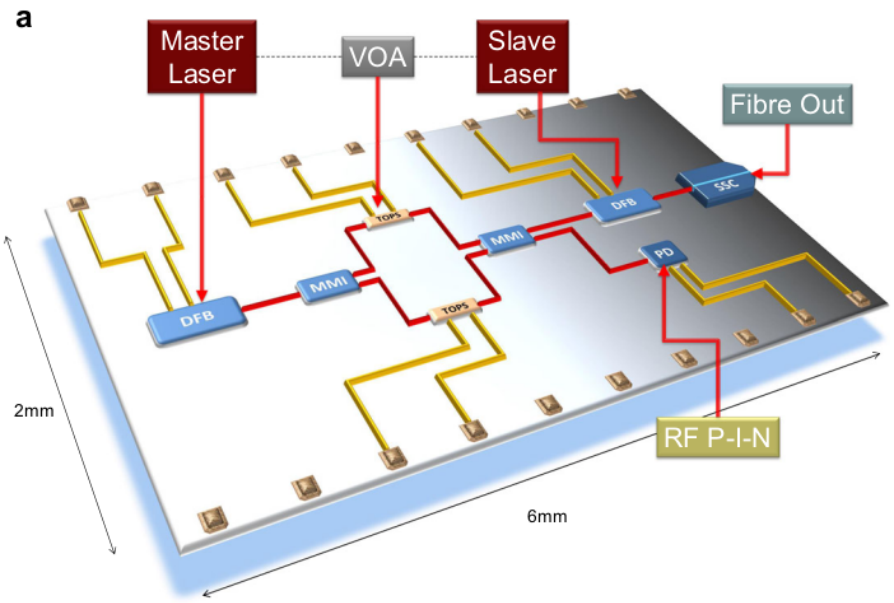

Figure 2.6: Schematic used in [25], the two DFB lasers are operated in optical injection locking. A Variable optical attenuator (VOA), composed by a tunable Mach-Zender interferometer using two thermo-optic phase shifters, is used to attenuate the power injected from the master to the slave.

able solution to integrate with lithographic precision multiple element, improving stability and reliability of the systems.

Part II

DEVELOPED TOOLS

In this part we present the simulation tool used for the simulations in this thesis.

3

AN INTERFACE TO RULE THEM ALL

This chapter expands the concepts and demonstrations that have been presented at the Photonic Benelux 2021 annual symposium. Typically, PICs designers are forced to work in two separate environments, one for the laser/circuit simulation and one for the mask layout.
The disconnection between the two environments can easily lead to errors and mismatch between the two circuits. Typical errors range from laser designs that fail to comply with manufacturing constrains to errors in translating physical parameters between the two environments, e.g. optical path lengths.
In this chapter, we present and dig into the details of the integration between two open source software programs: the layout tool Nazca-design [18] and PHIsim traveling wave simulation software[19]. First, we will exhamine the working principles of the individual software. After we will present our interface that bridges the two programs creating a single layout and simulation environments. We will demonstrate the use of the interface and compare it with experimental results.

3.1 INTRODUCTION

Figure 3.1 is a schematic of the usual workflow. The designer starts in the simulation space and reproduces a schematic of the circuit in this environment. In this environment is not possible to set the final geometry of the circuit but only a list of elements and the connection between them. The designer has to translate the circuit into a layout that will be used by the foundry to build the masks. In this step some commercial tools provide an automatic export features, but this requires the use of complex auto-routing algorithms that usually result in unpredictable and inconvenient shapes.
In fact, the simulation schematic does not contain the information about position of the elements but only their connections,

leaving to the automatic exporting tool the task to figure them out. Another underestimated factor, that is not taken into account in the simulation space, is the circuit footprint, this is often a critical information.
The result of the separation between the environments is that designers find them self going back and forth between environments to check parameters. This can easily lead in some cases to errors and mismatches between the simulated circuit and the mask layout or, in other cases, to mask layouts that due to time constrains are not simulated at all.

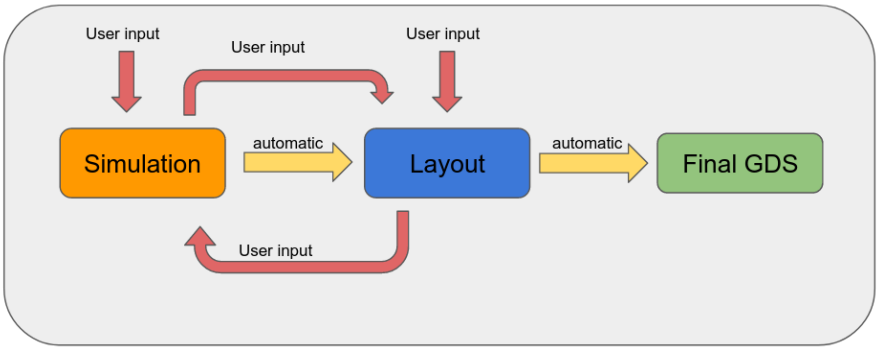

Figure 3.1: Schematic description of the typical workflow used in integrated photonics design. The user input (red arrows) is required in multiple parts of the design and creates a loop of back and forth between the layout design space and the simulation space.

Figure 3.2 visualizes the workflow proposed and used in this thesis. In this case, the designer inputs the circuit layout in the Nazca design framework. Since the circuit layout contains all the information to build the connectivity between the elements, an automatic exporting to simulation tool is always going to represent the designer's idea completely.
The designer can now import a series of simple parameters that are necessary only for the simulation, that can range from simulation length to gain of the active section. This working method saves the designer valuable time, since they don't have to translate the circuit manually any more. The automatic procedure of translation ensures the agreement between the layout and the simulated circuit, reducing the possible error sources in the final submission.

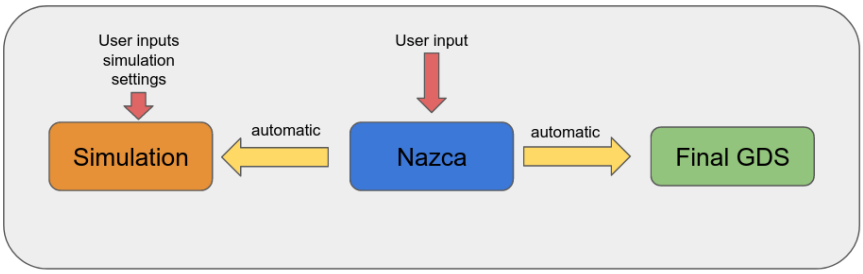

Figure 3.2: Unified workflow, the user input is required only two times and only once the user has to input the circuit, the second input is necessary only to set up the simulation parameters like duration, time step etc.

3.2 NAZCA-DESIGN

Nazca-design is an open source framework for photonic integrated circuit's design. It has been developed by Ronald Broeke and Xaveer Leijten and is currently distributed under the Gnu Afiero General public license v3. The name is inspired by the drawings located in Nazca (Peru), as can be inferred from the logo, corresponding to the Nazca's hands draw.

The main purpose of Nazca is the design of mask layout of integrated photonic circuits, it has been made with the designer's perspective in mind. This easy to use tool based on python-3 became quickly popular with thousands of downloads also thanks to its open source nature.
The main philosophy of Nazca can be summarized in the "make a Cell, put a Cell" motto. This easily conveys the simple idea behind the workflow in Nazca. The main element of the mask is the Cell, it can be of various size and complexity. A Cell can be put, meaning it is placed in a position in the layout, the same cell can be positioned (put) in different position at the same time, de facto making multiple copies of it. This action is technically called the instantiation of the cell. The putting of a Cell creates an instance of it, representing the cell with a specific position in the mask design.
A good analogy to a cell is a stamp: every time you press the stamp on paper you are instantiating the cell, the mark left on the paper is the instance of the cell, you can do it in multiple times with the same stamp in different places. It is easy to see how this method of work is compatible with the concepts of

generic photonic integration seen in Chap 1.
The possibilities in Nazca don't end here, in fact it supports full hierarchical design, meaning that each Cell in Nazca can be composed of instances of smaller Cells.

Under the hood, Nazca is a netlist builder composed by a series of trees(Cell), each composed of points that are instances of smaller trees(still Cells).
The layout built with Nazca not only represents the mask layout but also the entire circuit. It is natural to use Nazca not only to construct the final mask of the circuit but also to build the circuit that is then run in the simulation.

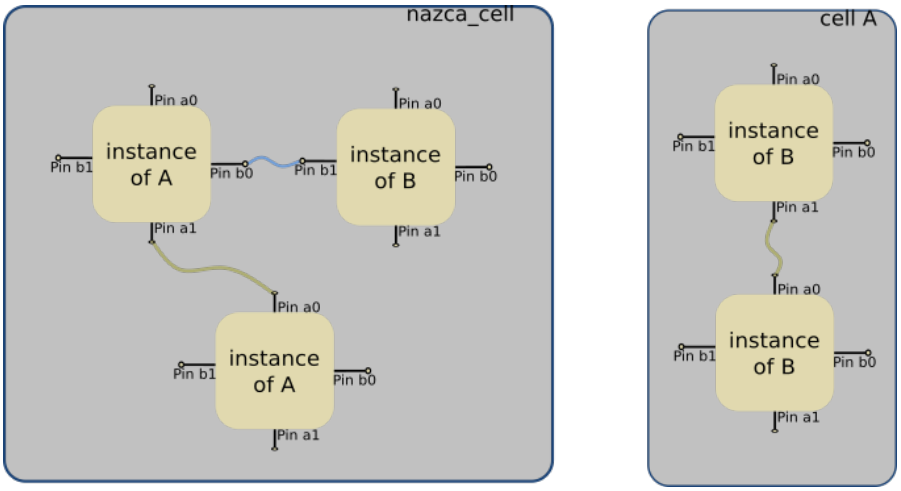

Figure 3.3: Representation of the Nazca tree, each cell is composed of instances of other cells. The instances are then connected using Nazca pins. Each Instance is the representation of a Cell that can have a geometry by itself or be the composition of other instances of different cells. The nazca_cell is the top cell of every design and it contains the full design.

3.3 PHISIM CIRCUIT SIMULATOR

PHIsim is an open source traveling-wave finite-time-difference circuit simulator written in C language and developed by Erwin Bente[19]. The circuit representation is carried out using a library of basic building blocks that can be found in a PIC e.g. waveguides, couplers, modulators, amplifiers and saturable absorber. The circuit elements are divided in small segments that are multiple integer of the simulation wavelength. The prop-

agation equations of lights are solved per each segment and this procedure repeats until the maximum number of simulation cycles is reached.
We can write the simulation step as:

$$\delta t = \frac{n \cdot \lambda \cdot n_g}{c} \tag{3.1}$$

Where n is a parameter decided by the user, λ is the simulation central wavelength, n_g is the group index of guided light, and $n \cdot \lambda \cdot n_g$ is the length of a circuit segment. Consequently, the total simulation time can be calculated as $\delta t \cdot n_{cycles}$ where n_{cycles} is the number of simulation cycles decided by the user. Every building block has to be composed of an integer number of segments.
Possible Building blocks that can be used in PHIsim are:

- Passive Waveguide (can include 2 photon absorpition):
  Is the simplest element, that transmits the field from one side to the other. Losses are implemented in this element and are defined by the user in the parameter file. The user can decide to use special waveguides that will take into account the effects of two photon absorption on the light transmission, the parameters for which can be defined separately.

- SOA:
  Is connected to a current source and implements a logarithmic gain approximation. Numerous effects are considered in the equations describing the gain section behaviour:
  - Gain compression: carrier heating and spectral hole burning, two photon absorption and free carrier absorption.
  - Carrier density linewidth enhancement factor.
  - Carrier temperature linewidth enhancement factor.
  - Non-linear refractive index

- Saturable absorber:
  The set of equations describing the behaviour are the same as that of the amplifier, although the parameters can be different. In particular to simulate the behaviour of the saturable absorber, the carrier lifetime is one of the critical parameters. In this case, the full dependency between the

voltage applied to the Circuit element and the carrier lifetime is not implemented, due to the lack of experimental results on this particular topic.

- Isolation Section:
  It is constituted by an amplifier section with no source attached, similar to the saturable absorber case, the parameters describing the behaviour of the isolation sections are separate from the amplifier ones, in particular, the carrier lifetime.

- Reflector:
  It acts as a mirror effectively positioned in the middle of the segment. The reflectivity can be adjusted per element, meaning that is possible to have multiple reflectors in the circuit with different reflectivity. Another parameter of the element are the losses associated with it, effectively it is possible to create a neutral density filter by setting the reflectivity to 0 and adding only losses.

- Phase modulator:
  The phase modulator element, gradually adds a phase to the field passing through it. It has to be connected to a source like the SOA element, but the phase shift is feed directly. The Phase difference supplied can be time dependent.

- Low pass filter:
  A low pass filter is implemented in order to limit the bandwidth of the circuit. The gain section in fact does not include a gain bandwidth, the effect of witch can be simulated only applying a filter inside the lasing cavity.

- IO components and terminators:
  A series of components for terminating the circuit. The necessary components are the IOleft and IOright ports, these are necessary to both inject fields into the circuit and to record the outputs. Every open connection of the circuit must be terminated using a termination segment, it will absorb all the radiation arriving to it.

- Splitters:
  Most common splitter elements are available as building blocks as 2x2 and 2x1 splitters. PHIsim allows the creation of custom NxM splitters with variable splitting ratios that can be defined in a separate txt file.

- Lopper element:
  PHIsims building blocks have a directionality and their ports are labelled as left and right port. The directionality consists in the possibility of connecting only a left port to a right port and vice-versa. This would limit the possible circuits that can be simulated using PHIsim if it wasn't for the existence of the lopper element. This element consist in 2 right and 2 left ports. Power coming in at one side in one port is returned to the other port on the same side. No signals cross from the left to the right side or vice versa. The use is the creation of loops in a circuit.

PHIsim takes into account a variety of physical effects that are present also on other available software. The amplifier model in PHIsim represents its uniqueness, in fact it includes two photon effects and the Kerr effect.
PHIsim does not come free of limitations. Firstly, the model does not include frequency dependent effects such as dispersion and the difference between self and cross-gain saturation. In the amplifier block gain,the gain spectra is flat giving the same response to every wavelength.
This limitation can be overcome using filters like a small MZI or a low pass filter, a multiparameter bessel filter is still under construction, it will allow to obtain a more realistic parabolic gain approximation.
Thirdly, PHIsim requires the manual creation of multiple text files to describe the circuit elements, their connections and the starting conditions for the simulation e.g. Listing 3.1.

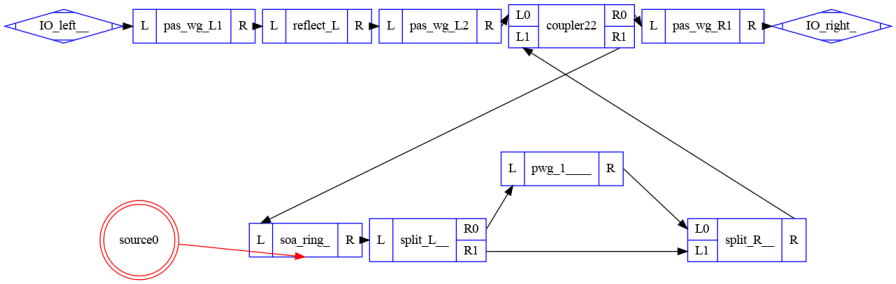

Figure 3.4: Schematic representation of the circuit in Listing 3.1

As evident from the Listing 3.1, the circuit description in PHIsim can become quite cumbersome. This type of description is suitable for simple designs but it quickly becomes problematic once the number of elements in the circuit increases.
The input file description lacks a visualization of the circuit in

Listing 3.1: An example of PHIsim device input file, taken from the PHIsim documentation CITE

```
IO_left__       8               # IO left
IO_right_       9               # IO right
pas_wg_L1   1   10          # passive waveguide
reflect_L       5   0.05  0.0   # reflector
pas_wg_L2       1   10          # passive waveguide
coupler22       103             # 2 x 2 coupler
pas_wg_R1       1   10          # passive waveguide
soa_ring_       2   100    0    # amplifier
split_L__   101             # splitter for filter
split_R__   102             # splitter R for filter
pwg_1____   1    1          # filter waveguide
-1 -1 # end of component list #- start of connections list
IO_left__  R0 pas_wg_L1  L0    #
pas_wg_L1  R0 reflect_L  L0    #
reflect_L  R0 pas_wg_L2  L0    #
pas_wg_L2  R0 coupler22  L0    #
coupler22  R0 pas_wg_R1  L0    #
pas_wg_R1  R0 IO_right_  L0    #
coupler22  R1 soa_ring_  L0    #
soa_ring_  R0 split_L__  L0    #
split_L__  R0 pwg_1____  L0    #
split_L__  R1 split_R__  L1    #
pwg_1____  R0 split_R__  L0    #
split_R__  R0 coupler22  L1    #
xxx  -1  xxx -1         # end connections start source list
0       0.2     # current source 0
-1 -1   # end of source list
```

the design phase and together with the complexity of the text files needed, it has been stalling the adoption of PHIsim by a larger community thus far.
In this work we present an interface with Nazca-design to reverse this later limitation and give PHIsim an easy-to-use circuit building tool that contains a clear visualization of the circuit.

3.4 THE INTERFACE

The connection between Nazca-design and PHIsim can be beneficial for the use of both tools. On one side Nazca will gain a quick and easy way to test and simulated the layout, on the

other side PHIsim will have now an easy way to input the circuit and a visualization of it. The interface presented is implemented fully for PHIsim, but it can be easily expanded to other circuit simulators that have a python API.

3.4.1 *The Simulation class*

The main element of the Nazca-PHIsim interface is the Simulation Class. It is responsible for collecting all the different parameters and perform the basic functions for simulation.
This class is responsible for the import of the Nazca cell that is achieved by solving the entire netlist tree. In the Nazca cells that represent actual circuit components a dictionary describing the basic parameters for the PHIsim simulation is included. The interface will consider every Cell with a description dictionary as a building block to translate to PHIsim without going deeper in the tree.

A exception to the general behaviour are the Nazca interconnects, these are elements that in Nazca are used mainly for waveguides and metal tracks. Interconnects are in fact not cell elements but cell generators, this poses a unique challenge in the development of the interface. In fact, adding the description dictionary in the cell at the moment of generation requires a modification at the Nazca source code that we decided to avoid. The solution to this problem is the automatic addition of the dictionary after the cell creation. For this reason the Interconnect behaviour is decided globally in the interface and not at the single cell level, meaning that for a given simulation all the cell generated from interconnects have the same behaviour.
The possible behaviours of interconnects are three: dummy, simple and 2photon.
Dummy interconnects are used when the user wants only a graphical representation of the waveguide but does not want to actually include the waveguide in the simulation.
Simple interconnects are instead considered as building blocks into the simulation as simple transmission lines.
2photon takes into account 2photon effects in the transmission of the signal along the waveguide but given the additional calculation steps it requires more time for simulation respect to the simple interconnect.

An additional function of the Simulation class is the managing of the lopper elements. In PHIsim every connection between element must be made between a Left and a Right port, this makes the creation of loops impossible.
To circumvent this problem a special element has been created in PHIsim, called looper. In the original PHIsim input method the user had to take care of adding the looper every time it's necessary.
When using the interface a looper is added every time a connection between ports of the same directionality is found, this increase the length of the circuit of one segment so it is advisable to avoid adding looper element when is not strictly necessary.

3.5 EXAMPLES

In the following chapter we will discuss some practical examples and compare them with the literature.

The first example will display a DBR laser with a detailed description of the simulation procedure used and the code snippet. In this example, we will describe the entire workflow of simulation and design to follow when using the interface.

The second example will represent the capabilities in simulating more complex laser behavior and will show a comparison of a Mode-lock laser found in literature, giving a better idea of the capabilities and limitation of this simulation method.

3.5.1 *DBR laser*

We will try to reproduce the results of the HHI design manual regarding a DBR laser. This example forms the ground work for the simulation of chapter 4 and 5.
The first simulation is the reflection of a DBR mirror. The wavelength dependance of the DBR is obtained inserting a delta shaped pulse into the circuit and take the fourier transform of the output.

The simulation results are visible in Figure 3.5, they are in good agreement with the similar figure that can be found in the HHI design manual [63].

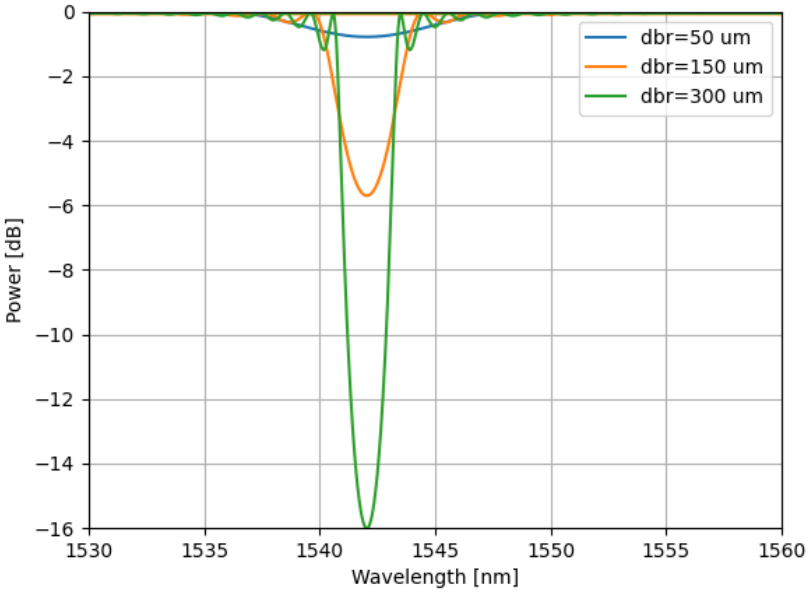

Figure 3.5: Simulation results of DBR mirror reflectance in perfect agreement with the experimental results in the HHI manual[63].

Once the DBR mirrors are simulated, we can simulate the entire laser structure. Also in this case we want to reproduce the results from the design manual in order to use them as a baseline for the design simulations. The structure under investigation is a DBR laser with a 50µm DBR front mirror and a 300µm rear one, the phase section is 150µm and one of the three possible SOA section of 200, 300, 400µm.
These simulations are used to set the gain parameters of the amplifier in order to better estimate the output of our real circuits. In this case since we want to vary the length of the gain section we create a function that returns a Nazca cell with the proper section dimensions, the code used can be found in listing 3.2.

In the Interface demo PDK a set of standard values for the simulation parameters are provided. This set of parameter are typical parameters of a InP platform e.g. SMART photonics or HHI but they need to be adapted case by case.
We will use this simulation to best guest the standard parameters for the HHI platform. The final results are the parameters used in listing 3.3.The results that can be obtained from the simulation are displayed in figure 3.7.
The blue line represents the light reaching the Left port of the

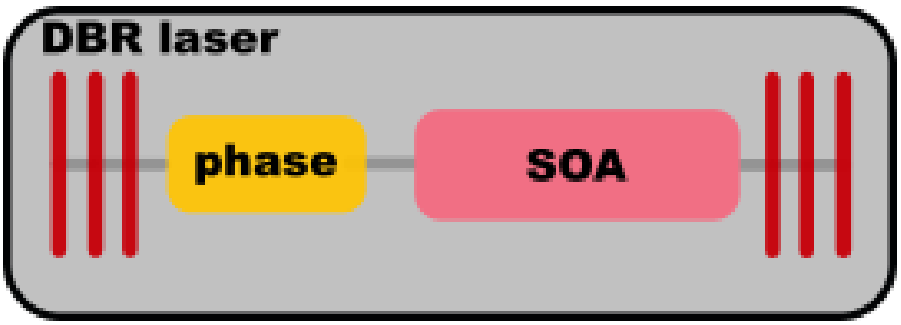

Figure 3.6: Schematic of the basic components of a DBR laser, the DBR gratings are represented by red vertical bars. The main parts are the SOA and the phase section, this last one can be used to fine tuning the emission frequency.

simulation, corresponding to the emission of the front mirror. Since this mirror is significantly smaller than the back mirror we expect most of the power to come out of the front mirror, and it is what can be observed in the Left figure. The initial spike is the reaction of the laser to passing from a $0mA$ current injection to a $100mA$, but we can see that after few nanoseconds the laser reaches equilibrium and both chirp and power output are stable.
The right figure of 3.7 is the Fourier transform of the output power in the left, from it we can get information on the spectral characteristics of the emitted light. In this case the laser is single mode with high side mode suppression ratio.

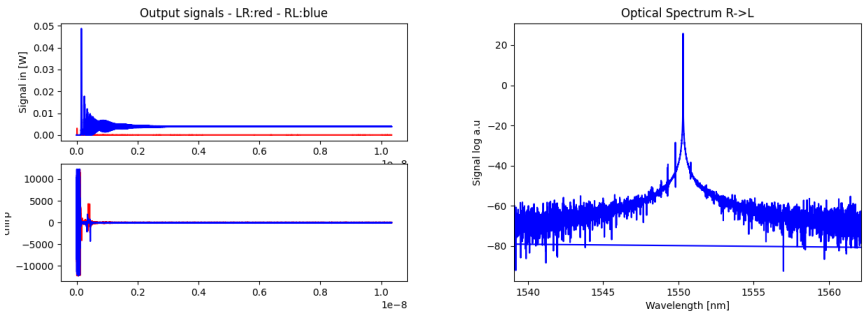

Figure 3.7: Simulation result of a DBR laser with a SOA length of $300\mu m$ and with a $100mA$ current applied to it. On the left the power output of the signal and the chirp are plotted for the two directions of emission. On the right the spectral emission of the front output is plotted.

The following step in the verification is the calculation of the LiV curves for different lengths of the SOA section. The interface

Listing 3.2: Code for the creation of a DBR laser Nazca cell, the phase modulator section is substituted by a straight waveguide for simplicity.

```
@nd.hashme("soa_length")
def create_dbr_sim_cell(soa_length):

      ph_length = 150
      isolation_length = 30

      with nd.Cell("dbr_laser") as dbr_laser:
            BB.io_left().put() # left input-output block for
                 PHIsim
            front = BB.dbr(length=50, coupling_strength
                =8500).put()
            BB.isolation_section(isolation_length).put()
            ph = wg.strt(ph_length).put() # we use a
                straight passive waveguide.
            BB.isolation_section(isolation_length).put()
            soa = BB.soa(soa_length).put()
            BB.low_pass().put()
            nph.create_and_connect_esource(soa, my_sim, 0.1,
                 "soa_dbr_laser")
            BB.isolation_section(isolation_length).put()
            back = BB.dbr(length=300, coupling_strength
                =8500).put()
            wg.strt(50).put()
            BB.io_right().put() # right input-output block
      return dbr_laser
```

is equipped with a Sweep object that allows users to sweep parameters and applied currents. Using this feature we can run a big amount of similar simulations with only one parameter difference between them.
In order to obtain an LiV curve we will sweep the current applied to the SOA from 0 to 140mA, equal to the range in the design manual. The results are reported in figure 3.8.

We can notice that the current Threshold is in agreement with the design manual and is has the expected dependency from the SOA length. The Output power instead differs form the experimental one, and this is due to the gain saturation that is not taken into account in the simulation. The deviation from the

Listing 3.3: Creation of the simulation object and import of the modified parameters for the HHI platform.

```
BB.initialize_sim_space()

for soa_length in [200, 300, 400]:
      my_sim = nph.Simulation()
      my_sim.import_sim_params(BB.Standard_parameters)
      wg = my_sim.set_interconnect("2photon")
      laser = create_dbr_sim_cell(soa_length)
      my_sim.import_cell(laser)
      #platform parameters
      my_sim.refractive_index = 3.7
      my_sim.linear_amplifier = 2 * 1.694e-19
      my_sim.free_carrier_abs_amp = 5.5 * 2.264e-21
      my_sim.transp_density_amp = 0.6 * 0.6577e24
      # simulation parameters
      my_sim.path_length = 10
      my_sim.n_cycles = 200000
      my_sim.wavelength = 1.55e-6
      # running sim
      my_sim.create_sim_files()
      my_sim.run(logout=False)
```

perfect straight line are due to mode hopping in the cavity.

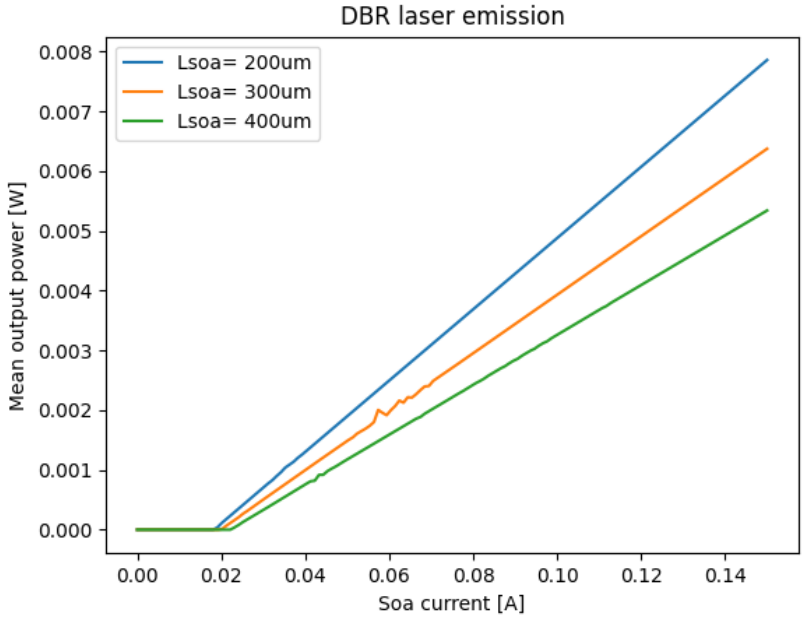

Figure 3.8: Simulation results of DBR Lasers with different SOA sections length, in agreement with the Design manual of HHI [63]. The gain saturation effect is not taken into account into the simulation.

3.5.2 *Mode lock laser*

To demonstrate the potential of the interface we have included the PHIsim dictionary into a Standard PDK with dimensions and rules similar to a real one. We used it to simulate the behaviour of a mode lock laser design and fabricated by Gordon et al [64]. An additional benefit of this approach is that Nazca will check the connectivity for us and warn us in case there are some design rules violations.
Similar to how we proceed with the DBR laser we can simulate a mode lock laser. The resulting power emission is represented in figure 3.10. The pulse train exhibits characteristics compatible with the experimental study with a pulse width of 66ps and a repetition rate of 55GHz.

Further examining the emission spectra, we can notice the spectral composition of the pulse in figure 3.11 is as expected composed by a fundamental mode of 34.5GHz and a pulse colliding mode double of that at 68.8GHz. In perfect agreement with the spectra reported in the literature of 34.88GHz and 69.76GHz. The shape of the spectra is different from the spectra reported

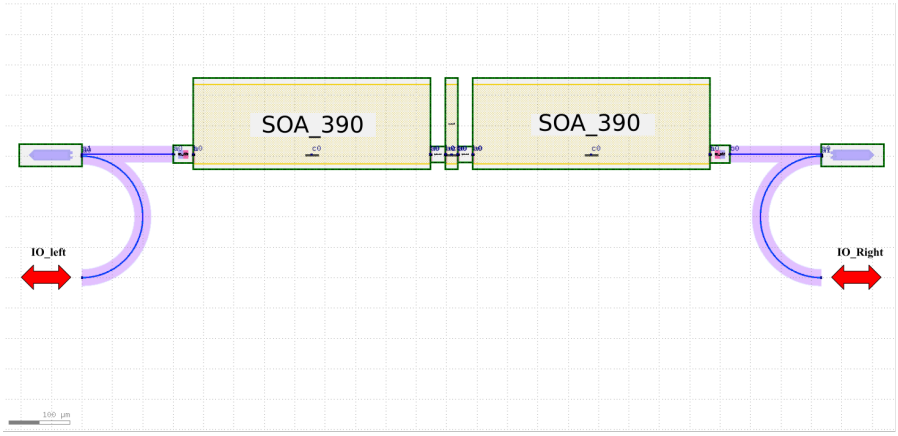

Figure 3.9: Mode Lock laser mask design that has been used for the simulation, this gds file is ready to be included in a chip design and does not need any extra steps.

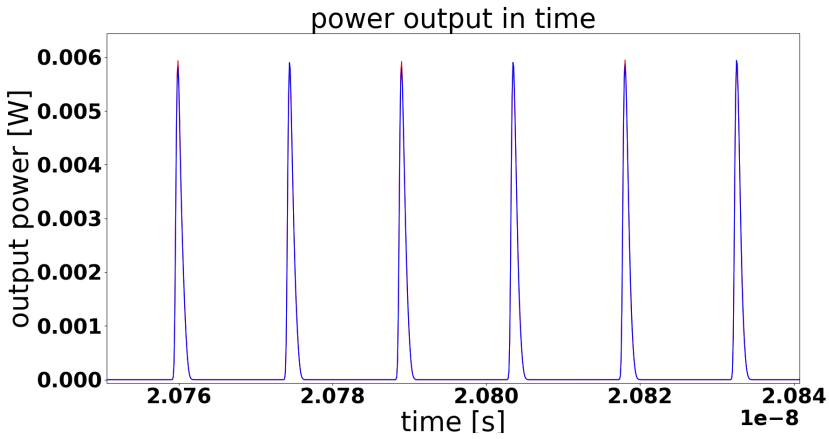

Figure 3.10: Output of the simulation with SOA current of 80mA, we can clearly visualize the pulse train and their shape. Since the laser is symmetric the output on the left is plotted exactly above the right output.

in Gordon et all, this is due to the flat gain approximation of PHIsim, that is mitigated using a low pass filter. This is still not enough for approximating the spectra precisely.

To conclude this study we have calculated the LiV curve of the laser, the threshold current is underestimated respect to the experimental results. This can be attributed to probably some fabrication inaccuracies that are not considered in the simulation or to the gain shape that has been discussed in the previous paragraph. This would lead to a higher gain in the SOA and as consequence lower threshold of the laser. The expected output

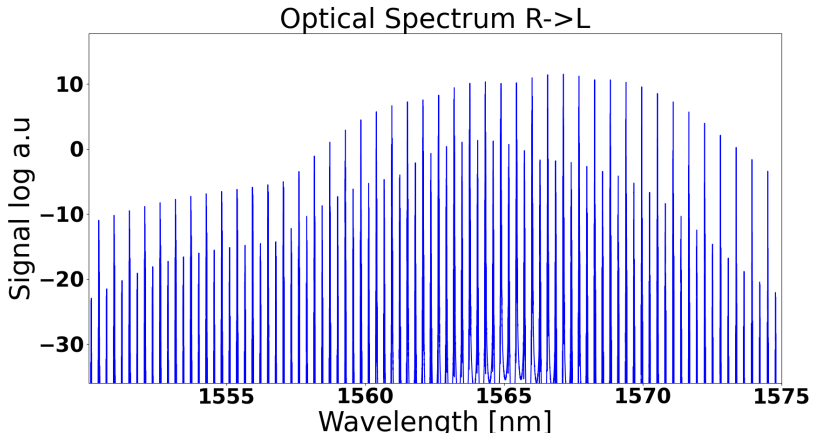

Figure 3.11: Spectral output of the simulated laser when the SOA is injected with 80mA of power. We can notice the decline of the power inside on the edges due to the low pass filter that approximates the wavelength dependency of the gain.

power is in line with the experimental one as shows in figure 3.12.

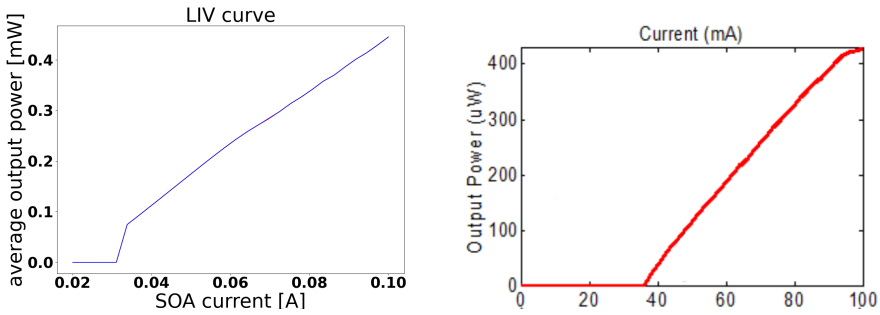

Figure 3.12: LiV curves of the Mode lock laser, on the left the simulated result and on the right the experimental results [64]. The threshold current is underestimated in the simulation and it can be due to the shape of the gain spectra being wider than the real case or to fabrication inaccuracies that add extra losses in the fabricated chip.

3.6 CONCLUSIONS

In this section we have discussed the connection between the layout framework Nazca-design and the simulation tool PHIsim. The connection between this tool is particular beneficial for designers saving time and allowing more reliable simulation

together with better design rule checking. We have discussed the tool individually and after we have presented an interface that connects the two in an easy and intuitive way. We have demonstrated the capabilities of the tools on a DBR laser and on a mode lock laser, comparing the simulation results with the experimental results reported in literature. The comparison results are displayed and discussed highlighting the limitation and advantages. Finally, we want to highlight the open source nature of all the tool involved including the interface.

Part III

CIRCUIT DESIGN AND MEASUREMENTS

In the following we discuss the integrated photonic circuits design and fabrication, together with the experimental verification of their basic functions.

4

COMBINED QKD AND QPSK TRANSMITTER

4.1 INTRODUCTION

As expressed in Chapter 2 every QKD protocol is composed of two fundamental phases: a first phase when the photons are exchanged using a quantum channel and a second phase, where, using a classical channel, information on the selected quantum basis for encoding is transmitted [20]. We have designed and fabricated a photonic integrated chip that can be used both as a DV-QKD and as coherent transmitter with 10GHz modulation speed.
This chip allows not only to have a single chip for the QKD protocol but also to use the same channel for transmission of the encrypted data.

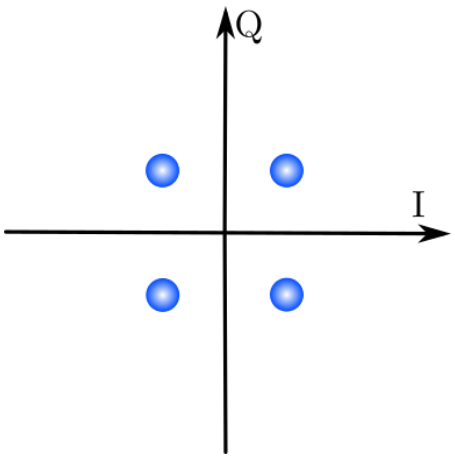

Figure 4.1: Constellation diagram of a QPSK modulation format, the blue dots represent possible phases that can be used to encode the signal. The I axis is the inphase signal, effectively representing the Real part of the electric field. The Q axis is the Quadrature signal that represent the imaginary part of the electric field.

The basic principle of coherent optical communication is to encode the bit stream into the phase and amplitude of a carrier optical wave. This approach guarantees a better SNR/bit, when transmitter through fiber and a better sensitivity of the receiver side resulting in longer reach for the signal [21, 22].

We have decided to use QPSK as method of coherent transmission in our chip. This method transmits the information bits in the phase of a wave, it is already widely employed in telecommunications [23]. A conventional way of representing a coherent scheme modulation is the constellation diagram in figure 4.1. In this diagram the possible amplitudes and phases allowed by the scheme are represented in the complex plane, in the case of a QPSK modulation we can see 4 point equidistant from the origin and located at $\frac{\pi}{4}, \frac{3\pi}{4}, -\frac{3\pi}{4}, -\frac{\pi}{4}$. Different modulation schemes have lower or higher number of points in this diagram, since the final representation is a binary the total number of point in a constellation diagram is usually a power of 2. In the case of QPSK we use a 4 point constellation meaning that we will encode 2 bits of information for each carrier modulation.

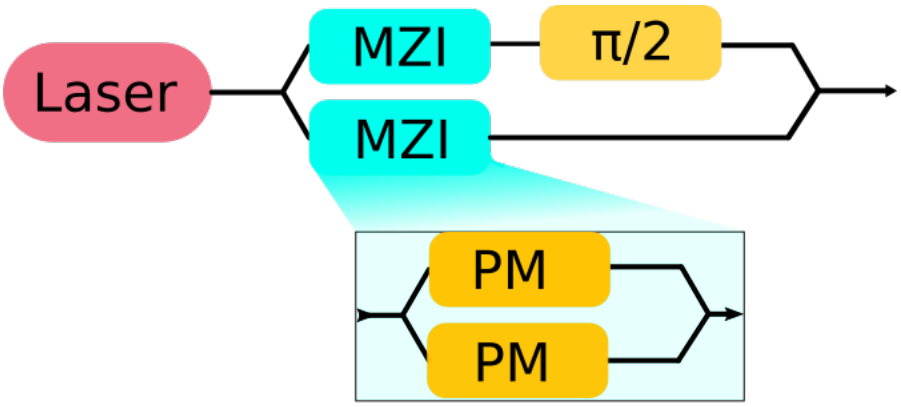

Figure 4.2: Basic schematic of a QPSK transmitter, the laser light is split in two arms, each of them contains a MZI interferometer these are used to modulate the signal, an additional $\pi/2$ phase shift on one of the arms allow for full QPSK functionality.

Phase modulation is a popular choice in wireless communication, but it has been investigated extensively also in optical fiber communication, given the easy implementation and the increased data rate. A transmitter's basic schematic for QPSK is presented in figure4.2 [24]. For the QKD part we have decided

to use the scheme realized by Paraiso et al in [25] based on optically injected lasers, that has been already discussed in the introduction chapter 2.

4.2 CIRCUIT DESIGN

4.2.1 *Schematic representation*

Both the circuit for QKD and the one for QPSK contain a MZI interferometer, we decided to use one of them as a selector between the two operation modes. Figure 4.3 represent a simplified diagram of the circuit. A DBR laser is used as main source, the light is then divided and directed to two identical MZIs. The top interferometer is used both to modulate the signal in the QPSK modulation scheme and also in the selection of power reaching the DFB laser for QKD. An additional phase shifter is used to add the π half for QPSK modulation.

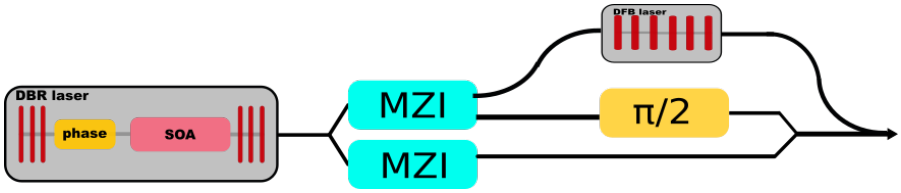

Figure 4.3: Schematic of the designed circuit. The output of a DBR laser is split in two paths going to two different MZI. The top MZI can be used to direct the light in the two different paths or to modulate the path in case the device is used as QPSK. The top path is then used to select a DFB laser to optically inject, recreating the QKD scheme proposed by [25].

Technology evaluation

The first step in the design of the circuit is the selection of the technology platform that will be used. We have decided to use a InP based platform since is the only mature material platform that can contain lasers and amplifiers. Without these building blocks would not be possible to create a monolithic chip with all the functionality desired.
Between the possible InP foundries we have selected the HHI platform [63]. We specifically chose this platform since:

- It contains DFB lasers and DBR lasers as building blocks with measured characteristics, the DFB also is default connected using RF lines that comes handy to modulate it.
- Spot Size Converter (SSC) building block available, that allows easier fiber allignement with lower losses.
- Fast electro optical phase modulators with f3dB higher that 25GHz according to the design manual.

4.2.2 *Mask Design*

The circuit design started with selecting the lasers that we wanted to employ in our design. The master laser has been selected to be a DBR laser, we have preferred it respect to a DFB lasers since it provides lower linewidth, resulting in better performances for QPSK. This laser will, in fact, be used for the coherent transmission purpose. In order to have higher output powers we have decided to use a 30µm DBR mirror for the front and a 80µm for the back, a SOA section of 400µm and phase section 200µm.
The DFB laser is constituted by a standard DFB building block, a SOA is positioned after the MZI and before the DFB in order to amplify the signal coming from the DBR laser.

We have decided to place the design in half of the MPW cell, and use the remaining space for a different design that will be discussed in Chapter 5. The resulting space is a 2mm by 8mm rectangle. The final mask design is in figure 4.4. The main DBR laser is located in the middle of the chip, one of its output is split into the two MZI and on the back of the laser we have placed a photodiode that allows us to easy monitor power output of the laser. The MZI are identical, we have chosen to have them as long as possible resulting in a 1.5mm balanced arms length. Each of the MZI can be driven using RF waves through the electrodes labeled as RF1 and RF2. The bottom interferomenter also has an output to fiber that will allow us to measure the standard characteristics of it.
On the top of the chip we can see the DFB and the SOA. The SOA has a double function in this circuit. On one hand if the circuit is used as a QPSK transmitter it can absorb the light that would go otherwise to the DFB and be reflected back or forward, it is not strictly necessary since the DFB is already absorbing this radiation when not biased, it is a safety addition. On the other

hand the SOA increases the injection ratio into the DFB laser making it easier to lock the two laser together. To complete the QPSK capabilities one output of the bottom MZI is phase shifted using a thermal shifter, this will add the $\pi/2$ phase in order to perform full QPSK modulation.

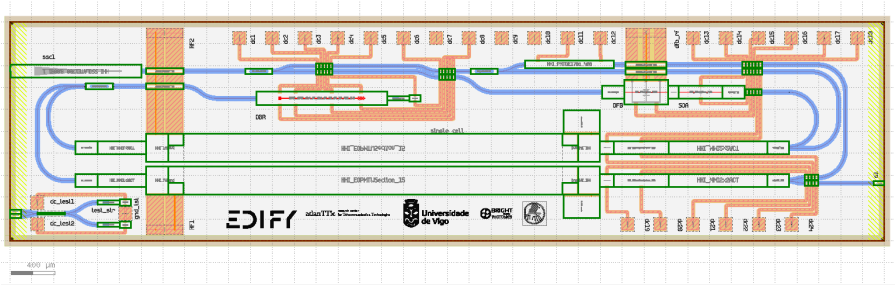

Figure 4.4: Mask design of the top part of the fabricated chip, it contains the QPSK and QKD circuit and a small test circuit on the bottom left.

4.3 MEASUREMENTS

Figure 4.5 is a photo of the fabricated chip. The yellow parts correspond to the gold plating of the electrical connections, the light blue parts are the waveguides. We can notice the spot size converter output in the top part with increased dimensions respect to the standard waveguide output on the bottom right. The imperfections that can be seen on some top pads are due to the probing of the chip. This operation results in partial scratches on the gold layer when landing the probe on the metal, these marks are visible at the microscope.

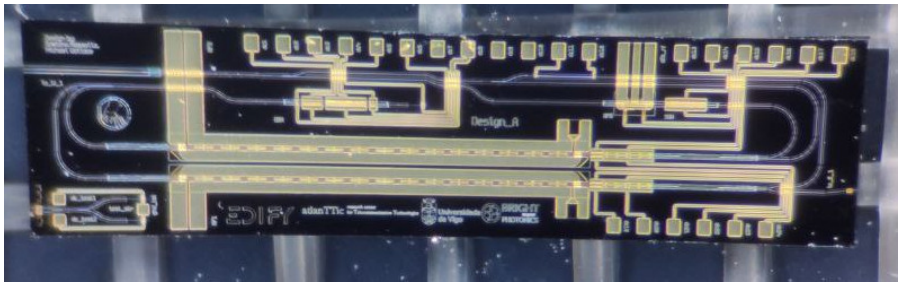

Figure 4.5: Photo of the fabricated chip under microscope. We can clearly see the metal tracks for electrical connection and the waveguides below them.

To characterize the chip we have used the custom setup built in the university lab. The setup allows the use of up to 4 DC probes and 2 RF-GSG probes. It also allows the coupling of fibers from left and right using two piezo-electric controlled positioning stages.

The first device under characterization is the DBR laser on the center of the chip. We can use the photodiode connected to the back of it in order to register the LiV curve, and use the right output port to characterize the output spectra.

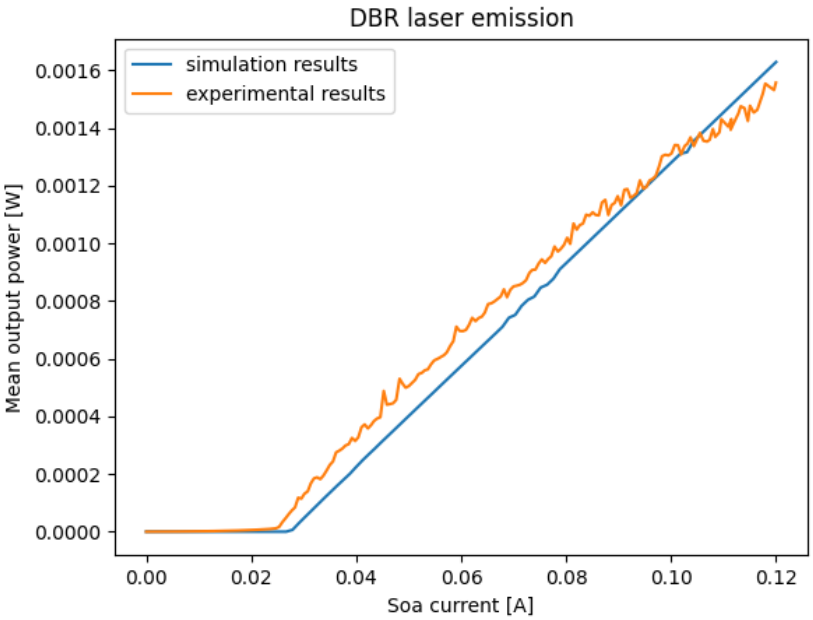

Figure 4.6: Comparison between the LiV curve of the simulated laser and the experimental results. The two results seam in good agreement, the experimental results show more evident mode hopping and a slightly lower threshold current.

In figure 4.6 we report the LiV curve that has been obtained by sweeping the current applied to the SOA and recording the power at the photodiode. We can also compare this result with the simulation, and notice the good agreement between the two. The experimental line is considerably more noisy and we can notice a lot of deviation from the straight line. This effect is generally considered to be caused by mode-hopping inside the laser. This effect is not present in the simulation. From this simulation we would expect the laser to be singlemode but we are not considering two additional effects. One of them is the

cross and self gain saturation effects, that are not part of PHIsim. This two effect can result in mode hop operation in some laser design.
A second consideration is the presence of fabrication defects and inaccuracies that cause some extra reflections resulting in unstable single mode operation.
We can look at the LiV curve in figure 4.6 noticing that in the first part of the graph, just above the threshold, the emission is linear. In the higher part the emission is more unstable.
We can see that we are in stable single power output only in the initial part of the curve close to the threshold.
The spectrum in figure 4.8 is the spectra of the laser with injection of 25mA, we can notice the single emission peak. This consequently proves the single mode operation at low current injection. We can observe the experimental spectra in figure 4.9. This experimental spectra has been recorded at 70mA of injected current and the laser exhibits a multi wavelength emission. At higher injection currents the mode hopping starts to change, and it makes the curve more noisy, this is demonstrated by the multi-frequency emission in the spectra 4.9. The multi-frequency emission spectra can be due to different effects, but the main effect can be due to the raise in temperature of the chip. This effect in fact changes the index of the material and can lead to multimode emission. A similar effect has been found on the DFB laser and will be discussed later.

The second laser present in the design is the DFB laser, that can be seen in the top right part of the chip connected by three straight metal lines in figure 4.5. The metal lines are a RF line that can drive the laser up to 10GHz. Close to it, we can notice the SOA used to amplify the signal coming from the DBR laser. The LiV curve of this laser will be discussed in the next chapter 5, when it has been directly measured using an integrated photodiode.
The spectra of the free running DFB laser is reported in figure 4.10. We can notice that in this case the laser operates in single mode even at 70mA. The emission wavelength is shifted with increased current injection as reported in the fabrication report. From this measurement we can also notice the side mode suppression ratio that is in the range of 50 dB.

After, characterizing the laser, we have focused our attention on the optical injection of the DFB laser. A full theoretical

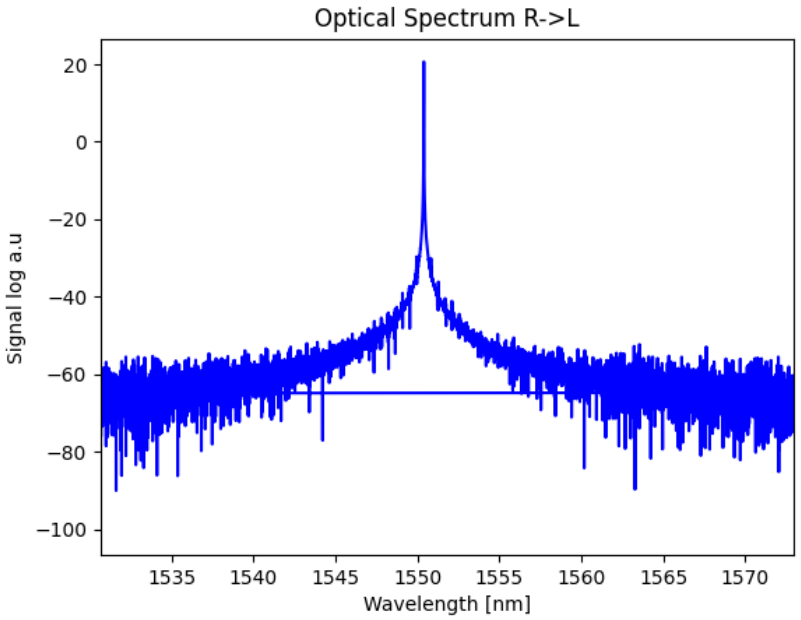

Figure 4.7: Simulated spectra of the DBR laser, The laser is single mode with 60dB of side mode suppression ratio at 70mA of injected current.

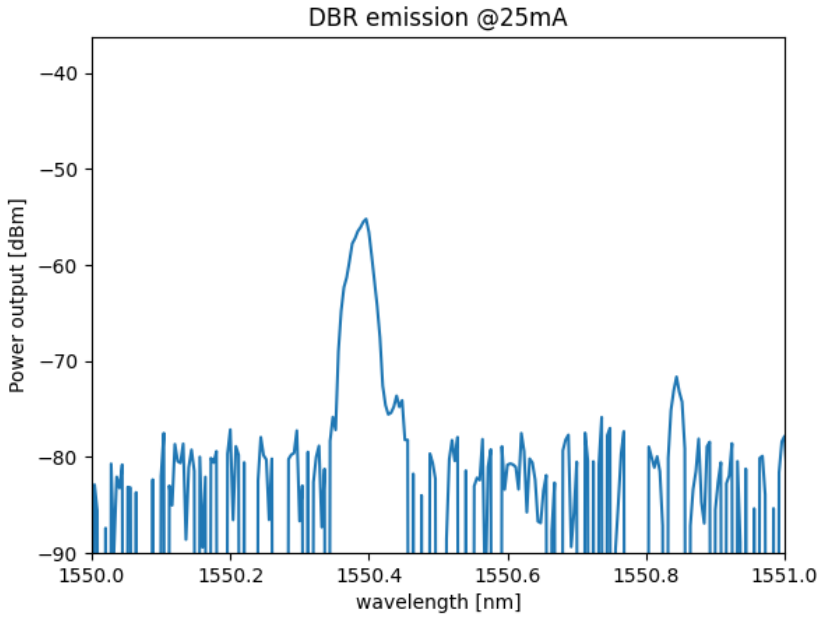

Figure 4.8: Experimental measurement of the output spectra of the DBR laser at 25mA current input, in this regime the laser is single mode and exhibits a single emission peak at 1550.4.

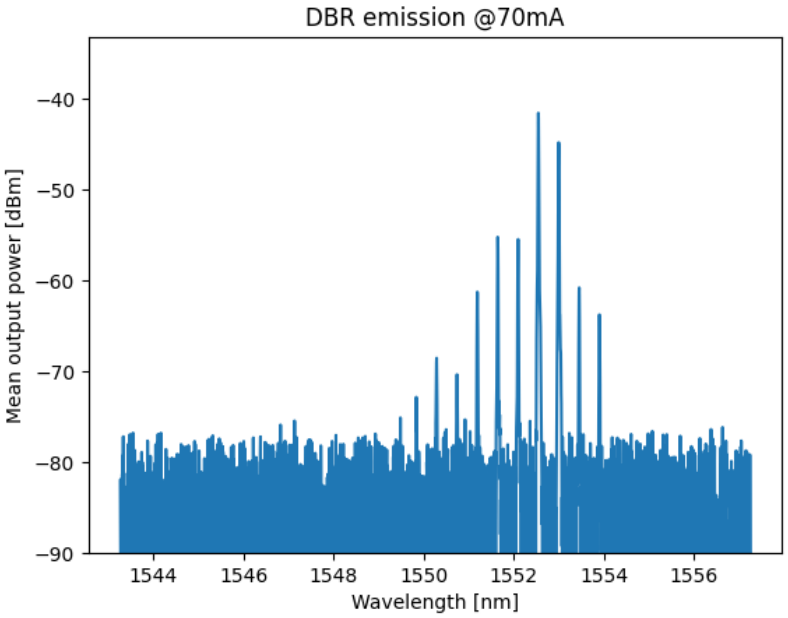

Figure 4.9: Experimental measurement of the output spectra of the DBR laser at 70mA current input, in this regime the laser is not single mode.

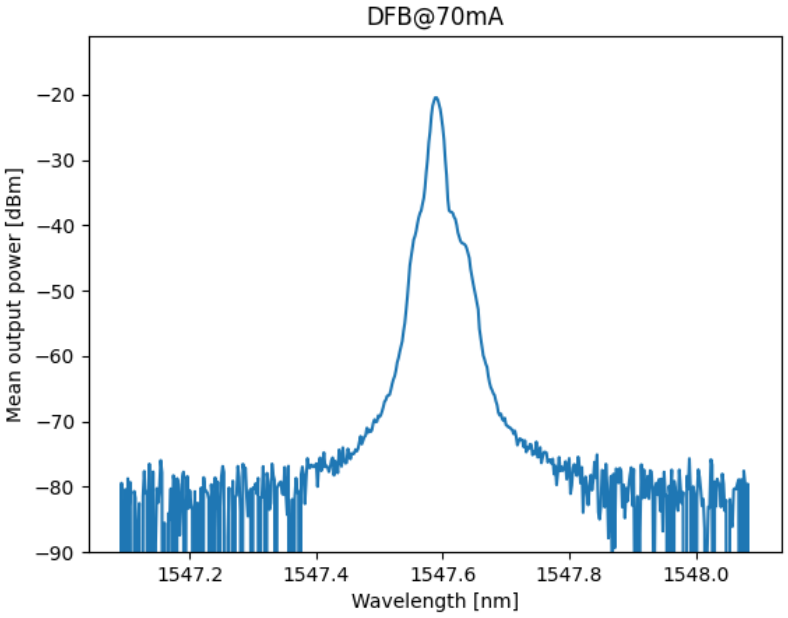

Figure 4.10: Experimental measurement of the output spectra of the DFB laser at 70mA current input, in this regime the laser is single mode. It is obtained using a OSA, it shows single emission peak at 1547.6nm.

framework of optical injected lasers will be discussed in the next chapter. Here we will limit our discussion to the prof of injection and the consequences of it.

The DBR and the DFB are separated by a MZI interferometer and a SOA. This last one is used to amplify the emission of the DBR reaching the DFB. We have also to point out that in the next part of the experimental verification we will be limited by the set-up. In fact, we have 4 DC probes and 2 RF probes available. This probes will be used : 2 DC probe for ground and signal of the DBR laser, 1 RF probe for the DFB and 2 DC probes for the SOA. The only probe left available is a RF probe of GSG type, that can not be used for any other component in the circuit. This will prove to be a critical limitation since we will not be able to tune any of the lasers emission. The final assessment of the circuit will then have to wait for the wire-bonding of the chip or alternatively the use of a probe card.

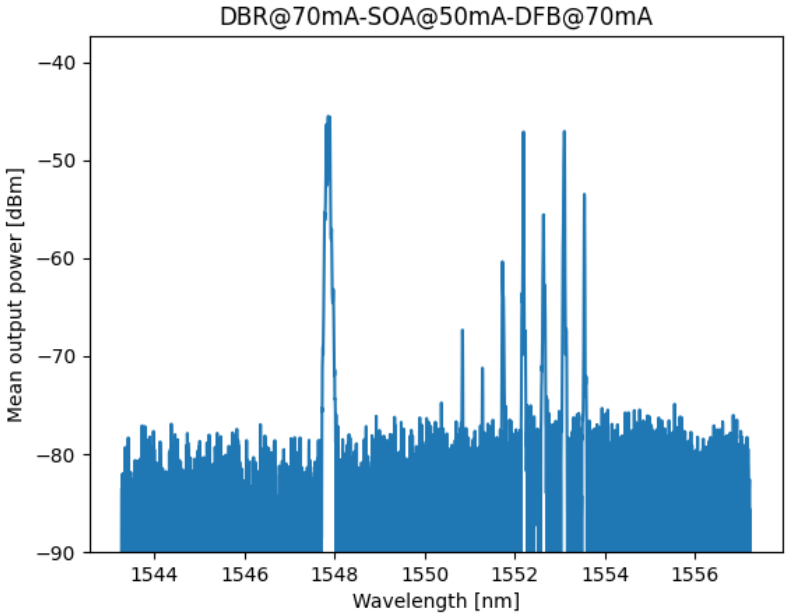

Figure 4.11: Experimental measurement of the output spectra of the DFB laser at 70mA current input injected with the emission of the DBR laser at 70mA with SOA at 50mA.

We have decided to test the injection of the circuit in two different regimes of the DBR laser.
In figure 4.11 the DBR laser is pumped at 70mA. This will make the DBR to emit multiple frequencies, we are interested in notic-

ing if any of these frequencies can lock with the DFB laser and subsequently lock the two lasers together.
We can see in the Figure that this is not the case, the emission of the DFB on the right is completely separate from the DBR emission on the left.
This is due to the emission of the DBR being too far in frequency from the DFB emission, making it not possible to lock.
The problem can be solved using current injection to tune both the DBR and the DFB. As mentioned above this was not possible due to lack of probes and space in the setup, to perform the full characterization of this circuit we will need to wirebond the chip to a PCB in order to have easy access to more electrical input/outputs.

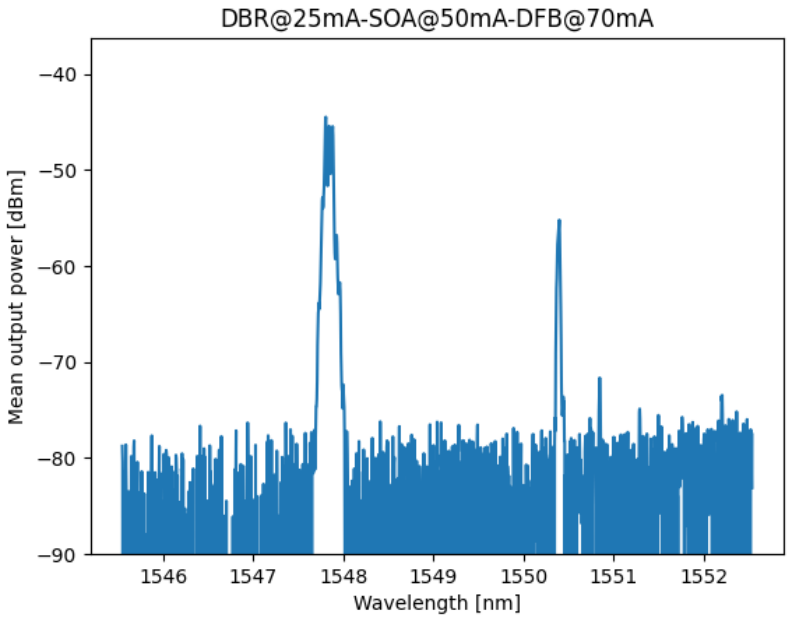

Figure 4.12: Experimental measurement of the output spectra of the DFB laser at 70mA current input injected with the emission of the DBR laser at 25mA, with the SOA at 50mA.

We can notice the shift in the DBR emission at different current injections. Moving from the 1550.6nm at 50mA to the 1552.7nm of the main peak at 70mA.
In Figure 4.12 the DBR laser is pumped at 25mA. This is to check both the behaviour of the DFB laser when injected with a single frequency and also to inject the laser with a frequecy closer to the free-running emission of the DFB. We can notice the two separate emission peak, the one on the left is the one of the DFB

and the one on the right of the DBR.
In the case of optical injection locking the two lasers would have the same output wavelength, and we should see only one peak in the graph. It is evident that this does not happen. In this figure the SOA current is 50mA, when the current in the SOA increases the spectra does not change significantly. This can out rule the effect of injected power in the locking.

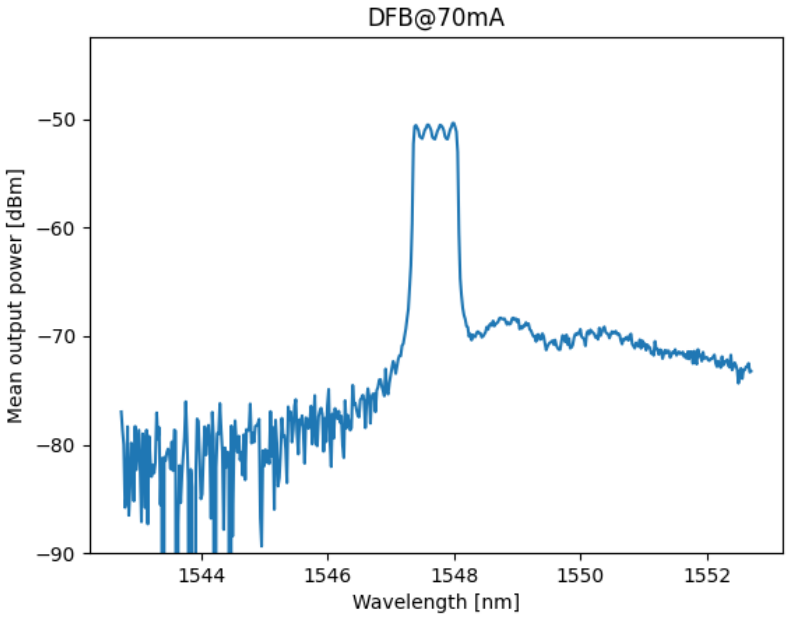

Figure 4.13: Experimental measurement of the output spectra of the DFB laser at 70mA current after running for about 30 minutes.

Comparing figure 4.11 and 4.12 we can notice the peak due to the DFB laser on the left gets more noisy.
On figure 4.13 we can see the emission of the DFB laser after 30 minutes of operation. We can notice that it is not single frequency any more. This degradation of the laser was completely unexpected. When controlling the temperature on the chuck we have noticed that our system got a temperature increase of about 0.5C° from 20.1C° to 20.6C° that can explain the strange emission of the laser. Lowering the injection current to 65mA brought the laser back to single mode operation.

4.4 CONCLUSIONS

In conclusions, we have designed and fabricated a photonic integrated chip in HHI InP platform. The designed circuit is capable of both QPSK and QKD. We have experimentally characterized the emission of the two main sources in the circuit and compared them with the simulations. The Optical Injection Locking of the lasers was not possible to recreate due to lack of equipment. We have discovered the high dependence of both laser from the temperature of the chip. In the future work the chip should be wire bonded allowing the simultaneous variation of all the parameter involved and the testing the QPSK and QKD capabilities.

5

QKD CIRCUIT BASED ON OPTICALLY INJECTED RING LASERS

5.1 INTRODUCTION

The technique that is used in the paper from Paraïso et al. is commonly refereed as acOIL. It is a technique to synchronize two lasers that can be used in various context and field, in this case is used in QKD.
In this chapter we are going to present two circuits based on OIL of ring lasers, this represents a first in our knowledge experimental demonstration of this technique on ring lasers in monolithically integrated photonics. As we saw in the previous chapter OIL of DFB lasers can be difficult to obtain since it needs precise frequency matching conditions.
In this chapter we will discuss and experimentally demonstrate Optical injection of ring lasers. This system respect to the DFB has more resonances leading to an easy injection locking.

We have designed, fabricated and measured two circuits in a HHI MPW run.
The first circuit is composed of a simple DFB laser that is used to inject a slave ring laser. We will use this system to characterize the basic behaviour of such systems, noticing that this simple circuit is already capable of QKD and QPSK.
The second circuit presented is composed by three lasers: a central DBR laser that is feed into two slave ring lasers. This system is capable of both QKD and high speed QPSK, being de facto and alternative design to the circuit presented in chapter 4.

5.1.1 *basic OIL principles*

OIL is a technique to synchronize the phase and emission of two lasers. The light from a master laser is traditionally injected

into a slave laser using a circulator or an isolator. When the free running emission frequencies of the two lasers are close enough, the slave laser is forced to synchronize with the master resulting e.i. in emission at the same frequency [65].
This technique is important for a variety of fields: optical communications [66], optical frequency combs [67], optical science and instrumentation [68] and microwave signal generation [69].
Other than frequency and phase synchronization OIL was demonstrated to increase the modulation bandwidth of the slave laser, reduce the modulation chirp and the relative intensity noise[70].

A description of the OIL dynamic can be obtained modifying the rate equations and introducing a term for the injected light intensity and one for the phase synchronization [71].

$$\frac{dA(t)}{dt} = \frac{g}{2}(N(t) - N_{th})A(t) + kA_{inj}\cos(\phi(t)) \tag{5.1}$$

$$\frac{d\phi(t)}{dt} = \frac{\alpha}{2}(N(t) - N_{th}) + \frac{A_{inj}}{A(t)}\sin(\phi(t)) - \Delta\omega \tag{5.2}$$

$$\frac{dN(t)}{dt} = J - \gamma_N N(t) - (\gamma_p g(N(t) - N_{th}))A(t)^2 \tag{5.3}$$

Equation 5.1 describes the behaviour of the field, we can notice the additional term $kA_{inj}\cos(\phi(t))$ that is added to take into account the injected field.
Equation 5.2 describe the total phase of the field, in this case we have added two extra terms: $\frac{A_{inj}}{A(t)}\sin(\phi(t)) - \Delta\omega$ that take into account the difference in frequency and phase of the fields.
The behaviour of the carrier density, equation 5.3, does not require any additional term.
It is worth notice that this description in terms of rate equation is a simplified model missing terms like free propagation losses and two-photon effects. Never then less it is an effective way of understanding the basic behaviour or such systems.
We have developed a python code to integrate this equation and have an intuitive understanding of the phenomenon [1]. The results of the integration are presented in Figure 5.1, the yellow part represent the stable OIL operation. We can notice the expected shape typical of this kind of phenomenon [65].

1 The code is released and is open-source, can be found at `https://github.com/Dam-masse/OIL_solver/tree/master`

parameter	description
$A(t)$	field amplitude normalized
$\phi(t)$	phase of the field
$N(t)$	number of carriers
g	laser gain coefficient
N_{th}	carrier density at threshold
k	coupling coefficient
A_{inj}	field amplitude of injected light
$\Delta\omega$	frequency offset
α	linewidth enhancement factor
γ_N	carrier recombination rate
γ_P	photon decay rate
J	pump current

Table 5.1: Parameters and functions of rate equations 5.1-5.2-5.3.

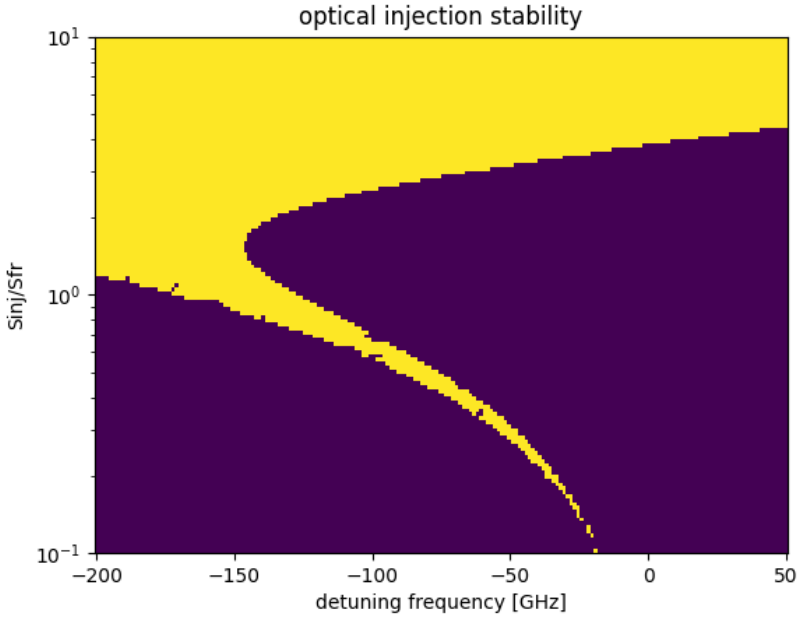

Figure 5.1: Stability analysis of OIL injection, the yellow part indicated stable operation, the blue part non-locked or unstable states.

5.1.2 *Linewidth reduction*

Narrow linewidth laser have a critical role in photonics, being fundamental for coherent communication and microwave gen-

eration. The standard approach to linewidth reduction consists in extending the photon lifetime using external cavities or by driving the laser using low noise electronics[72]. Both of these approaches result in expensive laser sources.
Using OIL it is possible to create multiple narrow linewidth laser sources from inexpensive large linewidth lasers. This lasers can be in fact injected with light from a high quality, narrow linewidth laser, resulting in a narrow linewidth emission from the slave laser. In [65] a 1.2MHz slave laser is OIL with a 5kHZ master laser. The resulting emission from the slave laser is a narrow linewidth emission of 5kHz corresponding to the linewidth of the master.
This approach allows to split a single narrow linewidth laser to inject multiple slaves and obtain a series of low-cost narrow linewidth lasers.

5.1.3 *Tone selection*

In a variety applications like microwave photonics, optical arbitrary waveform generation [68] and DWDM Communications [73], is common to isolate and amplify a single-frequency signal. The conventional way to obtain this is using a combination of Arreyed Waveguide Gratings (AWG) and amplifier, the amplifier is necessary since the AWG introduces extra losses in the circuit (3-5dB). This scheme reduces the signal-to-noise ratio of the communication and can have a significant footprint even in integrated photonics.
OIL is an alternative method to tone selection with low noise and high gain. A single wavelength slave laser can in fact be locked to a multi-wavelength signal. The slave laser with lock to the part of the signal closer to the free-running slave amplifying it and suppressing the rest of the signal. This configuration with multiple slave lasers can be used to demultiplex a multi-wavelength signal.

5.1.4 *Bandwidth enhancement*

The modulation bandwidth of a laser has been studied in [71] in the case of an isolated laser and can be estimated using the equation [74]:

$$f_{3dB} = \frac{3}{4\pi^2 q}\frac{\Gamma v_g \sigma_g}{V}(I_b - I_{th}) \tag{5.4}$$

parameter	description
f_{3dB}	frequency of 3dB attenuation
v_g	group velocity in the cavity
Γ	confinement factor
σ_g	differential gain
I_b	bias current
I_{th}	threshold current

Table 5.2: Parameters and functions of equation 5.4.

Equation 5.4 is not a full description of the laser dynamics, but it is useful to understand the dependency of the modulation bandwidth from the laser geometry.
From 5.4 we can see that there are effectively two method to increase the modulation bandwidth: having a short cavity or having a higher injection current. These methods are quite limited, in fact shortening the cavity results in smaller power. High bias current can result in additional heating of the laser and potential damages and instabilities.
OIL has proved to be an effective way to increase the bandwidth without major drawbacks [75].

5.2 SCHEMATIC

In this chapter we are going to design two different circuits that are integrated in the same mask design.
Each of them is used to demonstrate the possibility of OIL ring lasers in integrated photonics and subsequently use it for QKD.
The first circuit is presented in figure 5.2. In this circuit we use a simple DFB laser to inject the ring laser. The simplicity of this circuit is its main advantage respect to other QKD circuits. In the schematic we have omitted the MMIs blocks and the photodiodes used to monitor the state of the laser. A more extensive description of the circuit will be presented in the following sections.
It is worth notice that this circuit is both capable of QKD and QPSK, but both have quite limited bandwidth since it requires modulation of the DFB laser. This type of modulation in fact does not benefit from the characteristic mentioned above that

can be applied only to the slave laser, in this case the ring laser.

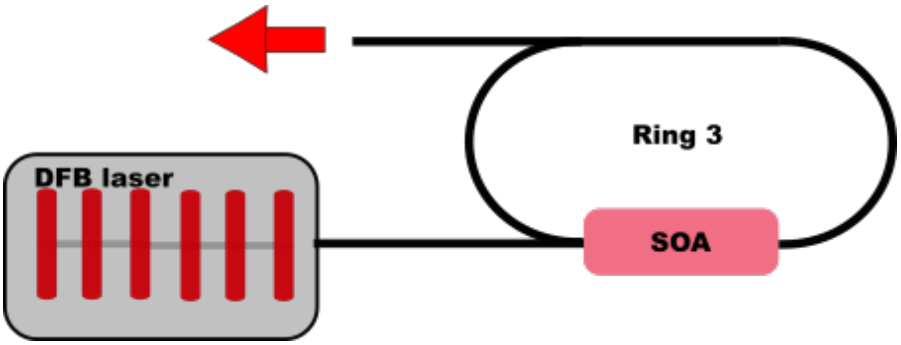

Figure 5.2: This schematic represents the first design of OIL ring laser. The ring laser is injected using a DFB laser.

A second circuit has been realized in the same mask design and is schematized in figure 5.3.
In this case we decided to exploit the two outputs of a DBR laser to OIL two ring lasers. The two rings output is then combined to a single output. This schematic can be used for both QKD and QPSK.
The main advantage respect to the first circuit is the possibility to use the modulation of the rings for encoding the bits of the QPSK scheme. For the use as QPSK transmitter we have added a phase modulator in the output of one of the ring laser, this allows to have the $\pi/2$ phase shift for QPSK. The modulation bandwidth in this case is enhanced by the OIL since we are going to modulate the two slave lasers and not the master laser. Also in this case we have omitted components that are not core parts of the circuit.
The ring lasers used for the two circuit are identical in dimensions and components used.

5.3 MASK DESIGN

In the previous chapter we have discussed the motivations for choosing the HHI platform. In this chapter we have choose the same platform for the same motivation and the design has been included in the same run as the previous chapter design. The MPW cell that we got allocated has been split in two equally spaced regions of 8mmx2mm. The mask design submitted for fabrication can be seen in Figure 5.4.

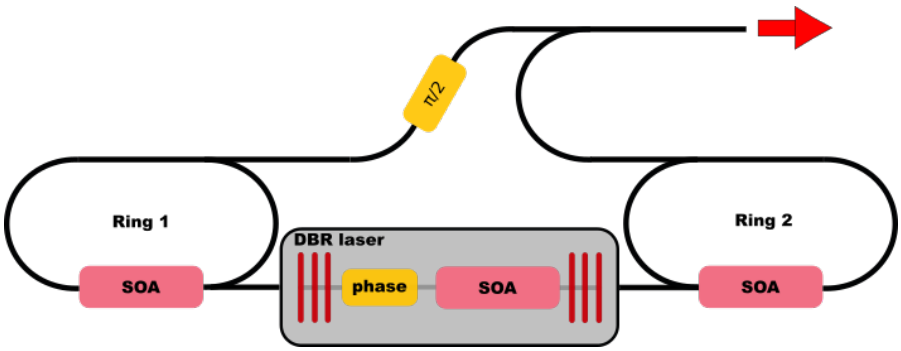

Figure 5.3: This schematic represents the second design of OIL ring laser. The two ring lasers are injected using a DBR laser.

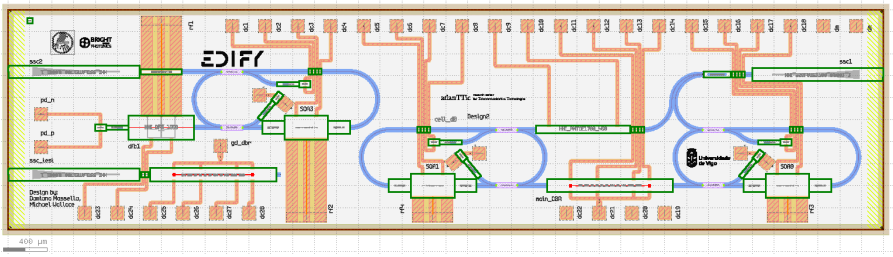

Figure 5.4: Mask design submitted for HHI MPW run. It contains both circuit of Figure 5.2 on the left and Figure 5.3 on the right.

The reader can recognize the first circuit on the top left part of the mask design. We used a standard DFB grating designed to emit at 1550nm, the left output of it is terminated using a photodiode. This photodiode will be used to characterize the DFB emission power. On the ring we have used custom MMI blocks, they are designed to split power unequally, 85% on the cross state and 15% on the bar. We have chosen this particular ratio to reduce the losses inside the ring and have a shorted gain section. The MMIs used in the rings are all 2x2 and the additional port is also terminated using a photodiode. The photodiodes inside the ring can be used to monitor both the clockwise directed power and the counter-clockwise. They will be an useful indicator when we achieve OIL. The SOA section has been connected using Radio Frequency (RF) lines in order to be able to drive the ring laser to higher frequency and verify the modulation bandwidth enhancement due to OIL.
A spot size converter is placed at the output of the circuit to minimize the losses when coupling to fiber.

Below the DFB laser, we can find a test structure. It is a DBR laser identical to the one connected to the two ring lasers on the

right. This structure will help us understand and test the output of the designed laser and to verify its working conditions. In fact, we do not have direct access to the DBR laser on the right circuit.

The circuit on the right side of the mask design correspond to the schematic of figure 5.3. The two ring lasers are designed identical to the ring of the left circuit. The DBR laser dimensions are: 30µm DBR mirrors, 400µm SOA length and 200µm phase modulation section. These parameters have been chosen in order to have high power output of the DBR laser, similarly to what has been considered for design A in Chapter 4.
Above the DBR laser is located the phase modulation section, it is constituted by a thermo-optical phase modulator of 450µm. This length is sufficient to ensure a $\pi/2$ phase difference between the two rings.

5.4 MEASUREMENTS AND DISCUSSION

In the following section we are going to present the experimental results on the basic functionalities of the circuit. The more advance functionalities could not be tested due to lack of equipment.

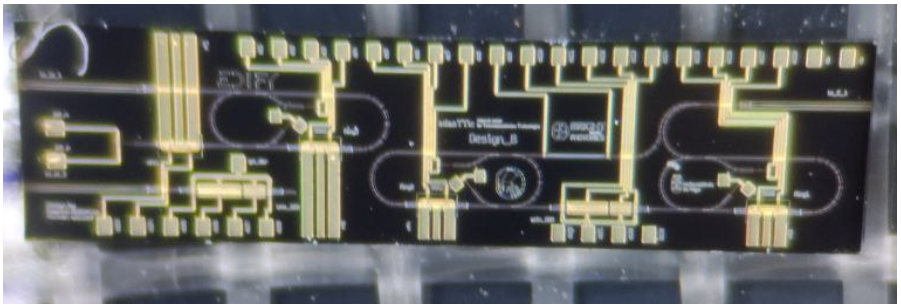

Figure 5.5: Photo of the realized circuit under microscope, We can clearly see the metal tracks for electrical connection and the waveguides below them.

5.4.1 *DFB and single ring circuit*

The first analysis completes the characterization of the DFB lasers. We have already seen the spectra in Figure 4.10, here we can analyse the LiV curve. It is evident that there have been some problem in the fabrication in fact in the threshold is above 60mA

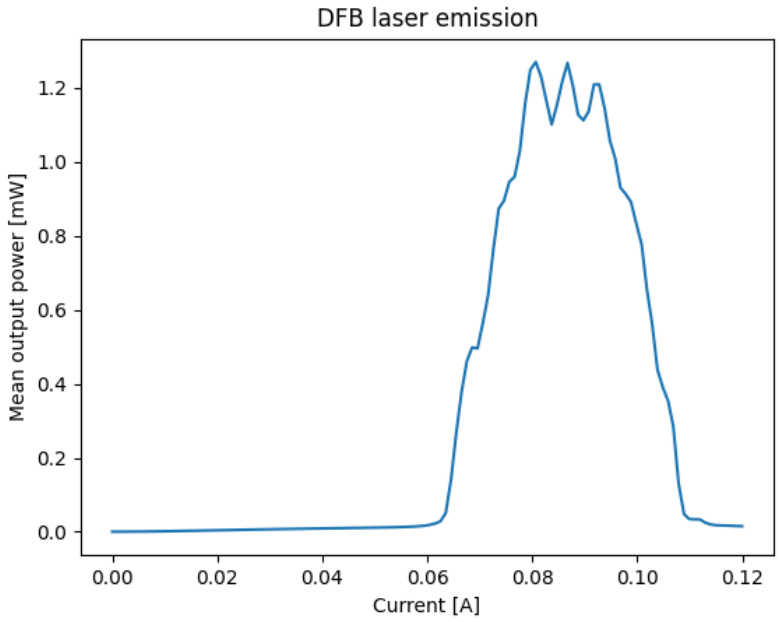

Figure 5.6: LIV curve of a DFB laser recorded on the photodiode directly attached to it. We can notice the high threshold current and the low power peak emission.

against the $25mA$ expected from the design manual. This has been confirmed from the fabrication report and in general we can observe a lot of variability in the behaviour of these components. We have measured other DFB laser fabricated in the same run and the threshold current ranges from $44mA$ to $60mA$ with maximum emitted power above $1mW$ only in the case of Figure 5.6. This issue is not present only in our fabbrication run but it has been observed in previous run.

The presence of two photodiodes that can measure the output of the DFB laser, one on the back of it and one in the middle of the ring, allows us to estimate the power split ratio of the MMI. To do so we have driven the DFB at $80mA$, resulting in a current at the direct photodiode of $-80\mu A$ whether the photodiode in the cross port of the MMI registered $-60\mu A$. Both the photodiodes were keep at $-2V$ during the measurement.
Assuming a $1dB$ losses for this kind of component we reach the result that the splitting ratio of the MMI should be 83% for the cross port and 17% for the through port. This ratio is close the designed ratio of $85 - 15$ and gives a good indication of the good design of this component.

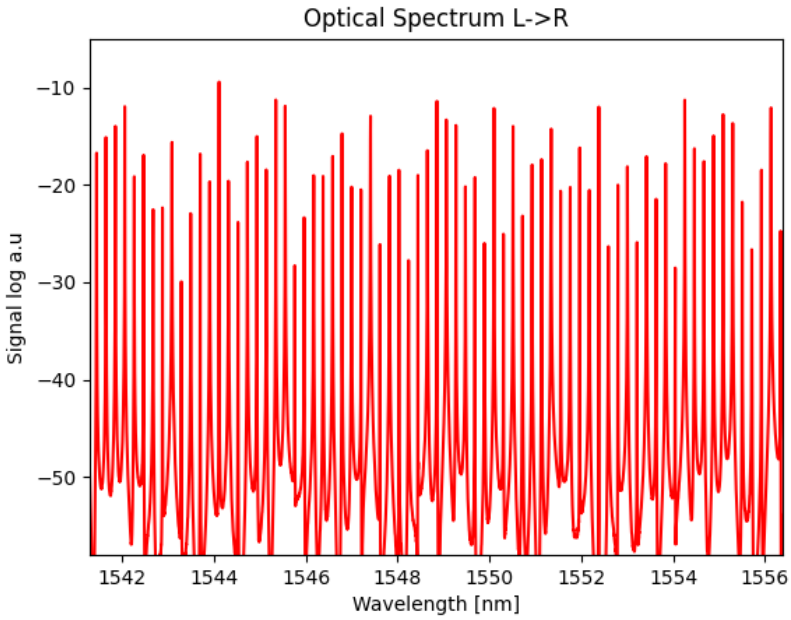

Figure 5.7: Emission spectra as simulated using Phisim with injection current of 100mA. The ring is too long to result in single mode emission and is instead constituted by a series of comb frequencies.

Before we discuss the optical locking of the ring laser, we have to address it's free running properties. We have used the nazca-phisim interface to simulate the behaviour of the laser, and Figure 5.7 reports the spectra obtained when simulating a 100mA current applied to the SOA. We can notice the almost uniform spectra composed to several peaks. This is due to the limitations discussed in the previous chapter in the modelling of the SOA at different frenquencies.

Figure 5.8 reports the experimental spectra recorded coupling a fiber to the chip. We can notice that in this case the laser is single mode with lots of small peaks representing the cavity resonances. We have to notice that the laser emission is not stable and tends to jump and side modes appear and disappear following non-predictable fluctuations. This is due to the intrinsic multimode nature of the laser.

In Figure 5.9 we have reported the LIV curve of the ring laser in both propagation direction clockwise (CW) and counter clockwise (CCW). We can notice that the CW direction delivers less power respect to the CCW, this is due to the small reflections in

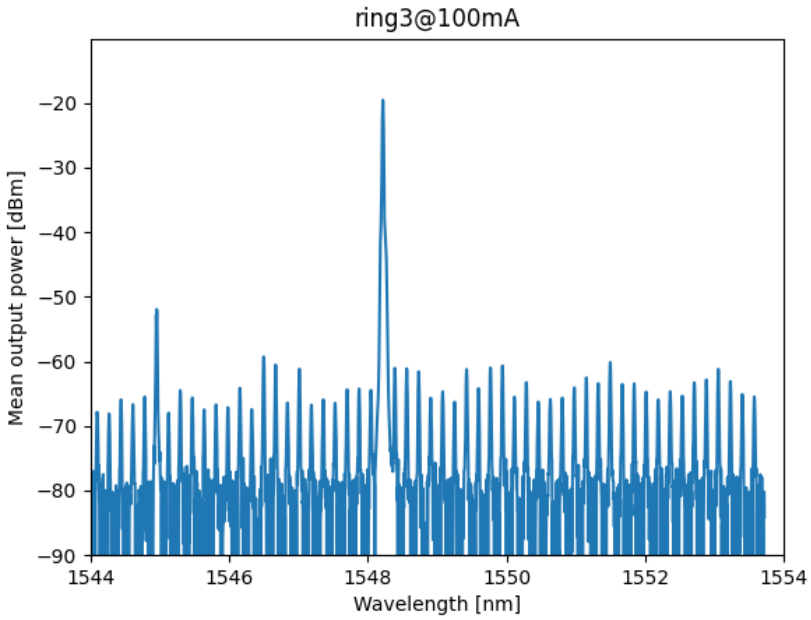

Figure 5.8: Emission spectra of the ring as measured in the lab. The single emission peak is due to cross-gain saturation and to fabrication defects that lead to internal reflections. We can notice the frequency comb in the low power regime.

due to the DFB laser. The bell shaped curve is characteristic of laser heating and gain saturation effects, we can see it also in the DFB laser in figure 5.6. When we compare the experimental result with the simulation we notice that the threshold is higher and the inclination of the curve is also higher. This difference can be attributed to additional losses inside the cavity and also the difference in emission between the multimode simulation emission and the single mode experimental.

The next step of the experimental verification is to verify the optical injection locking of the system.
Figure 5.10 report the resulting spectrum from optical injection of the ring laser. The spectrum is obtained applying a current of 100mA to the ring and 97mA to the DFB. The result is proving the optical injection locking, since we do not see any other peak, and the main peak is shifted respect to figure 5.8. Comparing the two figures we can also observe that the secondary peak at 1545nm disappear.

An additional proof of OIL is obtained comparing the photodiodes recorded power. In fact the optical injection of a ring laser

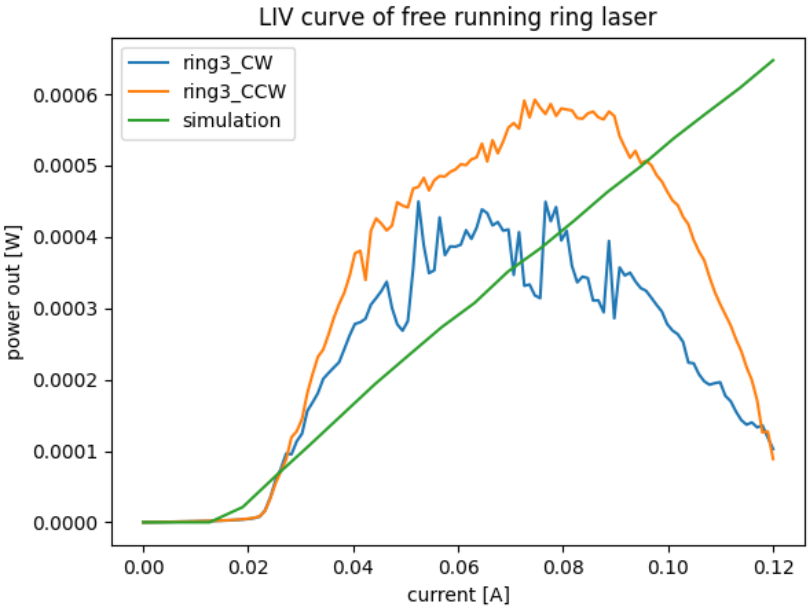

Figure 5.9: LIV curve of the ring laser, comparing the two direction of light propagation and the simulation. We can notice a preferred direction that is due to the reflection of the DFB structure.

ensures the unidirectionality of the light inside the cavity, completely suppressing the CW mode. In this case we have measured the current at the photodiode in the CW direction and turned on and off the DFB laser. Without DFB laser injection the ring laser in bidirectional as we can also see from the LIV in figure5.9, the current on the photodiode at $100mA$ is $-0.160mA$. When the DFB is turned in at $97mA$, the current measured on the CW photodiode is $-0.002mA$, demonstrating the high suppression of the CW light and the successful OIL.

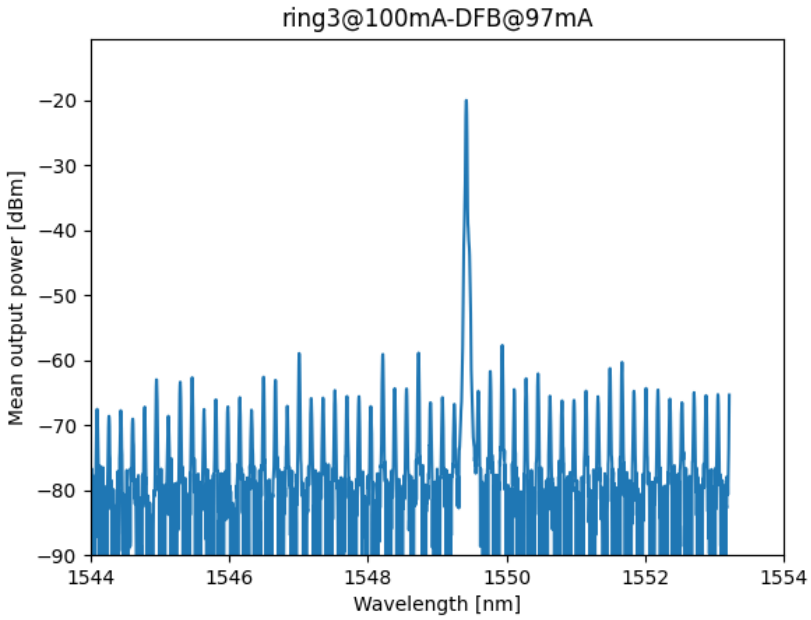

Figure 5.10: Spetra of the ring3 laser at 100mA when it is injected with the DFB at 97mA. We can notice the shift in wavelength respect to figure 5.8 that is due to the optical injection of the DFB.

5.4.2 *DBR and double ring circuit*

The second circuit under analysis is composed by two ring lasers, marked as ring1 and ring2 in the mask, and a DBR laser creating the schematic in figure 5.3. In the following we will analyse the behaviour of the rings, the DBR laser and the optical injection scheme.

We will start our analysis from ring2, this ring is identical to ring1 and really similar to ring3 analysed in the previous section. The main difference with ring3 is the presence, in ring1 and ring2, of the feedback of the DBR mirror of the master laser. This changes the behaviour of the ring, giving it a preferred lasing direction.
In figure 5.11 we have reported the LiV curve of ring2, we can notice that in this case, contrary to ring3, the threshold is in agreement with the simulation. This gives us the indication that the MMI splitting ratio and losses analysed in the previous section, and used for the simulation, are valid also in other rings and thus easy to reproduce from the fabrication point of view.
The slope of the curve is higher that the simulated one, this can

be due to an underestimation of the gain coefficient. In fact, in this design this factor has a high incidence on the curve slope but not on the threshold. A different explanation can be found in the spectra response of the laser.

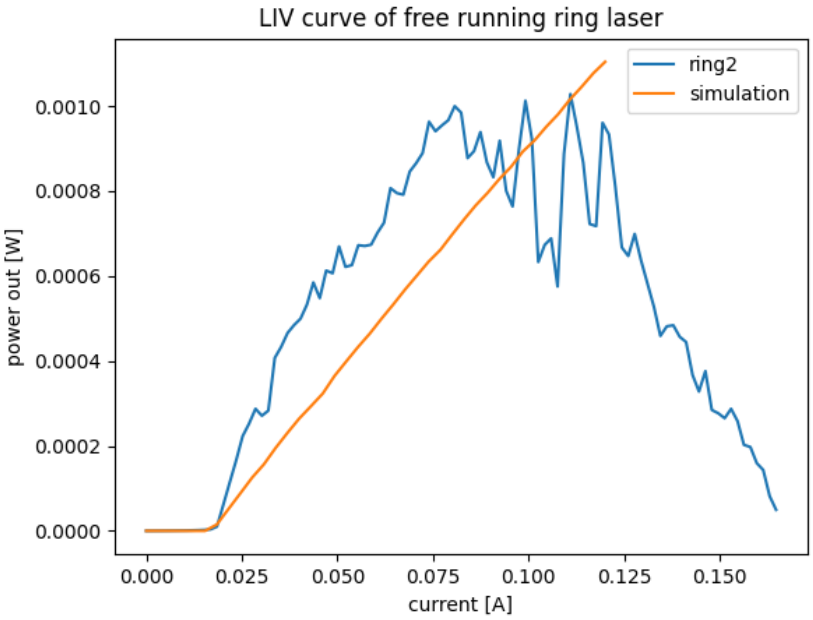

Figure 5.11: LiV curve of ring laser number 2 compared with the expected curve from simulation. In this case the threshold and the inclination of the curve is similar between them, confirming the high variability in performances between identical components on the same chip.

Ring2 experimental spetrum is presented in figure 5.13, and can be compared with the spectra expected from simulation in figure 5.12.
Here we find the same factors influencing the high difference between the simulation and the real case as for ring3: small reflections due to fabrication defects can lead to different cavity length and ultimately to single mode lasing. A second effect not taken into account is the cross-gain saturation effect that tends to make only a single wavelength lase.
The presence of this effect is also evident from the mode hopping characteristic of the LiV curve that can be seen in the figure 5.11. This is typical of a multimode laser that changes lasing frequency based on small changes in temperature and conditions of the cavity, leading to a highly unstable emission.

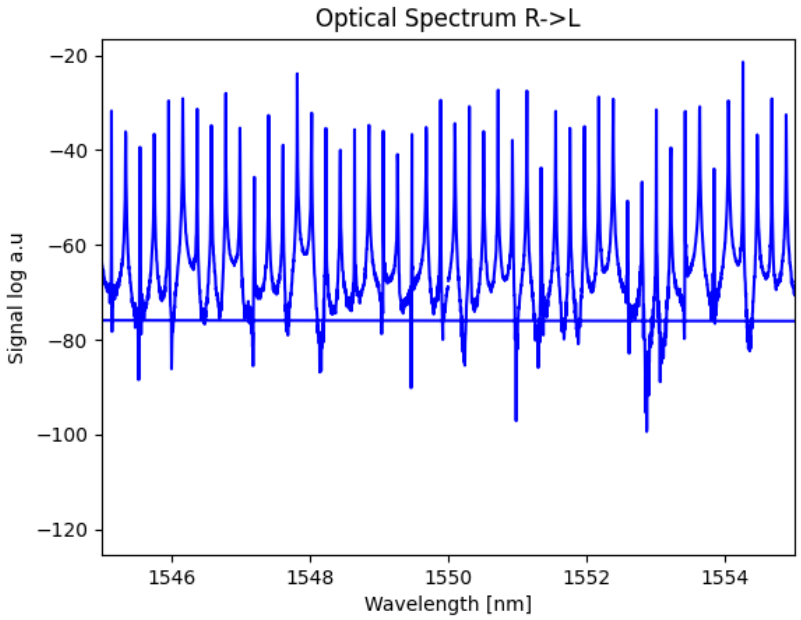

Figure 5.12: Emission spectra of the ring2 laser as simulated using the nazca-phisim interface. As with the previous ring laser, it shows different peaks in a homogeneous power distribution.

We now move our attention on the DBR laser, before discussing the OIL scheme.
In Figure 5.14 we compare the LiV curve of the DBR laser with the expected power from simulation. We can see that they diverge significantly and neither the expected power nor the threshold are in agreement. This is an unexpected result that will require further investigation in the future.
It can be partially attributed to the variation fabrication, but the discrepancy is hardly due to the simulation tool, since the prediction on similar laser were more accurate.
The linear increase in the beginnig part of the experimental curve still shows no mode-hopping and suggest a good laser stability.

In our application we can accommodate higher power outputs of the laser with just keeping the current injection lower.
In this design was not possible to have direct access to the laser, so we can not have a spectrum directly, and we have to rely on the simulation. Figure 5.15 shows the expected spectrum from the DBR laser, we can notice that differently from the previous case it exhibits high side mode peaks at around 30dB side mode

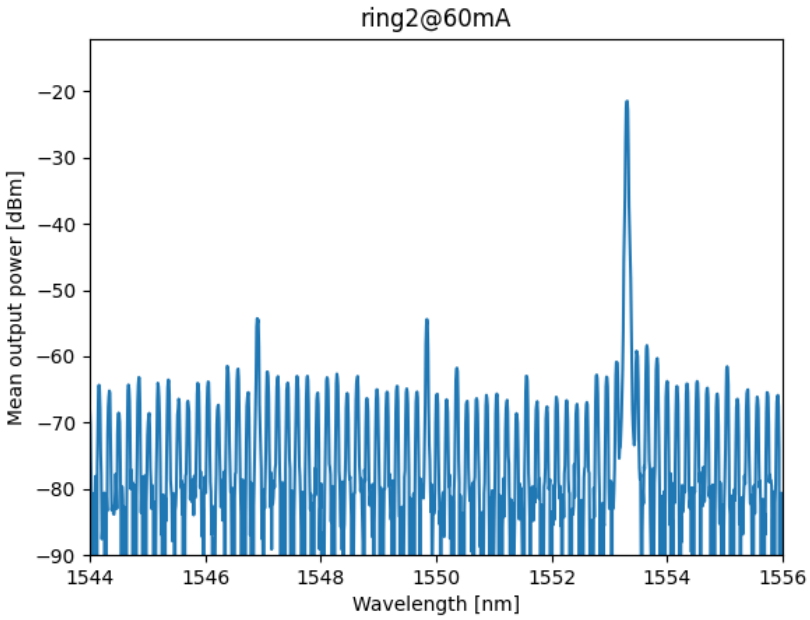

Figure 5.13: Emission spectra measured at 60mA current injection on the ring2 SOA. As in the previous case the ring exhibits single mode operation due to small imperfections in the fabrication and cross-gain saturation.

suppression. In this case we will use the OIL not only for isolating a single frequency of the slave laser but also to isolate a single frequency of the master laser. The challenging part will then be to lock both ring1 and ring2 laser to the same master frequency.

We can now discuss the OIL scheme, given the unexpected high power from the DBR laser we have first proved the locking with only one of the rings.
Figure 5.16 shows the output of ring1 laser when injected with the DBR laser.
The laser emission is single mode with a side-mode suppression of 45dB demonstrating the locking of the two lasers. In fact, we do not see the multimode emission of the DBR laser nor any sign of the multimode of the ring laser. This shows that this system can be used for QKD effectively.
Like in the case of the DFB and ring3 the current applied to the SOAs is critical and influences the locking mechanism, but we can find multiple couples of currents that achieve OIL. Here we have displayed the couple of currents that are closer to the spectra recorded for the free running lasers.

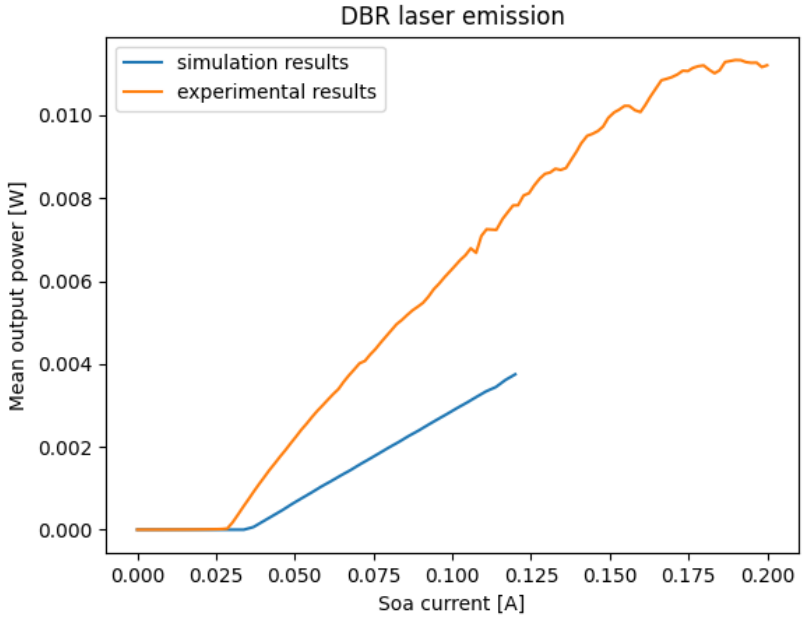

Figure 5.14: DBR laser LiV curve, comparison between the simulated line and the experimental results. In this case the output power of the laser is completely unexpected and is significantly higher respect to the expected power from the simulation.

This system is already capable of QKD like the previous one, but we also want to test if we are able to lock both ring1 and ring2 to the same DBR laser at the same time.

Figure 5.17 is the spectra resulting from activating both laser. We can notice that there is a series of other peaks in addition to the peak from ring1. We have varied the current applied to the different lasers in order to get to stable locking of both ring laser, but the best results so far has been the one in figure 5.17. These results are clearly not usable for QPSK since for this application we need a single wavelength. The main question raising from this plot is why the injection doesn't work for both rings ?

As a final test we have decided to vary the phase modulator in the DBR laser in order to check the influence of it in the locking of the lasers.
We have decided to drive the rings at the same power of 80mA and only vary the DBR laser SOA section and phase section. The best recorded spectra is visible in Figure 5.18, obtained with 77mA on the SOA and 29mA on the phase modulator. The resulting spectrum shows a main peak and few small peaks

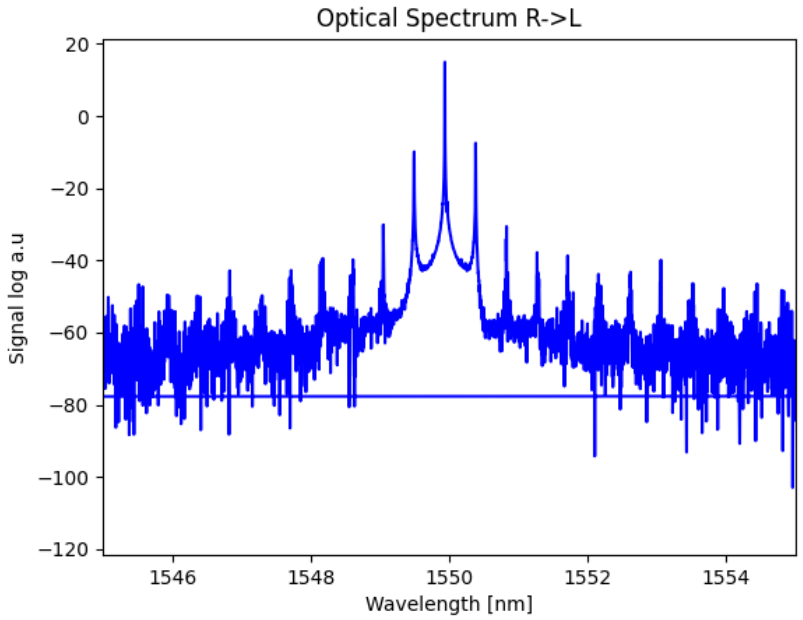

Figure 5.15: Emission spectra from the simulation of the DBR laser. In this case the emission is not single-mode, this doesn't represent a problem since we will use the optical injection to filter out the side-modes.

35dB lower. From this spectrum is still clear that the system is still not necessary locked and the three laser influence each other. In fact if we turn ring1 off the output spectra goes back to be multimode, spectra similar to figure5.17. This gives the indication that the rings themselves are influencing the emission of one another, even if in an optically injected system they should be lasing in a single direction as proven for ring3.
Further investigation in this system is thus necessary and the photodiodes inside ring1 and ring2 should be monitored to understand if there is light travelling in the counter-propagating mode of the laser.

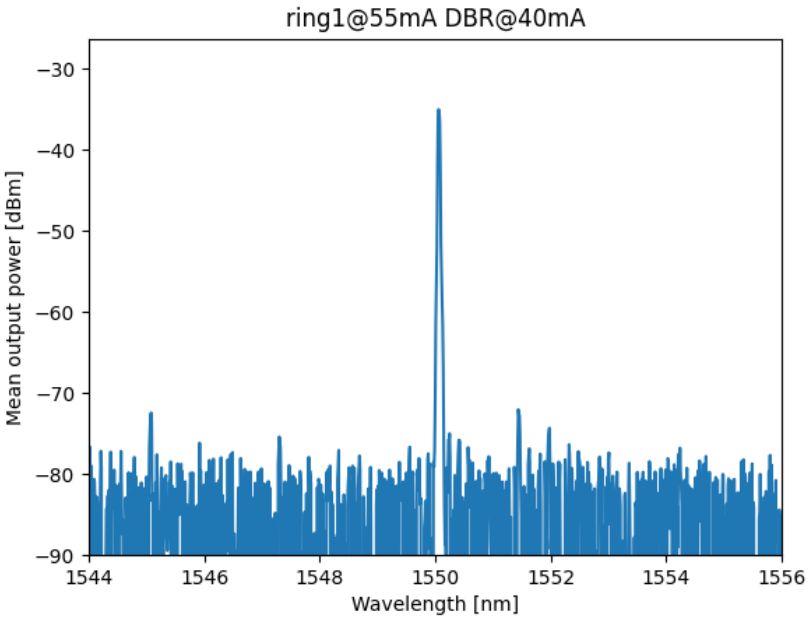

Figure 5.16: Emission spectra of ring1 at 55mA when injected with the DBR laser at 40mA. We can notice the single mode emission resulting from the locking of the DBR and the ring.

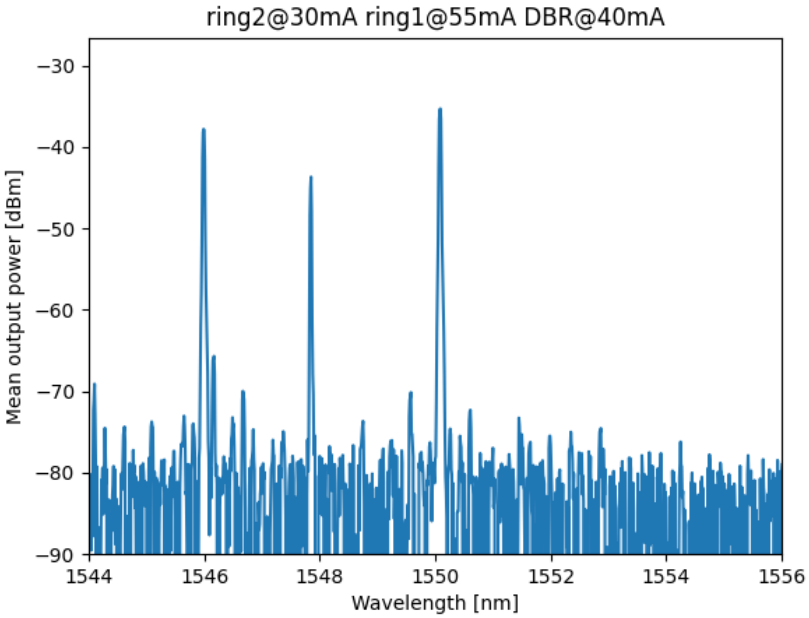

Figure 5.17: Emission spectra of ring1 at 55mA and ring2 at 30mA when injected with the DBR laser at 40mA. We can notice multiple peaks

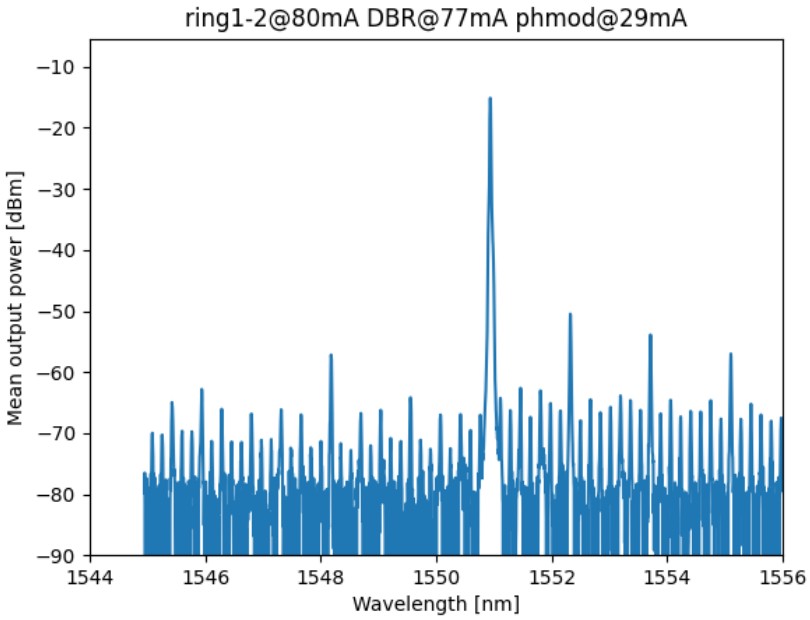

Figure 5.18: Spectrum, ring1 and ring2 are injected at 80mA, the SOA of the DBR laser is driven at 77mA whether the phase modulation section of the DBR laser is driven at 29mA. This combination of factor has been chosen to realize optical injection in both the rings.

5.5 CONCLUSIONS

In conclusion, In this chapter we have designed two photonic integrated circuits for QKD and QPSK both based on optical injection locking mechanism.
We first have summarized the benefits of optical injection locking, providing insight on the locking mechanism.

The first circuit presented in this chapter is composed by a DFB and a ring laser, we have characterized the laser behaviour when running independently. Using the integrated photodiodes and an optical spectrum analyser we have demonstrated the optical injection locking between the two lasers, resulting in single mode, single direction emission. Using the DFB and the two photodiodes has been possible to estimate the power splitting ratio of the custom MMIs, in agreement with the designed specifications and the simulations.

The second circuit is composed of two ring lasers and a central DBR laser. Using optical injection locking we want to achieve

high speed modulation of the ring lasers simultaneously. We have characterized the identical ring lasers and DBR laser LiV curve separately. They show good agreement with the simulation in the case of the ring laser whether the results for the DBR laser are unexpected the experimental realization shows higher power respect to the simulation results. We have demonstrated using the optical injection locking of one ring laser with the DBR laser, but when moving to locking both ring lasers to the master DBR laser we achieved it only using the phase tuning section. The unstable condition of this state poses some doubts regarding the optical injection and the effectivity of locking in this system.

6

MONOLITICALLY INTEGRATED TIME-BIN ENCODED QKD TRANSMITTER

In this chapter we are going to discuss a different design for QKD.
The main objective in this case is to design a combination of transmitter and receiver that do not require long delay lines. As can be noted in the discussion in chapter 2, the receiver side in particular requires long delay lines to interfere the two photons. In the design that we are presenting in this chapter this is not required. A delay line is still present, but it is only one centimetre long compared to the ten or more of centimetres long in more traditional approaches [26].
The working principle of this design is pretty straight forward. In time-bin encoding QKD the key is encoded in the phase difference between two pulses. In the traditional approaches the two pulses are transmitted with 1GHz clocking speed, resulting in long delay lines to recombine the two pulses.
Here we propose a different approach, we create a short pulse of few ps time width and use a short delay line to split it. This creates two entangled pulses with short time separation. At the receiver side the two pulses can be recombined using the same delay line of few millimetres.
Our design has a small footprint and the short length of the delay made it possible to be fabricated in an InP platform where high waveguide losses make it impossible to use long delay lines. We have submitted the design for fabrication in a SMART photonics MPW run.

Another advantage of this design is the symmetry between the transmitter and the receiver circuits. They, in fact, need to have the same identical delay line, resulting in a transmitter circuit that can be easily adapted to become a receiver.
In this chapter we will present both a receiver and a transmitter. We will discuss the advantages and the difficulties with perspec-

tive to the traditional implementation until now. Both designs are under fabrication, and they are integrated on the same chip together with other test structures and a novel tunable mode-lock-laser design.
The design is still under fabrication at the moment and we will focus our attention on the simulation results and the theoretical framework of this design.

6.1 SCHEMATIC

The circuit schematic is presented in Figure 6.1. In this figure we have omitted the MMI splitters and combiners.
We use a DBR laser as a laser source of our circuit.
A critical requirement for time-bin encoded QKD is the randomization of the absolute phase of the pulses. In our circuit this is achieved using a phase modulator right after the laser.
After the phase randomization stage, we need to create the pulses that we will use to encode our signal. To do so we use a MZI with fast electro-optical modulators, allowing us to obtain short pulse of few ps.
The structure that follows the MZI can be seen as an unbalanced MZI, in fact in this case the arms of the interferometer are not equal, a delay line is present on one of them. This structure will split the pulse in two separate pulses, the phase section in the shortest arm is used to tune the phase difference between the output pulses. It is worth notice that this structure has two inputs and two outputs. One of the inputs is connected to the MZI and the second input is instead coupled off chip. The two outputs are instead both coupled off chip. This characteristic of double input/output allows the circuit to be both used as a transmitter and as a receiver.

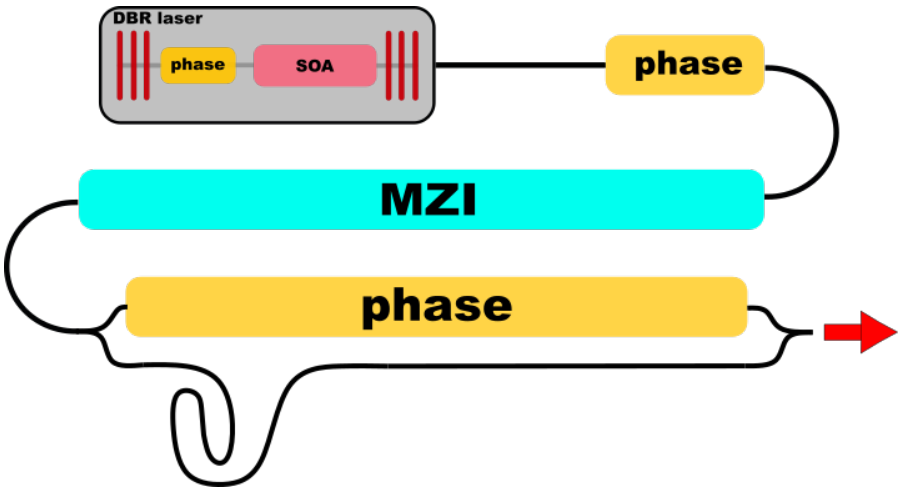

Figure 6.1: This schematic represents transmitter design presented in this chapter. The top DBR laser is phase randomized using the first phase shifter. Using a MZI the laser output is then pulse shaped in short pulses. The final structure splits the pulse in two and adds a phase to the pulse in the short arm.

6.2 MASK DESIGN

In figure 6.2 we show the mask design submitted for fabrication. It is a 4x4.6 mm chip in fabrication in a MPW run in SMART photonics.
This mask not only contains the transmitter and receiver for QKD but also two other circuits that we are going to discuss briefly later.

The DBR laser in this case has been assembled by individual components since it is not available as a single building block like in HHI. The DBR mirrors are 400µm and 200µm long. The difference with HHI DBR is substantial since these mirrors have lower coupling coefficient resulting in longer DBR with smaller reflection bandwidth and consequently easier single mode operation.
The SOA in the laser is 500µm long with a phase section of 200µm for fine-tuning of the resonance.
The phase section used to randomize the output phase of the laser follows the DBR laser in the first row of the chip. It is 1mm long this allows the phase to be randomized in the $0-\pi/2$ range, sufficient for QKD operation.
Following this structure on the second row of the chip we can see the balanced MZI. This structure is used for creating short

pulses from the continuous wave generated by the DBR laser. It is created using two 2.6mm long phase modulators that can be driven by RF. This type of configuration can be modulated up to 23GHz with only 3dB losses according to the SMART photonics design manual. There is also one additional input and output to this component for testing.

Following the MZI we have added a SOA section 1100µm long. This additional amplification has a double purpose: one one side can be used to amplify the signal in the testing operations. On the other side it can be used to absorb the incoming light when the circuit is used as a receiver. This section can also be overridden using the output of the MZI and connecting it directly to the following pulse splitting section.
In last stage of the transmitter the pulse is divided in two paths: the shortest path is constituted by a 2.5mm long phase modulator. This modulator is used to change the phase of the pulse between $0 - 2\pi$ effectively encoding the bit in it. The longest path is constituted by a delay line of 10mm, that will delay the pulse travelling in this path of more than 50ps. The two paths are then recombined creating a pulse train with arbitrary phase difference but randomized absolute phase.

The last part of the transmitter circuit is then replicated in the middle of the circuit, this part is used as receiver. Even if the transmitter by itself can be used as receiver we have added this part of circuit and terminate it with a RF photodiode. This structure gives us the possibility of testing both transmitter and receiver at the same time.

Below the receiver only circuit we have designed a mode-lock laser that can be operated at two different pulse repetition ratios of 1GHz and 5GHz. This is obtained using a MZI to select paths of different length, resulting in a different operation regimes. A more detailed description is presented in Appendix A.

The last circuit present in the mask design is an optically injected ring laser like the one presented in Chapter 5. The schematic of this circuit can be found in Figure 5.2, with the difference that in this circuit the DFB laser is substituted by a DBR laser. The DBR laser used in this circuit has the same components as the one in the transmitter circuit discussed above.

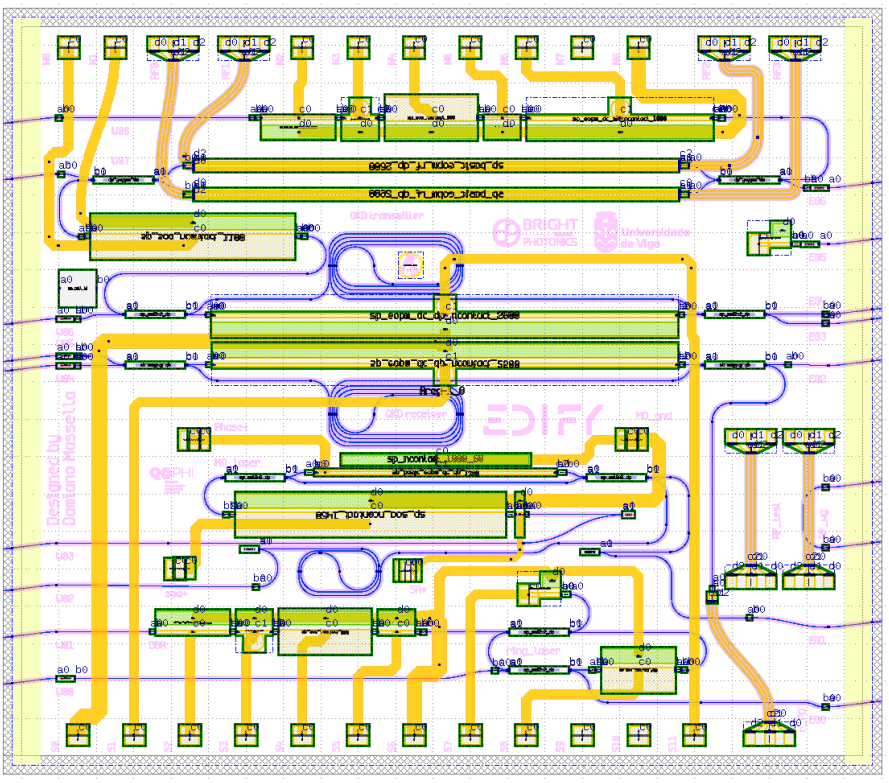

Figure 6.2: Mask design submitted for fabrication in an SMART photonics MPW run. on the top part of the chip we can see the QKD transmitter and exactly below it the receiver. In the middle we have designed a Mode-lock laser that can be tuned between two different states. On the bottom part we have replicated the circuit of chapter 5 using a DBR laser and a ring laser.

6.3 SIMULATIONS

The first simulated element is the DBR laser. Like in the case of HHI platform, we have first used experimental results to tune the parameters used in the PHIsim simulation. Unfortunately, it is not possible to show the comparison between the simulated DBR and the experimental results here since the measurement results used are property of Bright Photonics.
We have already demonstrated the reliability of the tool in predicting the behaviour of integrated laser one the proper parameters are choose.
The final experimental verification of the results of the following simulations will be possible only when the chip fabricated in Smart photonics in the SP40 MPW run will be delivered.

In the SMART photonics design manual the coupling coefficient of the DBR gratings is reported with a value of $50cm^{-1}$, versus the $85cm^{-1}$ used in HHI. The consequence of that is that the gratings in the Smart platform will need to be significantly longer and the reflectivity window will be narrower.
This in terms of laser design results in bigger footprint of the laser but makes it easier to achieve single mode operation even with long SOA.

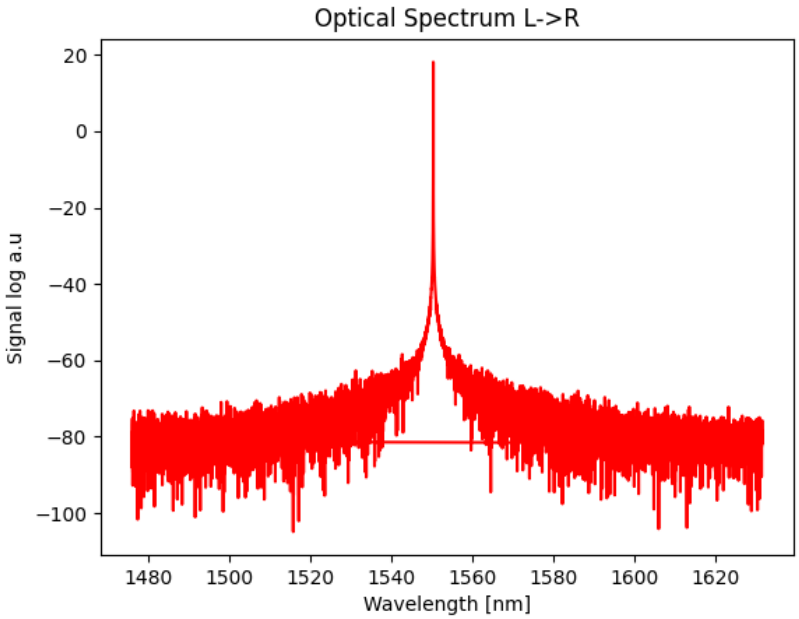

Figure 6.3: Simulated emission spectra of the DBR laser in mask 6.2. The SOA is injected with 80mA of current. The single mode operation is clear and the laser shows a 70dB side mode suppression.

The results of the simulations are reported in figure 6.3 and figure 6.4.
Figure 6.3 display the emission spectra of the DBR laser when the SOA is pumped at 80mA of current. Contrary to the HHI case, the emission in this laser is clearly single mode and has a high side mode suppression ratio of 70dB.
These characteristics are due to the smaller reflection bandwidth of the DBRs in this platform.
Figure 6.4 reports the simulated LiV curve of the laser. We expect from this kind of laser a threshold around 18mA of injected current in the SOA and an output power in the order of few milliwatts. We still have to keep in mind that this simulation

does not take into account the gain saturation at higher injection currents, this will result in lower emitted power from the laser, like what happened in the HHI platform. It is not possible to estimate the maximum power but, we can still see that the power output of the laser should be around $2-3mW$.
We can also notice a mode hopping characteristic around $60mA$. This does not change the behaviour of the laser above and below as we can notice from 6.3 the laser is still single mode.

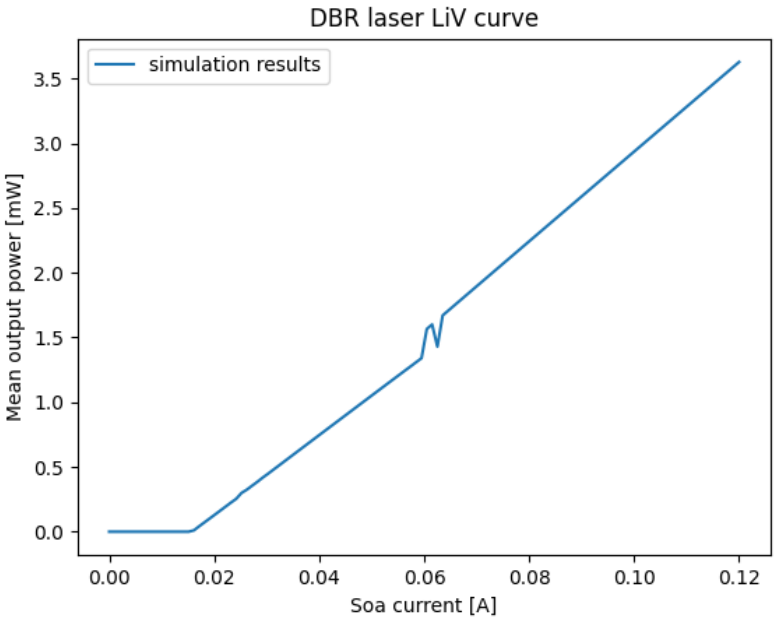

Figure 6.4: LiV curve of the DBR laser in mask 6.2, the threshold is estimated to be around $18mA$ injection current on the SOA and we can notice mode hopping only in around $60mA$ and stable output otherwise.

Once the expected behaviour of the DBR laser is calculated, we can turn our attention to the pulse shaping section.
The pulse shaping section is composed by two MZI interferometers. The first one is a balanced interferometer, meaning that the length of the two arms is the same. This interferometer is used to shape the light pulse into pulses of different width. In our case we want to have a pulse of around $10^{-10}s$ corresponding to a modulation of $10GHz$. The separation between two subsequent pulse will be of $10^{-9}s$.

The second MZI interferometer is not balanced and is composed by a short arm that contains a phase modulator and a long

delay arm of 10mm that will delay the up going pulse. A pulse in the longer arm of the MZI take 50ps more to travel through it respect to the short arm. Consequently, two pulses separated by 50ps, and of half intensity respect to the ingoing pulse, come out of the unbalanced MZI. The phase shifter present on the shorter arm of the MZI allows us to tune the phase difference between the two pulses. This tunability, together with the absolute phase of the pulses that can be randomized using the phase shifter right after the DBR laser, allows the implementation of QKD protocols using this circuit.

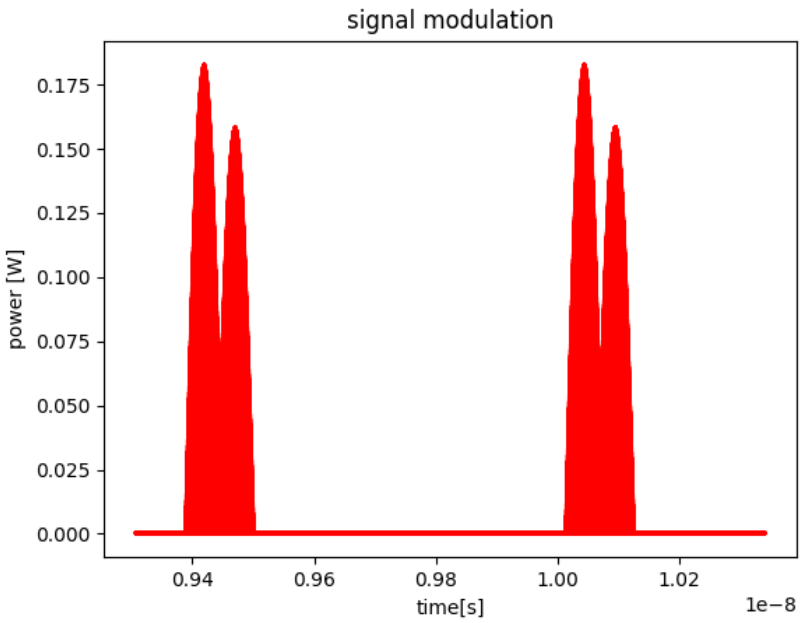

Figure 6.5: Power output of the circuit when the MZI is modulated using a square wave signal multiplied by a sine wave. The lower intensity pulse is due to the extra losses in the longer path of the unbalanced MZI. We can see the clear separation between the pulses that have a phase difference decided using the second MZI short arm.

Figure 6.5 shows the circuit output according to simulation. The modulation applied to the circuit is a square wave of 1GHz with 10% duty circle multiplied by a sine wave of 20GHz in order to simulate the modulator behaviour.
The results show the two peaks coming out of the unbalanced MZI. The higher one are the pulse part passing through the short arm of the MZI whether the lower one are passing through the

longer one thus having higher losses.

Figure 6.6 is the signal spectra of the circuit output. In it, we can see that the basic spectra of the laser is not modified, and the modulation only add a pattern of few GHz corresponding to the pulse beating and modulation.

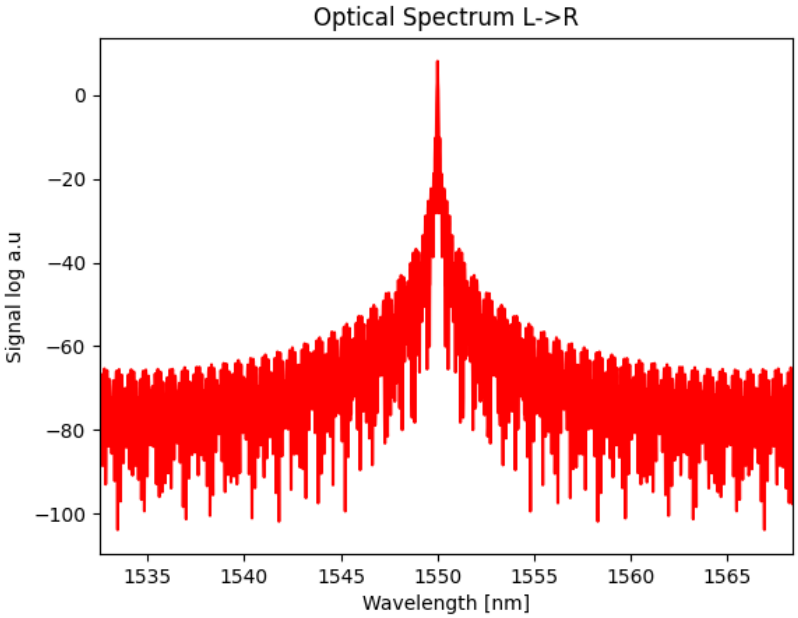

Figure 6.6: Spectrum of single wavelength 1550nm light after modulation from the two subsequent MZI filter. We can notice that there are no fundamental modification respect to figure 6.4.

6.4 CONCLUSIONS

In conclusion, We have designed and submitted for fabrication a novel QKD photonic integrated circuit. The novelty of our design consists in the pulse splitting procedure, in fact the two entangled photon pulses are obtained by splitting a single multimode pulse by means of an unbalanced MZI. This procedure allows the integration of both transmitter and receiver in photonic platforms with high waveguide losses. Our design uses shorter delay lines for the interference and creation of the optical pulse. At the receiver side the delay line length does not depend on the bit rate like in other designs, but it only depends on the transmitter design.

7

CONCLUSIONS AND PERSPECTIVES

In the introductory part we have presented two technologies that will shape the our future and are key foundation for the work presented in this thesis.
We have presented some basic concepts and the state of the art quantum cryptography. The technology is still facing numerous challenges in both the theoretical and experimental work. Current experimental work goes in multiple directions exploring solutions both in bulk photonics and integrated photonics. The later one constitutes an available solution to integrate with lithographic precision multiple element, improving stability and reliability of the systems.

We have summarized the development of the generic integrated photonics platforms. We have discussed the main photonic platforms and material. The concept of PDK has been presented and the main components has been described. Finally, a description of all the design workflow of an integrated photonic chip from the design to the packaging and testing has been discussed.

In the second part of the thesis we have discussed the connection between the layout framework Nazca-design and the simulation tool PHIsim. The connection between this tool is particular beneficial for designers saving time and allowing more reliable simulation together with better design rule checking. We have discussed the tool individually, and after we have presented an interface that connects the two in an easy and intuitive way. The capabilities of the tools presented have been verified on a DBR laser and on a mode lock laser, comparing the simulation results with the experimental results reported in literature. The comparison results are displayed and discussed highlighting the limitation and advantages. We want to highlight the open source nature of all the tool involved including the interface.

In the core part of this thesis we have presented different design for QKD and QPSK in integrated photonics.
In chapter 4, we have designed and fabricated a photonic integrated chip in HHI InP platform. The designed circuit is capable of both QPSK and QKD. We have experimentally characterized the emission of the two main sources in the circuit and compared them with the simulations. The Optical injection locking of the lasers was not possible to recreate due to lack of equipment. We have discovered the high dependence of both laser from the temperature of the chip. In the future work the chip will be wire bonded allowing the simultaneous variation of all the parameter involved and the testing of the QPSK and QKD capabilities.

In chapter 5 we have designed two photonic integrated circuits for QKD and QPSK both based on optical injection locking mechaninsm.
We first have summarized the benefits of optical injection locking, providing insight on the locking mechanism.
The first circuit presented in this chapter is composed by a DFB and a ring laser, we have characterized the laser behaviour when running independently. Using the integrated photodiodes and an optical spectrum analyser we have demonstrated the optical injection locking between the two lasers, resulting in single mode, single direction emission. Using the DFB and the two photodiodes has been possible to estimate the power splitting ratio of the custom MMIs, in agreement with the designed specifications and the simulations.
The second circuit is composed of two ring lasers and a central DBR laser. Using optical injection locking we want to achieve high speed modulation of the ring lasers simultaneously.
We have characterized the identical ring lasers and DBR laser LiV curve separately. They show good agreement with the simulation in the case of the ring laser whether the results for the DBR laser are unexpected the experimental realization shows higher power respect to the simulation results. We have demostrated using the optical injection locking of one ring laser with the DBR laser, but when moving to locking both ring lasers to the master DBR laser we achieved it only using the phase tuning section. The unstable condition of this state poses some doubts regarding the optical injection and the effectivity of locking in this system.

Chapter 6 present a circuit design submitted for fabrication in the SMART photonics platform:
We have designed and submitted for fabrication a novel QKD photonic integrated circuit. The novelty of our design consists in the pulse splitting procedure, in fact the two entangled photon pulses are obtained by splitting a single multimode pulse by means of an unbalanced MZI. This procedure allows the integration of both transmitter and receiver in photonic platforms with high waveguide losses. Our design uses shorter delay lines for the interference and creation of the optical pulse. At the receiver side the delay line length does not depend on the bit rate like in other designs, but it only depends on the transmitter design.

Part IV

APPENDIX

A

TUNABLE MODE-LOCK LASER

In this Appendix we are going to discuss the design of a tunable mode-lock laser. In this case the laser can be switched between two different repetition rates, corresponding to two different cavity lengths.

A.1 INTRODUCTION

A first concept to understand is how the emission of a mode lock laser depends on the desig parameters. The first concept tha we introduce is the one of gain bandwidth, with this term we indicate the frequency range where it is possible to obtain optical gain from the laser medium. It can range from the 1.5GHz of helium-neon lasers to the 128THz of a titanium-doped sapphire solid-state laser. In the case of quantum well based integrated laser the bandwidth is around 200nm and centered around 1500nm and depends on the applied current.

Another factor that influences the laser behavior is the cavity resonances. Considering the simple case of a Fabry-perot cavity, that is composed simply by two flat mirror separated by a gain medium. The light produced by the medium will bounce back and forth in the cavity creating interference patters. More precisely there will be some frequency that will fit the cavity and interfere constructively with themself and other not. This creates a set of standing waves at certain frequencies. Each frequecies that form a standing wave in the cavity is called a cavity mode. This frequencies are the only one that are self-regenerating in the cavity wether the other frequencies are destructively interfere. We can calculate the spacing between the cavity modes with the simple formula:

$$\Delta\nu = \frac{c}{2L} \tag{A.1}$$

Where L is the optical cavity length and c is the speed of light. In a simple laser all the modes oscillate independently, essentially behaving like a set of independent lasers that emit light at different frequencies. The phase of each frequency emitted is not controllable and depends from a variety of different effect like thermal and electrical noises. This makes Laser with only few modes results in power osciltion in the output due to the interference and phase changes in the modes.

Mode-locked laser are also refered to as phase-locked, since they fix the phase between all the mode in the cavity obtaining ad predictable behavior of the output. In fact in mode-lock laser the modes will all oscillate with the same phase and will preriodically constructively interfere with each other, resulting in intense pulses of light at fixed periodic intervals.
The time separation between pulses can be calculated as $\tau = 2L/c$ for a Fabry-Perot laser. In general we can calculate τ as the time the light takes to complete a cavity roundtrip, also corresponding to $\tau = 1/\Delta\nu$. The consequence is that the repetition frequency of the pulse correspond to the frequency distance between the cavity modes.

The duration of each pulse or the pulse width is determined by the number of cavity modes that are phase locked, it is not guaranteed that all the cavity modes are locked. The duration of the pulses is proportional to $N\Delta\nu$ given that N are the cavity modes that are phase locked. It follows that the wider the gain bandwidth the shorter the pulses. In practical terms the pulse duration is determined by the shape of each amplitude and phase relationship between the modes. In the example of a laser producing pulses with a Gaussian shape we have that the pulse duration is given by:

$$\Delta t = \frac{0.4441}{N\Delta\nu} \tag{A.2}$$

In integrated photonics mode-locking is achieved passivelly, meaning that there are no elements that need external modulation to produce the pulses. Passive mode-locking uses elements inside the cavity that are modulated by the light in the cavity itself, in integrated photonics these elements are saturable absorbers.
A saturable absorber is an element with an intesity-dependent transmission, this means that the device behaves differently based on the intensity of light going through it. A saturable

absorber absorbs low intensity light, but it becomes fully transparent when the light reaches a threshold intensity. The effect in a laser cavity is to absorb all the low intensity constant-wave light. In a mode lock laser the random fluctuations in intensity with higher intensity are transmitted. This process repeats as the light travels in the cavity ultimately leaving only the cavity frequency travelling in the cavity, resulting in o train of short pulses of high intensity. In integrated photonics we can use a reverse biased SOA as a saturable absorber.

A.2 DESIGN AND SIMULATIONS

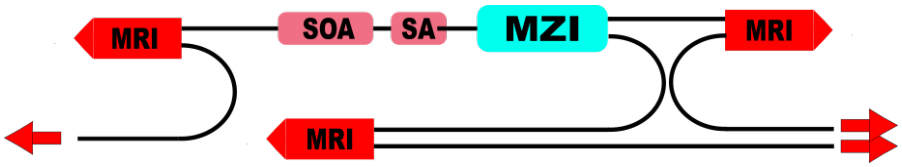

Figure A.1: Schematic representation of the Tunable mode-lock laser.MRI-> multimode refletor interferometer.

In the mask design of figure 6.2 we have designed a tunable mode-lock laser. It is tunable in the sense that the repetition rate can be choosen between two different possibilities. The way this is achieved is by changing the cavity length of the laser.
We are still talking about an intergrated laser, and the cavity selection can not be done by phisically elongating the cavity. It is instead achieved using a MZI that allows us to select between two different paths. This is similar to the MZI use we did in chapter 4 where we used the MZI to select between two paths. In this case both path are terminated with a broadband mirror and ensure feedback, effectively creating a laser cavity.
We have choosen the length of the two cavities using equation A.1 and targeting a repetition rate of 5GHz and 10GHz. The SOA length is set to 500µm in order to ensure enough gain given that we have extra losses in the cavity due to the MZI interferometer. The MZI is a balanced interferometer with phase modulation only in the upper arm that ensures the possibility of switching between the two paths.

We used the nazca-phisim interface to simulate the behaviour of this laser and check the expected performances of the laser. Figure A.2 shows the laser behaviour when the long cavity is selected using the MZI. We can see that the repetition rate is

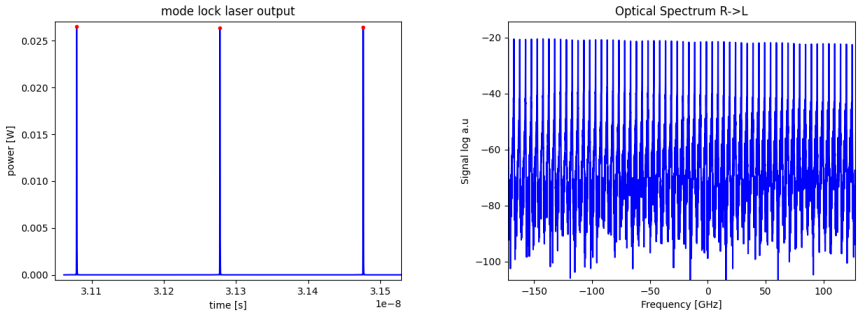

Figure A.2: On the Left part: the pulse train produced by the laser with frequency 5GHz and pulse width of $4.4\dot{1}0^{-13}$s and mazimum height of 25mW with injection current of 50mA on the SOA. On the right: Specrum of the laser output, we can see the typical frequency comb with 5GHz spacing equal to the repetition rate.

5.03GHz as expected from the design and the peak power is 25mW with SOA current at 50mA. The spectrum of the output confirms the repetition rate of the laser and shows a frequency comb with 5GHz spacing.
Figure A.3 reports the laser behaviour when the phase modulation element is set to π phase shift, meaning that we select the short cavity for lasing. In this case the repetition rate is 10.1GHz and the peak power is 10mW when the SOA is driven at 50mA power. The repetition rate is confirmed by the spectrum that shows a distance of 10GHz between the peaks.

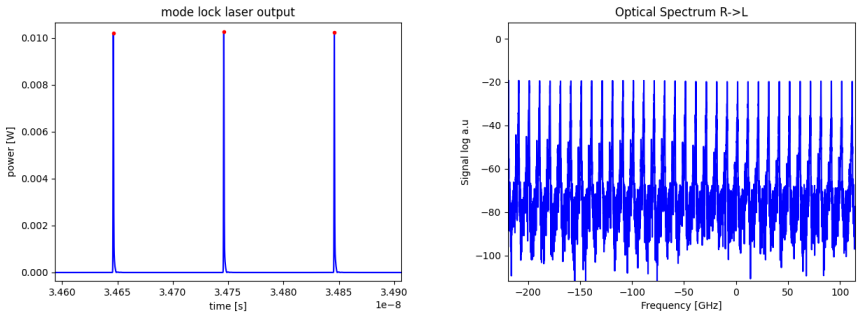

Figure A.3: On the Left part: the pulse train produced by the laser with frequency 10GHz and pulse width of $6.5\dot{1}0^{-13}$s and mazimum height of 10mW with injection current of 50mA on the SOA. On the right: Specrum of the laser output, we can see the typical frequency comb with 10GHz spacing equal to the repetition rate.

BIBLIOGRAPHY

[1] Charles H. Bennett and Gilles Brassard. "Quantum cryptography: Public key distribution and coin tossing". en. In: *Theoretical Computer Science* 560 (Dec. 2014), pp. 7–11. ISSN: 03043975. DOI: 10.1016/j.tcs.2014.05.025.

[2] Stewart E. Miller. "Integrated Optics: An Introduction". en. In: *Bell System Technical Journal* 48.7 (1969), pp. 2059–2069. ISSN: 1538-7305. DOI: 10.1002/j.1538-7305.1969.tb01165.x.

[3] Meint Smit et al. "An introduction to InP-based generic integration technology". In: *Semicond. Sci. Technol.* 29.8 (June 2014), p. 083001. ISSN: 0268-1242, 1361-6641. DOI: 10.1088/0268-1242/29/8/083001.

[4] Iñigo Artundo. "Photonic Integration: New Applications Are Visible". en. In: *Optik & Photonik* 12.3 (2017), pp. 22–25. ISSN: 2191-1975. DOI: 10.1002/opph.201700015.

[5] Radhakrishnan Nagarajan et al. "InP Photonic Integrated Circuits". In: *IEEE Journal of Selected Topics in Quantum Electronics* 16.5 (Sept. 2010). Conference Name: IEEE Journal of Selected Topics in Quantum Electronics, pp. 1113–1125. ISSN: 1558-4542. DOI: 10.1109/JSTQE.2009.2037828.

[6] G. S. Vernam. "Cipher Printing Telegraph Systems For Secret Wire and Radio Telegraphic Communications". In: *Trans. Am. Inst. Electr. Eng.* XLV (Jan. 1926), pp. 295–301. ISSN: 0096-3860, 2330-9431. DOI: 10.1109/T-AIEE.1926.5061224.

[7] C. E. Shannon. "Communication Theory of Secrecy Systems*". en. In: *Bell System Technical Journal* 28.4 (Oct. 1949), pp. 656–715. ISSN: 00058580. DOI: 10.1002/j.1538-7305.1949.tb00928.x.

[8] R. L. Rivest et al. "A method for obtaining digital signatures and public-key cryptosystems". In: *Commun. ACM* 21.2 (Feb. 1978), pp. 120–126. ISSN: 0001-0782. DOI: 10.1145/359340.359342.

[9] Peter W. Shor. "Polynomial-Time Algorithms for Prime Factorization and Discrete Logarithms on a Quantum Computer". en. In: *SIAM J. Comput.* 26.5 (Oct. 1997), pp. 1484–1509. ISSN: 0097-5397, 1095-7111. DOI: 10.1137/S0097539795293172.

[10] Lucamarini Marco and et all. "Implementation Security of Quantum Cryptography - Introduction, challenges, solutions". en. In: (), p. 28.

[11] Hoi-Kwong Lo et al. "Measurement-device-independent quantum key distribution". In: *Phys. Rev. Lett.* 108.13 (Mar. 2012). arXiv: 1109.1473, p. 130503. ISSN: 0031-9007, 1079-7114. DOI: 10.1103/PhysRevLett.108.130503.

[12] Stefano Pirandola et al. "Fundamental Limits of Repeaterless Quantum Communications". en. In: *Nat Commun* 8.1 (Apr. 2017). arXiv: 1510.08863, p. 15043. ISSN: 2041-1723. DOI: 10.1038/ncomms15043.

[13] Chip Elliott et al. "Current status of the DARPA Quantum Network". en. In: (Mar. 2005).

[14] M Peev et al. "The SECOQC quantum key distribution network in Vienna". en. In: *New Journal of Physics* 11.7 (July 2009), p. 075001. ISSN: 1367-2630. DOI: 10.1088/1367-2630/11/7/075001.

[15] FangXing Xu et al. "Field experiment on a robust hierarchical metropolitan quantum cryptography network". en. In: *Chin. Sci. Bull.* 54.17 (Sept. 2009), pp. 2991–2997. ISSN: 1861-9541. DOI: 10.1007/s11434-009-0526-3.

[16] M. Sasaki et al. "Field test of quantum key distribution in the Tokyo QKD Network". EN. In: *Opt. Express, OE* 19.11 (May 2011). Publisher: Optical Society of America, pp. 10387–10409. ISSN: 1094-4087. DOI: 10.1364/OE.19.010387.

[17] Samuel L. Braunstein and Stefano Pirandola. "Side-channel-free quantum key distribution". In: *Phys. Rev. Lett.* 108.13 (Mar. 2012). arXiv: 1109.2330, p. 130502. ISSN: 0031-9007, 1079-7114. DOI: 10.1103/PhysRevLett.108.130502.

[18] Ronald Broeke and Xaveer Leijtens. *Nazca-design*. en-GB.

[19] E. A. J. M. Bente. *Photonic Integrated Circuit Simulator*. it.

[20] Charles H. Bennett. "Quantum cryptography using any two nonorthogonal states". en. In: *Physical Review Letters* 68.21 (May 1992), pp. 3121–3124. ISSN: 0031-9007. DOI: 10.1103/PhysRevLett.68.3121.

[21] L.G. Kazovsky and O.K. Tonguz. "ASK and FSK coherent lightwave systems: a simplified approximate analysis". In: *J. Lightwave Technol.* 8.3 (Mar. 1990), pp. 338–352. ISSN: 07338724. DOI: 10.1109/50.50731.

[22] V.S. Grigoryan et al. "Nonlinear Penalty Reduction of RZ-DBPSK Versus RZ-OOK Modulation Format in Fiber Communications". In: *2002 28TH European Conference on Optical Communication*. Vol. 3. Sept. 2002, pp. 1–2.

[23] S.O. Popescu et al. "QPSK Modulator on FPGA". en. In: *2011 IEEE 9th International Symposium on Intelligent Systems and Informatics*. Subotica, Serbia: IEEE, Sept. 2011, pp. 359–364. ISBN: 978-1-4577-1975-2. DOI: 10.1109/SISY.2011.6034353.

[24] F. Derr. "Optical QPSK homodyne transmission of 280 Mbit/s". en. In: *Electron. Lett.* 26.6 (1990), p. 401. ISSN: 00135194. DOI: 10.1049/el:19900262.

[25] Taofiq K. Paraïso et al. "A modulator-free quantum key distribution transmitter chip". en. In: *npj Quantum Information* 5.1 (Dec. 2019), p. 42. ISSN: 2056-6387. DOI: 10.1038/s41534-019-0158-7.

[26] P. Sibson et al. "Chip-based quantum key distribution". en. In: *Nature Communications* 8.1 (Apr. 2017), p. 13984. ISSN: 2041-1723. DOI: 10.1038/ncomms13984.

[27] Ivan P. Kaminow. "Optical Integrated Circuits: A Personal Perspective". en. In: *J. Lightwave Technol.* 26.9 (May 2008), pp. 994–1004. ISSN: 0733-8724. DOI: 10.1109/JLT.2008.922149.

[28] S.C. Nicholes et al. "An 8$\,\times\,$8 InP Monolithic Tunable Optical Router (MOTOR) Packet Forwarding Chip". en. In: *J. Lightwave Technol.* 28.4 (Feb. 2010), pp. 641–650. ISSN: 0733-8724, 1558-2213. DOI: 10.1109/JLT.2009.2030145.

[29] *About openEPDA — openEPDA™ documentation*. https://openepda.org/about.html.

[30] epixfabe. *Home*. en-US. https://epixfab.eu/.

[31] Xaveer Leijtens and COBRA Research Institute. "JePPIX: the platform for InP-based photonics". en. In: (), p. 3.

[32] *Nazca-design*. en-GB. https://nazca-design.org/.

[33] S. Pirandola et al. "Advances in quantum cryptography". en. In: *Advances in Optics and Photonics* 12.4 (Dec. 2020), p. 1012. ISSN: 1943-8206. DOI: 10.1364/AOP.361502.

[34] W. K. Wootters & W. H. Zurek. *A single quantum cannot be cloned | Nature*.

[35] Peter W. Shor and John Preskill. "Simple Proof of Security of the BB84 Quantum Key Distribution Protocol". In: *Phys. Rev. Lett.* 85.2 (July 2000). arXiv: quant-ph/0003004, pp. 441–444. ISSN: 0031-9007, 1079-7114. DOI: 10.1103/PhysRevLett.85.441.

[36] Tobias Heindel et al. "Quantum key distribution using quantum dot single-photon emitting diodes in the red and near infrared spectral range". en. In: *New J. Phys.* 14.8 (Aug. 2012). Publisher: IOP Publishing, p. 083001. ISSN: 1367-2630. DOI: 10.1088/1367-2630/14/8/083001.

[37] B. Huttner et al. "Quantum Cryptography with Coherent States". In: *Phys. Rev. A* 51.3 (Mar. 1995). arXiv: quant-ph/9502020, pp. 1863–1869. ISSN: 1050-2947, 1094-1622. DOI: 10.1103/PhysRevA.51.1863.

[38] Norbert Lütkenhaus. "Security against individual attacks for realistic quantum key distribution". In: *Phys. Rev. A* 61.5 (Apr. 2000). arXiv: quant-ph/9910093, p. 052304. ISSN: 1050-2947, 1094-1622. DOI: 10.1103/PhysRevA.61.052304.

[39] Valerio Scarani et al. "Quantum cryptography protocols robust against photon number splitting attacks for weak laser pulses implementations". In: *Phys. Rev. Lett.* 92.5 (Feb. 2004). arXiv: quant-ph/0211131, p. 057901. ISSN: 0031-9007, 1079-7114. DOI: 10.1103/PhysRevLett.92.057901.

[40] Xiongfeng Ma et al. "Practical decoy state for quantum key distribution". en. In: *Physical Review A* 72.1 (July 2005), p. 012326. ISSN: 1050-2947, 1094-1622. DOI: 10.1103/PhysRevA.72.012326.

[41] Yi Zhao et al. "Experimental Quantum Key Distribution with Decoy States". In: *Phys. Rev. Lett.* 96.7 (Feb. 2006). Publisher: American Physical Society, p. 070502. DOI: 10.1103/PhysRevLett.96.070502.

[42] Zhiliang Yuan et al. "10-Mb/s Quantum Key Distribution". EN. In: *J. Lightwave Technol., JLT* 36.16 (Aug. 2018). Publisher: IEEE, pp. 3427–3433.

[43] Alberto Boaron et al. "Secure Quantum Key Distribution over 421 km of Optical Fiber". In: *Phys. Rev. Lett.* 121.19 (Nov. 2018). Publisher: American Physical Society, p. 190502. DOI: 10.1103/PhysRevLett.121.190502.

[44] Cheng-Zhi Peng et al. "Experimental Long-Distance Decoy-State Quantum Key Distribution Based on Polarization Encoding". In: *Phys. Rev. Lett.* 98.1 (Jan. 2007). Publisher: American Physical Society, p. 010505. DOI: 10.1103/PhysRevLett.98.010505.

[45] Danna Rosenberg et al. "Long-Distance Decoy-State Quantum Key Distribution in Optical Fiber". In: *Phys. Rev. Lett.* 98.1 (Jan. 2007). Publisher: American Physical Society, p. 010503. DOI: 10.1103/PhysRevLett.98.010503.

[46] Z. L. Yuan et al. "Unconditionally secure one-way quantum key distribution using decoy pulses". In: *Appl. Phys. Lett.* 90.1 (Jan. 2007). Publisher: American Institute of Physics, p. 011118. ISSN: 0003-6951. DOI: 10.1063/1.2430685.

[47] Yin Zhen-Qiang et al. "Experimental Decoy State Quantum Key Distribution Over 120 km Fibre". en. In: *Chinese Phys. Lett.* 25.10 (Oct. 2008). Publisher: IOP Publishing, pp. 3547–3550. ISSN: 0256-307X. DOI: 10.1088/0256-307X/25/10/008.

[48] Qin Wang et al. "Experimental Decoy-State Quantum Key Distribution with a Sub-Poissionian Heralded Single-Photon Source". In: *Phys. Rev. Lett.* 100.9 (Mar. 2008). Publisher: American Physical Society, p. 090501. DOI: 10.1103/PhysRevLett.100.090501.

[49] A. R. Dixon et al. "Gigahertz decoy quantum key distribution with 1 Mbit/s secure key rate". EN. In: *Opt. Express, OE* 16.23 (Nov. 2008). Publisher: Optical Society of America, pp. 18790–18797. ISSN: 1094-4087. DOI: 10.1364/OE.16.018790.

[50] D. Rosenberg et al. "Practical long-distance quantum key distribution system using decoy levels". en. In: *New J. Phys.* 11.4 (Apr. 2009). Publisher: IOP Publishing, p. 045009. ISSN: 1367-2630. DOI: 10.1088/1367-2630/11/4/045009.

[51] Z. L. Yuan et al. "Practical gigahertz quantum key distribution based on avalanche photodiodes". en. In: *New J. Phys.* 11.4 (Apr. 2009). Publisher: IOP Publishing, p. 045019. ISSN: 1367-2630. DOI: 10.1088/1367-2630/11/4/045019.

[52] Yang Liu et al. "Decoy-state quantum key distribution with polarized photons over 200 km". EN. In: *Opt. Express, OE* 18.8 (Apr. 2010). Publisher: Optical Society of Amer-

ica, pp. 8587–8594. ISSN: 1094-4087. DOI: 10.1364/OE.18.008587.

[53] M. Lucamarini et al. "Efficient decoy-state quantum key distribution with quantified security". en. In: *Optics Express* 21.21 (Oct. 2013), p. 24550. ISSN: 1094-4087. DOI: 10.1364/OE.21.024550.

[54] Bernd Fröhlich et al. "Long-distance quantum key distribution secure against coherent attacks". EN. In: *Optica, OPTICA* 4.1 (Jan. 2017). Publisher: Optical Society of America, pp. 163–167. ISSN: 2334-2536. DOI: 10.1364/OPTICA.4.000163.

[55] Z. L. Yuan et al. "Directly Phase-Modulated Light Source". en. In: *Physical Review X* 6.3 (Sept. 2016), p. 031044. ISSN: 2160-3308. DOI: 10.1103/PhysRevX.6.031044.

[56] L. C. Comandar et al. "Quantum key distribution without detector vulnerabilities using optically seeded lasers". en. In: *Nature Photonics* 10.5 (May 2016), pp. 312–315. ISSN: 1749-4885, 1749-4893. DOI: 10.1038/nphoton.2016.50.

[57] Chaoxuan Ma et al. "Silicon photonic transmitter for polarization-encoded quantum key distribution". en. In: *Optica* 3.11 (Nov. 2016), p. 1274. ISSN: 2334-2536. DOI: 10.1364/OPTICA.3.001274.

[58] Philip Sibson et al. "Integrated silicon photonics for high-speed quantum key distribution". EN. In: *Optica, OPTICA* 4.2 (Feb. 2017). Publisher: Optical Society of America, pp. 172–177. ISSN: 2334-2536. DOI: 10.1364/OPTICA.4.000172.

[59] Darius Bunandar et al. "Metropolitan Quantum Key Distribution with Silicon Photonics". In: *Phys. Rev. X* 8.2 (Apr. 2018). Publisher: American Physical Society, p. 021009. DOI: 10.1103/PhysRevX.8.021009.

[60] Yunhong Ding et al. "High-dimensional quantum key distribution based on multicore fiber using silicon photonic integrated circuits". en. In: *npj Quantum Inf* 3.1 (June 2017). Bandiera_abtest: a Cc_license_type: cc_by Cg_type: Nature Research Journals Number: 1 Primary_atype: Research Publisher: Nature Publishing Group Subject_term: Fibre optics and optical communications;Integrated optics;Quantum information;Quantum optics Subject_term_id: fibre-optics-and-optical-communications;integrated-optics;quantum-

information;quantum-optics, pp. 1–7. ISSN: 2056-6387. DOI: 10.1038/s41534-017-0026-2.

[61] G. Zhang et al. "An integrated silicon photonic chip platform for continuous-variable quantum key distribution". en. In: *Nature Photonics* 13.12 (Dec. 2019), pp. 839–842. ISSN: 1749-4885, 1749-4893. DOI: 10.1038/s41566-019-0504-5.

[62] Kejin Wei et al. "High-Speed Measurement-Device-Independent Quantum Key Distribution with Integrated Silicon Photonics". en. In: *Physical Review X* 10.3 (Aug. 2020), p. 031030. ISSN: 2160-3308. DOI: 10.1103/PhysRevX.10.031030.

[63] HHI. *HHI design manual*.

[64] Carlos Gordón et al. "On-Chip Colliding Pulse Mode-locked laser diode (OCCP-MLLD) using multimode interference reflectors". en. In: *Opt. Express* 23.11 (June 2015), p. 14666. ISSN: 1094-4087. DOI: 10.1364/OE.23.014666.

[65] Zhixin Liu and Radan Slavik. "Optical Injection Locking: From Principle to Applications". en. In: *Journal of Lightwave Technology* 38.1 (Jan. 2020), pp. 43–59. ISSN: 0733-8724, 1558-2213. DOI: 10.1109/JLT.2019.2945718.

[66] Keisuke Kasai et al. "80 Gbit/s, 256 QAM coherent transmission over 150 km with an injection-locked homodyne receiver". en. In: *Opt. Express* 23.22 (Nov. 2015), p. 29174. ISSN: 1094-4087. DOI: 10.1364/OE.23.029174.

[67] Aaron Albores-Mejia et al. "Optical-Comb-Line Selection from a Low-Power/Low-OSNR Comb using a Low-Coherence Semiconductor Laser for Flexible Ultra-Dense Short Range Transceivers". en. In: *Optical Fiber Communication Conference*. Los Angeles, California: OSA, 2015, W2A.23. ISBN: 978-1-55752-937-4. DOI: 10.1364/OFC.2015.W2A.23.

[68] David S. Wu et al. "Optical Fourier synthesis of high-repetition-rate pulses". en. In: *Optica* 2.1 (Jan. 2015), p. 18. ISSN: 2334-2536. DOI: 10.1364/OPTICA.2.000018.

[69] R.A. York and T. Itoh. "Injection- and phase-locking techniques for beam control [antenna arrays]". In: *IEEE Trans. Microwave Theory Techn.* 46.11 (Nov. 1998), pp. 1920–1929. ISSN: 00189480. DOI: 10.1109/22.734513.

[70] Changzheng Sun et al. "Modulation Characteristics Enhancement of Monolithically Integrated Laser Diodes Under Mutual Injection Locking". In: *IEEE Journal of Selected Topics in Quantum Electronics* 21.6 (Nov. 2015). Conference Name: IEEE Journal of Selected Topics in Quantum Electronics, pp. 628–635. ISSN: 1558-4542. DOI: 10.1109/JSTQE.2015.2478817.

[71] A. Murakami et al. "Cavity resonance shift and bandwidth enhancement in semiconductor lasers with strong light injection". en. In: *IEEE J. Quantum Electron.* 39.10 (Oct. 2003), pp. 1196–1204. ISSN: 0018-9197. DOI: 10.1109/JQE.2003.817583.

[72] A. Jiménez et al. "Narrow-line external cavity diode laser micro-packaging in the NIR and MIR spectral range". en. In: *Appl. Phys. B* 123.7 (July 2017), p. 207. ISSN: 0946-2171, 1432-0649. DOI: 10.1007/s00340-017-6777-9.

[73] G Bosco et al. "On the Performance of Nyquist-WDM Terabit Superchannels Based on PM-BPSK, PM-QPSK, PM-8QAM or PM-16QAM Subcarriers". In: *J. Lightwave Technol.* 29.1 (Jan. 2011), pp. 53–61. ISSN: 0733-8724, 1558-2213. DOI: 10.1109/JLT.2010.2091254.

[74] G. P. Agrawal. *Fiber-optic communication systems*. Fifth edition. Wiley series in microwave and optical engineering. Hoboken, NJ: Wiley, 2022. ISBN: 978-1-119-73738-4 978-1-119-73737-7.

[75] Kohroh Kobayashi et al. "Invited: Novel Optical Methods for High Speed Direct Modulation of Semiconductor Lasers". In: *Jpn. J. Appl. Phys.* 15.S1 (Jan. 1976), p. 281. ISSN: 0021-4922, 1347-4065. DOI: 10.7567/JJAPS.15S1.281.

COLOPHON

This document was typeset using the typographical look-and-feel `classicthesis` developed by André Miede and Ivo Pletikosić. The style was inspired by Robert Bringhurst's seminal book on typography "*The Elements of Typographic Style*". `classicthesis` is available for both LaTeX and LyX:

`https://bitbucket.org/amiede/classicthesis/`

Final Version as of November 29, 2022 (1.0).

Universidade Vigo

" Low Loss InP Waveguides for Integrated Photonics - Amdrea Volpini

TESE DE DOUTORAMENTO

Low Loss InP Waveguides for Integrated Photonics

ANDREA VOLPINI

Ano: 2022

Universidade Vigo

ramento

Universidade Vigo
Escola Internacional de Doutoramento

Andrea Volpini

TESE DE DOUTORAMENTO

Low Loss InP Waveguides for Integrated Photonics

Dirixida polos doutores:

Dr. Francisco Javier Díaz Otero

Ano: 2022

International Doctoral School

Universidade Vigo

Escola Internacional de Doutoramento

Francisco Javier Díaz Otero

Declara que o presente traballo, titulado "*Low Loss InP Waveguides for Integrated Photonics*", que presenta Andrea Volpini para a obtención do título de Doutor, foi elaborado baixo a súa dirección no programa de doutoramento En Tecnoloxías da Información e as Comunicacións pola Universidade de Vigo

Vigo, 10 de xunio de 2022.

Os Directores da tese de doutoramento

Dr. Francisco Javier Díaz Otero

International Doctoral School

Contents

List of Figures

Chapter 1

Resumo

A maioría das innovacións tecnolóxicas que o mundo veu nos últimos 20 anos baséanse nunha revolución da microelectrónica que se remonta á década de 1970. Nesa década os circuítos integrados microelectrónicos experimentaron un enorme aumento da capacidade de produción e unha redución dos custos de realización. Isto foi posible grazas a unha reorganización das fundicions que operaban nese campo. Inicialmente, ditas fundicions encargábanse tanto do deseño como da produción dos circuítos integrados. Este enfoque é sostible cando os circuítos son simples con poucos compoñentes. Con todo, si a complexidade dos circuítos aumenta, é desexable que haxa unha separación entre estas dúas tarefas. De feito, con esta división algunhas fundicions poden especializarse no desenvolvemento e a optimización dos poucos compoñentes estándar dos circuítos integrados, mentres que outras empresas poden centrarse en como utilizar estes compoñentes para deseñar circuítos para as máis diversas aplicacións. É evidente que ao ter poucos compoñentes que se utilizan nunha gran variedade de circuítos, redúcense drasticamente os custos de investigación e desenvolvemento, xa que eses custos son compartidos e financiados por máis clientes. Tamén se reducen os custos de fabricación, xa que se poden utilizar as mesmas máquinas e pasos de produción para diferentes clientes sen apenas modificacións. Grazas a esta especialización, a producción de dispositivos microelectrónicos creceu exponencialmente, e os chips microelectrónicos convertéronse en algo fundamental na economía moderna. Hoxe en día, os circuítos integrados utilízanse na maioría das aplicacións, desde a informática ata a condución autónoma dos coches modernos, pasando polas telecomunicacións e as aplicacións médicas. Chegamos a un punto no que a produción de chips non pode seguir o ritmo da demanda mundial, polo menos para aplicacións específicas.

Aínda en 1969, S.E. Miller teorizó a posibilidade de fabricar chips fotónicos integrados (PIC). Os PIC poden pensarse en primeira aproximación como os

respectivos chips electrónicos nos que se utilizan fotóns en lugar de electróns. A luz de diferentes lonxitudes de onda xérase mediante un ou varios láseres, diríxese a través de guías de onda no chip e manipúlase con elementos como moduladores ópticos, amplificadores, rotadores de polarización, etc. Do mesmo xeito que na electrónica, os PICs permiten a miniaturización de aparellos que doutro xeito serían de gran tamaño e teñen o potencial de impactar en moitos campos diferentes. dadas estas similitudes moitos han teorizado para os PICs un crecemento similar ao experimentado pola microelectrónica. Si por unha banda isto parece plausible, doutra banda hai pescozos de botella tanto económicos como técnicos que deben superarse para que isto ocorra. O primeiro problema é a enorme fragmentación do mercado e a ausencia de estándares: a miúdo dise na literatura que: "hai case tantas tecnoloxías como aplicacións". Isto significa que cando un PIC deséñase e realiza para unha aplicación específica, require uns compoñentes peculiares deseñados á mantenta para esa aplicación. O resultado é que os custos de desenvolvemento e investigación dos compoñentes do circuíto non poden compartirse con outros clientes. Como consecuencia adicional, só os mercados o suficientemente grandes para soster estes custos poden investir e utilizar esta tecnología. Ademais destes problemas económicos, tamén existen algunhas limitacións tecnolóxicas.

O número de bloques de construción dun circuíto é unha boa estimación das capacidades do propio circuíto. Con todo, coas tecnoloxías actuais parece haber oun límite superior ao que se pode conseguir en termos de densidade de integración. Ter máis elementos activos nun PIC require ter máis conexións eléctricas para manexalos. Hai que evitar as interferencias ópticas e eléctricas e o mesmo ocorre co quecemento dos compoñentes do chip. Só coas novas tecnoloxías de produción pódense superar estes obstáculos, facendo que os PIC sexan máis máis potentes.

A pesar de todas estas dificultades, os PIC seguen sendo moi atractivos. O seu principal campo de aplicación segue sendo o mercado das telecomunicacións. Hoxe en día Internet apóiase nas fibras ópticas para transmitir información, e o volume de datos que se transmite aumenta cada ano. Xunto coas fibras ópticas hai outros elementos como os transmisores ópticos, os amplificadores e os receptores para dirixir o sinal óptico ao destino correcto. Todos estes elementos poden existir como obxectos individuais a granel, pero non é sorprendente telos integrados nun só chip de menos de 1cm2, o que reduce drasticamente o custo de construír, operar e manter unha rede óptica. Os PIC tamén se utilizan para aplicacións de detección: por exemplo, observando o cambio no índice de grupo ao longo dunha de grupo ao longo dunha fibra óptica é posible estimar a tensión á que está exposta. Si a fibra insérese na á dun avión obtense unha lectura das forzas que actúan sobre

a á e pode conducir a un mellor deseño das ás. Neste caso, a vantaxe de utilizar un PIC radica no escaso peso do este sensor comparado cun eléctrico que realice a mesma tarefa. Estes dous son só algúns dos moitos campos nos que se utilizan os PICs, outros son Biosensing, conexión de fibra ata o fogar, metrología, fotónica de microondas.

1.1 Introdución

As guías de onda de baixas perdas son necesarias para unha variedade de aplicacións como a detección, as liñas de retardo e a clave cuántica (distribución) QKD. Normalmente, cando se necesitan valores de perdas extremadamente baixos, as plataformas baseadas en silicio son as que mellor funcionan, con perdas tan baixas como $0,03 dB/cm$. Con todo, presentan un inconveniente principal: os compoñentes activos, como os láseres, os amplificadores, os detectores e os moduladores electroópticos non están dispoñibles nestas plataformas, o que limita a súa potencialidade. Unha alternativa son as plataformas baseadas en InP . A InP é un semiconductor de banda prohibida directa e permite a integración monolítica de compoñentes activos e pasivos no mesmo chip. Isto elimina a necesidade dunha fonte de luz externa, o que fai que o produto final sexa máis lixeiro, pequeno e barato. Con todo, en comparación co Si, as perdas son da orde de $2 - 4 dB/cm$. Podemos identificar tres fontes principais de perdas: as perdas intrínsecas, a rugosidade da superficie e as perdas por dopaxe. As perdas intrínsecas están relacionadas co índice de refracción da InP, non se pode facer moito para controlar esta contribución, pero é importante ter un material libre de defectos para evitar que estas perdas sexan aínda maiores. Con diferentes técnicas de litografía, as paredes das guías de onda poden facerse lisas (ou mesmo eliminarse nas guías de onda en tira), reducindo así a rugosidade como fonte de perdas. Na miña tese centrareime nas perdas inducidas pola presenza de átomos dopantes.

1.2 SMART Photonics

Para entender o meu traballo é necesario primeiro ter unha idea xeral de como funciona a plataforma de fotónica SMART Photonics. SMART Photonics é unha fundición puramente dedicada á produción de PICs que traballan a 1550 nm. Partindo dunha oblea de InP cultívanse diferentes capas de InP , InGaAsP e InGaAs. Estas capas teñen diferentes propiedades optoelectrónicas e forman a chamada pila de capas. A través de diferentes procesos de gravado e pasos posteriores, os elementos ópticos, como o láser, os detectores, os

moduladores e as guías de onda, distribúense no chip creando un circuíto integrado fotónico. Podemos identificar tres capas principais: o substrato, o núcleo e a capa superior. A capa do núcleo é onde se propaga o modo óptico e está feita da aliaxe cuaternaria InGaAsP. A relación de concentración do catro elementos controla o bandgap do semiconductor e permite a xeración de luz a nivel do chip. A capa superior serve de espazador entre as conexións metálicas e a capa do núcleo que, doutro xeito, sufriría grandes perdas. O máis difícil á hora de establecer as propiedades das capas é obter unha pila de capas que sexa óptima para todos os compoñentes dispoñibles. Isto non sempre é posible e ás veces hai que facer concesións. O principal refírese a a concentración de dopante na capa de revestimento. Na seguinte sección veremos como a dopaxe é necesaria para mellorar as conexións eléctricas e o rendemento dos compoñentes activos, pero tamén como afecta as perdas.

1.3 A dopaxe e o seu impacto

A dopaxe ten un impacto en varios elementos do PIC e a elección do perfil de dopaxe óptimo para a pila de capas implica moitas compensacións. Cando unha capa dopada con p crece sobre unha capa dopada con n, créase unha unión pn. As unións pn (para ser máis precisos, unións Pin) son fundamentais para ter amplificadores ópticos de semiconductores (SOA) e desplazadores de fase (PH). Os SOA explotan a emisión estimulada para amplificar unha fonte de luz, isto é posible cando se crean pares de ocos de electróns nun semiconductor e se recombinan cando son estimulados por unha fonte de luz entrante. Unha unión Pn con polarización positiva permite inxectar portadores e amplificar a luz. A dopaxe afecta directamente o número de portadores inxectados porque afecta á resistencia do semiconductor. A resistividad do InP pode calcularse mediante as fórmulas:

$$\rho_n = 10^{-0.918log(n)+13.88}[\Omega cm] \tag{1.1}$$

$$\rho_p = 10^{-0.971log(p)+16.19}[\Omega cm] \tag{1.2}$$

Onde ρ_n é válido para o InP dopado negativamente e ρ_p para o dopado positivamente. Vemos que unha maior concentración de dopaxe dá lugar a unha menor resistencia, isto é bastante beneficioso para o rendemento da SOA porque está a levar a unha baixa voltaxe de condución, baixa disipación de enerxía e menos ruído termoeléctrico. Os PHS tamén se benefician da dopaxe: Os PHS funcionan grazas aos efectos electro-ópticos inducidos por unha unión de pines con polarización inversa. En efecto, o investimento da polarización crea un esgotamento da carga nas interfaces dos semiconductores que conduce á creación dun campo eléctrico. Estes campos eléctricos,

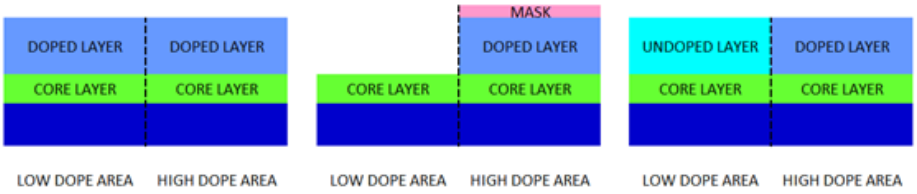

Figure 1.1

xunto co esgotamento da carga, inducen un cambio no índice de refracción do material que pode aproveitarse para cambiar a fase dun modo óptico que se propague no dispositivo. Para ter un dispositivo eficiente, a rexión de esgotamento da unión debe superporse o máis posible co modo óptico para maximizar o cambio no índice de refracción. Obtense un bo solapamiento entre o modo óptico e o campo eléctrico cando a fronte de depleción de p atópase no bordo do núcleo da guía de ondas.

Unha figura de mérito crave para os PHS é V_π, definida como a tensión que crea un desprazamento de fase igual a π en comparación co PHS non nesgado. Ter V_π baixo é crucial para unha modulación rápida do PHS porque é máis fácil de conseguir polo sinal de condución de RF. Do mesmo xeito que na SOA, a dopaxe reduce a resistencia do semiconductor ao diminuír V_π. Ademais, obtéñense fortes efectos electroópticos coa dopaxe, o que permite que os PHS ocupen menos espazo. Con todo, a dopaxe ten un inconveniente: aumenta as perdas ópticas do InP. Estas perdas débense á absorción da banda de intervalo e caracterizáronse na literatura. Ata o de agora, non había ningún método eficaz que limitase a dopaxe á pila de capas de elementos activos. Por tanto, o revestimento dopado utilízase ao longo de toda a oblea aumentando as perdas dos elementos pasivos tamén. Na seguinte sección describo como se pode localizar a dopaxe só onde sexa necesario.

1.4 Técnica de butt-joint e simulacións de rendemento.

A técnica Butt-joint permite ter diferentes pilas de capas no mesmo chip crecendo e gravando selectivamente porcións da oblea. Na Figura 1.1 vemos como se fai. As capas cultívanse epitaxialmente no substrato da oblea ata unha altura predeterminada. A continuación, deposítase unha máscara dura na superficie da oblea e, mediante fotolitografía, ábrese onde queremos facer crecer unha capa diferente. A continuación, grávase o semiconductor e, coa

máscara dura aínda no seu lugar, cultívanse nuevo capas ata a altura das capas depositadas anteriormente. Despois destes pasos, as capas compartidas restantes poden crecer en todo o chip. A unión non é unha técnica nova e xa está implementada na plataforma para diferenciar a capa central de activos e pasivos. Con todo, por primeira vez realicei un butt-joint nas capas de revestimento das obleas para confinar a dopaxe só na rexión activa, reducindo así considerablemente as perdas. O impacto nas perdas desta técnica simulouse co software comercial Lumerical: reproduciuse a pila de capas utilizada en SMART e realizáronse diferentes simulacións con diferentes grosores da xunta. Na figura 1.2a, a liña azul representa os resultados da simulación. Da simulación despréndese que un espesor de 1200nm é óptimo para reducir as perdas nos seus mínimos. Cabe mencionar que a rugosidade da superficie non se pode simular de forma efectiva.

1.5 Resultados

Na figura 1.2b, á esquerda, informamos da perda da medida. Os puntos vermellos son os datos experimentais obtidos. A liña continua azul foi xerada con Lumerical . Os resultados non son os esperados xa que o comportamento simulado non é reproducido polos datos. Ademais, a oblea A (a que ten a pila de capas antiga) é a que ten menores perdas. Con todo, si observamos o gráfico da dereita da Figura 1.2b na oblea B e na oblea C, onde se realizou o butt-joint, vemos que, como era de esperar, as guías de onda cunha rexión de alta dopaxe máis longa experimentan maiores perdas e que a dita contribución aumenta linealmente cando se incrementa a lonxitude da illa de alta dopaxe.

1.6 Investigación errada

Disponer dunha segunda unión de boa calidade é fundamental para mellorar o rendemento dos dispositivos. Para avaliar a bondade da nosa unión, fabricamos dúas obleas cun grosor de xunta de 1200nm. Unha das obleas, con todo, só se fabricou parcialmente. Despois do recrecemento da capa non dopada, a oblea dividiuse en dúas metades. Unha metade mantívose separada (mostra A) mentres que a segunda metade someteuse ao recrecimiento das capas superiores finais (mostra B). Nas figuras 1.3b e 1.3c móstranse dúas imaxes da (mostra A) tomadas co microscopio electrónico. Vemos que a superficie da oblea non é plana e dúas protuberancias están presentes. Este é o coñecido efecto das orellas de coello.

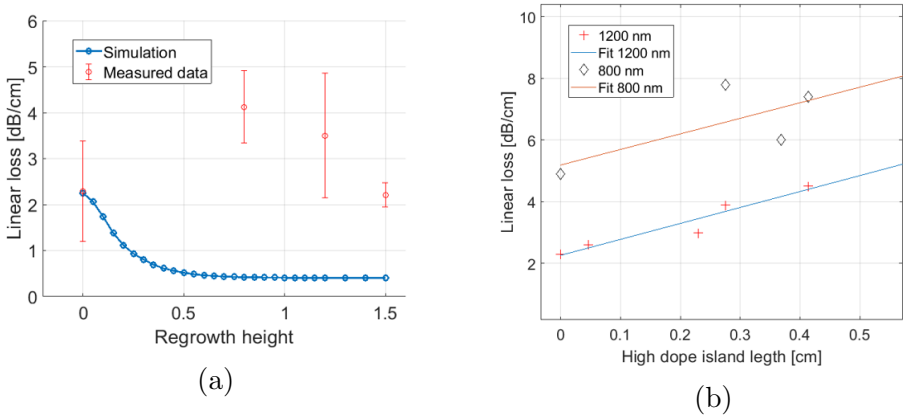

(a) (b)

Figure 1.2

A protuberancia ten unha altura de 700nm. Cando se depositan as capas superiores na mostra B (Figura 1.3d e Figura 1.3e), estes defectos son máis grandes, ata 1940nm. Na Figura 1.3a vemos unha vista superior destas estruturas. O que ocorre é que as capas superiores crecen, as rexións adxacentes á máscara mostran un aumento da taxa de crecemento de InP . O efecto de mellora local pode ser crítico por varias razóns. As topologías da superficie poden impedir unha propagación uniforme do material fotorresistente. Cando o espesor da capa fotorresistente non é uniforme, isto pode dar lugar a unha exposición insuficiente ou excesiva e a unha litografía deficiente dos compoñentes ópticos. Outro inconveniente é que a irregularidade producida nos planos cristalinos podería interactuar cos modos próximos, creando perdas adicionais e dispersión, afectando as prestacións ópticas.

Unha topoloxía irregular da oblea tamén pode actuar como punto de partida para a fractura das capas de pasivación de sílice. Un enfoque para limitar estes defectos consiste en utilizar produtos químicos específicos de gravado en húmido para crear a chamada socavación. A técnica de socavación consiste en eliminar parte do semiconductor por baixo da máscara dura utilizada para definir os puntos de alta densidad. Isto crea literalmente un oco debaixo da máscara que se enche co exceso de material durante a epitaxia. Dado que o exceso de material depositase na focha, evítase o efecto SAG.

1.7 Superficies da guía de onda

A oblea A pasou por menos pasos de procesamento en comparación coas demais obleas e ten o valor máis baixo de perda: isto suxire que temos que

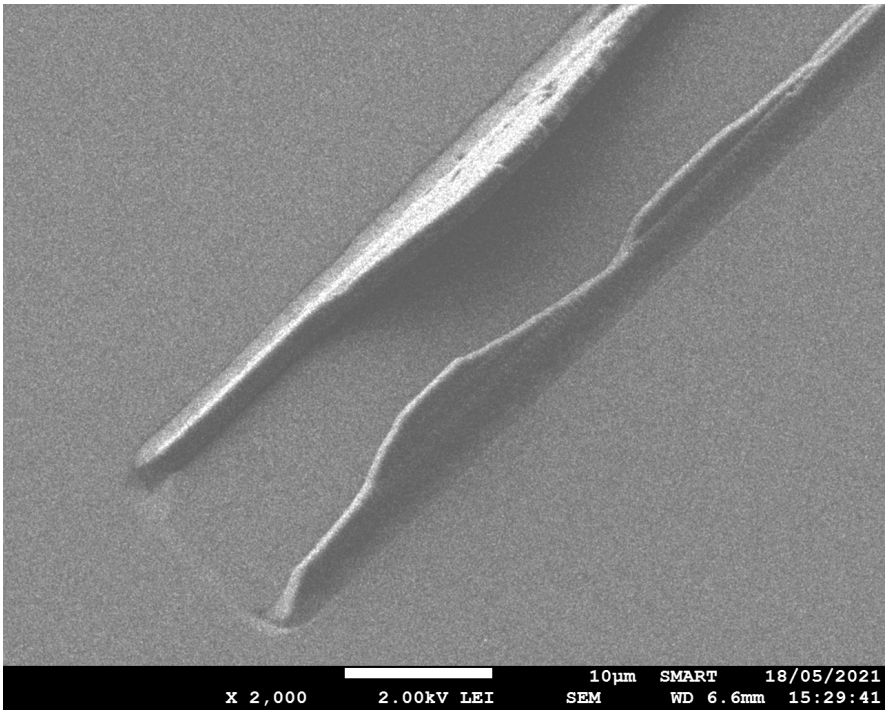

(a)

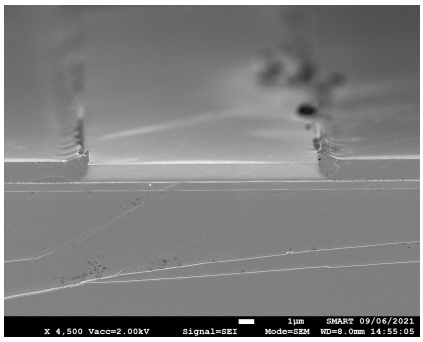

(b)

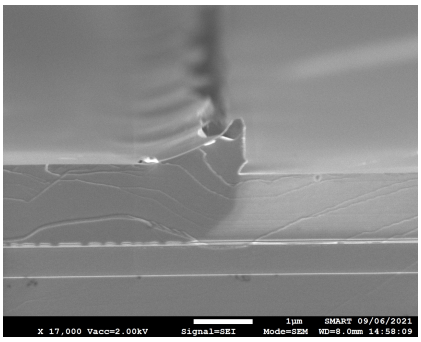

(c)

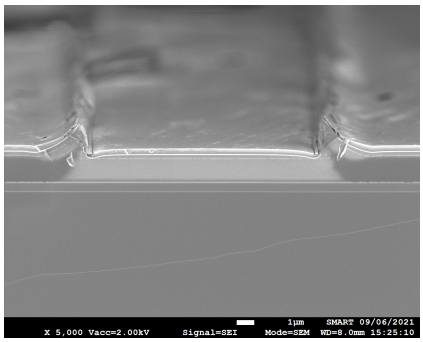

(d)

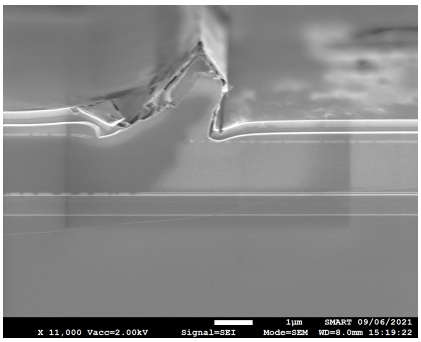

(e)

Figure 1.3

investigar e optimizar o esquema de integración da nosa unión. A figura 2b demostra que a dopaxe ten un impacto nas perdas e que o método presentado pode reducir este impacto. Ademais, vemos que a oblea C ten de media maiores perdas que a oblea D. Isto é coherente coa idea de que ter a dopaxe lonxe do núcleo reduce as perdas da guía de onda. As imaxes SEM das obleas D,C,B (Figura 1.4, 1.5, 1.6) explican, polo menos parcialmente, por que non se obtivo ningunha mellora. As obleas C e B presentan unha liña (frecha) a diferentes alturas ao longo das paredes laterais da guía de onda. A altura da liña é compatible coa altura dos chanzos da xunta de tope reengranada. Dita liña non está presente na oblea D na que non se realizou ningunha xunta. Pódese intuír que polo menos parte destas perdas adicionais débense a este nova interfaz creada pola xunta a lume de biqueira, e que aumentan considerablemente as perdas.

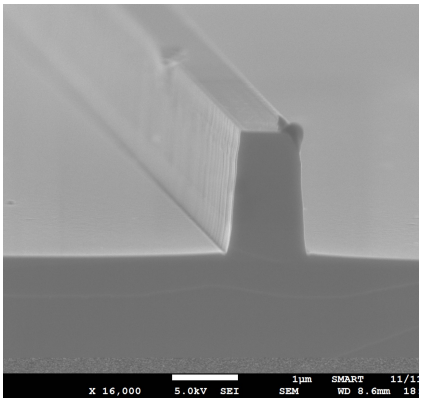

Figure 1.4

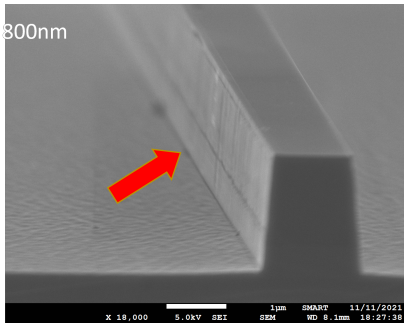

Figure 1.5

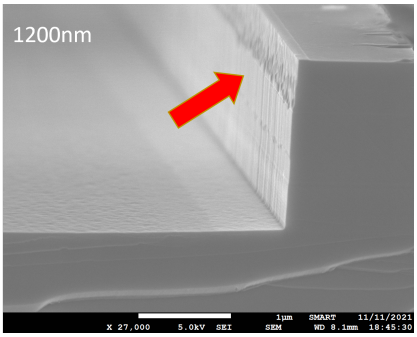

Figure 1.6

1.8 Conclusión

A redución das perdas dos compoñentes pasivos mediante a integración da segunda xunta demostrou ser un reto. Na figura XXX vimos que a primeira implementación non tivo éxito. Con todo, coa figura YYY puidemos demostrar unha vez máis que a dopaxe ten un impacto significativo nas perdas e que restrinxir o seu uso cando sexa necesario é fundamental para mellorar o rendemento da plataforma. No mesmo capítulo amosamos como se poden medir eficazmente as perdas de resonadores en anillo, e como o uso de resonadores en anillo de diferentes lonxitudes permiten extraer a perda de inserción da MMI. A estabilidade e sintonización do láser é fundamental para obter medidas fiables, non obstante a resposta foi a esperada e o método é válido tanto para fontes láser integradas ou externas. Tamén establecemos un nuevo esquema de gravado húmido para limitar o efecto das orellas de coello. A solución de acedo sulfúrico resultou ser a máis eficaz para limitar o fenómeno. Para concluír, presentamos un nuevo método para crear unha guía de ondas de baixas perdas na plataforma de integración fotónica InP de Smart Photonics. As perdas medidas son maiores do esperado, pero poden estar relacionadas coa migración de dopaxe e a rugosidade adicional creada pola interacción dos nuevo pasos do proceso e o gravado. É necesario seguir optimizando o esquema de integración, pero unha vez optimizado, este método dará lugar a compoñentes pasivos con menores perdas.

Chapter 2

Introduction

Most of technological innovations the world has seen in the last 20 years relay on a revolution in microelectronic dating back to the 1970s. In that decade microelectronic integrated circuit went through a tremendous increase in production capability and a reduction in realization costs [1]. This was possible thanks to a reorganization of foundries operating in that field. Initially such foundries were responsible both for the design and production of integrated circuits. This approach is sustainable when circuits are simple with few components. However, if circuits complexity increases, it is desirable to have a separation between these two tasks. Indeed, with such division some foundries can specialize in developing and optimizing the few standard components of integrated circuits, while other companies can focus on how to use such components to design circuits for the most various applications. It is evident that having few components that are used in a wide variety of circuits, reduces the research and development cost drastically since those costs are shared and financed by more customers. Fabrication costs are reduced as well since same machines and production steps can be used for different clients with little to no modifications. Thanks to such specialization, production of microelectronic devices has grown exponentially and microelectronic chips have become fundamental in modern economy. Nowadays integrated circuit are used in most different application ranging from informatics to modern cars autonomous driving, from telecommunication to medical application. We have now reached the point where chip production cannot keep up with global marked demand at least for specific applications [2].

Still in 1969, S.E. Miller [3] theorized the possibility of fabricating photonic integrated chips (PICs). PICs can be in first approximation thought as the respective of electronic chips where photons are used in place of electrons [4]. Light at different wavelength is generated by one or more lasers, it is routed through waveguides on the chip and it is manipulated with element

such as optical modulators, amplifiers, polarization rotator etc. Like in electronics, PICs allow for the miniaturization of otherwise large apparatus and has the potential to impact in many different fields. given these similarities many have theorized for PICs a growth similar to the one undergone by microelectronic [1]. If on one hand these seems plausible, on the other hand there are both economical and technical bottlenecks that must be overcome for this to happen.

First problem is the huge fragmentation of the market and the absence of standards: it is often said in literature that "there are almost as many technologies as applications" [5]. These means that when a PIC is designed and realized for a specific application, it requires some peculiar components designed on purpose for that application. The result is that the costs of developing and researching the building blocks of the circuit cannot be shared with other customers. As a further consequence only markets big enough to sustain such costs can invest and use this technology. Beside these main economical problem there are in prospect some technological limitations too. The number of building blocks on a circuit is a good estimation of the capabilities of the circuit itself. However, with current technologies there seems to be an upper limit to what is achievable in terms of integration density. Having more active elements on a PIC requires to have more electrical connections to drive them. Optical and electrical cross talk must be avoided and the same goes for thermal heating of chip components. Only with new production technologies these obstacles can be overcome, making PICs more powerful.

Despite all these difficulties, PICs are still extremely attractive. Their main field of application remains in telecommunication market. Nowadays internet relays on optical fibres for transmitting information, with the volume of data transmitted increasing every year. Together with optical fibres other elements such as optical-transmitters, -amplifiers and -receivers are required to route optical signal to the correct destination. All these elements could exist as individual bulk objects, but not surprisingly having them integrated on a single chip smaller $1cm^2$ drastically reduces the cost of building, operating and maintaining an optical network. PICs are also used for sensing applications: for instance by looking at the change in group index along an optical fiber is possible to estimate the tension stress at which the fiber is exposed. If the fiber is inserted in the wing of a plane these gives a readout of the forces acting on the wing and can lead to better wings designs [6]. In this case the advantage of using a PICs comes in the small weight of such sensor compared to an electrical one performing the same task. These two are only some of the many fields where PICs are used, others are Biosensing [7], fiber to home connection, metrology, microwave photonics [8]

2.1 State of the art

As explained in this introduction, we understood that having few integration technologies with few standardized components is the key to open PICs production to new markets and lower production prices. In the last 15 years progress have been made in these direction with the development of few integration platforms. I will now present some of this platforms, that are currently state of the art in this field: TripleX, HHI and SMART Photonics. Table 1.1 will summarize the comparison. However before starting is better to first introduce some terminology:

- Layer stack: we refer to a series of layers of materials such as $SiNx$, $SiOx$, InP, $InGaAs$, $InGaAsP$ epitaxially grown on top of each other. Each layer can be characterized by different physical properties such as resistivity, doping, refractive index and others.
- Active components: this are all the elements in an optical circuit that require an electrical connection to operate. Examples are: modulators, lasers, photodiodes.
- Passive components: this are all the elements in an optical circuit that do NOT an electrical connection to operate. Examples are: waveguides, mmi, couplers.
- Doping: the act of adding impurities (atoms) to a semiconductor to change is electrical properties.
- Substrate-, Core-, Cladding- layer: substrate layers are the first layers grown on the wafer. They can be negatively doped. On top of those the corelayer is where light is confined or generated when propagating along the circuit. Really often it has the highest refractive index compared to substrates and top layers. Cladding layer: this is used as a spacer between the core layer and the metal connections necessary for active components to operate.

2.1.1 TriPleX

The first platform we are going to present is $TriPleX^{TM}$. In this platform different layers of stochiometric silicon oxide and silicon nitride are deposited on a silicon wafer. It is well known that such materials do not allow for direct integration of lasers and amplifiers. This is because silicon is an indirect semiconductor, that implies that stimulated emission is less probable to occur thus preventing the realization of active components. There has been

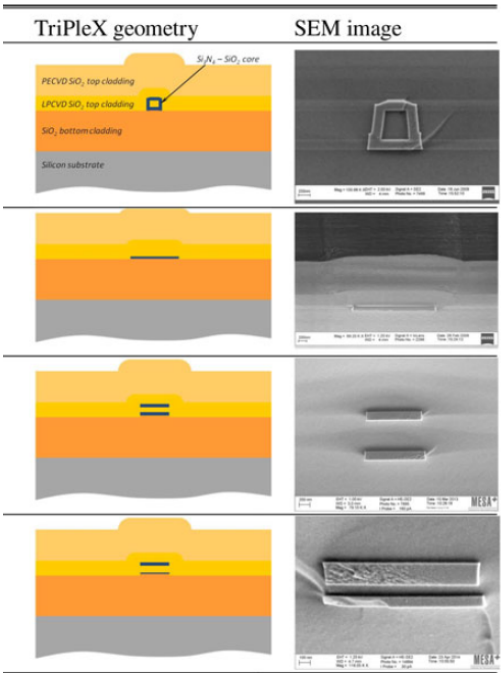

Figure 2.1: Typologies of waveguides availabale in the TriPleX platform [9].

attempts to force the crystallographic structure of silicon into a different configuration to obtain a direct semiconductor [10], but this technology is not mature yet.

Let us now present the building blocks available in the platform. Four types of waveguides as shown in Figure 2.1 are available. First waveguide is the $BoxShell$ where $SiOx$ is the core of the waveguide buried in Si_3N_4. This comes in two configurations that guarantee high index contrast for devices where small radius of curvature is needed. An interesting feature is the possibility to counterbalance polarization dispersion caused by material by changing the shape of the box.

The Second configuration is a single stripe of Si_3N_4 whose main purpose it to reduce propagation losses at the minimum value. The mode is weekly confined by a single Si_3N_4 stripe. Given the low confinement it does not suffer from optical scattering due to the absence of sidewalls. The losses can be as low as $0.007dB/cm$ [11]. However, the low confinement has the drawback to require big radius of curvature ($2000\mu m$) when bends along the waveguide are necessary limiting the optical components density. To ensure an higher confinement double waveguides are used in two possible configurations.

These configurations are the symmetric and antisymmetric double striped waveguide. As the name suggests two stripes of Si_3N_4 core layers are used one of top of each other. The two stripes can be identical in size (symmetric configuration) and separated by $500nm$ or the top one can be smaller and closer($100nm$) to the lower one (antisymmetric configuration). The thickness of the upper waveguide can be controlled to reduce the minima radius of curvatures required for bends on the platform. Once done the bend the waveguide can be tapered to zero to go back to the single striped configuration with extreme low loss.

Last three element available in the platforms are spot size converters splitters/couplers and phase modulators based on heating. Despite the lack of active components, the platform is used for a range of interesting applications in different fields: Microwave-photonics, Optical Coherence Tomography and MR sensing system [12].

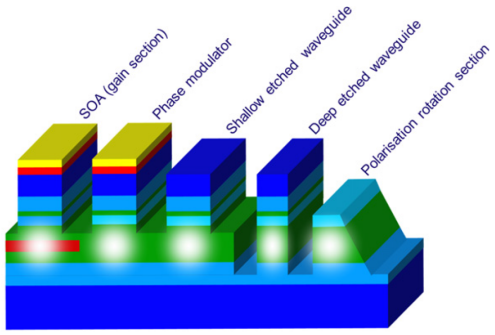

Figure 2.2: A schematic view of optical elements and their layer stack available in SMART Photonics [4].

2.1.2 SMART Photonics

SMART Photonics is an InP Based platform. Opposite to silica, InP is a direct band structure semiconductor and this is its main strength [13]. With a direct band structure, is possible to have stimulated emission and therefore is possible to have a laser on chip level. The building blocks of the platform are designed for working in the C-band ($1530 - 1565nm$), but research is done to extend platform capabilities to other wavelengths. Wafer production works as following. Starting from a substrate, different layers of InP, InGaAsP and InGaAs are grown. These layers have different optoelectronic properties and form the layer stack. Trough different fabrication steps, optical elements such as laser, detectors, modulators and waveguides are pattered in the chip

creating a PIC. In Figure 2.2 is reported the layer stack of most relevant building blocks in the platform. The green layer is made of the quaternary alloy InGaAsP. The concentration ratio of the four elements controls the semiconductor bandgap and refractive index and allows for guiding light at chip level. Red layers are also made of $InGaAsP$, but with different bandgap and they are used for light generation in active elements. The top layer serves has a spacer between metal connections and the core layer that would otherwise suffer from high loss. Different shades of blue represent layers of InP with different doping concentration. Yellow layers are of $InGaAs$ and are used for electrical connections.

A trade off in the layer stack structure is needed to make all the components available. One of the most important aspect to discuss is choosing the dopant concentration in the cladding layers. In the next chapter we explain how this doping is necessary for good electrical connections and excellent performances of active components.The first building block displayed on the left is the semiconductor optical amplifier (SOA). The mode is confined in the core layer (green) and cladding layers allow for electrical pumping. The red layer allows for stimulated emissions of photons. Next building block is the phase modulator: here a reverse bias is applied and trough electro optical effects the phase of the signal is changed. The platform also has two types of waveguides: shallow and deep. Shallows have lower losses but also lower confinement, while deep on the opposite have higher loss and higher confinement. It is up to the designer chose the one that best fits the application. The polarization converter block is still under optimization in the platform and will allow to change the polarization of the optical propagating mode. A Last building block not display in the picture is the photodetector, that allows to measure optical powers. We have seen how this platform has more building blocks compare to $TripleX$. However, as it will be explained later on with more details in this thesis, InP is has higher losses compared to Si_3N_4 and this limits the applications and performances of this technology.

2.1.3 HHI

HHI is another platform based in Berlin that manufactures InP chips. It is interesting to notice that despite using the same materials as SMART photonics it has a different layer stack and integration strategy [15]. From Figure 2.3 we understand the philosophy of this platform. In the layer stack four layers made of the quaternary alloy InGaAsP(Q) are present. The upper layer however is the only one effectively used as core layer. The lower three are used to expand the mode and allow for a more efficient coupling thanks to a spot size converter device. The platform as can be seen from the lower

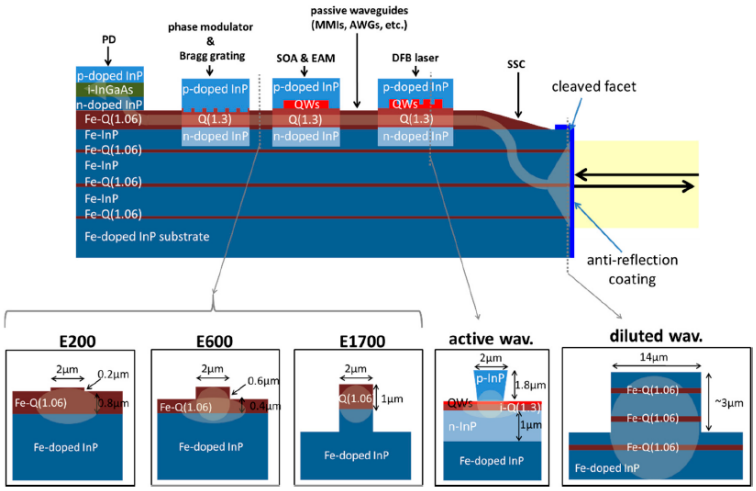

Figure 2.3: A schematic view of the layer stack used at HHI [14].

part of Figure 2.3 has three different types of waveguides with different index contrast. This is obtained by using three different etch depths. As in smart there are active elements such as laser and phase shifter, moreover a spot size converter is present allowing for an easy coupling.

	TriPleX	HHI	SMART Photonics
Waveguide loss	0.1 dB/cm	2 dB/cm	3 dB/cm
Spotsize loss	0.5 dB	2 dB	In develop
Bending radius	150μm	250 μm	100 μm
SOA gain	×	40 dB/cm	30 dB/cm
PD 3dB bandwith	×	45Ghz	30 Ghz

Table 2.1: Comparison of the three different platforms

2.2 Thesis motivation

From Table 1.1 we see that the main advantage of using silicon materials based platform are the lower losses. InP based chips on the other hand allows for active components directly integrated in the platform at the price of higher losses. Reducing loss is potentially beneficial for applications like sensing [16], delay lines [17], metrology and many more. An example is

the integrated wavelengthmeter that will be discussed in Chapter 6 of this thesis. There is a specific field however where having low loss is fundamental that is Quantum Key Distribution (QKD). QKD is a field of research that deals with communicating keys for encrypting sensible information. In QKD information is codified in quantum states of single photons. Two people (Alice and Bob) can exchange information by exchanging single photons one to each other. To do so they both need an emitter and a transceiver. For this purpose phonics integrated chips are perfect since the permit to generate and detect such photons. Some photons however will be lost in the receiver chip because of scattering and absorptions. If to many phothons get lost it becomes impossible to exchange information. The intrinsic losses of a platform are thus fundamental to work with this technology, when to high they can exclude a platform from this market. For instance we see in [18] that losses of 0.5dB/cm are acceptable for the application, while 2dB/cm is defenetly to high.

So, we understand that losses are critical in many applications of PICs. My Phd work consists precisely in identifying a production method capable of reducing losses in SMART Photonics foundry, making the platform more attractive and suitable for new applications and offer better performances. Obtaining the same level losses as in Silicon based platform is currently impossible, but there is the possibility of reducing current losses considerably. A first study on reducing losses at smart photonics has been done by Domenico Dagostino in his thesis *Capability extensions to the COBRA generic photonic integration platform* [19]. In his thesis he proposes a different approach at the problem. Throughout my thesis comparison with his work will be frequent. In the conclusion section I will draw conclusions on the two approaches.

2.3 In this thesis

The thesis is divided as following:

- **Chapter 2:** In this chapter we first show why doping is necessary in SMART Photonics platform and how it affects the performance of the chip. Then we show an integration technique that allows to confine doping only where needed in the optical chip. The chapter ends with a simulation showing the expected performances of the solution proposed.

- **Chapter 3:** In this chapter we focus on the three techniques we will used to estimate the losses of our chips. The maths behind the measures is presented and finally the chip layouts are explained.

- **Chapter 4:** In this chapter we present the collected data: we show the results of the measurements and relative data analysis.
- **Chapter 5:** In this chapter we study in details problems emerged during the fabrication process, we will focus on rabbit ears effect, doping migration and sidewalls scattering.
- **Chapter 6:** In this chapter I present an application that would directly benefit from low loss waveguides: an integrated wavelength meter whose speed and accuracy depend on the loss of the waveguides.
- **Chapter 7:** In this chapter conclusions are drawn over this new technique, discussing its convenience and possible further steps into the research.

Chapter 3

Towards low loss waveguides

3.1 Sources of loss

In SMART Photonics platform we can identify three major sources of optical loss: intrinsic losses of InP, losses due to surface roughness and losses due to doping. Intrinsic loss is connected to the refractive index of InP: in the c-band, InP spontaneously present some absorption and not much can be done to diminish this source of loss. However, it is important to have a defect free crystalline structure of InP to avoid making this losses even higher.

Surface roughness loss are introduced by the defects along waveguides sidewalls [20]. Ideally one would like to have the smoothest sidewalls to prevent the photons to get scattered. This can be done by optimizing the settings of the machines involved in processing (for instance by changing temperature, pressure, plasma intensity just to give few parameters) or by changing the chemicals during lithography [21]. Some platforms use ridge waveguides to eliminate waveguide walls altogether. In this configuration mode confinement is obtained thanks to a stripe of different material deposited locally on top of the guiding core layer. This is sufficient to create a region of higher effective index where the mode can propagate without physical bounds but remaining confined. This solution however has a lower confinement factor compared to standard waveguides and therefore puts a limit on the minimum radius of that must be used when designing bended waveguides. As a consequence the size of the optical circuit becomes larger resulting in a lower density of components on the chip.

The third source of loss is the presence of dopant atoms. We quickly remind that doping is the act of adding impurities (for example zinc atoms) to a material to change some of its properties. Generally speaking, losses are introduced mathematically by making the refractive index of a material

complex i.e. considering $n = n' + ik$. However, when dealing with waveguides is more useful to work with absortion coefficient of the lambert beer law α, or even more practical to express the loss in dB/cm. The relations between these quantities are the following [22]:

$$k = \frac{\lambda}{4\pi}\alpha[m^{-1}] \tag{3.1}$$

$$\alpha[dB/cm] = \alpha[m^{-}1]\frac{log_{10}(e)}{10} \tag{3.2}$$

When N type-doping is used for InP, losses increase due to three types of scattering that we indicate as follows: [23], electro optical phonon scattering $\alpha_{eo}(N)$, electro acoustical phonon scattering $\alpha_{ea}(N)$ and electron-ionized impurity scattering $\alpha_{imp}(N)$. The letter N indicates a dependency of this parameters from the dopant concentration in the material. The total absorption coefficient $\alpha(N, \lambda)$ becomes

$$\alpha(N, \lambda) = \alpha_{op}(N)(\lambda/\lambda_0)^{2.5} + \alpha_{imp}(N)(\lambda/\lambda_0)^{3.5} + \alpha_{oa}(N)(\lambda/\lambda_0)^{1.5}$$

Where λ is the wavelength we are interested in expressed in μm and $\lambda_0 = 10\mu m$. For P-type doping instead, there is single main source of loss due to the excitation of light and heavy holes. In [23] tables with experimental values of the absorption coefficients as a function of doping are reported, in the appendix A of [19] a fit of such tables is present. Is important to point out that the real part of the refractive index is affected as well by doping according to the following relation:

$$\delta n = -\frac{e^2\lambda^2 N}{8\pi^2 c^2 \epsilon_0 n m_{p,n}} \tag{3.3}$$

Where N is the doping concentration expressed as atoms per cm^3, $m_{p,n}$ the effective mass of the charge carrier and all quantities have their usual meaning. The reader interested in the numerical detail of the model is again referred to the appendix of [19].

In Figure 3.1 we see the behaviour of InP at $1.555\mu m$ for different doping concentrations. The plot shows four lines: red lines show the change in refractive index, blue lines express losses in dB/cm. The variation is minimal (less than 1%). We see that the nature of doping (positive or negative) has different impact on refractive index change. More interesting is to have a look at the increased absorptions due to doping (blue lines). The solid line refers to a p dopant material. We see that this loss are overwhelming compared to the one induced by negative doping. Concentrations of N type doping must be an order of magnitude higher before having similar values of absorptions as the one introduced by positive doping.

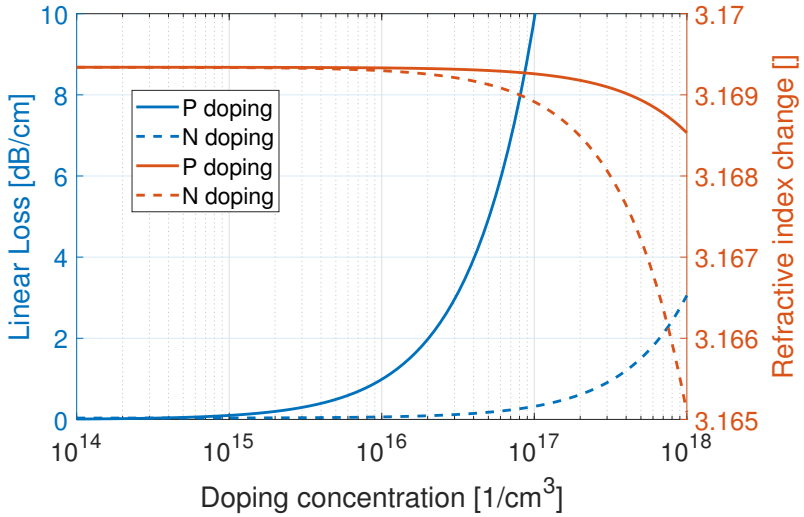

Figure 3.1: The variations of linear loss (blue line) and refractive index (red line) as a function of the concentration of P doping (solid line) and N doping (segmented line)

3.2 Doping and its impact

Doping plays a fundamental role in photonics since it allows to have PN junctions on a chip level. PN junctions are necessary for photons generation and detection and are constituted by a positively doped semiconductor in contact with a negatively doped semiconductor. At the interface of this two semiconductors charge recombination occurs leading to a depletion region. By applying a direct or reverse bias to the junction is possible to make the depletion region wider or narrower. The properties of the PN junctions are affected also by the dopant concentration both on the P and N side of the junction. Refering to Figure 2.2 in smart photonics platform the positively doped semiconductor stays on top of the core layer(green) while the N doped layers are below. Depletion region is more or less overlayed to the core layer. Doping has also an impact on the resistance of the semiconductor. The next two formulas show the resistivity per unit length of InP at different doping concentrations [24]:

$$\rho_n = 10^{-0.918log(n)+13.88}[\Omega cm] \tag{3.4}$$

$$\rho_p = 10^{-0.971log(p)+16.19}[\Omega cm] \tag{3.5}$$

Where ρ_n is valid for negatively doped InP and ρ_p for positively doped one. We observe that higher doping concentration results in lower resistance, both

for negative and positive doping. Given a slab with thickness h, width w and length L, its total resistivity can be computed as:

$$R = \frac{h\rho}{wL}$$

The general goal is of course to reduce resistance as much as possible, higher resistance implies higher energy consumptions and most of all an higher amount of heat generated than can affect the functioning of an entire PIC.

3.2.1 Doping and lasers

Let us now study more in details the impact of doping on some devices. We start by simulating the performance of a laser. Lasers work thanks to electron-hole pairs recombination that can lead to stimulated emission and therefore light amplification. The higher the number of electron-hole pairs, the more the light is amplified. Doping is crucial because allows a more efficient and abundant injection of electrons, thus increasing radiative recombination in the device.

Second benefit is that doping reduces the contact resistance of the lasers, this leads to a lower driving voltage and therefore lower power dissipation. With the software Harold we have simulated the response of a simple laser to the variations of doping distribution (self-heating simulation). We have used an uniform doping concentration of $5e17$ and changed the penetration depth of doping into the layer stack. We have simulated a configuration where doping is $144nm$, $73nm$, $0nm$ apart from quantum wells and a situation where the upper quantum wells are doped (up to $30nm$). The doping concentration profile is a simplified version of the real one, nonetheless it gives a meaningful insight on doping impact. In Figure 3.2a we see a variation in the maximum output power of 10%, while in Figure 3.2b we see how the gain spectrum is affected. This variation does not seems to critical, a simple characterization of the laser seems to be sufficient to know how to operate it.

If this is reasonable for scientific experiment where few chips are used, it becomes unfeasible for mass production, where tighter variations are acceptable and reproducibility is a vital importance.

3.2.2 Doping, phase shifters and optical modulators

Another component that is affected by doping is the phase shifter (PHS). PHSs work thanks to electro-optical effects induced in a reversely biased pn junction. When a pn junction is reversely biased the charge depletion at the interface of the two semiconductor extends considerably and this leads

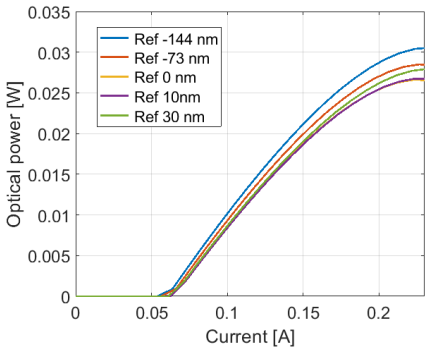

(a) Change in Laser output power for different doping profiles

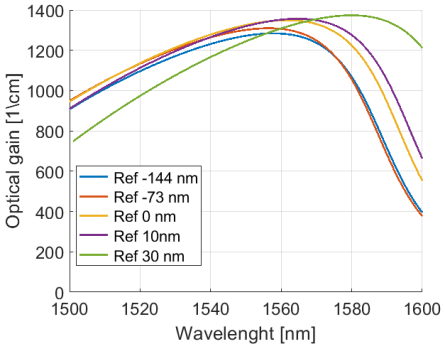

(b) Impact of different doping profiles on laser emission spectra

Figure 3.2: Different doping distributions (caused by low reproducibility during production)have an impact on laser performances.

to the build-up of an electric field. In InP this electric field together with the charge depletion itself induces a refractive index change in the material [25]. In particular four phenomena contribute to the change in refractive index: Pockels Effect, Kerr Effect, Plasma Effect and Band Filling Effect. The Pockels effect affects only the TE mode, and depends on the direction of propagation of the optical mode. Its contribution is positive for the mode propagating in the $< 1\bar{1}0 >$ direction and negative in the $< 010 >$. It is expressed as:

$$\Delta n_{Pockels} = \frac{1}{2} n^3 r_{41} E$$

The Kerr effect is quadratic with the field intensity and it is expressed as:

$$\Delta n_{Kerr} = \frac{1}{2} n^3 r_{Kerr} E^2.$$

The other two effects are linearly induced by doping and can be expressed as a change in refractive index proportional to doping concentration: $\Delta n_{bf} = 5 * 10^{-21} N_d$ and $\Delta n_{plasma} = 3.63 * 10^{-21} N_d$. All this phenomena changes locally the refractive index as:

$$\Delta n = \Delta n_{Pockels} + \Delta n_{Kerr} + \Delta n_{bf} + \Delta n_{plasma}$$

Such variation changes the effective refractive index and can be exploited to change the phase of an optical mode propagating in the device creating a phase modulator. The change in phase $\Delta\phi$ introduced by the modulator can

be computed with:

$$\Delta\phi = \frac{2\pi}{\lambda}\Delta n_{effect} L \tag{3.6}$$

where L is the length of the modulator. To have an efficient device the depletion region of the junction must overlay as much as possible with the optical mode to maximize the change in the refractive index. This occurs when the p dope front is at the edge of the waveguide core. In Figure 4.3a and Figure 4.3b we see an example of this. The two graphs have been obtained from a simulation in Lumerical where the electric field for different applied bias was calculated inside the optical modulator. In Figure 4.3a the doping is closer to the core layer and this leads to a nice overlap between the mode and electric field. On the contrary in Figure 4.3b the doping is $300nms$ further away from the core and the overlap is lower.

With an efficient PHSs is possible to create an efficient optical modulator, a device capable of generating light pulses at decades of GHz. Fast modulators are of key importance in modern society because they are used for the internet. An easy examples of modulator consist of a Y splitter that sends a propagating mode to two PHSs where only one is electrically driven and a second Y makes the two mode to interfere. The active PHS is driven such to add a phase shift $\phi = \pi$ to its side propagating mode. When the two modes recombine destructive or constructive interference occurs leading to signal modulation. In modulator a key Figure of merit is the voltage value V_π, necessary to create the phase shift $\phi = \pi$. Having V_π low is crucial for a fast modulation because lower values V_π easier to be achieved by the electronics controlling the modulator.

We now show how having control of the doping concentration is fundamental for the performance of the modulator. In Lumerical we have simulated how the required length of the modulator changes for four different voltages when an offset is applied to the doping profile. The results are reported in Figure 3.4 of and clearly show the importance of having a precise control of doping. An offset of $100nm$ is sufficient to require a significant correction in modulators length. This is of course not possible and would imply serious problems in the functioning of the device.

3.3 Second butt joint

From Figure 3.1 we learned that doping has a strong impact on losses, especially considering that doping concentration close to 10^{18} are standards in the platform. Luckily using a graded doping profile is possible to keep a greater distance between the optical mode and doping. Some degree of interaction

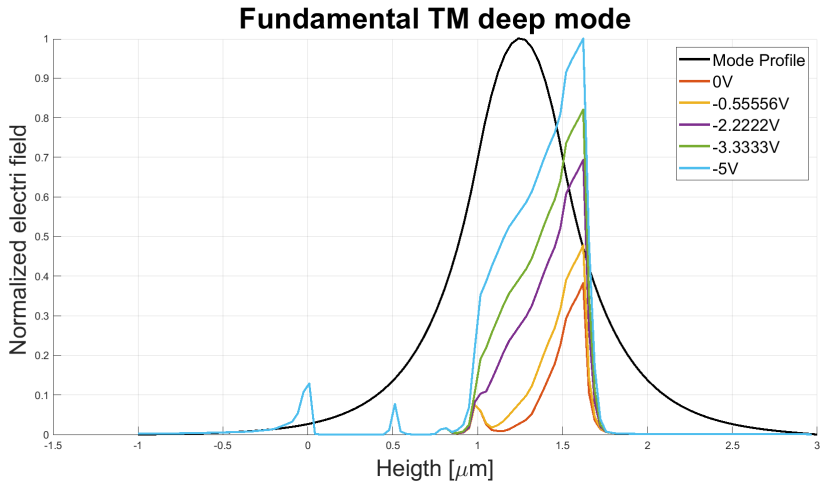

(a) In this simulation doping is in contact with the core layer of the chip

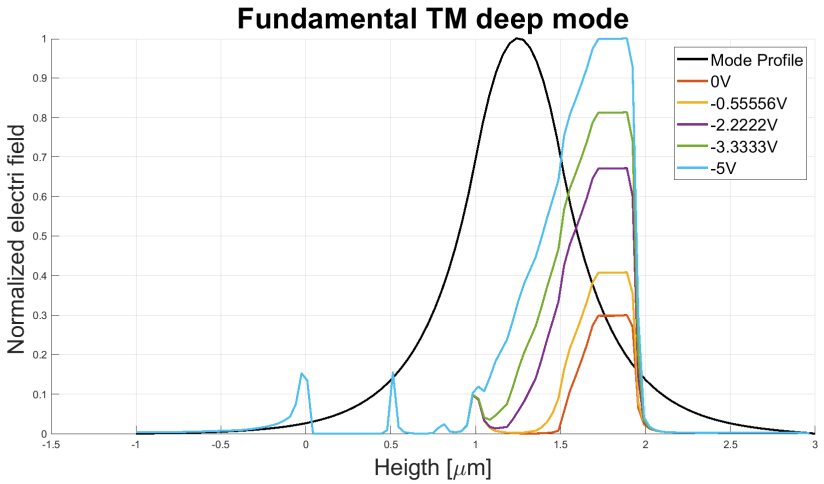

(b) In this simulation doping is at a distance of 200nm from the core layer of the chip

Figure 3.3: Differences in the overlap between electric fields and optical mode when the chip is biased with different voltages and the doping has a different distribution

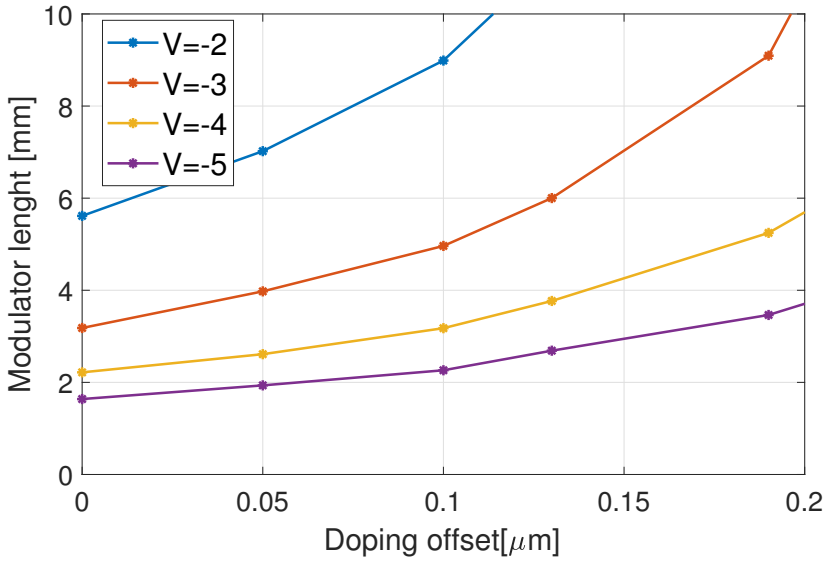

Figure 3.4: Impact of doping distance from core layer on modulators required length for generating a π phase shift: different lines represent different operating voltages.

however, is unfortunately unavoidable. If doping is necessary for active components to work, this is not true for passive elements such as waveguides and interferometers. Right now, the integration process is such that the doping is diffused everywhere in the top layers, thus increasing unnecessary waveguides loss.

We understood that undoped layers significantly reduce absorption losses. Two main approaches have been developed to tackle this problem. The first one consists in letting zinc diffuse from wafers surface down into cladding layers. This approach has been investigated deeply in Dagostino thesis [19] whose research was carried out at SMART photoncis. Despite very promising results in reducing passive elements losses, the integration with active devices has proved to be challenging. During the diffusion process it is hard to keep under control the boundaries condition and to stop zinc diffusion where needed. From internal data at Smart photonics we have observed differences in the doping penetration depth up to $140nm$. As a consequence unwanted doping profiles are obtained, with doping penetrating down into the core of active elements. The simple simulations shown in sections 3.2.1 and 3.2.2 show that doping variations have significant impact on device performances. This is particularly true for modulators, a key component for

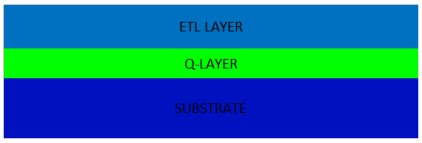

(a) The layers are grown up to a predetermined thickness.

(b) A mask is used to protect the high dope region, InP is removed at other locations.

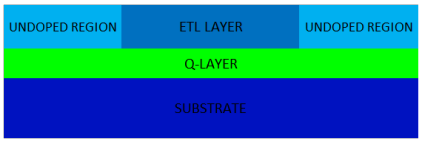

(c) Undoped InP is regrown up to level with doped one.

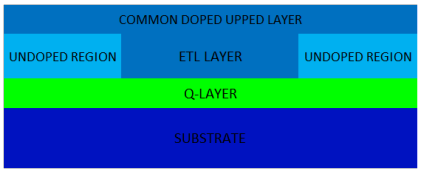

(d) The final doped layers common to all the wafer are grown.

Figure 3.5: The epitaxial steps used to implement the butt join techniques

SMART photonics success. The difficulty in controlling zinc diffusion, has convinced us to try a different approach, that is to perform a butt joint in the cladding layers. In Figure 3.5 we show how it works. A generic wafer is grown up to a predetermined level of the top cladding (Figure 3.5a). At this point, rather than proceeding with the lithography of optical components, a hard mask is deposited on the wafer. The mask is used to protect the sites of the wafer where active elements are necessary. Everywhere else the mask is etched open and InP is etched down to the core layer (Figure 3.5b). With the hard mask still in place, new layers are grown up to the height of previously deposited layers in the areas not opened in the hard mask (Figure 3.5c). InP is keep as pure as possible (we expect an unwanted doping of 10^{15} $1/cm^3$). After removal of the hard mask, remaining shared layers can be grown on the entire wafer (Figure 3.5d). In this way two different claddings are obtained, one is used for passive components and has no intentional doping, the second one is suitable instead for all active elements. Butt-joint is already implemented in the SMART platform to integrate the active and passive core layers. However, for the first time, we performed a butt-joint in the cladding layers of the wafers to confine doping only in active region, thus strongly reducing loss. Having a defect free regrowth is not trivial and the chances of introducing defects gets bigger the larger the regrowth height. There is a trade-off to be done. The thicker is the regrowth, the farther is the doping from the core layer and lower are the losses, but this also introduces more defects. With simulations is possible to try to identify what the optimal

thickness is.

3.4 Simulations

As said, the impact of regrowth thickness on losses can be simulated using commercial softwares. This is however no trivial task because usually there is not a predefined model of InP and $InGaAsP$ that takes into account the impact of doping on losses. We decided to use the model described in section 3.1 to estimate the refractive index of InP with different doping concentrations. We took some real data of the typical doping profile we have in our substrate and we discretized the cladding in blocks of constant doping levels. In Figure 3.6b we see the result of this discretization. Then we simulated different regrowth thickness defining volumes of undoped InP in the simulation in place of doped one. The results are shown in Figure 3.6a. We see that the losses are drastically reduced when the regrowth thickness is larger than $400nm$. Moreover, we also checked what unintentional doping concentration we can tolerate in our experiments. Unintentional doping occurs because to grow InP precursors gas are used (Chapeter 6.1). Some of the atoms present in these precursors remain sometimes trapped in InP creating doping effects.

In Figure 3.6a lines represents doping concentration equal to 10^{14}, 10^{15} and 10^{16}. We see that the increase in loss is negligible and since we know that we can keep contaminations below 10^{15} we consider this technique worth to be tested.

When dealing with loss simulations it is worth to keep in mind that rather than looking at absolute numbers is more interesting to look at trends. From Figure 3.6b we see that increasing the thickness of regrowth decreases losses. Is however not safe to pick a single value to use. For this reason we decided to test three regrowth thickness: $400nm$, $800nm$, $1200nm$. The first one should be easy to be grown but maybe not sufficient to keep doping far enough, second one seems a good trade-off between easiness of fabrication versus doping distance while the last one is the more challenging under an epitaxial point of view but potentially also the more effective. To this three wafers we have added other two: the firs one has the standard doped layerstack while the second one is fully undoped. In this way we can evaluate easier how much have we improved from the standard results and how far are we from the best of the best results. Unfortunately the $400nm$ wafer broke during production, thus reducing the total number of wafers to four.

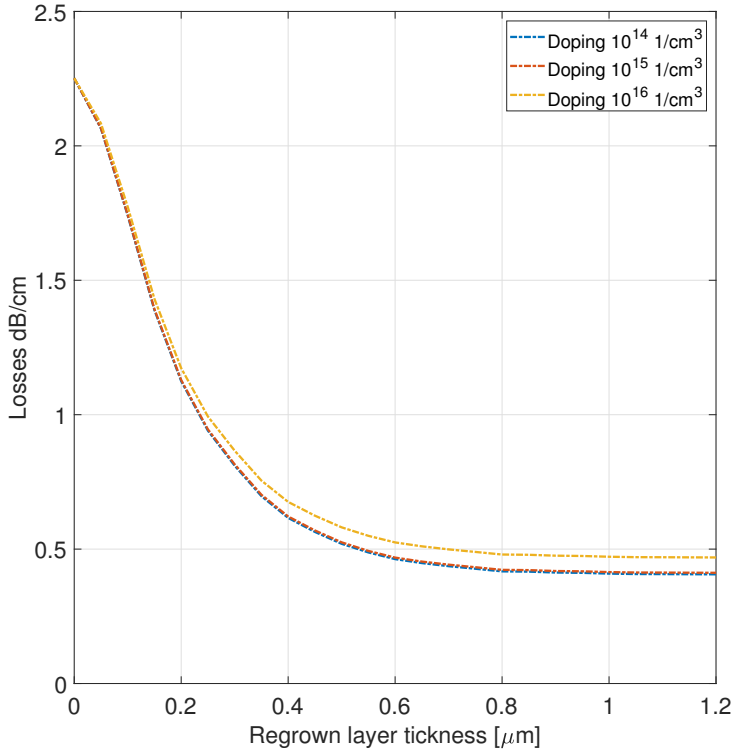

(a) Simulated reduction in losses as a function of butt joint thickness. Different lines represent different concentration of unwanted doping contamination during the regrowth.

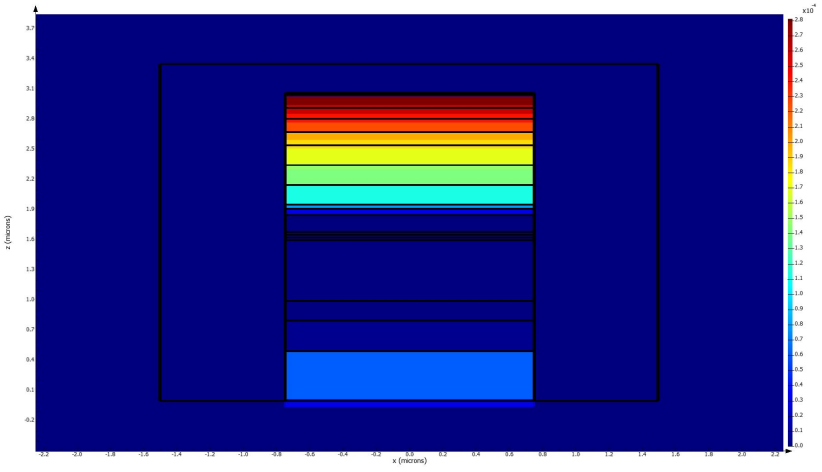

(b) Layerstack used to simulate with Lumerical the propagation losses. Different colours represent different values of the absorption coefficient α.

Figure 3.6: Simulations showing the impact of doping on loss.

Chapter 4

Loss measurements

4.1 Introduction

We want to test if the double but joint gives a real improvement in reducing losses in waveguides. For this purpose, I designed four chips with three different type of structures that allows to measure chip losses.

4.2 Fabry-Perot method

The first type of test structure aims at creating Fabry Perort cavities with shallow and deep waveguides. The physics of such cavities is simple: light is coupled between two mirrors and propagates back and forward. This multiple reflection leads to destructive or constructive interference at the output of the cavity. In our chips the waveguides act as the cavity and the facets of the chip, due to the different refractive index between InP and air, become mirrors with reflectivity of about 30% The transmission spectra of the cavities is described by:

$$I(\lambda) = \frac{(1-R)^2 e^{-\alpha L}}{(1-Re^{-\alpha L})^2 + 4Re^{-\alpha L} sin^2(2\pi L/\lambda)} \tag{4.1}$$

Where R is the reflectivity of the facets, l the length of the cavity, n is the refractive index of the material, λ the wavelength of the travelling mode and α are the linear losses of the cavity. All the parameters are well known in SMART photonics platform (except for α of course) and by looking at the transmission spectra is easy to extract the losses value. Actually,it is not even necessary to acquire the transmitted power versus the wavelength. By inspection of eq.4.1 we notice that for $sin^2(2\pi L/\lambda) = 0$ we have a maximum in transmitted intensity $I(\lambda)$ and when $sin^2(2\pi L/\lambda) = 1$ we have a minimum.

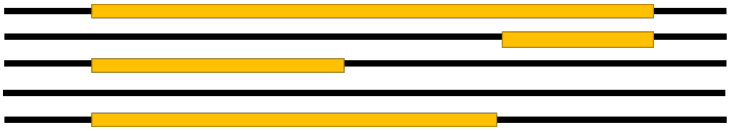

Figure 4.1: Yellow blocks represent high dope regions present along waveguides. In such regions absorption is higher due to higher doping concentration.

The ratio between the maximum and minimum value of eq.4.1 is defined as Power Transmission Ration (PTR) and can be expressed as:

$$PTR = \frac{(1 + Re^{-\alpha L})^2}{(1 - Re^{-\alpha L})^2} \tag{4.2}$$

That is easy to be inverted and to find the parameter α. In our chips we have inserted 13 shallow and 13 deep waveguides. However, the waveguides are not designed the same but rather we made them pass through doped regions of different length. The idea is schematized in Figure 4.1, black lines are waveguides while yellow blocks represent high dope regions obtained with the double butt joint technique. In this way is possible to create graphs like the one in Figure 5.2, where estimated losses are plotted versus the length of the high dope area. In this way with linear regression is possible to extract the extra losses due to the presence of doping with more accuracy.

4.3 Ring resonators method

Second kind of structures used in our chips are optical ring resonators. The optical response of a ring resonator in the all pass configuration is well explained in literature [26]. We took inspiration from this main description but we made a slight modification of the equation that describes the response of the ring. In particular we start with a more generic description of the MMI properties. We use four parameters: t_u, x_u, t_l, x_l that are respectively the *transmission* in the *upper* half of the MMI, *cross* coupling in the *upper* half, the *transmission* in the *lower* half and the *coupling* in the *lower* half. In Figure 4.2a we see a visualization of the parameters.

These coefficients refer to electric field propagating in the MMI. However it is much easier to deal with field power that is proportional to the square of the electric field. This also implies that when we deal with transmitted and coupled power, we need to consider the square of those parameters. If we define the following quantities (see Figure 4.2b): E_1 input field, E_2 output

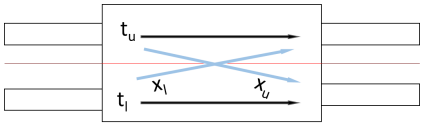

(a) The coefficients characterizing the coupling properties of the MMI.

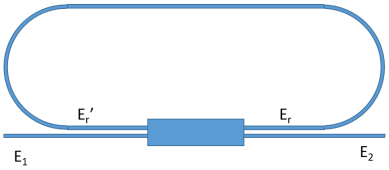

(b) Electric fields labelling system.

Figure 4.2: Labelling of characteristic electric fields and MMI coefficients used in the model

field, E_r field coupled to the ring and E'_r as the field in the ring after one round trip, we can write the following equations:

$$E_2 = t_l E_1 + i x_u E'_r \tag{4.3}$$

$$E_r = i x_l E_1 + t_u E'_r \tag{4.4}$$

$$E'_r = \widetilde{\alpha} E_r \tag{4.5}$$

Where $\widetilde{\alpha} = \alpha e^{\phi}$ is the propagation factor of the cavity with ϕ the phase delay accumulated during propagation and $0 < \alpha < 1$ are the ring loss. By substituting for E_r we can find the relation between E_2 and E_1. From square module of the ratio E_2/E_1 we get the following expression.

$$\left|\frac{E_2}{E_1}\right|^2 = \left|t_l - \frac{\alpha e^{i\phi} x_l x_u}{1 - t_u \alpha e^{i\phi}}\right|^2 \tag{4.6}$$

Remembering that $e^{i\phi} = cos(\phi) + sin(\phi)$ we can express 4.6 as:

$$\left|\frac{E_2}{E_1}\right|^2 = \frac{(t_1 + cos(\phi)\alpha(t_u t_l + x_u x_l))^2}{(1 - cos(\phi) t_u \alpha)^2} \tag{4.7}$$

Now we see that this expression has a maximum value with $cos(\phi) = 1$ and a minimum for $cos(\phi) = -1$. These values are easily accessible from experimental data since in the response of the ring is sufficient to take the values of peaks and valleys. We can define the power transmission ration (PTR) has the ration between these two quantities and see that becomes:

$$PTR = \frac{(t_l + \alpha(t_u t_l + x_u x_l))^2}{(t_l - \alpha(t_u t_l + x_u x_l))^2} \frac{(1 - t_u \alpha)^2}{(1 + t_u \alpha)^2} \tag{4.8}$$

And this is the most general expression we can get. Now we can make some assumptions on the MMI coefficients. If the MMI is symmetric along its

longitudinal axes (red line in Figure 4.2a than we can assume that $x_u = x_l = x$ and $t_u = t_l = t$, and that $t^2 + x^2 = 1$. Second assumption is that the MMI is not perfect, but some losses are present. We can write this as $t^2 + x^2 = I^2$ with $0 < I^2 < 1$. A third assumption we make is that I affects in the same way t and x, so to say that $t'^2 = t^2 * I^2$ and $x'^2 = x^2 * I^2$. We can now rewrite eq.4.8 as

$$PTR = (\frac{(t'^2 + \alpha(t'^2 + x'^2))}{(t'^2 - \alpha(t'^2 + x'^2))} \frac{(1 - t'\alpha)}{(1 - t'\alpha)})^2 \tag{4.9}$$

Finally, we have an equation that allows us to predict the PTR when the linear loss of the ring and the MMI loss are known. For the seak of simplicity let us assume an ideal MMI ($I = 1$) and plot eq. 4.9 in Figure 4.4.

We see that for a same value of Power transmission ratio ($3dB$) two roundtrip losses can be associated. This means that Eq. 4.9 is not bijective and that inverse function does not exists. Eq. 4.9 can be made explicit for alpha to a fourth order equation. Such equation being fourth order has potentially four solutions. However only solutions where $0 < \alpha < 1$ are valid and this leads to the two possible solutions as shown in 4.4. The only possibility to distinguish between the two is to choose wisely the length of the ring having a rough idea of expected roundtrip loss. To understand how let's first notice that in the plot the blue line peaks at a $3dB$ value on x axis. It can be proved that for such condition the ring is in the critical coupling regime [27], that is the regime where no optical output power is measured on resonance. The fact that almost no output power is measured at resonance, makes the PTR to explode to a large value, since the denominator of eq.4.9 gets close to zero. Best practice is to design the ring to be quite far from that condition, for instance if I expect the loss to be about $2.8dB/cm$, I won't be using a ring that is $1cm$ long because that would pose me close to that peak with a PTR of 708. The linear loss associated with such PTR are either $2.8dB/cm$ or $3.2dB/cm$ and I am then unable to pick the correct one. If instead I make the ring only $5mm$ long I get a PTR=7.23. To such PRT we have associated losses of $2.8dB/cm$ and $12.3dB/cm$, in this case having a priori knowledge makes it easy to identify $2.8dB/cm$ as the correct loss value. In Eq. 4.9 all the coefficient characterizing the MMI must be known a priori if we want to measure losses with a single ring. However, by using more rings is possible to measure linear loss even if the coupling coefficients of the MMI unknown. We proved this idea using the software Lumerical interconnect. Here we simulated four rings with length respectively of 2mm, 4mm, 6mm, 8mm, linear loss of 2dB/cm and a MMI insertion loss of 0.2dB. From the simulation we have obtained for PRTs values. For instance, the first ring has $PTR = 2.2$. For this PRT we have computed the associated

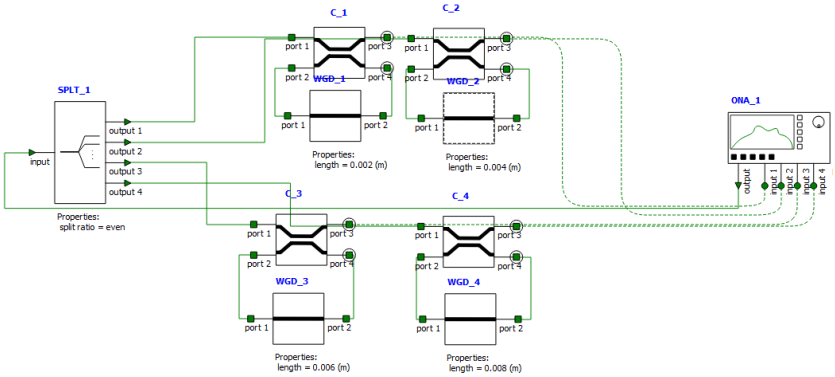

(a) The optical circuit implemented in Lumerical Inerconnect

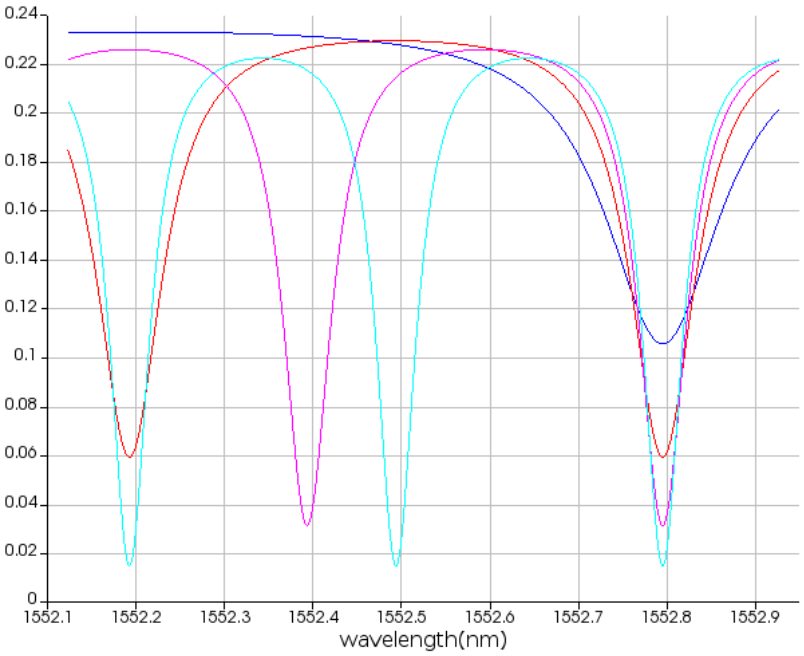

(b) Simulated transmission of 4 rings

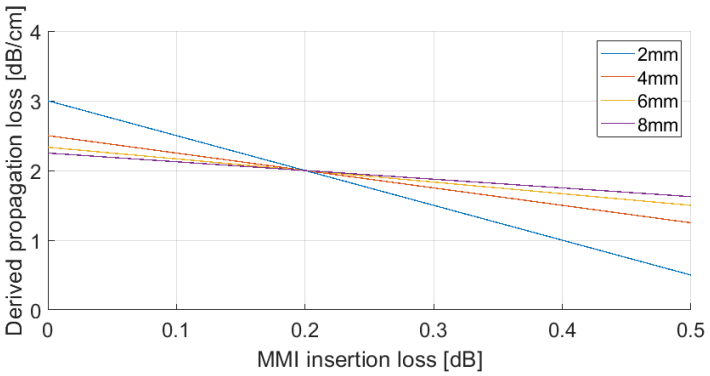

(c) The influence of MMI insertion loss in measuring linear loss

Figure 4.3: The result of the simulation based on four rings measurements

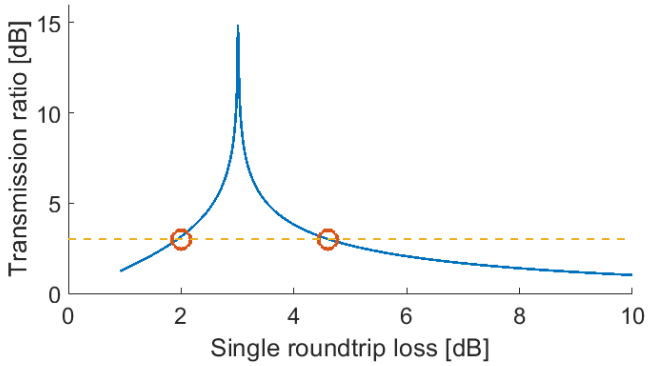

Figure 4.4: The resulting power transmission ration given a round trip loss, from a measured transmission ration of 3dB (yellow segmented line) two possible round trip losses are extracted (red circles)

linear loss assuming different values for the MMI loss. In Figure 4.3c we have plotted such variation such dependence of estimated loss given the insertion loss of the relative MMI for each ring. We see that all the lines intersect in one point. In other words, there is only one combination of MMI insertion loss and waveguide loss that can gives such combinations of PTRs for the rings. In theory two rings are sufficient to determine such point but with real rings is better to have more because any defects can shift the lines leading to an inaccurate estimation of loss. In the next chapter we will present some experimental data and develop further this aspect.

4.4 Spirals method

This third and last method of measuring loss can be considered more as a backup and it is expected to be less accurate than the other two. The idea is simple: two spirals s_1 and s_2 with the same number of turns and same bending radius are used. The spiral s_1 is designed to be as long as possible (it has length l_1) while the second spiral s_2 is as short as it can be (length l_2). Light is coupled to the spirals and optical powers p_1, (p_2) are measured after propagating in s_1, (s_2). Since $l_1 > l_2$, we expect that $\delta p = p_1 - p_2 > 0$. Given that s_1 and s_2 share the same number of turns we can say that the excess loss δp is mainly due to extra length of s_1 respect to s_2. The linear loss can be extracted as:

$$\alpha = \frac{\delta p}{l_2 - l_1}$$

This simple method relies on many assumptions that are not trivial to fulfil:

- If we define the coupling loss of the spirals as c_1 and c_2 we must be able to couple in such a way that $\delta c = c_1 - c_2 << \delta p$,
- The facets on the chip act as mirrors and this could lead to have a Fabry-Perot cavity. This inconvenient can be easily solved with the deposition of an anti-reflection coating on the sides of the chip,
- The waveguides must be mono-mode and the fundamental mode should be excited when coupling,
- With linear regression is possible to extract the bending radius loss. Indeed, if we plot measured absorption vs spiral length and we do a linear regression over such data, the value of the intercept will be giving the bending loss of the structure.

4.5 Chips layout

In Figure 4.5 we present four pictures of the designed chips taken with the optical microscope. In Figure 4.5a we see 8 rings: the four smaller ones are made with deep waveguides, while the others are made of 4 shallow waveguides. Both sets of rings has length equal to $2mm$, $4mm$, $6mm$ and $8mm$. However deep waveguides rings appear smaller because the minimum radius of curvature allowed for deep waveguides is $100nm$ while for shallow waveguides is $400nm$ due to the different capability of confining the mode. In the top part of the chip $MMIs$ are present to try to measure their capabilities. In Figure 4.5b 26 waveguides (13 deep and 13 shallow) are present. They will be used as Fabry-Perot cavity. In this picture high dope island are not visible. In chips of Figure 4.5c and Figure 4.5d four spirals are present. Notice that each cheap has deep and shallow spirals. Both deep and shallow spirals have the same number of turns and same bending radius. In this way is possible to do the differential measures described above. On the same wafer we tested three different widths for shallow and deep waveguides. Therefore on a wafer copies of this chips are present with different waveguide widths. The widths used are $1\mu m$, $1.5\mu m$ and $2\mu m$ for deep waveguides and $2\mu m$, $2.5\mu m$ and $3\mu m$ for shallow waveguides. This has been done to try to estimate scattering loss due to sidewall roughness. When the width changes also the overlap of the optical mode with the sidewalls changes and this should lead to a decrease in loss. However, all of this comes at the cost of potentially making the waveguide multimode. Is however something that is worth trying given that it comes at no extra production cost. As already mentioned

(a) Ring resonators

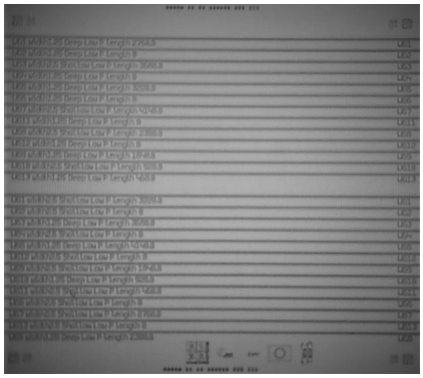

(b) Fabry-Perot cavities

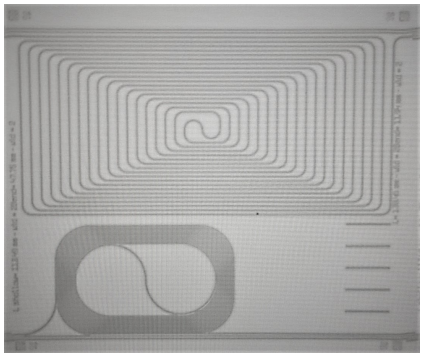

(c) Spirals

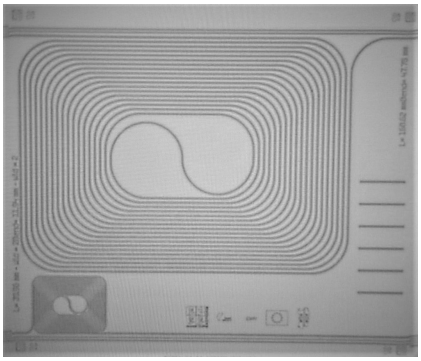

(d) Spirals

Figure 4.5: The four chips designed to measure losses at the end of fabrication process.

in the previous chapter, we have produces 4 wafers with 4 different doping distributions. This makes the total number of chips equal to 48! (4 designs $\times$ 4 wafers $\times$ 3 widths).

Chapter 5

Data analysis

Out of all the 48 chips designed it has been possible to characterize only 8 and only partially. This has to do with difficulties in producing chips, since a company cannot focus only on fundamental research but it must also product products for costumers so to be able to finance further research. As a consequence is not unusual for tools to be used by production for many consecutive days, with no slot to process wafers dedicated to research process. Also covid pandemic has played a role, since it has forced a key supplier to strongly delay the realization on the antireflection coating necessary to measure data from chips. Non-the-less it is already possible to draw significant conclusions from the chips measured. In particular we have used the Fabry-Perot method described in section 4.2 to characterize the losses of deep waveguides. All waveguides measured are on chips with the design shown in Fig.4.5b. We have measured losses on chips from the all the 4 wafers we have produced, so that we have data from wafers with standard doped layerstack, fully undoped layerstack and second butt joint of $800nm$ and $1200nm$ thickness. Estimated losses are reported in 5.1, the error bar is obtained from the standard deviations of different losses recorded value of different waveguides. The blue line is the trend the data should follow according to simulations. The results are not the one expected since the simulated behaviour is not reproduced by data. We see that the losses recorded in the doped wafer are of $2dB/cm$. The wafer with a regrowth of $800nm$ has losses of $4dB/cm$ that only slightly decrease to $3.5dB/cm$ when we increase the thickness of the regrowth. Moreover the wafer that has no doping at all still presents losses in the order of $2dB/cm$.

However this does not mean that doping has no impact on losses. In fact in wafers with the butt-jointed method, high doped island of different lengths are presents along waveguides (Figure 4.1). This can let us extract the impact of doping directly as a function of highland lengths and see if doping is so

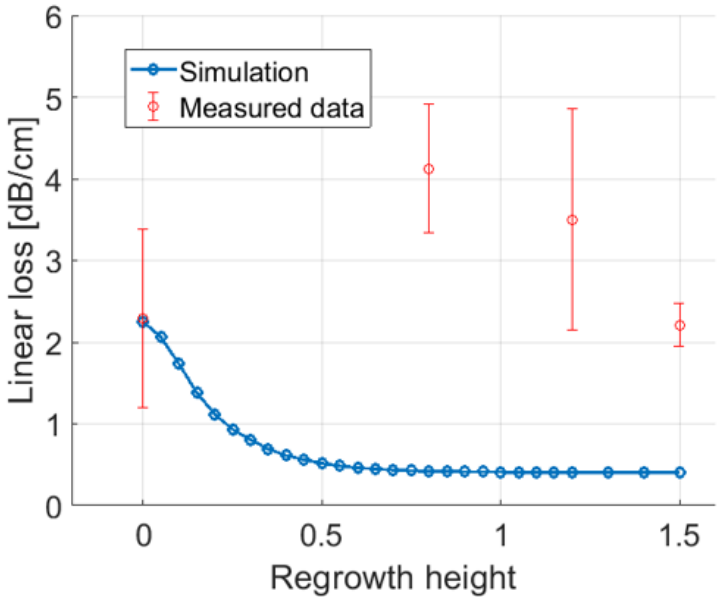

Figure 5.1: First data showing actual loss (red mark) and trend expected from simulation (blu line).

critical in affecting waveguides performance. From plot in Figure 5.2 we see that, as expected, waveguides with longer high dope region experience higher loss and that such contribution increases linearlyn (in a logarithmic scale) when the length of the high doped island is increased. Both fitting lines have similar slope indicating that the losses have indeed an impact on loss. From this set of data it appears also that the difference between the $800nm$ regrowth and the $1200nm$ one is bigger than in Fig. 5.1. We have then asked ourselves if the butt joint techniques induce defects in the regrowth. All of this will be discussed in detail in the next chapter.

5.1 Electrical to electrical loss measure

Before moving to the next chapter is interesting to analyse some measure of loss obtained with the technique of section 4.3. For a side project in Smart Photonics, I was in charge of designing chips for losses measurements on a wafer level. In other words the task is to measure the loss electrically on chip using electrical probes, without cleaving the wafer, but rather by using an on-chip laser source. In Figure 5.5 we can see a photo of the test chip we used to take the measures. An integrated laser with tunable wavelength is

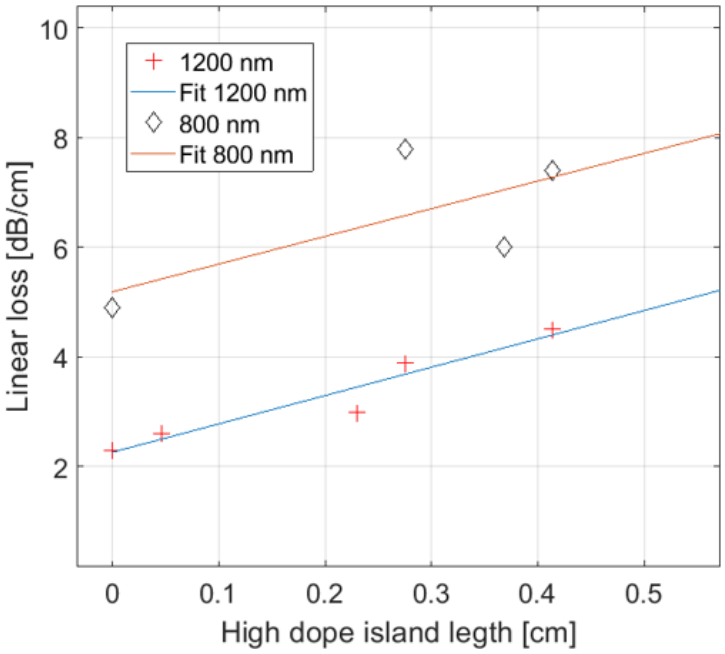

Figure 5.2: Evaluation of doping impact on waveguide losses.

used to generate light (bottom left part of image). Light is then routed to 4 rings in the all pass configuration with lengths respectively of $2mm$, $4mm$, $6mm$, $8mm$. The transmission spectra of the rings is then recorded with 4 photodetectors at the end of each ring. Yellow path are metal connections that allow to provide supply current to different components and read data.

The analysis of the data obtain then is completely identical to the one already reported in previous chapter. Main difference is in laser tuning, that cannot be swept for long wavelength spans. The laser is a linear Fabry Perot cavity laser where distributed brag gratings act as mirrors. A phase shifter is used to tune laser wavelength and the active part of the laser is constituted by a standard SOA. A Photodiode is placed at the back of the lasers and it is useful to normalize recorded transmission spectra. We have tested several settings of the laser to optimize the measure. In particular the we have acquired and analysed data of 48 test cells, coming from three different wafers. For each cell we have used 4 levels of SOA supply current: $0.3A$, $0.4A$,$0.5A$ and $0.6A$. For every supply current we have swept the phase shifters both in current ($0, 0.30A$ range) and voltage ($0, -10V$ range). Figure 5.3 shows all the data that are acquired in one measure. In the first row we have the raw data acquired by the photodetectors for the first rings. The photodetector generates a negative current the higher the photon intensity. Images are ordered according to the length of rings, so first graph is the response of the ring that is $2mm$ long, the followings are $4mm$, $6mm$ and $8mm$ long. We see that moving from left to right the number of peaks recorded increase. This is in agreement with what the theory predicts. In bottom right part we have the acquisition obtained with photodetector at the rear of the laser. This intensity is used for renormalizing the data recorded for the incident power. In the second row we see the results of this normalization. On the Y axes arbitrary units are used. The absolute value is not relevant since as explained in previous chapter we are interest of the ratio of maximum over minimum values recorded. Finally in the bottom left part we see the estimated loss of the chip. In this case the estimated losses are $1.4dB/cm$ with $0.25dB$ insertion loss of the MMI.

However one problem is striking evident. The yellow line corresponding to the $6mm$ long ring is completely off. Worst thing is that looking at the data acquired there is no obvious reason for being so off. Moreover if we move to Figure 5.4 we can spot another problem. The Figure is chaotic but it must be interpreted as following: for every ring line corresponding to the acquisitions at different SOA current are plotted. The colors are the same as in Figure 5.3, the $2mm$ ring is blue, the $4mm$ ring is red, the $6mm$ ring is yellow and $8mm$ ring purple. In an ideal case we would expect lines from the same colors to be overlapped and indistinguishable, since changing the

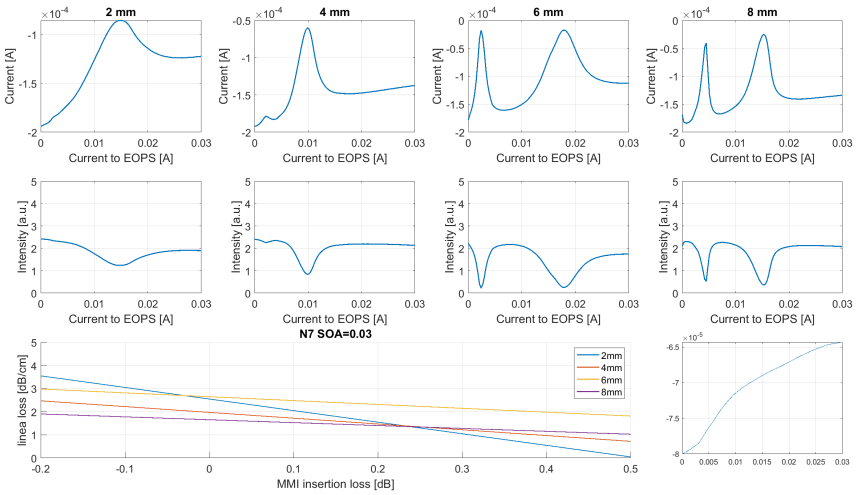

Figure 5.3: The full set of data measured from a test cell: in the upper row there is the signal measured at the four photodiodes. Second row the signal is normalized using the laser output power. Bottom row: estimated losses for the each ring as a function of MMI loss. Laser output power also plotted in the right and side

SOA power does not change the linear loss of the system. This is not the case. The estimated loss fluctuates a lot from $1.4dB/cm$ to $1.7dB/cm$. Is interesting to note though, that the separation between the lines of the same color maintains more or less a constant ratio among different colors. Other test cells were not any better, actually having three lines crossing in one point is already a significant result. Out of the 15 cells present on a wafer, only one or two chips have three line crossing in one point. The main problem is that the system is too much sensible to fluctuation in acquired data. Integrated lasers are not stable enough at the moment and moreover, it might be that higher optical modes are excited or that a defect in one single ring change its propagation loss. To investigate the possible source of failure would be instructive to measure the rings with an external laser source characterized by a wider tunable range. The fabrication of the chips for such test in in progress.

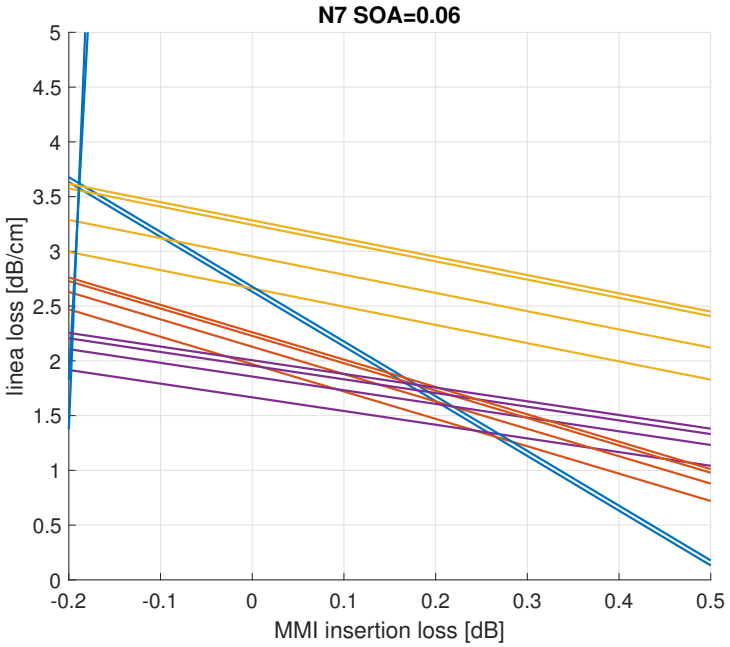

Figure 5.4: For each ring estimated losses at four different laser output powers are plotted. Line of same colour should ideally overlap since losses should not depend on laser power.

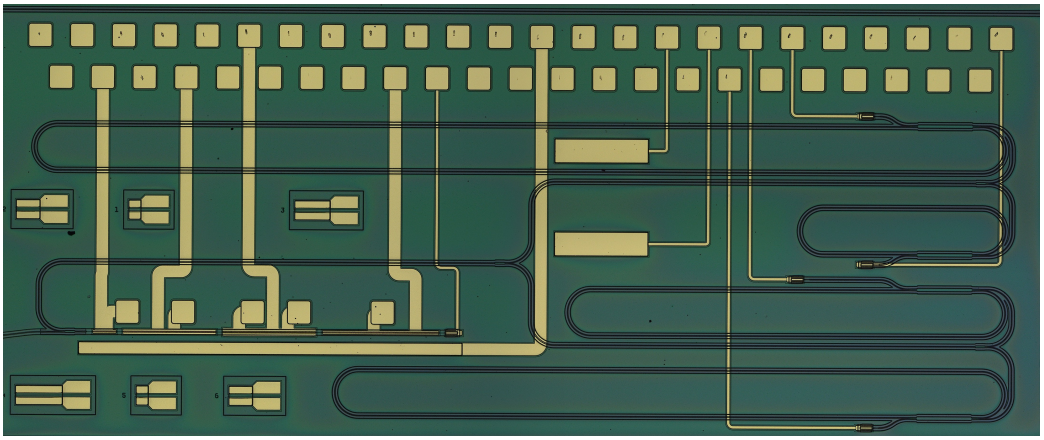

Figure 5.5: The chip used to measure losses on wafer level before cleaving, the four rings used for the measurement (on the right) and the metal connection to the laser (on the left) are visible

Chapter 6

Technique integration

In Chapter 4 we have shown some early results of the experiment. The chips were fabricated with no active elements such as lasers, modulators or detectors. This choice has been done to speed up the wafer fabrication and to limit the sources of uncertainties in the process. Many difficulties however have already emerged. In this chapter we will investigate selective are growth, doping migration and surface roughness.

6.1 Selective area growth

Having a second butt joint of good quality is fundamental for improving the performances of the devices. To evaluate the goodness of our but joint, we have fabricated two wafers with the butt-joint thickness of $1200nm$. One of the wafers however, only went partially trough the fabrication process. We stopped it at the moment of doing the butt joint. After the regrowth of the undoped layer (Figure3.5c), the wafer has been cleaved in two halves. One half has been kept apart (sample A) while the second half has undergone the regrowth of the finals top layers (sample B) as in Figure 3.5d. In Figure 6.1b and 6.1c we see two images of (sample A) are shown taken with the electronic microscope. We see that the surface of the wafer is not flat and two protuberances are present. This is the well known rabbit hears effect. The protuberance has an height of $700nm$. When then the top layers are deposited on sample B (Figure 6.1d and Figure 6.1e) such defects get even bigger, up to $1940nm$. In Figure 6.1a we see a top view of this structures taken from a different wafer.

What is happening is that top layers are grown, regions adjacent to the mask show an enhancement of InP growth rate. To understand why we need to describe the process used to deposit InP on the wafer, that is metalorganic

chemical vapour deposition (MOCVD). The wafer is inserted into a vacuum chamber, is heated up to a predetermined temperature and the so called precursors gasses are injected into the chamber. In the case of InP the precursors are trimethylindium ($(CH_3)_3In$) and phosphine (PH_3). When the precursors hit the wafer, chemical reactions occur on surface of the waver and In and P are bounded. If the flux of gas is uniform on the wafer, the wafer grows flat. In our case when we insert wafers in the chamber, SiO_2 masks , used to protect the high dope area, are present. The precursors do not bound with the mask but rather tend to flow on it [28]. Therefore, when precursors hit a mask they tend to accumulate at its edges. This leads to an higher concentration of precursors creating the local enhancement of the growth. The local enhancement effect can be critical for several reasons. The surface topologies can prevent an uniform spreading of photoresist material. When photoresist layer is not uniform in thickness, this can result in under/over exposure and poor lithography of optical components. Another drawback is that produced irregularity in crystalline planes could interact with nearby modes creating extra losses and scattering, affecting optical performances. An irregular wafer topology can also act a starting point for fracturing silica passivation layers. In the next section I will present the investigation we did to mitigate this problem.

6.1.1 SAG vs angle and width

One of the first thing we tried to mitigate rabbit ears was to see if using different angels of the mask together with different widths could have eliminated effect. In Figure 6.2a a SEM acquired image of our test structure is reported. The widths tested where of 2, 3, 5 ,10 ,20 ,30 μm. We also investigated masks of 3 μm width positioned at angles of 105, 90, 85, 75, 60, 45, 30 degrees. The samples were etched down to $1240nm$ and then regrowth was performed. With the electronic microscope and the software $ImageJ$ we have measured the height and width of the resulting SAGs. From plot 6.2b we clearly see that having an angle of 90 degrees between the mask and the 011 plane reduces the SAG height. As it comes to mask width we see the results in Figure 6.2c. Here we can identify a trend were for larger masks we have higher and wider rabbit ears. Choosing the correct angle and reducing the mask area as much as possible the problem, however sag remains present and different solutions must be found and investigated.

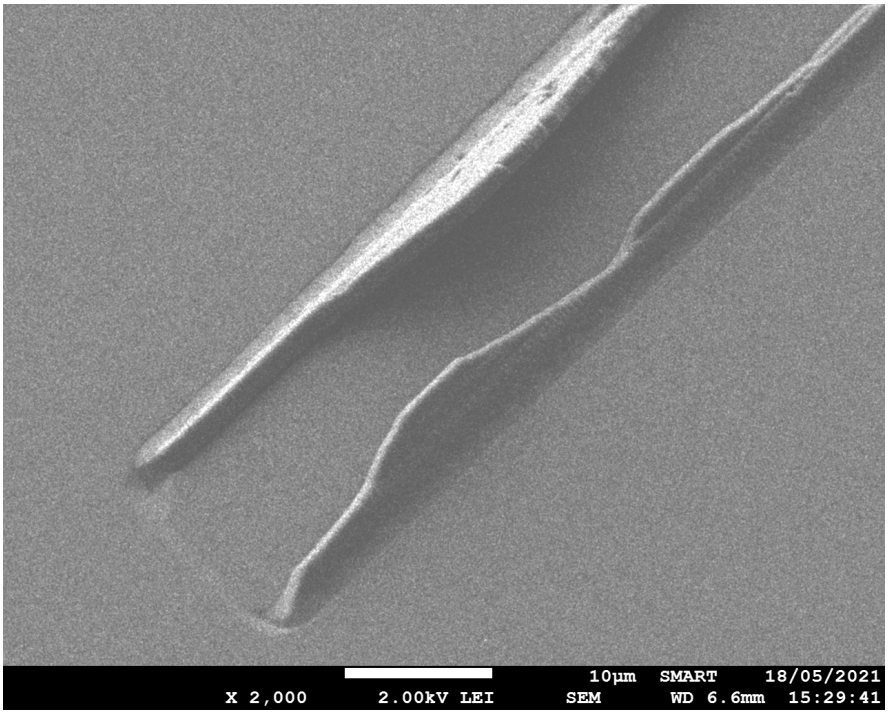

(a) Enhanced selective growth: Top view

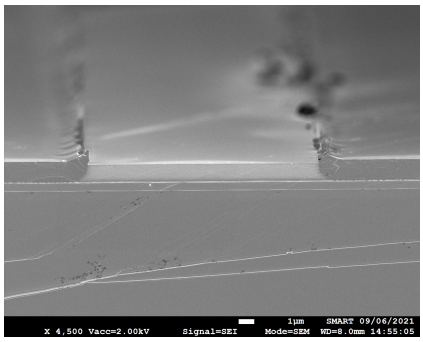

(b) Samples before common top layer deposition, general view

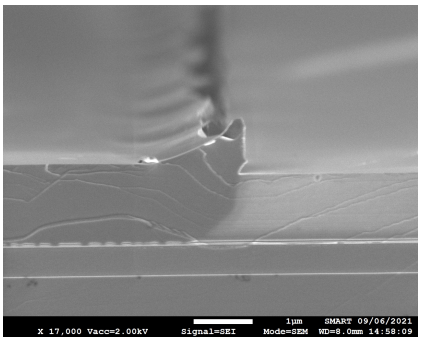

(c) Samples before common top layer deposition, zoom

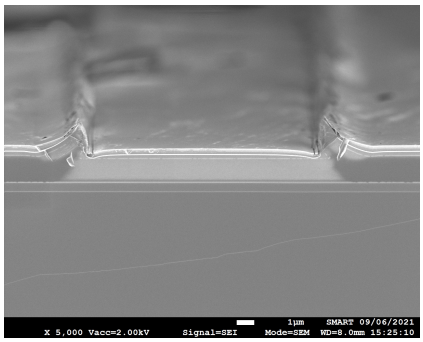

(d) Samples after common top layer deposition, general view

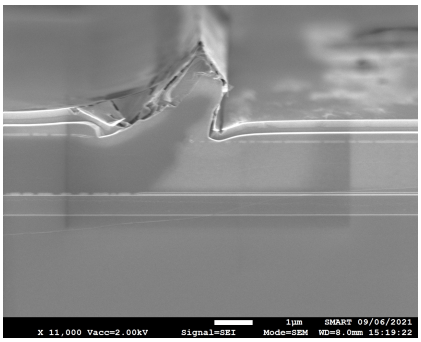

(e) Samples after common top layer deposition, zoom

Figure 6.1: Examples of rabbit ears effect

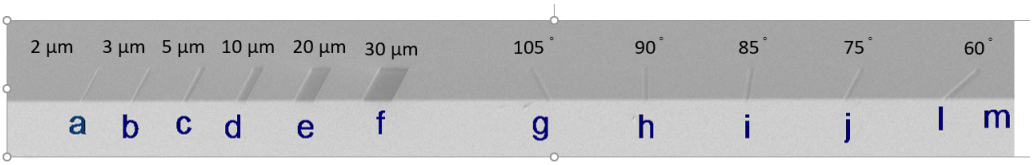

(a) The mask variations we investigated

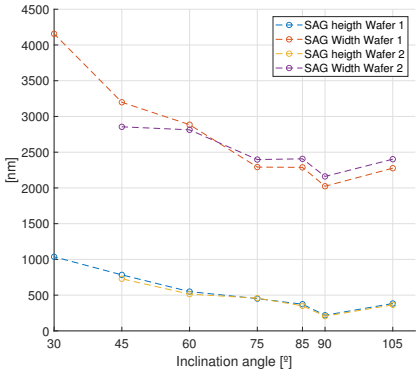

(b) The impact of angled mask on sag width and height

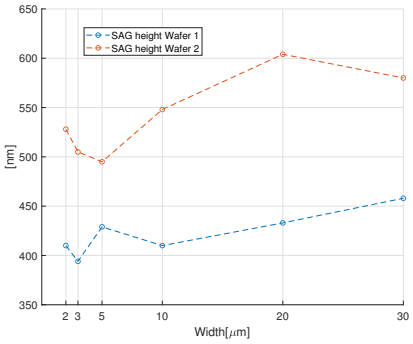

(c) The impact of mask width on sag height

6.1.2 Mask opening

An interesting solution comes from the paper of Wang [29]. Here the mask defining the butt joint is almost completely opened in its center before the regrowth process. In this way only a thin border of the original mask is preserved. After the definition of this frame layers are deposited as usual and, the mask being open, layers grown into the mask as well. Compared to the solid mask configuration, there is much lower concentration of precursors at mask edges and the SAG is diminished by 20 times.

Despite being very promising this technique presents some drawbacks. The first one is that many extra steps are necessary in production. The proposed technique presents many extra steps that we would like to avoid at least at this early stage of investigation. Right now, the goal is to prove that the second but joint is beneficial to loss reduction. Second is that the size of the mask tested in the paper is much bigger than ours. The width of frame that is left after processing 10 is comparable to the width we already have. Therefore we could say that this technique seems to be more useful for having few large doped area on the wafers rather many single tiny ones like the one we need.

Variations on this idea are possible: for instance in [30] the process is similar but inverted. In Figure 6.4 we see a scheme of this solution. Here

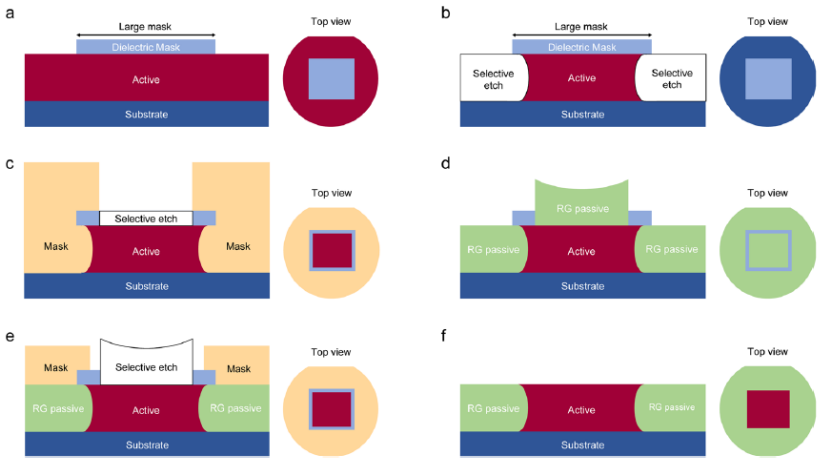

Figure 6.3: The mask is opened during processing to reduce SAG [29]

the masks are used for etching little wells in the core layer 6.4.b, new layers are deposited everywhere on wafer surface (red in Fig 6.4.d), but are then subsequently etch expect for where need 6.4.e). The paper presents the process as a technique to integrate the active and passive core layers, but for sure in can be re-adapted to our investigation. To summarize both ideas are interesting and worth to be investigated further. The main concern is how narrow the masks can and has to be made, to prevent rabbit ears formation.

6.1.3 Wet etching techniques

An alternative (or even complementary) approach consists in using specific wet etchant chemicals to create the so called *undercut*. The *undercut* technique consists in removing part of the semiconductor below the hard mask used to define high dope are like in Figure 3.5b. This literally creates a trench below the mask that gets filled with the excess of material during the epitaxy. Since the excess of material is deposited in the undercut, this prevents the SAG effect. Despite the simplicity of the idea this is not easy to be achieved. To understand why let us quickly speak of the crystalline structure of InP. In Crystallography Miller index are used to define planes in crystals. In Smart Photonic wafers, the flat surface of a wafer corresponds to the [001] plane. The vertical direction of the wafer (often called North-South direction) corresponds to the $1\bar{1}0$ direction while the 110 is the horizontal (Est-West) direction. The planes are shown in Figure 6.5b.

One thing to consider for instance is that given the Zincblende struc-

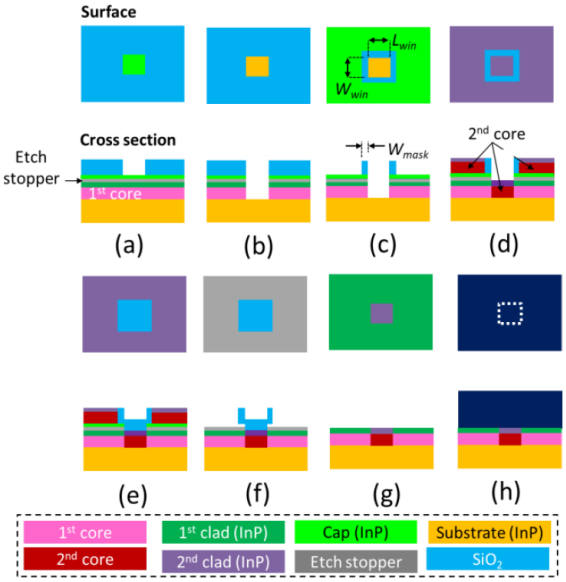

Figure 6.4: The mask is used to create a well where layers are regrown [30]

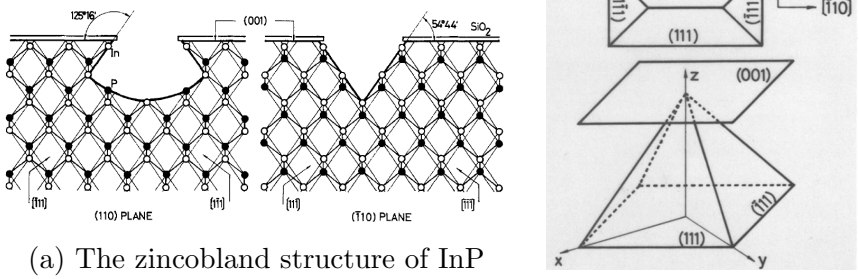

(a) The zincobland structure of InP

(b) Definition of planes

Figure 6.5: InP crystal structure along different planes [31]

ture of InP, The [110] and [$\bar{1}$10] planes have different chemical and physical properties due to different atomic disposition [32] [33]. In Figure 6.5a we see such atomic dispositions along the two planes. Solid circles represent P while empty ones represent In. Along the two directions In and P are exchanged in position. This implies that the crystallographic plane [111] (Figure 6.5b) exists in two types: one made purely of P and the other made purely of In.

If we look at atoms of the plane [111], when such layer is exposed at air, the atoms have only three bondings with the rest of the semiconductor instead of four like for bulk atoms. Let us remember In has three electrons in the outer shell while P has five. This implies that when they are exposed as surface atoms, In still has all his electrons involved in a covalent bond. P on the other hand has two spare electrons ready to bond with other chemicals, thus making it much more chemically active. This asymmetry makes the etching along the planes [110] and [$\bar{1}$10] different even when the same chemical is used. As a result in not unusual to have different etching speed along the planes or even different planes exposed. The most extreme consequence is that the undercut might be present only in one of the two planes.

Another criticality is that the amount of undercut required must depends mainly on the mask area and on the thickness of the regrowth necessary. To address all this question we have decided to test three different etchants along the North-South and Est-West wafer directions. Different combinations of dry and wet etch were also tested. The selected etching solutions are: phosphoric acid $H_3PO_4 : H_2O_2(1 : 1)$, sulphuric acid $H_2SO_4 : H_2O : H_2O_2(1 : 1 : 5)$, and citric acid $HOC(CO_2H)(CH2CO_2H)_2 : H_20(1 : 2)$. It is interesting to explain why we used water peroxide instead to water: this is because it triggers the oxidization of InP making it much more reactive with both Phosphoric and sulphuric acid.

From previous experimented we got an estimation of the etching speed of the chemicals: the phosphoric acid we obtained an etching speed of $7.5nm/s$ with a later etching speed of $7nm/s$ and $3nm/s$ respectively in west-est and north-south direction. Sulphuric acid had a vertical etching speed of $7nm/s$ while citric acid etching speed is only $1.5nm/s$.

Given that from chapter 4 we discovered that doing a partial regrowth is not beneficial for the quality of the chips, we have decided to simulate a full regrowth of the $ETL3$ so with a total thickness of about $1500nm$. All the information are summarized in Table 5.1.

For each of the sample reported here we have made a cross section in the North-South direction and one in the Est-West. The samples were imaged before and after the regrowth process so evaluate how the different proportion of wet and dry etch affect final rabbit ears dimensions. In the following pages we see the images of the samples acquired with SEM. Images are

	WET	DRY	WET	DRY	WET	DRY
H_3P0_4	660 nm	990 nm	1148 nm	507 nm	1550 nm	-
H_2SO_4	-	-	450 nm	500 nm	700 nm	-
Citric acid	530 nm	970 nm	-	-	-	-

Table 6.1: Summary of the test samples created

grouped together based on the etchant and cross section direction. Let us start our analysis by Figure 6.7 to evaluate the quality of Phosphoric acid based etch in north south direction. In subfigures $(a), (c), (e)$ rabbit ears are still present. We notice in particular when we increase the proportion of wet etch to dry etch, rabbit ears gets bigger. The measured values for the three images are respectively $530nm$, $592nm$ and $830nm$. Compared to Figure 6.1e, where we had ears of $2\mu m$ the improvement is quite evident, but why do we get such differences in height among the thee samples? Let us analyse the sub Figures $(b), (d), (f)$. The angle of the sidewalls in the three pictures is different. It particular we measured 56 deg, 49 deg and 48 deg. Are this two different angles sufficient to explain the difference? Not easy to claim. From Figure 6.6a we see that InP grows also on sidewalls in the MOCVD process, However is not straightforward to predict the angle of this growth. If the angle of the sidewalls where the main source of rabbitears, we would than expect for sample in Figure 6.7.(c) to have rabbit ears dimension closer to sample in Figure 6.7.(e) given that they have similar sidewalls angles. This is however not the case. More in-depth studies (for instance doing SEM of samples during different stages of regrowth) would be required to give a definite answer to the question.

If we move on to samples of Figure 6.8 we can look at the same three samples from the EW direction. Here we get the opposite problem that is undergrowth: InP does not growth until the desired height and a valley originates. In subfigures (b) and (e) we see that the volume created with the undercut increases with the ratio wet etch/dry etch. It would therefore beneficial to diminish this ratio so to have shorter trenches below the mask. Before moving on to the other samples is worth to point out one thing: in Figure 6.7 rabbit ears are absent in the north-south direction (perpendicular to the viewer). This is caused by the width of the mask that is only of $3\mu m$. In other images taken from the same perspective but with wider mask width rabbit ears regrowth is clearly visible. This triggers a new question, what would happen if instead of rectangular masks we were to use mask with more irregular shapes, for instance segment with so to say bays and promontories

of $2 - 3\mu m$ characteristic dimensions? Still in combination with undercut it could diminish even further rabbit ears.

Anyway, of all the solutions tested the most promising recipe seems the one of Figure 6.9a that is a sample where $450nm$ of material where dry etched and other $500nm$ were wet etched with the sulphuric acid solution. Here no rabbit ears at all are present and other waveguides on the same chip have same quality. If we look at the est west direction as in Figure 6.10a some undergrowth is still present, but less pronounced compared to Figure 6.8. Unfortunately samples of Figure 6.10c and Figure 6.9c where overgrown and no interesting information can be deduced from this samples.

Last samples to show are the one etched with citric acid of Figure 6.6. Given the extremely low etching speed of citric acid ($1.5nm/min$) we have prepared only one sample that had to remain in citric bath for 8 hours. For this chip the regrowth process happened to be shorter than needed and is therefore not clear what the final outcome would have been. However is interesting to notice in Figure 6.6d and Figure 6.6b how exposed walls are different from the others etchant used.

At the end of this investigation we can say that the undercut has proved the capability of mitigate rabbit ears effect, the best results have been obtained with a sulphuric acid test where the ratio of wet and dry etch was close to one. This is excellent starting point but is likely that the technique can be improved further. A more systematic study with many more variations of mask critical dimensions is mandatory if rabbit ears need to be further reduced.

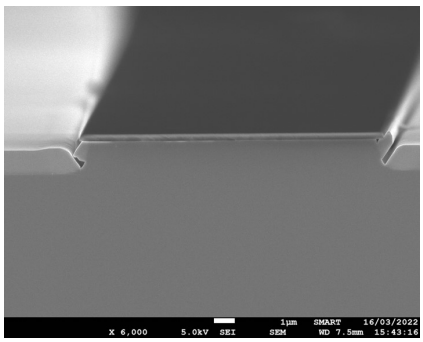

(a) Wet etch: 1/3, Dry etch: 2/3 NS direction

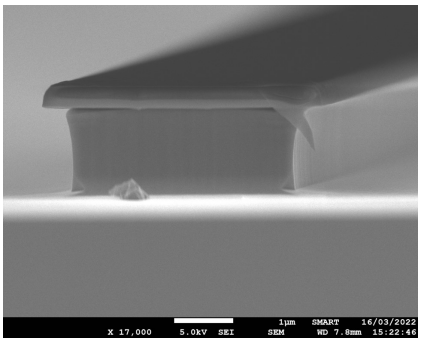

(b) Wet etch: 1/3, Dry etch: 2/3 NS direction

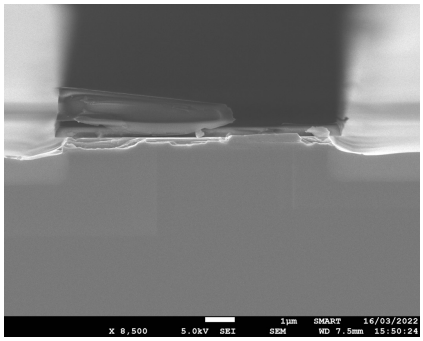

(c) Wet etch: 1/3, Dry etch: 2/3 EW direction

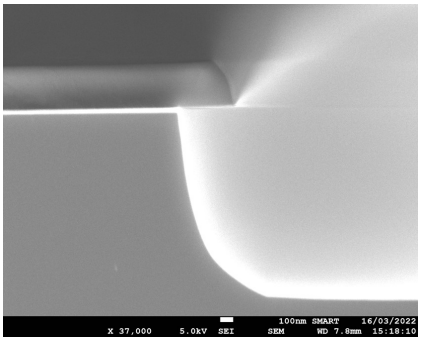

(d) Wet etch: 1/3, Dry etch: 2/3 EW direction

Figure 6.6: Citric acid sample etched in both direction

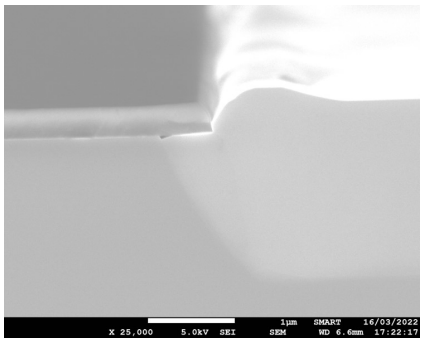

(a) Wet etch: 1/3, Dry etch: 2/3

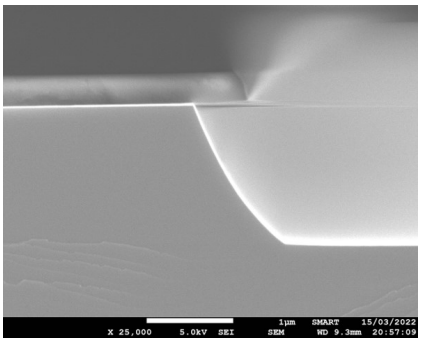

(b) Wet etch: 1/3, Dry etch: 2/3

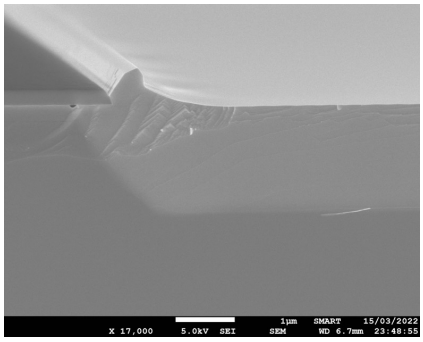

(c) Wet etch: 2/3, Dry etch: 1/3

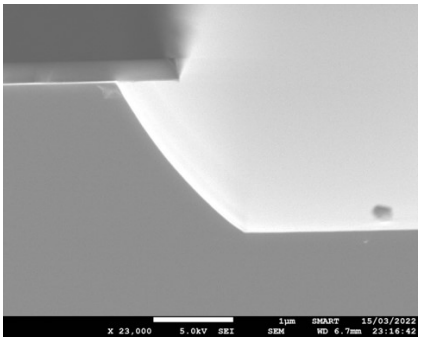

(d) Wet etch: 2/3, Dry etch: 1/3

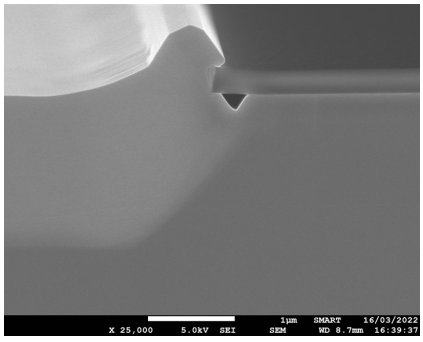

(e) Wet etch: 3/3, Dry etch: -

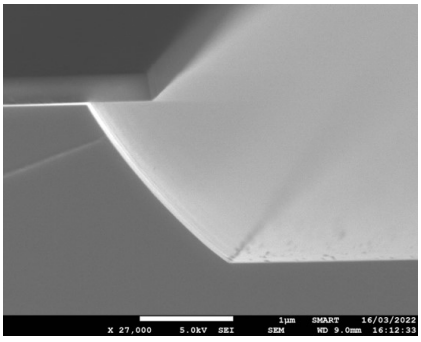

(f) Wet etch: 3/3, Dry etch: -

Figure 6.7: Samples etched with H_3PO_4 in NS direction, cross section

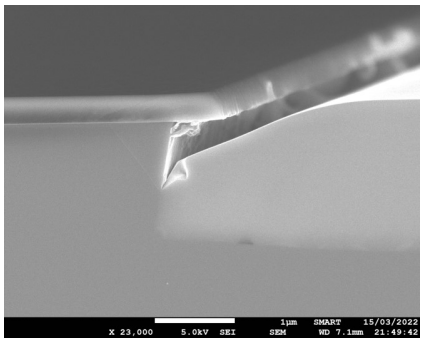

(a) Wet etch: 1/3, Dry etch: 2/3

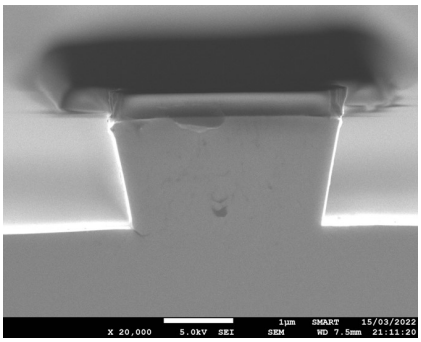

(b) Wet etch: 1/3, Dry etch: 2/3

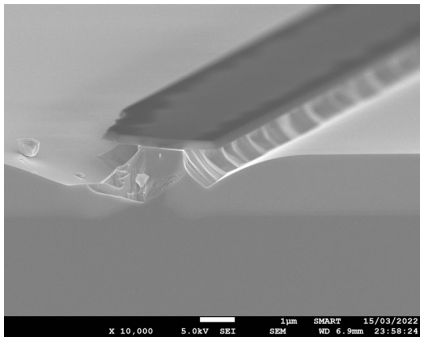

(c) Wet etch: 2/3, Dry etch: 1/3

(d) No available sample

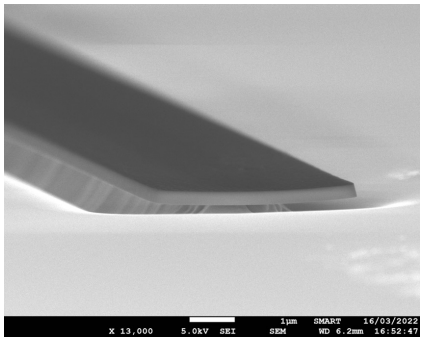

(e) Wet etch: 3/3, Dry etch: -

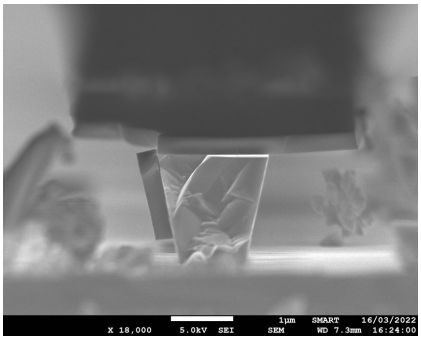

(f) Wet etch: 3/3, Dry etch: -

Figure 6.8: Samples etched with H_3PO_4 in EW direction, cross section

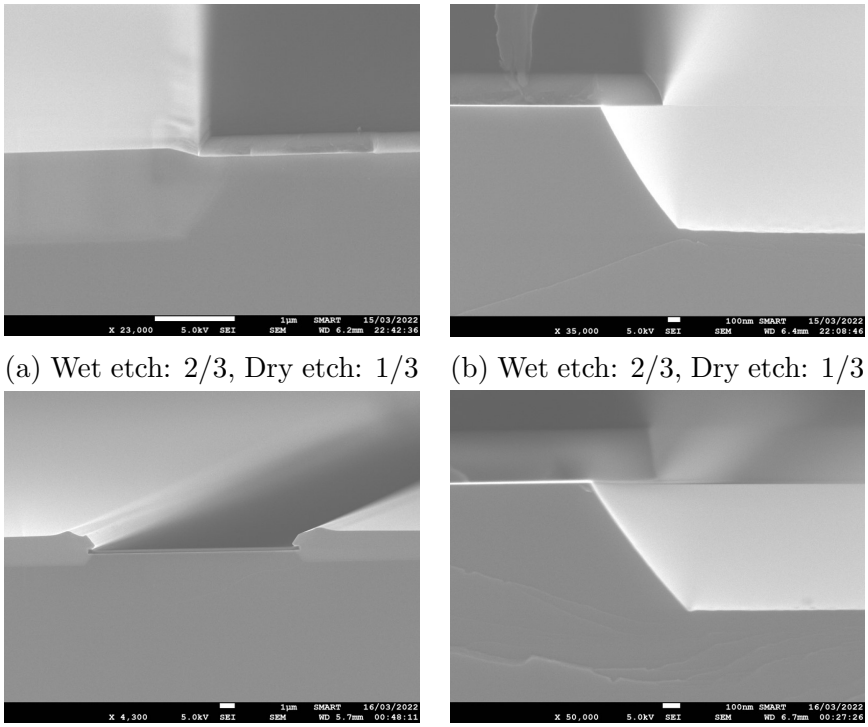

(a) Wet etch: 2/3, Dry etch: 1/3

(b) Wet etch: 2/3, Dry etch: 1/3

(c) Wet etch: 3/3, Dry etch: -

(d) Wet etch: 3/3, Dry etch: -

Figure 6.9: Samples etched with $H2SO4$ in NS direction, cross section

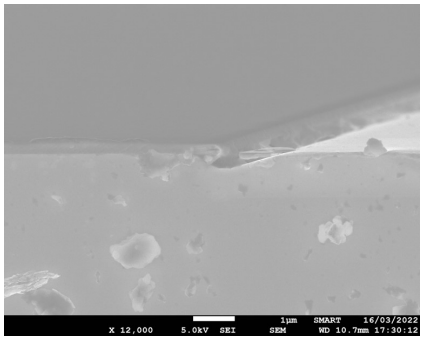

(a) Wet etch: 2/3, Dry etch: 1/3

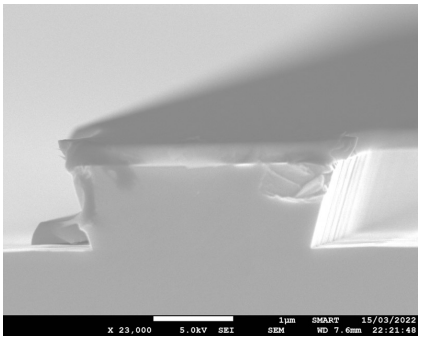

(b) Wet etch: 2/3, Dry etch: 1/3

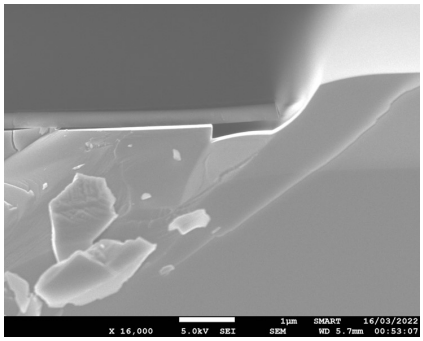

(c) Wet etch: 3/3, Dry etch: -

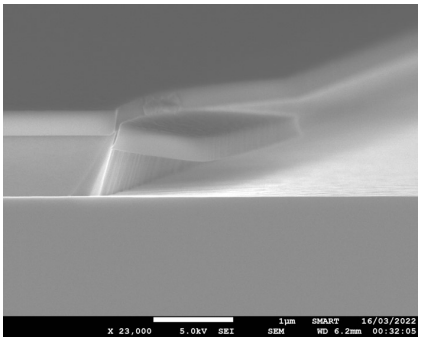

(d) Wet etch: 3/3, Dry etch: -

Figure 6.10: Samples etched with $H2SO4$ in EW direction, cross section

6.2 Doping migration

The main advantage of double butt joint compared to the Zinc diffusion approach is the fact that is possible to deposit doping at the required concentration in the required position in the layerstack. There is however the chance that in the regrowths process (Figure 3.5d and Figure 3.5c) the heat up of the wafers causes the doping to migrate anyway. To test this hypothesis we did the following experiment. One wafer has been grown with the standard layerstack and standard doping concentration up to the $InGaAsP$ layer. Such layer will be grown later. The wafer was then cleaved in four quarters (A, B, CD) which underwent different heat treatments. The quarter A has been kept aside and used as a reference. The quarters B, C, D have been heated a first time to simulate the growth of the undoped layer Figure 3.5c. The quarter B was then kept aside. Quarter C and D has been heated again as to simulate the second regrowth step in Figure 3.5d. Only the quarter D was regrown with the final layers of $InGaAsP$. The doping profiles of the four samples has been measured with two different techniques: CV and SIM measures. In the first technique the sample is etched from the bottomside in a bath of acid. The conductivity of such acid is changed

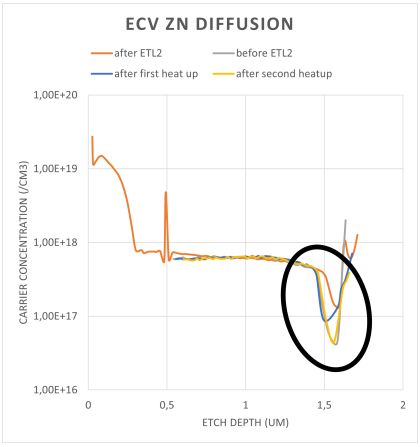

(a) The doping profiles obtained for the four samples

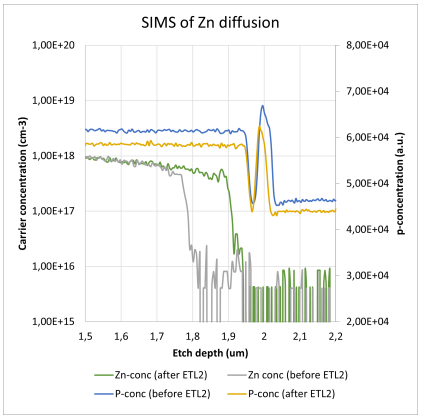

(b) The doping profiles obtained for samples A and D

by the concentration of Zinc present in the chip. Such conductivity is measured and gives an estimation of Zinc concentration. This technique is faster and cheaper than SIM but it also less accurate. After the first measure we haven't been able to draw any significant conclusion. Therefore we decided to use SIM. In this technique the sample is bombarded by ions. Resulting particles are collected and analysed with a mass-spectrometer that allows to

determine the concentration of the doping. In Figure 6.11a the doping concentration of the four samples is plotted versus the distance from the surface of the wafer. We are interested to what happens to the dopant concentration inside the black circle, at a depth of $1.5\mu m$ from surface. Here the doping concentration must decrease because we are approaching the core layer of the waveguides. Gray line corresponds to sample A, and is the doping concentration we want to preserve. If we look at the orange line (sample D) we see that zinc has diffused more in depth for about $80nm$. This has not happened for the other two samples (blue and yellow line). The migration of doping is more accurately characterized in Figure 6.11b. Here grey and green line represent Zinc concentration in sample A and D respectively. The offset is clear and confirmed and estimated in $120nm$. Yellow and Blue line are Phosphorous concentration and used as a reference to properly offset the two measures. So with this experiment we have been able to show that zinc migrates during the heat up necessary to grow the butt joint. This phenomena will have to be taken into account when choosing the doping of the layerstack.

6.3 Etching quality

One possible explanation for the higher losses measured in Chapter 4 may be related to the fact that wafers with a butt joint has undergone many more steps in fabrications compared to wafers with standard layerstack. This extra steps could have lead to considerably more defects so that the benefits of doping reduction is overwhelmed by fabrication induced losses. Figure 6.12, Figure 6.13 and Figure 6.14 compare waveguides on three different chips. In Figure 6.12 we see that sidewalls are smooth and with no evident irregularities, this indeed was the wafer were no butt joint was performed. In Figure 6.13 and 6.14 we see waveguides where the butt joint was performed respectively at $800nm$ and $1200nm$. It is possible to notice some roughness along the waveguides (shown by red arrow) at an high compatible with the butt joint thickness. Such irregularities are probably present also inside the waveguides, where they can interact strongly with the optical mode. New investigations are required to try to smooth such defects, that are probably linked to the high loss value measured.

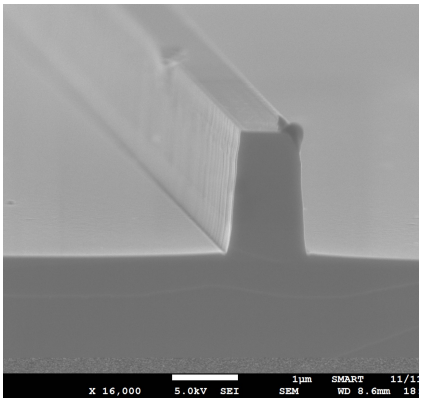

Figure 6.12: SEM cross section, standard layerstack

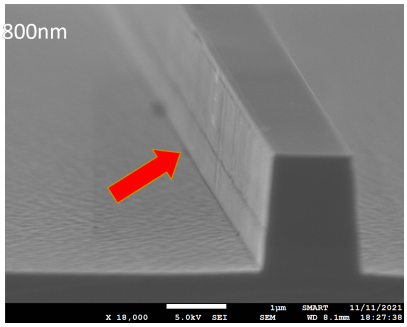

Figure 6.13: SEM cross section, 800nm butt joint, red arrow points at roughness introduced by butt joint process

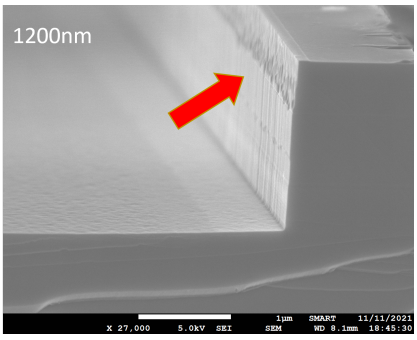

Figure 6.14: SEM cross section, 1200nm butt joint,red arrow points at roughness introduced by butt joint process

Chapter 7

A novel wavelength meter concept

Over the recent years, development of integrated wavelength meters has drawn significant attention from the scientific community. Miniaturized wavelength meters are employed in numerous applications, such as Wavelength Division Multiplexing, spectroscopy, metrology, and operational control of tunable lasers. State of the art integrated wavelength meters centred at $1550nm$ wavelength have either very narrow bandwidth and high precision ($5nm \pm 8pm$) [34] ,[35] or increased operation bandwidth compromising the resolution ($40nm$, $\pm$ $0.075nm$) [36]. In this chapter I will present a novel design that increases the operational bandwidth of a ring resonators based wavelength meter maintaining a high accuracy limited by the Full Width Half Maximum ($FWHM$) of the resonators. As it will be evident at the end of the chapter, low loss waveguides can improve the performance of the device.

7.1 Wavelength meter design

In Figure 7.1 the schematic of the circuit is reported. An input source is coupled from the left-hand side and guided to four resonant rings in the so called all-pass configuration. In every ring a Phase shifter (PHS) permits to add an extra phase shift θ to the optical path. At the *through* port of every ring a photodetector is present. The wavelengths λ resonance condition for the n^{th} ring is:

$$\lambda_n(i) = \frac{l_n n_{eff}}{i + \theta(V)/2\pi} \tag{7.1}$$

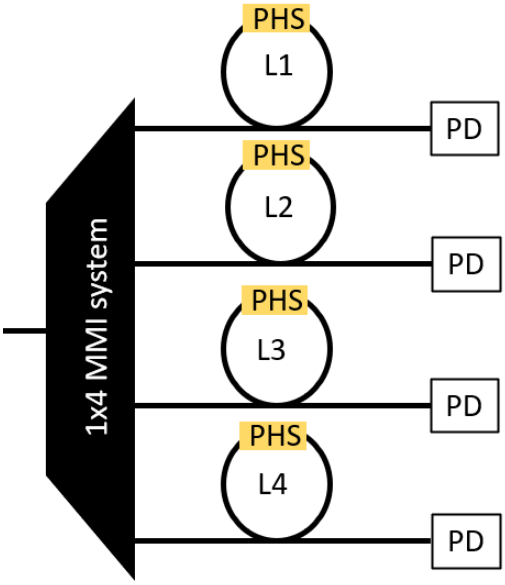

Figure 7.1: A schematization of the wavelength meter. The unknown laser source is guided to 4 ring tunable ring resonators and the signal is measured with 4 photodiodes.

given i a positive integer, l_n radius of the ring, n_{eff} the effective index of the ring and $\theta(V)$ the phaseshift added. When this condition is fulfilled, a minimum is registered at the photodiode. By changing the phase $\theta(V)$ in the range $[0 - 2\pi]$, we obtain a unique subset of wavelengths on resonance with the ring. We can identify those wavelengths with $\lambda_n(i, V)$ where n identifies the ring, i an index that counts the resonance wavelength and V is the applied voltage. The subsets of $\lambda_n(i, V)$ could be calculated theoretically, however, accurate modelling is challenging, so we opted for an external calibration of the system. We will explain the calibration further below. For now, let us assume that we know exactly all the subsets $\lambda_n(i, V)$ for all the possible triplets (n, i, V). When an unknown laser source is coupled to the device, the source is carried to all the rings and the intensity of the light transmitted through the rings is measured at the detectors. PHSs are driven to sweep the phase $\theta(V)$ in the interval $[0, 2\pi]$. During this sweep all the 4 detector signals are acquired. All PDs have a minimum in transmission that can be associated with a voltage V_n that makes the wavelength resonate with the ring (Figure 7.2). Using the calibration database it is possible to obtain the subsets of wavelengths $\lambda_n(i, V_n)$ that resonate with the ring in that specific condition (Figure 7.3). From the four rings we obtain four different subsets of

wavelengths that resonate with the ring in such condition. The intersection of the four subsets determines a unique wavelength that is the input unknown wavelength (Figure 7.4).

7.2 Rings design

All the rings are of different length in order to allow for the Vernier effect. It is advantageous to keep the ring length as short as possible. A shorter ring has higher Q factor and consequently a smaller $FWHM$, thus improving the resolution of the wavelength meter. Shorter rings also have a wider free spectral range, thus increasing the operational bandwidth of the device. The all-pass ring configuration has been preferred to the add and drop because it allows to keep the rings shorter and prevents extra losses due to the presence of a drop port. The minimum length of the ring is fixed by a number of design constrains. Every ring must have a directional coupler, a PHS long enough to guarantee a 2π phase shift and two 180 degrees bends with a small radius of curvature. This typically leads to a minimum length in the range $1-3mm$ depending on the platform. The shortest ring we were able to design in the chosen platform has a length of $L_1 = 3318\mu m$. With a single ring is already possible to measure wavelengths after calibration, however the bandwidth is possible to investigate is equal to the FSR of the ring. Indeed if the source is unknown in an interval wider than the FSR of the ring, in such interval there are two or more wavelengths that fulfil Eq.7.1 We can estimate the FSR using the equation:

$$FSR = c/(n_g l_n)$$

With our shortest ring and taking $n_g = 3.5$ we expect an FSR close to $25GHz(0.2nm)$ at a central frequency of $193THz$. By using additional rings however, we can expand the operational bandwidth of the device. The resonances of the n^{th} ring is expressed in Eq.7.1.

By changing the phase $\theta(V)$ of each ring we can tune both rings on resonance with the unknown source. Given that the FSR of the two rings is different, only few resonances will be in common among the two rings. In particular we can chose the rings lengths such that in a known bandwidth center at a specific frequency, only a wavelength resonates with both rings when the potentials V_1 and V_2 are applied. In this way the second added ring lets us expand the operational range of our device. We can compute the new combined free spectral range as [37]:

$$FSR_{1-2} = FSR_1 L_1/(L_1 - L_2)$$

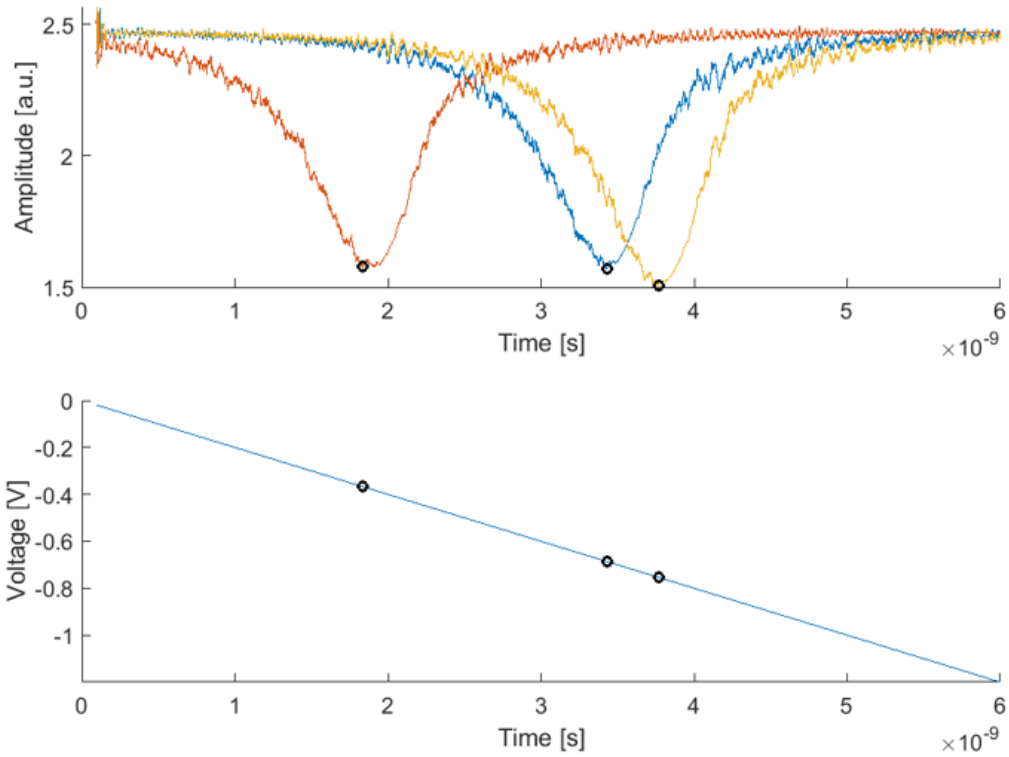

Figure 7.2: Linearly changing voltage signal fed to phase modulators makes the rings (only three in this image) resonate with unknown wavelength. Resonances associated voltages (black circles) are identified.

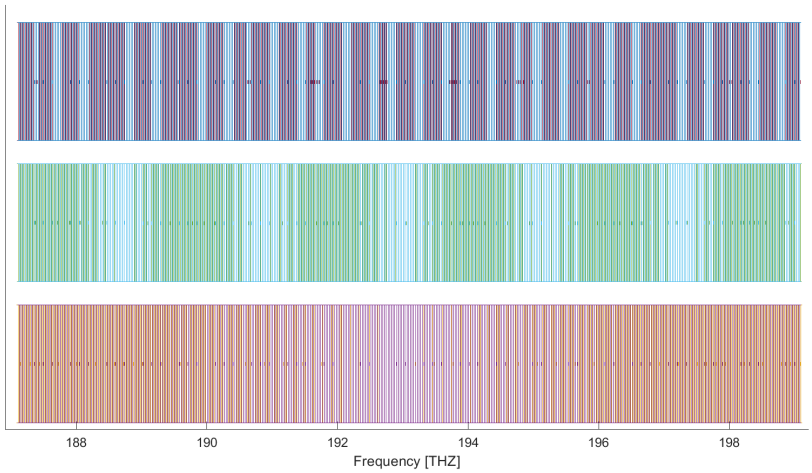

Figure 7.3: Vertical lines correspond to resonant wavelengths of the rings. The three horizontal band are obtained by plotting all individual resonances of the couples of rings L_1L_4, L_1L_3, L_1L_2.

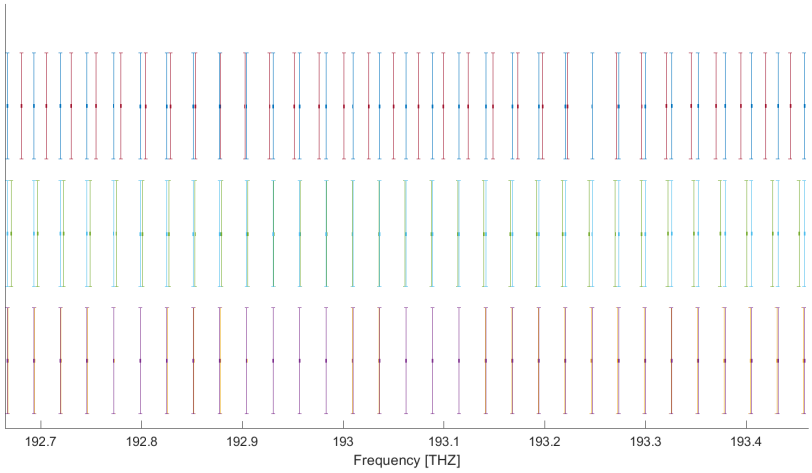

Figure 7.4: A zoom of previous image. Horizontal bars are the uncertainty on wavelength position. The resonance at $198.88Thz$ is the only one in common to all the rings, thus it correspond to the unknown wavelength.

We have used a second ring with length $L_2 = 3324\mu m$ that corresponds to $FSR_{1-2} = 14.3THz$ $(100nm)$. However, a new problem arises: the resonance peaks are not perfectly sharp. They have a $FWHM$ that limits the resolution on resonances reading. Knowing the Q factor of the cavity we can derive the $FWHM$ of the peaks as $FWHM = \omega/Q$ where ω is the resonance frequency. Potentially this means that if $(\lambda_1(i) = \lambda_2 j))$ is valid for indexes $(i_0;\ j_0)$, it might also be true for the indices $[(i_1, j_1),\ (i_2, j_2) \ldots]$. We can solve this ambiguity of having only a couple of indexes $(i_0,\ j_0)$ by adding a ring of length $L_4 = 3578\mu m$. This length has been chosen such that the difference $FSR1 - FSR4 > FWHM$. With our lengths this led to $FWHM$ $1.8GHz$. Such constrain on the full width half maximum corresponds to having $Q > 10^5$. We can see a visualization of this process in Figure 7.2 and Figure 7.4. The joint FSR_{12} covers the full bandwidth of the device and identifies a single region where $(\lambda_1(i) = \lambda_2(j))$. This condition is satisfied for several couples of values of (i, j). With the joint FSR_{14} we can identify the single couples of indices $(i_0; j_0)$ that fulfil $(\lambda_1(i0) = \lambda_2(j0))$. However, simulating the device spectral response in VPI, we have seen that three rings are still not sufficient to find a single couple of indexes $(i0;\ j0)$. This has been solved by adding a ring of length $L_3 = 3378\mu m$ and using an identical procedure to remove such ambiguity.

7.3 Calibration procedure

In order to calibrate the device an external known tunable laser source is necessary that ideally covers the entire operational bandwidth. In practice, even a source with a narrower range can be used and the calibration expanded using a polynomial fit. The laser is swept over the bandwidth and fed to the circuit. Transmission spectra are recorded for every ring. The procedure is repeated for different voltages storing the different acquisitions. This creates a calibration database that can be used to track the resonant wavelengths. Even using few voltage points is possible to use a polynomial fit to predict the resonances for an unknown voltage.

7.4 Measurement speed

A ring resonator has a typical cavity lifetime that is determined by the Q factor: $Q = \omega\tau_s$. A time $T = 3\tau_s$ is necessary before considering the ring to be stabilized [27]. The applied voltage span mast be sufficient to tune the phase shifter up to 2π. To tune the ring on resonance with the unknown

source, a voltage ramp in the range $(0 - V_{2\pi})$ is applied to the phase shifter. We know that the source will not be continuously varied but will be similar to a staircase. It is important to choose the correct number of steps (m) of this stair, in order not to lose resolution on the readings, but also not to oversample the curve thus increasing considerably the readout time. Given that the limit resolution is equal to the $FWHM$ of the ring, we have decided to take: $m = 2FSR/FWHM = Q(2FSR)/\omega$ We can express this equation in terms of Q to estimate the time T necessary for a complete measurement as: $T = m\tau_s = 6FSRQ^2/\omega^2$. This is because for every single voltage increment we supply to the ring we want to wait a time τ_s for the ring to stabilize. We can notice from this equation that the measurement speed scales with the square of the Q factor. In the following table we estimate the speed of our device for different Q factors at constant single ring $FSR = 30GHz$ and $\omega = 193THz$. An important remark is necessary, the measurement speed does not depend on the number of rings since all the rings are measured simultaneously.

Q factor	reading time	resolution
10^4	500 ps	160 pm
10^5	50 ns	20 pm
10^6	$5\mu s$	1.6 pm

7.5 Conclusions

A new photonic-integrated wavelength meter based on multiple ring resonators has been presented. The theory shows that the measurement speed scales with the square of the Q-factor of the ring resonators, while the measurement resolution scales inversely proportional with the Q-factor. The development of low losses waveguides will allow to increase the Q factor thus increasing the performances of the device The possibility of integrating high speed modulators combined with the simultaneous measurement of multiple ring resonators, allows for fast wavelength measurement speeds.

Chapter 8

Conclusion

Reducing passive components losses trough second butt joint integration has revealed to be challenging. From Figure 5.1 we have seen that the first implementation has not been successful. However, with Figure 5.2 we have been able to prove once more that doping has a significant impact on losses and that restricting its use where needed is fundamental to improve platform performances. In the same chapter we have shown how losses can be effectively measured using ring resonators, and how using ring resonators of different lengths allow to extract MMI insertion loss. Laser stability and tunability is fundamental to obtain reliable measures, nonetheless the response was the one expected and the method is valid both for integrated or external laser sources. In Chapter 6 we established a new wet etching scheme for limiting rabbit ears effect. The sulphuric acid solution has turned out to be the most effective in limiting the phenomena. We have also established that a doping migration of $100nm$ occurs in the regrowth and that sidewalls roughness is introduced by the technique. If we compare the second butt joint to zinc diffusion proposed in [19]we can affirm:

- Zinc diffusion is hard to control, the butt joint however has many possible source of defects not easy to eliminate.
- The impact of the two techniques on active components is basically unknown. An experiment comparing the real performances of active building blocks such as lasers, modulators and phases shifters is mandatory to prefer one method over the other.
- Both techniques suffer in some degree from the difficulty of controlling the diffusion of zinc. At the moment not many data are available, a detailed investigation with many wafers and samples taken from different

location of wafer is necessary to address the uniformity and repeatability of zinc diffusion. This investigation would be beneficial for both techniques.

- Zinc diffusion is simpler to implement, but limited control is achieved on doping profile. Second butt joint is more elaborated, but when successful it guaranties a higher control on doping profile.

To conclude we have presented a new method of creating low loss waveguide on the Smart Photonics InP photonics integration platform. Measured losses are higher than expected, but they can be related to doping migration and extra roughness created by the interaction of the new process steps and the etching. Further optimization on the integration scheme is necessary but once optimized this method will lead to lower loss passive componentes.

Bibliography

[1] Meint Smit, Kevin Williams, and Jos van der Tol. Past, present, and future of InP-based photonic integration. *APL Photonics*, 4(5):050901, May 2019.

[2] Xiling Wu, Caihua Zhang, and Wei Du. An analysis on the crisis of "chips shortage" in automobile industry ——based on the double influence of COVID-19 and trade friction. *Journal of Physics: Conference Series*, 1971(1):012100, jul 2021.

[3] Stewart E. Miller. Integrated optics: An introduction. *Bell System Technical Journal*, 48(7):2059–2069, 1969.

[4] Smit et all. An introduction to InP-based generic integration technology. *Semiconductor Science and Technology*, 29(8):083001, June 2014.

[5] Giovanni Gilardi and Meint K Smit. Generic InP-Based Integration Technology: Present and Prospects. *Progress In Electromagnetics Research*, 147:13, 2014.

[6] Francisco Pena, Benjamin Martins, and W. Lance Richards. Adaptive load control of flexible aircraft wings using fiber optic sensing. In *26th International Conference on Optical Fiber Sensors*, page WF101. Optica Publishing Group, 2018.

[7] Jennifer M. Morales, Pak Cho, Justin R. Bickford, Paul M. Pellegrino, Gerald Leake, and Michael L. Fanto. Development of army relevant wearable Photonic Integrated Circuit (PIC) biosensors. In Jason A. Guicheteau and Chris R. Howle, editors, *Chemical, Biological, Radiological, Nuclear, and Explosives (CBRNE) Sensing XXII*, volume 11749, pages 98 – 106. International Society for Optics and Photonics, SPIE, 2021.

[8] E Emil Kleijn. Passive components in indium phosphide generic integration technologies. 2014.

[9] Chris GH Roeloffzen, Marcel Hoekman, Edwin J Klein, Lennart S Wevers, Roelof Bernardus Timens, Denys Marchenko, Dimitri Geskus, Ronald Dekker, Andrea Alippi, Robert Grootjans, et al. Low-loss si3n4 triplex optical waveguides: Technology and applications overview. *IEEE journal of selected topics in quantum electronics*, 24(4):1–21, 2018.

[10] Fadaly E.M.T. Dijkstra A. Suckert J.R. et al. J.r. et al. direct-bandgap emission from hexagonal ge and sige alloys. volume 580, pages 1–21, 205–209.

[11] Jared Bauters, Martijn Heck, Demis John, Ming-Chun Tien, Wenzao Li, J.S. Barton, Daniel Blumenthal, John Bowers, Arne Leinse, and R.G. Heideman. Ultra-low-loss single-mode si3n4 waveguides with 0.7 db/m propagation loss. pages 1–3, 01 2011.

[12] R. G. Heideman, A. Leinse, M. Hoekman, F. Schreuder, and F. H. Falke. TriPleX™: The low loss passive photonics platform: Industrial applications through Multi Project Wafer runs. In *2014 IEEE Photonics Conference*, pages 224–225, San Diego, CA, December 2014. IEEE.

[13] Luc M. Augustin, Rui Santos, Erik den Haan, Steven Kleijn, Peter J. A. Thijs, Sylwester Latkowski, Dan Zhao, Weiming Yao, Jeroen Bolk, Huub Ambrosius, Sergei Mingaleev, Andre Richter, Arjen Bakker, and Twan Korthorst. InP-Based Generic Foundry Platform for Photonic Integrated Circuits. *IEEE Journal of Selected Topics in Quantum Electronics*, 24(1):1–10, January 2018.

[14] Francisco M. Soares, Moritz Baier, Tom Gaertner, Norbert Grote, Martin Moehrle, Tobias Beckerwerth, Patrick Runge, and Martin Schell. InP-Based Foundry PICs for Optical Interconnects. *Applied Sciences*, 9(8):1588, April 2019.

[15] F. M. Soares, M. Baier, T. Gaertner, D. Franke, M. Moehrle, and N. Grote. Development of a versatile inp-based photonic platform based on butt-joint integration. In *2015 11th Conference on Lasers and Electro-Optics Pacific Rim (CLEO-PR)*, volume 2, pages 1–2, 2015.

[16] Rohith Chandrasekar, Zachary J. Lapin, Andrew Nichols, Rebecca Braun, and Augustus W. Fountain III. Photonic integrated circuits for Department of Defense-relevant chemical and biological sensing applications: state-of-the-art and future outlooks. *Optical Engineering*, 58(2):1 – 11, 2019.

[17] Lee H. Chen T. Li J. et al. Ultra-low-loss optical delay line on a silicon chip. volume 3, 2012.

[18] Sibson, P., Erven, C. Godfrey, and M. et al. Chip-based quantum key distribution. *Nat Commun*, 8, 2017.

[19] D D'Agostino. *Capability extensions to the COBRA generic photonic integration platform*. Technische Universiteit Eindhoven, 2015. OCLC: 8086815628.

[20] Payne F.P. Lacey J.P.R. A theoretical analysis of scattering loss from planar optical waveguides. volume 26, page 977–986, 1994.

[21] Daniel K. Sparacin, Steven J. Spector, and Lionel C. Kimerling. Silicon waveguide sidewall smoothing by wet chemical oxidation. *J. Lightwave Technol.*, 23(8):2455, Aug 2005.

[22] Lukas Chrostowski and Michael Hochberg. *Silicon Photonics Design: From Devices to Systems*. Cambridge University Press, 2015.

[23] Walukiewicz W., J. Lagowski, L. Jastrzebski, Rava P., Lichtensteiger M., Gatos C. H., and Gatos H. C. Electron mobility and free-carrier absorption in inp; determination of the compensation ratio. *Journal of Applied Physics*, 51(5):2659–2668, 1980.

[24] R.G. Broeke. *A wavelength converter integrated with a discretely tunable laser for wavelength division multiplexing networks*. PhD thesis, Delft University of Technology, Eindhoven University of Technology, 2003. FLAMENGO Project.

[25] J.-F. Vinchant, J.A. Cavailles, M. Erman, P. Jarry, and M. Renaud. Inp/gainasp guided-wave phase modulators based on carrier-induced effects: theory and experiment. *Journal of Lightwave Technology*, 10(1):63–70, 1992.

[26] W. Bogaerts, P. De Heyn, T. Van Vaerenbergh, K. De Vos, S. Kumar Selvaraja, T. Claes, P. Dumon, P. Bienstman, D. Van Thourhout, and R. Baets. Silicon microring resonators. *Laser & Photonics Reviews*, 6(1):47–73, 2012.

[27] Stefano Biasi, Pierre Guilleme, Andrea Volpini, Giorgio Fontana, and Lorenzo Pavesi. Time response of a microring resonator to a rectangular pulse in different coupling regimes. *J. Lightwave Technol.*, 37(19):5091–5099, Oct 2019.

[28] N. Dupuis, J. Décobert, P.-Y. Lagrée, N. Lagay, F. Poingt, C. Kazmierski, A. Ramdane, and A. Ougazzaden. Mask pattern interference in algainas selective area metal-organic vapor-phase epitaxy: Experimental and modeling analysis. *Journal of Applied Physics*, 103(11):113113, 2008.

[29] Yi Wang, Jorn van Engelen, Rene van Veldhoven, Tjibbe de Vries, Victor Dolores-Cazadilla, Meint Smit, Kevin Williams, and Yuqing Jiao. Versatile butt-joint regrowth for dense photonic integration. *Opt. Mater. Express*, 11(8):2478–2487, Aug 2021.

[30] Ueda Yuta, Saito Yusuke, Ozaki Josuke, Ogiso Yoshihiro, Shindo Takahiko, Hashizume Yasuaki, and Ishikawa Mitsuteru. Partial regrowth of optical-gain section for improved wafer process flexibility of inp photonic integrated circuits. *Journal of Lightwave Technology*, pages 1–1, 2021.

[31] Sadao Adachi and Hitoshi Kawaguchi. Chemical etching characteristics of (001) InP. *Journal of The Electrochemical Society*, 128(6):1342–1349, jun 1981.

[32] John J. Kelly and Harold G.G. Philipsen. Anisotropy in the wet-etching of semiconductors. *Current Opinion in Solid State and Materials Science*, 9(1):84–90, 2005.

[33] Sadao Adachi, Yoshio Noguchi, and Hitoshi Kawaguchi. Chemical etching of InGaAsP / InP DH wafer. *Journal of The Electrochemical Society*, 129(5):1053–1062, may 1982.

[34] R. M. Oldenbeuving, H. Song, G. Schitter, M. Verhaegen, E. J. Klein, C. J. Lee, H. L. Offerhaus, and K.-J. Boller. High precision wavelength estimation method for integrated optics. *Opt. Express*, 21(14):17042–17052, Jul 2013.

[35] Caterina Taballione, Temitope Agbana, Gleb Vdovin, Marcel Hoekman, Lennart Wevers, Jeroen Kalkman, Michel Verhaegen, Peter J.M. van der Slot, and Klaus-Jochen Boller. Temperature-drift-immune wavelength meter based on an integrated micro-ring resonator. In Pavel Cheben, Jiří Čtyroký, and Iñigo Molina-Fernández, editors, *Integrated Optics: Physics and Simulations III*, volume 10242, pages 39 – 48. International Society for Optics and Photonics, SPIE, 2017.

[36] Rajat Dey, Jonathan Doylend, Jason Ackert, Andrew Evans, Paul Jessop, and Andrew Knights. Demonstration of a wavelength monitor comprised of racetrack-ring resonators with defect mediated photodiodes operating in the c-band. *Opt. Express*, 21(20):23450–23458, Oct 2013.

[37] Tin Komljenovic, Linjun Liang, Rui-Lin Chao, Jared Hulme, Sudharsanan Srinivasan, Michael Davenport, and John E. Bowers. Widely-tunable ring-resonator semiconductor lasers. *Applied Sciences*, 7(7), 2017.

Thesis outline

I will write this part once everything settles

Chapter 1 – Introduction

1.1– history and significance of integrated systems

1.1.1 – importance of integration in electronics

While semiconductor research for electronics started in 1940s, and the electronics itself existed since the vacuum tube invention in 1904, the electronic systems remained bulky, expensive, and rarely met in everyday life[1]. Still, electronics played a major role in the early XX century, from radar operation up to radio and television transmissions. Electronics' influence on mankind only increased after invention of the transistor by Brattain, Bardeen and Shockley (honored with Nobel Prize in 1956) [2].

Initially, electronics circuits were discrete, meaning that each fundamental element (transistor, resistor, capacitor, coil) was independent from the structural point of view. All the elements had to be connected separately, wire-by-wire. This approach resulted in bulky systems that were difficult and expensive in terms of manufacturing. Furthermore, those circuits consumed relatively large amount of power due to the size of the components. Also, switching time of logical gates was rather slow due to large distances between them. Those disadvantages made electronics very rare outside of scientific or military use ~~almost a luxury good,~~ [3], [4].

Comentado [SK1]: You might argue they are still a luxury good. Instead, poor performance, high cost and large size were preventing the use of semiconductor diodes outside of a laboratory environment.

A successful approach to combat those deficiencies was devised by Jack Kilby, Robert Noyce, and Texas Instruments / Fairchild in 1958[5]. Chosen approach was to manufacture all the components, already connected in one process. This allowed for significant miniaturization, increase in reliability and made mass-production more scalable. Kilby's contribution to civilizational development was acknowledged with a Nobel Prize in the year 2000 [6].

This has fundamentally changed the civilization, allowing for more portable, cheaper, and more powerful electronics, that quickly became available not only to governments and big companies, but to all the citizens.

1.1.2 – History and advancement of photonics

With the T.H. Maiman's invention of the laser in the year 1960 a new era began. The advent of semiconductor devices that could detect or modulate light, as well as invention of the optical fiber, a new field of physics emerged called "photonics". There was a need to describe systems with interplay of optics and electronics, where semiconductors played central role. There have been two historically significant definitions of photonics. The one, partially anecdotal is attributed to French physicist Pierre Agrain: "the science of the harnessing of light. Photonics encompasses the generation of light, the detection of light, the management of light through guidance, manipulation, and amplification, and most importantly, its utilization for the benefit of mankind" [7]. Another, coined in 1974 by a Dutch engineer, L.J. Poldervaart is the following: "photonics is the name given to the field of science covering systems in which photons are the principal carriers of information" [7]. Both definitions are very broad, which only emphasizes the vast application potential of this research field.

A branch of that new field was "integrated photonics" dealing with Photonic Integrated Circuits (PICs). Earliest research in this field dates back to 1969, when Miller suggested creation of planar optical circuits containing various passive and active elements to control the transmission of light [8], [9]. Such miniaturization appeared very advantageous, because optical signal can transmit data at much higher frequency than the electronic signal. It is because electronic signals of high frequencies face very large impedance from the conductors. To counter the impedance issues, coaxial cables may be employed for electrical signals of circa 100 MHz, facing the impedance of 5 dB/km. This is sufficient for communication of a building scale, but not nearly enough for an intercity or intercontinental scale. This is where optical fiber communications started gaining traction. Since optical communications require optical transceivers, the drive towards monolithic integration of components was inevitable since it promised high cost efficiency, miniaturization, and high reliability [10]. From photonic point of view, telecom transceiver requires integration of WDM filters, lasers, photodiodes, waveguides, and mode-size converters. On top of that, there's a strong desire to integrate photonic and electronic components on the same chip (or using a reliable heterogenous integration scheme) [11]. Quoting from a very recent review on integrated photonics in data centers: "Conventional (non-silicon-photonic) optical modules are complex micro-optical systems made with many discrete components, often hand-assembled, and packaged in low densities with relatively high packaging costs. To catch up, the level of integration and manufacturing automation needs to be raised" [12]. The authors of the review admit that because silicon cannot be used for laser material, III-V type materials (capable of laser action) must be developed to a point of low-loss integration with passive, silicon-based components.

Comentado [SK2]: This warrants more explanation. What are the components of the transceiver that require integration? Up until the present day most transceivers are not (monolithically) integrated devices.

Comentado [MJZ3R2]: I elaborated on that. Is this what you had in mind, or should I add/remove something?

Another important aspect of integrated photonics, is the growing capabilities of “lab on chip” devices, which enable telemedicine, personalized and cheap medical diagnostics, environment sensors etc. [13]–[16]. Jeppix consortium recognizes the following fields, where integrated photonics will play an important role in the upcoming decades [17]:

- Agrifood – sensors for indication of food spoilage
- Biomedical – Biosensors for pathogen detection
- Automotive & Aerospace – Sensors for obstacle avoidance
- Industry 4.0 – Precise manufacturing and quality control
- Information and communication – Multiple uses, such as sustainable internet
- Smart Cities & Smart Living – air quality monitoring, disaster prediction
- Energy & Environment – Detection of dangerous substances, optimization of energy systems.

Other uses of integrated photonics can be for example quantum key distribution, and miniaturized spectrometers. In fact it is agreed upon that Quantum Key Distribution needs mature PIC platforms for their high reliability [18].

Because of importance of all those fields, and the immensely growing data production and transmission, European Comission has recognized photonics as a Key Enabling Technology, marking it strategically important for the technological security and sovereignty of European Union [19], [20].

1.1.3 –Generic integration

Generic Integration – how it is done in the microelectronic industry

Manufacturing of semiconductor devices is a complex process that relies on vast engineering and physical knowledge, while circuit design itself relies on expertise in more abstract fields such as logic and signal processing. It is therefore not effective to specialize in manufacturing process and circuit design at the same time. Hence microelectronic industry uses so called “generic integration technologies”. This approach relies on separation of manufacturing process from the circuit design.

Manufacturing company (called a “foundry”) researches and perfects the manufacturing process for a substantial range of necessary basic circuit elements (such as transistors, resistors, coils, etc.). Those elements are known as BBB (Basic Building Blocks). Detailed, and standardized description of each BBB is included in foundry’s Process Design Kit (PDK), which is shared by the foundry with a circuit designer. PDK also includes important information to be considered in design process, such as BBB’s parameters, their uncertainties, design rules, general description of a process etc. Because BBBs can be used in large amount of completely different designs, it is economically justifiable to spend large efforts on perfecting those blocks, allowing for increased reliability at the fundamental level of circuit structure. Such

standardization also allows for creation of standard software tools and libraries, that can be used by designers, facilitating the design cycle [21].

Processing of a single wafer by a foundry is expensive and can be too costly for a single customer who just wants to manufacture a PIC prototype. Therefore, many foundries offer a service called “Multi Project Wafer”. This way many customers can purchase separate “cells” on a single wafer and order a foundry to manufacture their PIC designs in purchased cells, sharing the cost of manufacturing. This approach makes prototyping affordable and accelerates the design cycle. An institution that acts as an intermediary between foundries and customers in need of fabrication within MPW service is called a broker. One of most significant entities that offers brokering service in the field of electronics is MOSIS, with more than 5000 institutional users [22].

Generic integration in photonic industry

In the early days of integrated photonics it was difficult to obtain funding for development of manufacturing process development without a well-defined application. This approach to funding resulted in plenty of manufacturing technologies, each yielding a particular application-specific photonic circuit[23]. Such large market fragmentation made research of new devices more difficult due to lack of capital concentration and high cost of materials, cleanrooms, equipment and highly specialized staff. Generic processes were introduced in electronics in 1979, but only in 2008 in photonics [21].

In little more than last decade, in the photonic industry there have been strong drive towards introduction of economical model that made electronic device so successful. A pioneering work in the field of generic integrated photonic technology was done by COBRA institute[24]. Its leader, prof. dr. Meint Smit was awarded with John Tyndall Award for “leadership in building a photonic integration ecosystem, and pioneering contributions to key photonic devices including the arrayed waveguide grating.”[25]

In the European integrated photonic ecosystem there are two main consortia that facilitate the growth of research and businesses in integrated photonics:

- JEPPIX
- ePIXfab

JEPPIX was founded in 2006 and has a headquarter in Eindhoven. Material platforms of Jeppix members are Indium Phosphide and Triplex [26]. ePIXfab, founded in 2004, works with silicon photonics and is based in Ghent[27]. Both consortia offer brokering services for MPW runs.

Comentado [SK4]: This section mainly discusses the economical benefits of generic integration. I would suggest adding some more technical details about how generic integration works in photonics. What are the equivalent BBBs compared to electronics etc. Adding a schematic would aid the reader.

There are several parallels between photonic and electronic integrated circuits and their respective basic building blocks. Below I will shortly describe those components and focus on the crucial aspects of them.

Electronic BBB	Role in the circuit	Photonic counterpart	Photonic counterpart's crucial characteristics
Transistor	Signal amplification	Semiconductor Optical Amplifier (SOA)	Threshold current at transparency, Internal Quantum Efficiency, T_0, T_1
Resistor,Capacitor and Coil	Signal transformation	Phase shifter	Strength of electro-optic effect, loss [28]
		Polarization converter	Polarization purity, loss, threshold current density for infinite length [29]
Wire	Signal transmission	Waveguide	Loss, mono-mode behaviour, minimal curve radius, polarization independence [28]

Table 1 - Basic Building Blocks of electrical and photonic circuits

1.3 –InP platform as a natural choice for generically integrated laser diodes

To answer why InP is a platform of choice for laser-containing PICs, I have to describe basics of semiconductor laser's mechanisms. To clarify the further discussion, I also define basic metrics that are used to assess a laser's performance. Afterwards, I describe two most popular material systems (AlGaInAs and InGaAsP) that are used in InP platform to produce quantum well lasers, and why is AlGaInAs preferred.

1.3.1 – Basics of laser physics – Why quantum wells? Why InP?

InP – a great material for modern telecommunications

In semiconductors, electrical conduction happens because of the carriers (electrons and holes) that move within two bands: conduction band, and valence band. Those bands arise due to crystalline structure of the semiconductor, which impacts motion of the electrons moving within it. Electrons with certain energies cannot move within a lattice – those energies lay within so called band gap. Depending on their k-vector, the carriers can have different energies (see Figure 1). If the bottom of the conduction band and the top of the valence band are aligned – it is so called "direct bandgap semiconductor". Otherwise, it's an "indirect bandgap semiconductor". For both types, the emission of a photon happens because of recombination of an electron from the bottom of the conduction band with a hole from the valence band. However, recombination requires the law of momentum conservation to be obeyed, meaning that mismatch of k-vector must be compensated with a momentum from another particle – a

Comentado [SK5]: You are making quite a jump here from economics of Photonics Generic integration to benefits of InAlGaAs. Please explain a bit more about compound semiconductors and how InP came to be the dominant material for long haul transceivers.

Also, here you can introduce the development from homo-epitaxy to hetero-epitaxy, bulk active layers to quantum wells and strained quantum wells. Otherwise, the introduction of the conduction band offset is not very meaningful to the inexperienced reader.

Comentado [SK6]: It would also be good to introduce working of a laser medium in general (doesn't have to be semiconductor laser even) and to introduce LIV measurement and terms like wall plug efficiency, slope efficiency, T_0

Comentado [MJZ7R6]: Following your advice, I explained the most important metrics with illustrations. But general working principle of a laser seems a bit too much. Florian Lemaitre didn't write about it, and his thesis was nice. Also my description of laser basics can't even compete with a generic handbook.

phonon. Since a process involving three particles is less probable than one involving two particles, and radiative recombination is a stochastic process, emission is much more efficient for a direct bandgap semiconductor – for example Indium Phosphide.

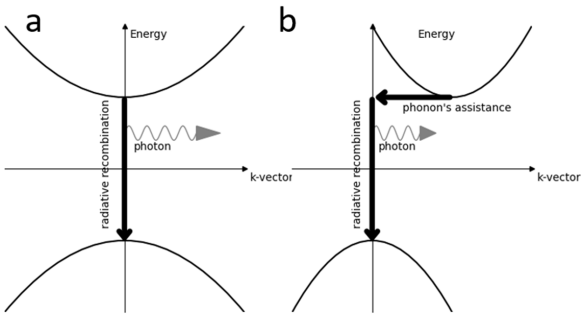

Figure 1 - (a) direct transition, (b) indirect transition

Furthermore, InP has relatively large electron mobility, compared to e.g., Silicon. This is of particular importance in telecommunication transceivers, where device's speed relies on electron mobility. InP can serve as a substrate for growth of GaAs, InAs, AlAs, and their ternary and quaternary alloys (lattice matched and strained), which allows to cover entire range of bandgaps from 0.9 µm to 2 µm. This means InP can be used in manufacturing of fast devices emitting in the 1300 nm window of optical fiber low dispersion and 1550 nm window of optical fiber low loss. All those factors mean that InP is a very suitable material system for fast telecommunication devices, that are cornerstone of modern civilization.

On the other hand, InP presents several challenges. Wafers made of InP, unlike their Si counterparts, are very brittle. This makes their handling more troublesome, especially in the facilities that aren't fully robotized. This increases the entry barrier for new companies entering the already difficult semiconductor market. Furthermore, manufacturing of InP wafers requires pressurized chambers and use of white phosphorus, which is itself a very dangerous substance that ignites upon contact with air. It is a stark contrast with silicon wafer manufacturing, which is based on comparatively simple and safe Czochralski method. Such technical issues limit the diameter of InP wafers (4 inches biggest commercially available) compared to Si wafers (17.7 inches biggest commercially available). This limitation, in turn decreases the manufacturing throughput of InP technologies.

Semiconductor lasers – from bulk to quantum wells – their use and the physics behind them

First semiconductor lasers consisted of forward-biased p-n junction of GaAs – so called homostructure laser. In such laser, the electron-hole recombination occurs in the depletion region of the p-n junction. Because of no way to confine the carriers, the region with sufficient gain to cause lasing is very narrow in such structure (about 0.01 µm). Such devices had threshold currents in the range of 50 kA/cm^2,

meaning that their operation was difficult to keep at room temperature and consumed a lot of power. Later, around 1963 it was suggested to improve the working characteristics by sandwiching a low-bandgap semiconductor between two semiconductors of high bandgap, a so-called “double heterostructure” (DH). This type of structure traps the carriers in the low-bandgap region, allowing for better chance of radiative recombination. Such growths required large progress in epitaxial technologies, therefore only in 1970 it was the first time when a double-heterostructure laser operated in a CW (continuous wave) mode. In the DH lasers, the carrier recombination occurred in the region of 100-300 nm, meaning that no quantum confinement of the carriers took place [30], [31]. Such lasers are often called “bulk lasers” because their recombination region is relatively large, compared to the quantum well lasers, in which recombination region usually measures from few to tens of nanometers.

Since confining the electrons within the DH proved a strong performance improvement, a better electron confinement strategy was searched for, and in the 1974, the term “Quantum Well” (QW) was coined to describe a DH with the recombination region so narrow it causes strong electron trapping with the quantization of their levels. The first electrically pumped QW laser was published by Dupuis et al. in 1974 [32]. Gain media based on quantum wells have many advantages and are very popular within photonic industry. The comparison with bulk lasers can be seen in Table 2 - comparison of bulk- and quantum well- lasers.

	Quantum Well SOA	Bulk SOA
Pros	• High efficiency • Low threshold currents • Narrow linewidth [33]	• Doesn’t affect the polarization of the passing light [34] • Wide and flat emission spectrum [35]
Cons	• Affects the polarization of the passing light	• Low efficiency • High threshold current

Table 2 - comparison of bulk- and quantum well- lasers

1.3.1 – Metrics of laser performance

To clarify further discussion, here I define the metrics used in discussion of a laser diode performance. Below, Figure 2 shows IV curve, LI curve, and a curve used to find the wall-plug efficiency. Data shown on the figure can be collected using a bar tester. In case of lasers described in this thesis, measurement details are described in chapter 2.2 – Measurement details.

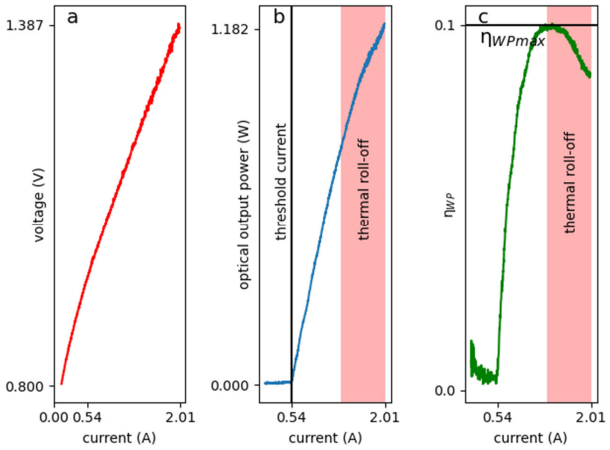

Figure 2 -example of LIV curves: (a) IV curve, (b) LI curve, (c) wall plug efficiency curve. Example taken from InGaAsP broad area laser, operating at 70 degrees Celsius

Threshold current (J_{th})

Is the current at which the lasing is achieved. Is found by inspecting the LI curve. Usually it is desirable, to keep this parameter as low as possible, meaning that not much energy is required for lasing. Dividing the threshold current by the electrode's area results in **Threshold Current Density (J_{th})**. Threshold current depends on material quantity and the size of the laser diode's contact. Therefore, J_{th} is preferable for the purpose of analysis. In order to properly measure the laser diode's contact size, it is preferable to use Broad Area Laser structure (BAL), because in such lasers, the area through which current flows is approximately equal to the size of the contact, unlike e.g. ridge lasers, in which current spreading makes it more difficult to assess the actual current density.

It is however important to note, that Threshold Current Density also depends on the contact width, following an exponential decay trend, meaning that it is best to measure diodes with wide contacts [36]. This way J_{th} measurement is the most robust against measurement imperfections.

Threshold Current at Transparency (J_{tr})

Threshold current density has linear dependence against $\frac{K}{L}$, where L is cavity length and K is a coefficient dependent on *inter alia* material quality, layerstack structure, etc. This means that various

researchers using different L can obtain incomparable results. Therefore, it is of importance to calculate the linear regression of J_{th} against 1/L. Resulting intercept corresponds to J_{th} at infinite cavity length, known as Threshold Current at Transparency. Such quantity allows for comparison of different lasers – no matter the cavity length. This quantity should be minimized.

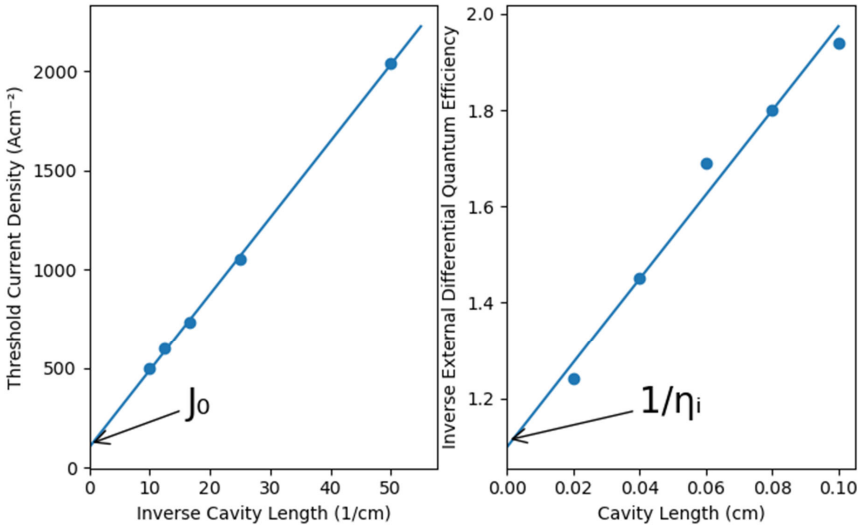

Figure 3 - illustration of linear models of Threshold Current Density at Transparency (J_{tr}), Internal Quantum efficiency (η_i) and internal loss (α_i). Numbers are arbitrary, only for illustration purpose.

Maximum Wall Plug Efficiency

Defined by the formula $\eta_{WPmax} = max(\frac{P_{out}}{I \times V})$, where P_{out} is optical output power, I is current applied to the diode, and V is the voltage readout. It should be as high as possible.

Internal Quantum Efficiency (η_i) and Internal Loss (α_i)

This quantity is obtained from the LI curve using the following steps:

- Find the slope of the LI curve (disregard the thermal roll-off region). The result is so called "slope efficiency" (SE), measured in W/A
- Find the External Differential Quantum Efficiency, using formula: $\eta_d = SE\frac{q\lambda}{hc}$, Where q =1.16022×10^{-19} C, h=6.6262×10^{-34} J×s, c=2.99×10^{8} m/s, and λ is the emitted wavelength.

- Measurements of η_d are carried out for several lengths. Subsequently, formula X is used to fit the parameters for Internal Quantum Efficiency and the Internal Loss

$$\frac{1}{\eta_d} = \frac{1}{\eta_i}(1 + \frac{\alpha_i}{ln(1/R)}L)$$

  Where η_i is the Internal Quantum Efficiency (IQE), R is facet reflectivity (assuming both facets are identical)

T_0

T_0 is a figure of merit that represents the device's robustness against the temperature. It is obtained using the following formula:

$$T_0 = \frac{\Delta T}{\Delta ln(J_0)}$$

High T_0 means that the Threshold Current Density at Transparency doesn't change much over the temperature range, which is very desired in practical applications.

T_1

This metric is analogous to T_0 but refers to the Internal Quantum Efficiency robustness against temperature.

1.3.2 – Advantages of AlGaInAs over InGaAsP for Semiconductor Optical Amplifiers

When an application requires PIC to contain active elements (such as SOA or a detector), it is convenient to use a platform with the material naturally providing gain, with a direct bandgap. III-V materials are usually chosen in such cases. Those materials can be conveniently grown on Indium Phosphide. Manipulating the chemical composition it is possible to create devices useful in 1300 nm and 1550 nm spectral windows of low dispersion and low loss respectively[37]. This is of great use in telecommunication applications, but more new applications are in development, including sensing, imaging, and signal processing. In fact, InP-based integrated photonics is the biggest part (circa 4 bln. Dollars) of the entire photonics market [37].

Until early 1990s a material of choice for laser fabrication was InGaAsP [38]. It was due to ease of fabrication and possibility of obtaining a wide range of bandgaps and strains by varying composition of the material. InGaAsP has a fundamental issue however, namely low conduction band offset, $\Delta E_c / \Delta E_g = 0.4$. This means that in practice, quantum wells made with this material are rather shallow, which in turn results in low electron confinement and therefore high leakage current (which lowers the efficiency) [39]–[42]. This becomes a large issue in higher temperatures, where thermal energy allows electrons to escape the quantum well rather easily without radiative

recombination. InGaAsP lasers often require active cooling systems to emit efficiently at the elevated temperatures found in modern data centers. These cooling systems need their own power supply, further decreasing the transceivers overall efficiency. This becomes a large issue in data centers, which consumed up to 1.5% of world's electrical energy in 2010 and are projected to consume up to 13% in 2030. Even nowadays ICT infrastructure's carbon footprint matched the one of aviation industry [43].

Aforementioned (high threshold current and low efficiency) deficiencies also decrease the 3db bandwidth, which is expressed by formula 1 [44]:

$$f_{3dB} = \frac{1.55}{2\pi}\sqrt{\frac{g_n \eta_i (I - I_{th}) v_g}{q V_0}} \quad (1)$$

Where g_n is differential gain, η_i is the internal quantum efficiency, I_{th} is threshold current, v_g is group velocity, q is electron's charge, and V_0 is the optical volume.

To prevent the issues caused by the poor confinement of electrons, it is favorable to use AlGaInAs as a material. It is known to have conduction band offset $\Delta E_c / \Delta E_g = 0.7$, which allows for relatively "deeper" wells for the electrons [45]. AlGaInAs, depending on its stoichiometric composition allows for manufacturing semiconductors with bandgap energies that enable production of devices working at the 1300 nm and 1550 nm. AlGaInAs, depending on the composition can have strain in circa -2% to 2% range, which is of use in manufacturing strained quantum well lasers[46].

Because of those advantages, research into AlGaInAs multi quantum-well lasers have been ongoing since the early 1980s, with first AlInAs MQW laser made at Bell Labs in 1983 (Temkin et al.) and first AlGaInAs MQW laser made at Siemens in 1989 (Gessner et al) [47], [48]. One of the earliest reviews of this topic, published in 1992, offers a glimpse into early AlGaInAs research history and indicates breakthroughs which made AlGaInAs a technologically important material [49].

There aren't many direct, experimental comparisons between AlGaInAs and InGaAsP lasers. Below I present two such studies relevant for the wavelengths used in the telecommunications.

Minch et al. have experimentally compared Buried Heterostructure lasers operating around 1560 nm of wavelength. AlGaInAs lasers had five compressively (-0.78%) strained wells and InGaAsP lasers had seven -0.9% strained wells. Intrinsic Loss, depending on the current, was calculated to be in the range of 30 to 37 cm^{-1} for the InGaAsP samples and 28 to 30 for AlGaInAs samples. Measured T_0 was 38 K for InGaAsP and 53 K for AlGaInAs[50]. Disparity of number of quantum wells makes the comparison quite biased though.

Silva et al. carried out another experimental comparison, for the 1300 nm ridge waveguide lasers[40]. Measured T_0 was 50K for InGaAsP lasers and 100K for AlGaInAs. This study however used very strained material for AlGaInAs and much less strained material for InGaAsP wells. It is known that strain strongly impacts laser's performance (transparency current, effective mass of electron, differential gain, T_0), so it cannot be said that this study is perfectly fair comparison[51]–[53].

Comentado [SK8]: Only one deficiency (bandgap offset) was mentioned? Please explain how the 3db bandwith is negatively impacted by electron leakage. Otherwise, having this equation in print is not required.

1.3.3 – Design considerations for AlGaInAs SOA layerstack

Strain

In discussion of strain (denoted as ε), it is important to pay attention to naming and sign convention, because various authors interpret "tensile" and "compressive" in opposite ways. For this thesis, it is assumed that compressive means "with equilibrium lattice constant larger than InP" and a negative sign. This usually corresponds to high Indium content. This convention follow the one in references [50] and [46] and is illustrated in Figure 4.

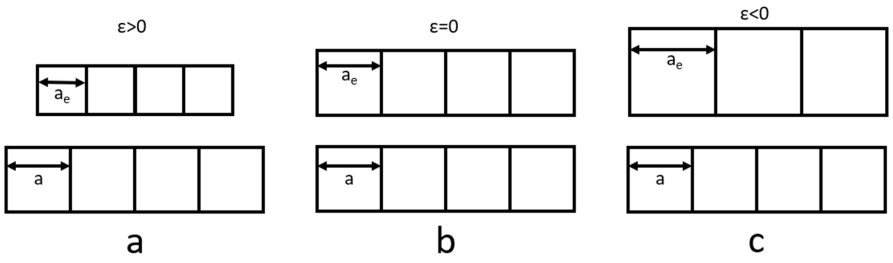

Figure 4 - Illustration of strained and lattice matched epitaxy. The substrate is on the bottom and has lattice constant of a. The epitaxial layer is on the top and has lattice constant of a_e. The following situations are shown: (a) tensile, (b) lattice matched, (c) compressive.

Strain of the quantum wells has profound and intricate impact on the laser performance. Some authors believe that maximum achievable amount of strain is the best choice from the performance perspective [38]. Relationship between strain and laser performance is however more subtle. Indeed Minch et al. observed improvement in internal loss, confinement factor and modal gain for samples with 0.78% of compressive strain compared to lattice-matched ones [50]. Zah et al. experimentally confirmed that dependence between compressive strain of the InGaAs well and threshold current is non-linear [54]. It is also shown that for several types of III-V lasers, threshold current is a parabolic function of strain. This is because heavily strained quantum wells must be very narrow to avoid dislocation formation. Such narrow wells provide poor optical confinement and poor electron-hole spatial overlap. The optimal strain magnitude improves threshold current by reducing non-radiative recombinations, which are a big issue at long (1550 nm) wavelengths. Both compressive and tensile strain result the material gain increase, compared to lattice matched alloys. Furthermore, strain sign (compressive or tensile) affects the polarization of emitted light (TE for compressive and TM for tensile). ~~Difficulty of growth of tensile-strained quantum wells, as well as i~~Industry's preference of TE mode results in compressively strained quantum wells being a medium of choice [55]. Growing a strained quantum well is not only a question of laser performance, but also practical fabrication. Excessively strained material will relax, resulting in dislocations, which reduce crystalline quality and contribute to performance degradation. Growth conditions should be selected to limit such possibility. Zhao et al. studied the impact of *inter alia* temperature on the growth of 1550 nm AlGaInAs strained quantum wells. It was demonstrated that growth at 700 °C favors better crystalline quality, since lower and higher temperatures increase alloy

Comentado [SK9]: Please explain using a schematic. Also, introduce the concept of lattice constant, to which strain is linked.

Comentado [SK10]: Can you rephrase this? I'm not sure what you mean.

Comentado [SK11]: 43 is a great reference, but I don't see how it supports the statement that tensile strain is hard to grow. Where does this come from?

Comentado [MJZ12R11]: I said it is difficult, based on the following words, however I choose to delete the mention of "difficulty" because it is a bit convoluted.:

tensile-strained lasers with their high gain, low transparency, and radiative current density would appear to be the design of choice. However, for other practical reasons, compressively strained lasers seem to be much more widely used. For example, if one wishes to grow In1−x Gax As/InP lasers operating at 1.5 µm, as the Ga fraction x is increased to incorporate tension the bandgap of the alloy increases. To offset this to maintain 1.5-µm operation, it is necessary to increase the well width and, therefore, reduce the quantum confinement. However, one may then have problems with the strain–thickness product approaching the critical thickness for dislocation formation

disorder and amount of impurities [56]. To grow multiple, highly strained quantum wells, it is necessary to compensate their compressive strain by growing tensile-strained barriers. Such compensation results in the reduction of net strain, which in turn increases the critical thickness of such multilayer, allowing for high crystalline quality with desirable optical and electronic properties [57]. Kuo et al. have used simulations to show that tensile strain within barriers can increase material gain, decrease the Auger recombination, and increase T_0. On the other hand, too large barrier strain can cause non-uniform distribution of electrons between neighboring quantum wells. Those effects are attributed to increase in the barrier's height in the energy domain [58].

Comentado [SK13]: T_0 has not been introduced before this.

Less studied is the impact of strain in the barriers of the layer stack on device's performance. Yekta et al. carried-out a numerical study on the effect of barrier strain on a 1300 nm ridge laser performance. They studied three structures with the same layerstack, except for the barriers, that were varied between -0.2%, 0% and +0.2% of strain. This study indicated that use of compressively strained barriers is superior to other options because of lowered Auger current, lower leakage, and higher gain (all at 20 °C and 85 °C) [59]. It is important to emphasize that this is simulation-based study, and high net strain of such structure might cause problems due to dislocations formation.

Comentado [SK14]: Impact on what? Device performance?

Number of Quantum wells

Number of quantum wells is another parameter with an impact on laser performance. Internal loss of the gain medium is linearly proportional to the number of quantum wells [42], [60]. Similar findings were reported by Tandon et al. [42]. Wada et al. have theoretically and experimentally discovered that for an AlGaInAs laser operating at 1300 nm, increasing the number of quantum wells increases T_0 (also confirmed in Tandon's work) and the maximum working temperature, but also decreases the T_1. They proposed a different figure of merit, power reduction at constant current, ΔP, as a metric to evaluate laser's robustness against temperature. They inferred that optimum ΔP can be achieved with seven wells if the cavity mirrors entail high losses, while four QWs offer best ΔP for a cavity with low mirror losses [42], [61].

Well thickness

Well thickness is another important parameter in the laser design. Ishikawa and Shoji explored the impact of well thickness on threshold current and T_0 of a 1300 nm AlGaInAs laser with electron-stopping layers and 10 wells with 1.5% compressive strain. They found out that the thinnest wells (2 nm) result in the worst parameters, while increasing the thickness improves the performance. Thickest wells they fabricated had 6 nm and had T_0 of about 95 K. They explained this phenomenon by a fact that energy levels of a narrow quantum well are higher than the ones of a wide one. This results in low confinement energy (difference between QW energy level and barrier's conduction band edge)[62]. It is however very difficult to grow high quality, strained, thick quantum wells. Yong et al. use theoretical model of 1300 nm laser to explain that at fixed emission wavelength and fixed barrier composition, one can optimize the quantum well thickness either for high gain or for low threshold current at transparency. Reducing the width increases the gain. This is due to reduction of density of states within a well. On the other

hand, to lower the threshold current at transparency one must widen the quantum well, because it improves the electron confinement. According to their presented data, T_0 decreases nonlinearly with increase in -QW width, with T_0 of 264K for 4.5 nm and 6 nm wells, and with 221K for 7.5 nm well [63]. Those results are theoretical, and to my best knowledge higher than any T_0 value reported experimentally. Using thick quantum wells reduces the Auger recombination coefficients, which can be very beneficial for the efficiency [64]–[66].

SCH doping

In case of III-V lasers, optimization of only the quantum wells can yield limited improvement of characteristics. For example, even the most optimized strain is proven to achieve T_0 improvement limited by condition $T_0 < T/3$ where T is the surrounding temperature[55]. Obviously, the AlGaInAs composition itself imposes a limit on the possible depth of a quantum well, and therefore electron confinement. Therefore, it is of importance to study and optimize not only quantum wells, but also Separate Confinement Heterostructure (SCH) and the surrounding parts of layerstack. For example, Tandon et al. have proven that slight doping of SCH on the p-side of the laser diode results in improvement of Threshold current densities, T_0 and T_1 [42]. They explain this phenomenon by change of band structure caused by the doping, which decreases amount of leakage current. Similarly, Seki et al. shown strong improvement in high-temperature operation for lasers with n-side doping, which limited hole leakage[60]. It is however important to be aware of a trade-off brought by such approach: doping within p-layer increases the threshold current [67].

Electron Stopping Layers and Hole Stopping Layers

Use of electron-stopping layers and hole-stopping layers was proven to reduce thermionic emission of carriers from the active layer of 1300 nm MQW AlInGaAs laser, which improves performance at higher temperatures, as shown by Kazarinov et al. [67], [68]. Takemasa et al. have experimentally shown that AlGaInAs MQW lasers operating at 1300 nm could benefit with T_0 increase by 10 K just by implementing an electron stopping layer placed within SCH [69].

Liou et al. have carried-out a computational comparison of a MQW structure emitting at 1550 nm with a standard SCH, and a structure with same layerstack, but containing an AlInAs electron-stopping layer at the p-side, 5 nm away from Quantum Wells. Performance improvement coming from such ESL turned-out to be strongly dependent on the ESL's thickness (varied from 5 nm to 30 nm) and doping (varied from $10^{22}m^{-3}$ to $10^{25}m^{-3}$). Structure with optimal ESL had T_0 circa 5K higher than a reference structure. Across temperature range between 300 K and 350 K, optimal structure had consistently 0.02 W/A higher

slope efficiency than the reference structure. At 300 K there is almost no difference in threshold current between the ESL-enhanced structure and a reference one. It is however important to note, that the impact of ESL's thickness and doping is not straightforward and has plenty of local optima, meaning that there is no such thing as a "recipe for the best ESL" [70].

A separate type of ESL and are so called Multi-Quantum Barriers (MQB). They are placed within SCH and are made of high-bandgap alloy (usually AlInAs) and can be designed as Bragg reflectors for electrons in a desired energy spectrum. Such design allows to reflect Auger hot electrons back into the quantum wells from within the SCH.
Irikawa et al. shown experimentally that, for AlGaInAs 1500 nm lasers, presence of such MQB layers on the p-side was proven not to affect hole injection and current-voltage characteristic. Such modification also strongly reduces the recombinations within SCH. Such effect plays especially important role at higher temperatures. Such modification employed within p-side SCH improved high-frequency response of a 1500 nm laser, did not however improve its T_0 [71]. On the other hand, Ohnoki et al. have shown that a spectacular thermal performance of 1550 nm AlGaInAs MQW laser with $T_0 = 122K$ can be achieved by implementing an electron stopping AlAs layer outside of the p-side SCH, which is very large improvement compared to an identical reference laser without MQB ($T_0 = 92K$). Use of very narrow AlAs layers (1 nm) prevented from laser degradation caused by strain-caused dislocations. Oxydation of AlAs also didn't seem to be an issue [72]. Similar findings have been reported by Fukushima et al [73]. Another team, Pan et al. have demonstrated that for 1300 nm AlGaInAs lasers one can reach about 5 K improvement in T_0 if one applies MQB on the both sides of active region, compared to structures with MQB only at p-side. They attribute it to hole leakage suppression on the n-side of the device being almost as important as electron leakage on p-side [74]. It should be however marginally useful for 1500 nm lasers, because Yong et al. used calculations to prove that for for such heterostructures, hole leakage is an order of magnitude lower than electron leakage [75].

SCH band profile

Another way to improve the performance of a laser is to optimize the electronic band profile of SCH. Since SCH can be modified in numerous ways, in this section I describe several completely different approaches.
Yong et al. have systematically studied impact of SCH on the 1550 nm AlGaInAs laser performance. They carried out simulations of several structures with Step Index SCH (STEP-SCH) and several Graded Index SCH (GRINSCH). They found that four-steps STEP SCH is nearly equivalent in performance to GRINSCH. There was very pronounced confinement factor improvement (by 15%) for a SCH with just two steps, compared to default SCH. Furthermore, such grading drastically decreases number of carriers in SCH, decreasing wasteful spontaneous recombination and free carrier losses. Yong's study also emphasized two tradeoffs: increasing the SCH thickness increases the threshold current, however it also decreases slope efficiency. Furthermore, increasing the bandgap gradient of SCH improves threshold current but worsens the slope efficiency. It is however important to note that strong gradient can be advantageous at high temperatures, improving T_0. Experimental structure that employed those considerations reached T_0 of 105 K without even using electron stopping layer [76].

To overcome the abovementioned trade-off, Yong et al. developed a concept of an asymmetric SCH. In such design, the n-side of the SCH is a flat, low-bandgap, lattice-matched AlInAs, while the p-side is graded from the QW's barrier energy up to $In_{0.52}Al_{0.48}As$, which offers highest-possible bandgap for a lattice-matched AlInAs. The rationale behind such design is to facilitate in-flow of the electrons from the n-side with the flat SCH, while making leakage to the p-side energetically demanding. Such Non-Symmetric SCH (NS-SCH) was numerically tested against a symmetric SCH. NS-SCH offers 20% reduction of threshold current at room temperature and 43% improvement in maximum output power. While this study did not calculate T_0, from LI curves at various temperatures one can assume that performance at high temperature is significantly improved compared to a reference [77].

Another aspect of SCH asymmetry is the position of the Quantum Wells within the SCH. Usually wells are placed at the center of the SCH, however in some designs this symmetry was broken and tested. In recent years there have been strong interest in positioning the Quantum Wells closer to p-cladding than to n-cladding. This is mainly for two reasons. Firstly, undesirable free carrier absorption tend to happen in the p-SCH than in n-SCH. Secondly, proximity of the wells to the cladding offers better cooling of the quantum wells, which limits effects of self-heating [78]. Volkov's team made an asymmetric structure with promising performance at high pumping current, however decided to compare their asymmetric structure with a symmetric structure with an SCH of greater thickness. This modification makes the comparison flawed [78]. Theoretical, fair comparison of structures with various degrees of asymmetry have been presented by Ryvkin and Avrutin for InGaAsP structure working at 1550 nm. They clearly shown that a properly designed asymmetric structure can have IQE increased by about 50% compared to a standard SCH [79].

Veselov et al. experimentally shown introducing high bandgap, doped barriers between the SCH and the cladding results in higher maximum power because the power-limiting mechanism changes. Use of doping and large distance from quantum wells was strongly distinct from a typical ESL. For a typical structure, limiting factor is the leakage current, while for the modified structure, the limit is imposed by the internal loss caused by the electrons present within the SCH. It also means that leakage current is a more serious threat to laser's output power and thermal roll-off than internal loss [64]. It also shows that carriers should be also prevented from leaking into SCH. Marmalyuk et al. built upon this idea and used a strained AlInAs barrier between the SCH and cladding. Their results were not reported in detail, however strained barrier provided favorable LIV curves compared to lattice matched one, due to bandgap increase caused by strain. Such increase contributed to barrier's height and further leakage limitation [80].

Another important parameter of SCH geometry is its thickness. Marmalyuk et al. have studied impact of SCH thickness on the 1500 nm laser performance. They describe several phenomena that play a significant role in such impact. Thickness of SCH impacts the threshold current in a nonlinear way, with a single minimum. This means that one can reach the same threshold currents with either very thin or very thick SCH, however the lowest point has to be precisely determined. Thicker SCH means that optical mode is away from the doped cladding, meaning that at low temperature such structure displays low internal loss. However thick SCH means worse electrical and thermal conductivity due to it's low doping, which plays significant role at higher temperatures or pumping currents. Furthermore, at large currents, thick SCH offers plenty of space for overflowing electrons to recombine at undesired energy. Their experimental approach resulted with T_0 of 50 K for a wide SCH laser and 65 K for a narrow SCH laser. At a constant temperature, narrow SCH structure had 97% of Internal Quantum Efficiency and a

loss of 3.5 cm^{-1} while a wide SCH had lower IQE (91%) and lower loss (2.2 cm^{-1}). Authors however note, that wide SCH provides better LI curve at low pumping current, while narrow SCH performs much better at higher currents [81]. This study well portrays the subtlety and trade-offs involved in layerstack design.

Wu et al. have demonstrated that band profile of transition between the substrate and the n-side SCH is important, by showing experimentally (for 1300 nm laser) that introducing a graded bandgap layer between n-InP and the n-SCH decreases threshold current by about 5 mA for all temperatures and improves T_0 by about 20 K (depending on temperature range). Such improvements are explained by the lower energy requirement for an electron that passes by a graded layer, compared to one that has to face an abrupt energy profile.

1.4 – Relation between composition and properties of AlGaInAs

Relation between AlGaInAs composition and its bandgap is of practical importance for growth of semiconductor devices. There are three known formulas to derive the bandgap from the composition. First one is developed by Olego et al., obtained from regression-derived formulas that describe bandgap of lattice-matched ternaries (AlGaAs, InGaAs, InAlAs) on InP. For the purpose of clarity we will refer to it as “Olego I” model.

$$E_g = 0.360 + 0.629y + 2.093x + 0.436y^2 + 0.577x^2 + 1.013xy \qquad 2$$

Second formula devised by Olego and his team is very similar, however it contains a direct link with the amount of Indium (1-x-y). We will call it “Olego II” model.

$$E_g = 0.360 + 0.629y + 2.093x + 0.436y^2 + 0.577x^2 + 1.013xy - 2(1 - x - y) \qquad 3$$

Third formula is a weighted average of three binaries (AlAs, InAs, GaAs) and three ternaries. It is expressed by a set of following equations, taken from reference [82]:

$$z = 1 - x - y \qquad 4a$$

$$u = \frac{1 - x + y}{2} \qquad 4b$$

$$v = \frac{1 - y + z}{2} \qquad 4c$$

$$w = \frac{1 - x + z}{2} \qquad 4d$$

$$T_{Al-Ga} = u \times E_{g,GaAs} + (1-u) \times E_{g,AlAs} + C_{AlGaAs} \times u \times (1-u) \quad 5a$$

$$T_{Ga-In} = v \times E_{g,InAs} + (1-v) \times E_{g,GaAs} + C_{InGaAs} \times v \times (1-v) \quad 5b$$

$$T_{Al-In} = w \times E_{g,InAs} + (1-w) \times E_{g,AlAs} + C_{AlInAs} \times w \times (1-w) \quad 5c$$

$$E_{g,AlGaInAs} = \frac{x \times y \times T_{Al-Ga} + y \times z \times T_{Ga-In} + x \times z \times T_{Al-In}}{x \times y + y \times z + x \times z} \quad 5d$$

All those models, however, describe so called "unstrained" bandgap, which does not consider the strain caused by depositing AlGaInAs of arbitrary composition on InP. Changes in electronic structure caused by strain are described by so called Model Solid Theory, which is often used in semiconductor laser design[44], [46], [50], [83].

To use Model Solid Theory well described in [46], [50], one needs to know the following parameters:

- Elastic Stiffness Constant C_{11} for each binary
- Elastic Stiffness Constant C_{12} for each binary
- Hydrostatic Deformation Potential of Conduction Band a_c for each binary
- Hydrostatic Deformation Potential of Valence Band a_v for each binary
- Shear Deformation Potential of Valence Band b for each binary
- Lattice Constant a for each binary
- Parameters of Unstrained Bandgap formulas

This results in the following number of parameters, depending on unstrained bandgap calculation approach:

- 24 in case of Olego I
- 25 in case of Olego II
- 24 in case of Weighted Average

In the known literature there is large scatter of reported values of the parameters. For example, $a_c(AlAs)$ is reported in the range of 0.7 to -5.64, which is circa 800% of uncertainty[84]. While measuring the deformation potential is difficult, more straightforward properties also entail large uncertainty. Bandgap of InAs is reported in the range 0.41–0.45eV, which is not large span in energy domain, however in the wavelength domain it corresponds to more than 250 nanometers[84]. Such large uncertainties make it difficult to properly design quaternary alloy with arbitrary composition.

Chapter 2 – Experiment and result discussions – AlGaInAs SOA

2.1 – Fabricated layerstacks

We used MOVPE process to grow several layerstacks, characterized in the table 3:

Number of Quantum Wells	Remarks	Designation
3		3QW
4	Doping within p-SCH	4QW doped
4	No modifications of SCH	4QW
4	GRINSCH	4QW GRINSCH
5		5QW
6		6QW
secret	Existing SMART InGaAsP layerstack (reference)	P reference

Table 3 - Layerstacks discussed in this thesis

The quantum wells have been designed using empirical methodology provided by Bhat et al. aiming at at least 150 meV of confinement energy [85]. We aimed at moderate strain within the Quantum Wells and for proper strain compensation within wells. For the sample with GRINSCH we aimed for lattice-matched alloy with the lower bandgap matching the bandgap of quantum barriers, and the higher bandgap matching the bandgap of the cladding.

2.2 – Measurement details

BALs used for our study had cavity width of 50 µm and lengths of 500, 1000, 1500 and 2000 µm.
To automatically characterize the BALs, we used bar tester made of Wentworth Pegasus S200 wafer prober and Keithley 2520 Source-Meter Unit, and Thorlabs' Optical Spectrum Analyzer 203C, with custom controlling elements and thermostatic system.
From the center of each wafer, we cleaved-out bars, each containing up to 20 BALs of given cavity length (one cavity length per bar). The automated test was carried out at 20, 40, and 70 degrees Celsius, using pulsed current mode (pulse width 5 µs, duty cycle 1%). In processing of the LIV curves, we took into account that optical power measurement took place only at one facet [86]

Schedule of LIV curves collection is presented in Table 4. Note that for several layerstacks, measurements done at 85 °C were carried out with certain delay with respect to the measurements at other temperatures.

layerstack	Cavity length (μm)	Temperature (°C)			
		20	**40**	**70**	**85**
6 QW	**500**	10	10	Not measured	Not measured
	1000	9	9	9	9
	1500	9	9	9	9
	2000	9	9	9	9
5 QW	**500**	12	12	12	12
	1000	9	9	9	9
	1500	9	9	9	9
	2000	9	9	9	9
4 QW	**500**	Not measured	Not measured	Not measured	Not measured
	1000	10	10	10	10
	1500	10	10	10	10
	2000	10	10	10	10
4 QW doped	**500**	8	8	8	12
	1000	8	8	8	11
	1500	8	8	8	11
	2000	8	8	8	11
3 QW	**500**	8	8	8	12
	1000	8	8	8	11
	1500	8	8	8	11
	2000	8	8	8	11
4 QW GRINSCH	**500**	8	8	8	12
	1000	8	8	8	11
	1500	8	8	8	11
	2000	8	8	8	11
InGaAsP reference	**500**	7, 8	7, 8	7, 8	12
	1000	7, 8	7, 8	7, 8	11
	1500	7, 8	7, 8	7, 8	11
	2000	7, 8	7, 8	7, 8	11

Table 4 - Measurement schedule table. Month of the year 2020, during which given bar was subjected to the measurement.

2.2.1 – Data processing

To characterize the gain medium, I wrote python scripts to analyze the LIV curves and to subsequently process the analysis outcomes. In this section I will display the main ideas behind the entire process.

LIV curves – discarding bad measurements

LI and IV curves obtained by bar tester are the raw sources of performance characteristics, however due to variety of reasons, sometimes the data can be anomalous. The sources of anomaly can be:

- Bar tester applying the current in the wrong part of the chip
- Local defects in the lithographic structure of a laser
- Locally damaged facet of the laser, drastically hampering the laser's output
- Discontinuous behavior of the LI curve caused by inhomogeneous pumping along the cavity [87]
- Bad performance of the gain medium, especially at elevated temperatures.
- Other technical issues (difficult to pinpoint)

Those issues contribute to certain LI curves shapes that can be categorized as follows:

- Maximum output power less than 0.0025 Watt
- Strong discontinuities in the slope region of the LI curve
- Noisy (despite application of Savitzky-Golay filter) and poorly defined slope region

I designed the processing software to reject all such LI curves and to provide statistics on their occurrence.

Finding the values of Threshold Current Density and Inverse External Quantum Efficiency

To find the values, each LI curve was subjected to the following:

1. Filtering the data with Savitzky-Golay filter
2. Filtered dataset is subjected to discrete differentiation
3. Numpy's np.signs() function is applied, to find which differentials are positive or negative
4. KMP algorithm is used to find all the regions of at least 19 consecutive positive differentials
5. First datapoint of the first such region is considered to be threshold current
6. Values of wall-plug efficiency are calculated for each current value
7. Maximum of wall-plug efficiency is found
8. Linear regression is carried out for all the LI points between the threshold current and the maximum wall-plug efficiency value. The slope of the regression line (W/A) is equal to slope efficiency, used to calculate EQE

Transparency Threshold Current Density and Inverse External Quantum Efficiency

Not only the both quantities are naturally varying, but the magnitude of their measure is impacted by the bar tester variability, and processing software imperfections. To mitigate the effect of those variations, for every population of lasers of given length, at every temperature, I reject top 30 percentiles and bottom 30 percentiles of the results.

2.2.2 – Pitfalls of the linear models

Threshold Current Density

After collecting and processing all the LIV curves, two phenomena were observed. Threshold current densities plotted against the inverse cavity length are non-linear. Furthermore, Inverse External Differential Quantum Efficiency plotted against cavity length was also nonlinear. Nonlinearities were the strongest at higher temperatures, but sometimes were apparent even at 20 degrees Celsius.

To give examples of Threshold Current Density nonlinearity, in Figure 5 I present relevant plots

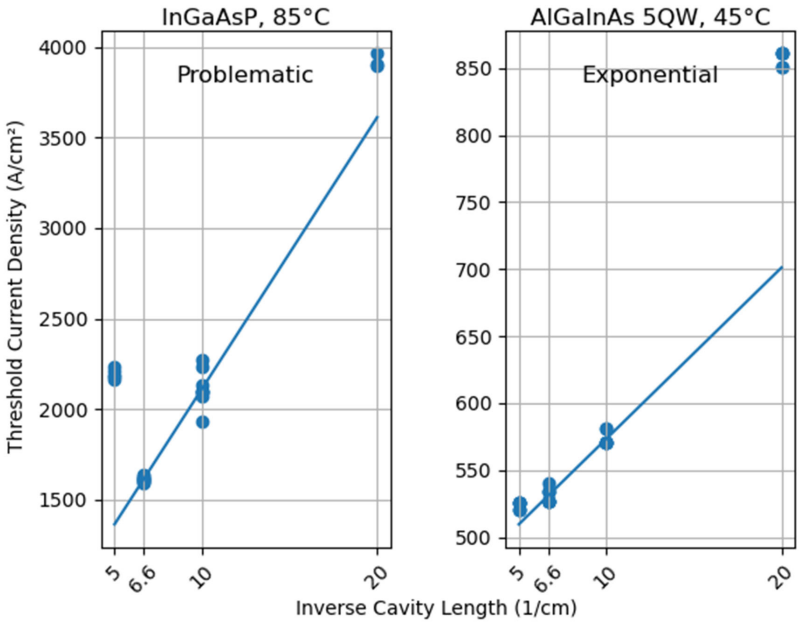

Figure 5 - Threshold Current Density as a function of Inverse Cavity Length for the InGaAsP layerstack at 85 degrees and 5QW AlGaInAs layerstack at 45 degrees. To emphasize nonlinearity plotted are also regression lines fitted to datapoints from 6.6 and 10 cm^{-1}

Figure 5 displays two types of nonlinearity: Problematic and Exponential. First I will discuss the exponential.

This type of nonlinearity was investigated by Shieh and his team [88]. They attribute the phenomenon to the small optical confinement factor of the optical mode, however Taylor gives more complex answer based on electronic effects [89]. Here I base my explanation on the Shieh's findings. Wilcox gives the following formula to describe the threshold current density as a function of inverse cavity length [90]:

$$j_{th} = \frac{N_z J_{tr}}{\eta_i} exp\left[\frac{1}{b j_0 \Gamma}\left(\frac{1}{2L} ln\left(\frac{1}{R_1 R_2}\right) + \alpha\right)\right] \quad 6$$

Where N_z is number of quantum wells, J_{tr} is transparency threshold current density, η_i is Internal Quantum Efficiency, b is gain-current coefficient, Γ is optical confinement factor, L is cavity length, R_1 and R_2 are facet reflectivities and α is distributed optical loss in the laser. It can be demonstrated, that for larger values of Γ, function displays linear increase with the inverse cavity length. For small Γ, threshold current density grows exponentially, invalidating the linear model outlined before.

The problematic nonlinearity on the other hand, to the best of my knowledge, wasn't previously reported. TCD is drastically large for the long cavity lasers. One might speculate that the culprit is lower internal quantum efficiency. One research group noticed that the laser performance depends on chip's geometry, which influences distribution of the pump current [91]. Inhomogeneous pump hypothesis is supported by the fact, that measurement of lasers was carried-out using a bar tester, that supplied entire current in one place, using a point-probe needle, with assumption that the chip's metallization will distribute the current along the entire cavity. The nonlinearity is particularly pronounced at larger temperatures, even further reinforcing the hypothesis, because metallization's resistivity increases with temperature, impeding the homogeneity of the pump current.

Internal Quantum Efficiency and loss

Analysis of the obtained External Quantum Efficiency data revealed the presence of three effects that impede the extraction of IQE and loss. Phenomena are shown on Figure 6 and are discussed in detail in the following paragraphs

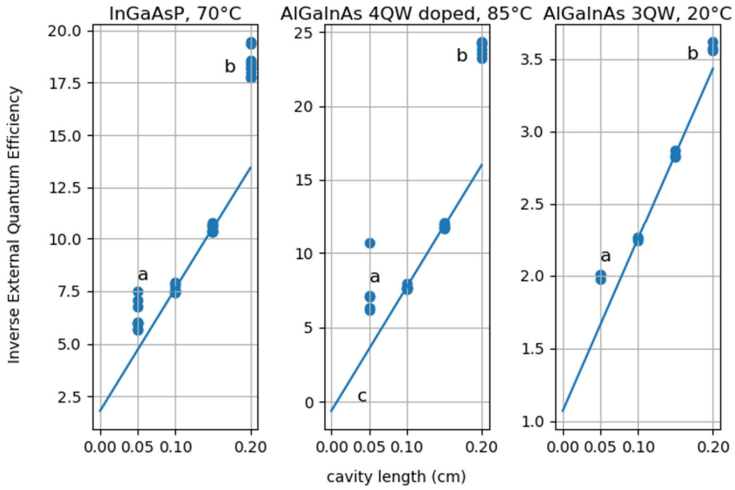

Figure 6 - Illustration of the problems in the determination of IQE and loss. (a) Anomalously low quantum efficiency due to short cavity. (b) Anomalously low external quantum efficiency due to poor current distribution along the cavity. (c) Unphysical value of IQE. To emphasize the nonlinearity, plots include regression lines fitted to the datapoints from 0.5- and 1-mm cavities.

Phenomenon a – large IEQE for short-cavity lasers

Piprek et al. have demonstrated theoretically and experimentally, that internal loss (α_i) and IQE are dependent on cavity length [92]. According to Piprek's findings, for short cavities, IQE decreases exponentially, while the internal loss grows exponentially. Those two facts combined together explain the high value of Inverse External Quantum Efficiency for the short lasers. Camps et.al advise do add more quantum wells to reduce this detrimental effect for short cavities [33].

Phenomenon b – Large IEQE for long-cavity lasers

According to my best knowledge, there isn't any effect that would impede the efficiency of long-cavity laser, therefore just as in previous section about Threshold Current Density, I have to assume that the issue was caused by non-uniform pumping of the cavity [91]. This is consistent explanation for both the anomalies appearing in the IEQE and in Threshold Current Density diagrams.

Phenomenon c – Unphysical value of Internal Quantum Efficiency

Exact explanation of this effect is difficult due to experimental limitations, however there are two promising explanations.

Yoshida et al. have observed that gain-current dependence changes with the duration of a current pulse used for the LI curve measurement [93]. The linear model described in section 1.3.1 – Metrics of laser

performance assumes the linear gain-current relationship. Yoshida's team showed that using long pulses (20 µs) results in strongly nonlinear dependence. Even very short pulses (200 ns) yielded slight nonlinearity. In Yoshida's work, such nonlinearities are blamed for non-physical values of IQE.

Many researchers who characterize photodiodes use pulsewidths equal to shorter than 500 nanoseconds [94]–[98]. For this thesis, 5 µs pulses were used due to technical limitations. Such long pulsewidth might be the reason for non-physical results.

Another explanation is offered by Aaviksoo et al. who proved that when IQE is large and photon recycling occurs, traditional method of finding IQE gives nonphysical results [99]. They offer a method to overcome those limitations, however it requires specific experimental setup that was unachievable during this research.

Conclusions, taken action, and proposed improvements

Determination of Transparency Threshold Current Density is slightly impeded by the aforementioned nonlinearies, however this obstacle can be overcome by exclusion of the shortest- and the longest-cavity lasers. This way, the inherent under-estimation caused by the linear model can be minimized. On the other hand, the final results still have to be interpreted with the possible under-estimation in mind.

Proper determination of the IQE and loss is far more difficult. To demonstrate reliable comparison between various layerstacks, I decided to follow the following steps:

- Utilizing only the results coming from the 1 and 1.5 mm long laser diodes for search of the Transparency Threshold Current Density, IQE and internal loss.
- Not presenting the IQE and loss of layerstacks that achieved only the non-physical performance results.
- Seki et al. have proposed another metric of laser diode performance: Power penalty incurred by the temperature change. It is calculated using formula:

$$\Delta P = 10log_{10}\left(\frac{P(T_1)}{P(T_2)}\right) \quad (7)$$

  Where P is optical power at the same current, and T is temperature, with $T_1<T_2$. This power penalty is a very practical measure that encompasses the threshold current change and the IQE change. This metric is necessary to compare the layerstacks, that cannot be compared in terms of IQE.

The following steps should be taken for any other research of layerstacks in SMART photonics:

- Short lasers (less than 0.7 mm) shouldn't be used for determination of IQE and loss.
- Measurements on long lasers (longer than 1.5 mm) is necessary, and bar tester should be always configured towards homogenous current spreading in mind to avoid efficiency loss.

2.3 – Results and discussion

2.3.1 – Yield

Figure 7 shows the percent of working lasers made with various layerstacks, at various temperatures. A "not working laser" is determined by analyzing the LIV curves according to criteria outlined in the section 2.2.1 – Data processing.

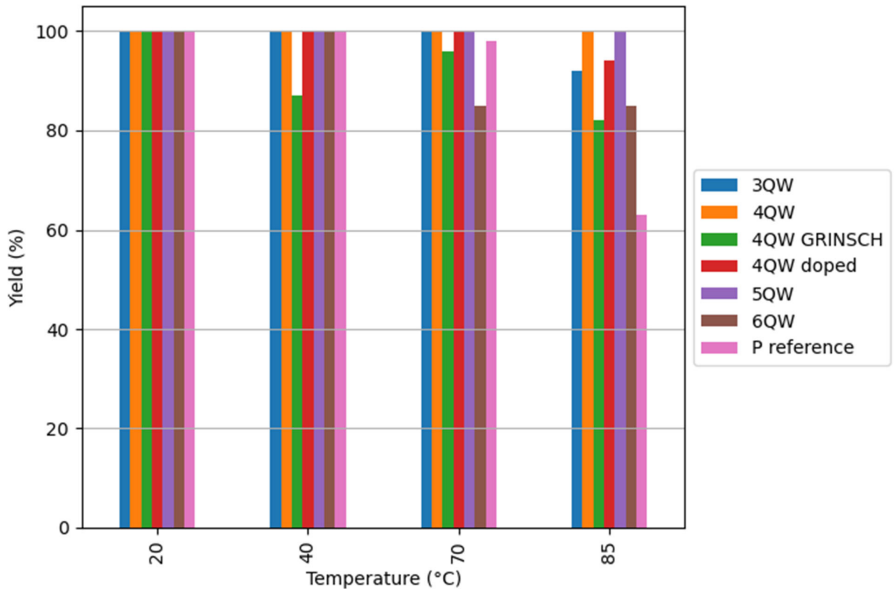

Figure 7 - Yield of manufactured lasers

Understandably, high temperature is detrimental for laser functioning. One can get the following conclusions from that graph:

- 6QW laser is the faultiest structure of all the AlGaInAs devices
- GRINSCH has higher yield at 70 °C than at 40 °C. This suggests that several curves were mis-processed at the initial stage. The difference is about 10 percent points, and this number therefore can be considered as uncertainty.
- At 85 °C the InGaAsP layerstack performs the worst, 23 percent points below the worst Al-based structure
- 4QW GRNISCH, 4QW doped, 3QW layerstacks perform worse at 85 °C than 4QW and 5QW. The only difference between those groups is that the underperformers were exposed months longer to the air. AlGaInAs is sensitive to oxidation (see ref. [100]), however this finding displays that even hours spent on a gradually warming bartester and days spent in a box are not a big threat

to the yield. It takes long time to oxidize AlGaInAs structure layerstack into absolute degradation. Following sections however show that while oxidized laser works, its performance is noticeably deteriorated.

2.3.2 – Maximum Wall-Plug Efficiency

Due to issues outlined in section 2.2.2 – Pitfalls of the linear models, in this analysis, for fairer comparison, I use only the devices with the length of 1- and 1.5-mm. Furthermore I only analyze the devices that are included in the subsequent sections (i.e. after rejection of bottom and top 30 percentiles for each cavity length in terms of J_{th} and external efficiency). This is to avoid LI curves that contain mode hopping or have optical power barely above the minimum required value.

To characterize how the various AlGaInAs layerstack variations compare to the InGaAsP one, for each temperature and cavity length I averaged the maximum wall-plug efficiency of each layerstack. Subsequently each of those figures was divided by corresponding figure achieved by InGaAsP.

The results are shown on Figure 8. One can see that AlGaInAs laser with three quantum wells consistently performs significantly better across temperatures and cavity lengths. Botez et al. emphasize that to achieve high wall plug efficiency, low internal loss is needed [101]. High maximum wall plug efficiency of 3QW structure aligns well with findings of section 2.3.5 – Internal Loss, where I demonstrated that this is by far the least lossy of all the layerstacks.

The layerstack with six quantum wells is always performing poorly compared to other AlGaInAs layerstacks. At lower temperatures (20 °C and 40 °C) it even performs worse than the InGaAsP layerstack. As shown in the section 2.3.3 – Threshold Current Density at Transparency, it is also the layerstack with the highest J_{tr}, which is undesirable.

Figure 8 also allows to observe the impact of SCH doping and GRINSCH on the 4QW layerstack variant. In the 20-70 °C there are no clear differences between all the 4QW layerstacks. At 85 °C it is visible that the doped and GRINSCH structures perform worse than the non-modified 4QW variant. I attribute it to the measurement schedule (see Table 4), which resulted in long exposure of the doped and GRINSCH structures to the air. This could've resulted in facet degradation by oxidation.

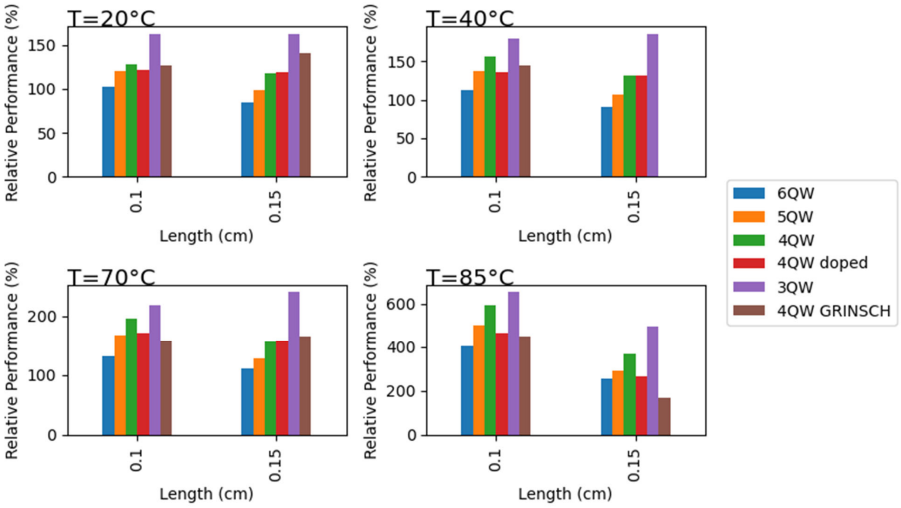

Figure 8 - Maximum Wall Plug Efficiency of various AlGaInAs layerstacks, relative to corresponding InGaAsP devices.

To give an idea about the absolute numbers, Figure 9 shows the absolute maximum wall-plug efficiency of the InGaAsP layerstack:

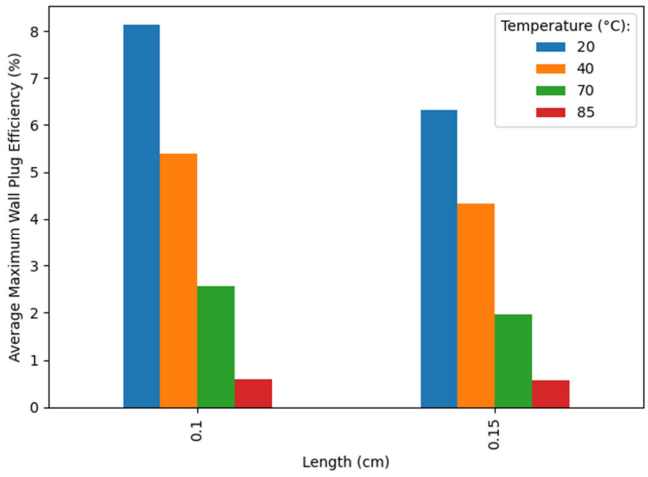

Figure 9 - Average Maximum Wall Plug Efficiency of InGaAsP lasers.

2.3.3 – Threshold Current Density at Transparency

Figure 10 shows Threshold Current Densities at Transparency for investigated layerstacks.

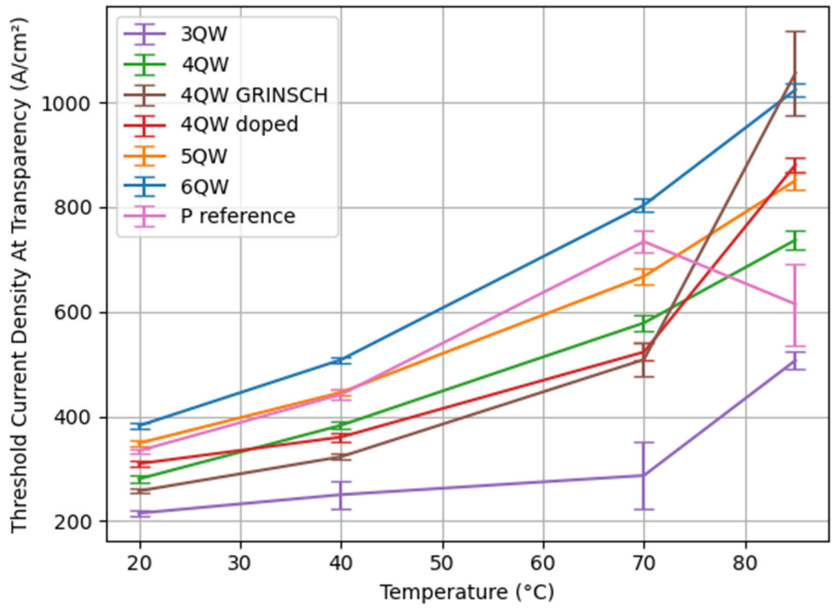

Figure 10 - Transparency Threshold Current Densities of investigated layerstacks, as a function of temperature.

Before further analysis, one has to address certain anomalies occurring at 85°C. While J_{tr} of 6QW, 5QW, and 4QW layerstacks follow the expected exponential increase, four other layerstacks display unusual behaviour:

- J_{tr} of InGaAsP laser decreases sharply. This is due to exceptionally poor performance of this layerstack at high temperature. Datapoints used to find this value are highly scattered, and make no physical sense (see Figure 11). This is result of two factors: problems described in section 2.2.2. and signal being so weak, that the software used to process the LI curve produces highly scattered data. While one might be tempted to manually choose the “reasonably” looking set of LIV curves, one has to remember it would be dishonest considering that top and bottom 30 percentiles of performers have been already removed.

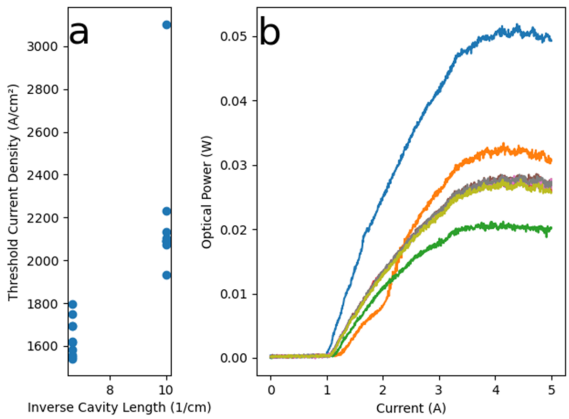

Figure 11 - InGaAsP layerstack performance at 85 C. (a) Scatterred Threshold Current Density datapoints, (b) LIV curves corredsponding to the 10/cm datapoints.

- J_{tr} of 3QW, 4QW doped, 4QW GRINSCH all increase drastically at 85 °C, while metrics of all the other AlGaInAs layerstacks follow smooth exponential increase as expected. This might be explained by looking at Table 4 with time schedule of the measurement campaign. All the "as expected" datapoints at 85 °C come from measurements done soon after datapoints from 70 °C. The anomalously increased results were obtained with lasers that had to wait for the 85 °C measurement. This indicates that anomalously high values are a result of oxidation, which degraded laser's performance.

The two above-mentioned issues mean that to determine T_0 I must use only the values coming from the measurements done at 70 °C and lower.

For temperatures lower and equal to 70 °C InGaAsP layerstack has third or second worst performance. Only AlGaInAs lasers with the largest number of quantum wells have higher J_{tr}.

T_0 of all the layerstacks is presented on Figure 12. All the AlGaInAs structures offer at least slight performance improvement over InGaAsP. Data of all the lasers with four quantum wells indicate that as predicted – inclusion of GRINSCH or extra doping is beneficial for the performance. GRINSCH offers lower J_{tr} than doped, however doped offers far superior T_0.

The layerstack with highest T_0 is the one with three quantum wells. This can be expected from equating two different formulas for threshold current density:

$$j_{fit} exp\left(\frac{T}{T_0}\right) = \frac{N_z J_{tr}}{\eta_i} exp\left[\frac{1}{b j_0 \Gamma}\left(\frac{1}{2L} ln\left(\frac{1}{R_1 R_2}\right) + \alpha\right)\right]$$

Where left-hand side represents the exponential dependence of threshold current density on temperature (with j_{fit} being a fitted constant), and right-hand side is already discussed in section 2.2.2 – Pitfalls of the linear models. After taking a logarithm of both sides, one can see that when the number of quantum wells (N_z) decreases, T_0 grows:

$$\frac{T}{T_0} = ln\left(\frac{N_z j_0}{\eta_i}\right) + \frac{1}{b j_0 \Gamma}\left(\frac{1}{2L} ln\left(\frac{1}{R_1 R_2}\right) + \alpha\right) - ln(j_{fit})$$

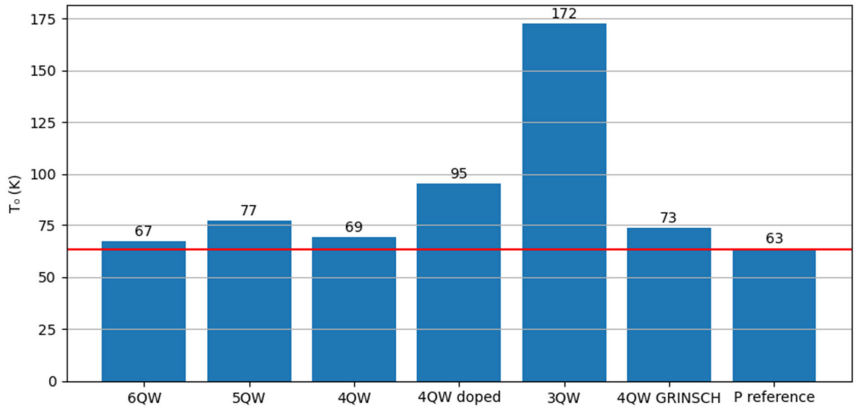

Figure 12 - Characteristic Temperature T_0 of investigated layerstacks

Those results are very good, compared to Broad Area Lasers reported by Tandon et al. Not only T_0 of InGaAsP layerstack from SMART Photonics is 14K higher than the one by Tandon (49K). T_0 of all the AlGaInAs layerstack is higher than Tandon's (64K) [42]. It is however important to note, that Tandon's layerstacks had 5 quantum wells of different strain and bandgap, and had doped SCH, therefore there is no straightforward direct comparison. Our lasers however present worse performance than that by Ohnoki (T_0=122K), but his layerstack had seven wells and contained an MQB [72]. This result highlights the potential usefulness of such modification.

2.3.4 – Internal Quantum Efficiency

As was discussed in section 2.2.2 – Pitfalls of the linear models, the measurement imperfection, and good diode performance, introduced nonlinearities that made the IQE determination impossible in most cases. Majority of the AlGaInAs layerstacks displayed the IQE larger than 1, with non-monotonous behaviour as a function of temperature. The only layerstack that yielded plausible outcome across the entire range of temperatures is InGaAsP, with IQE exponentially decreasing with the temperature,

however for reasons explained in section 2.3.5 – Internal Loss, the datapoint from the 85 °C should not be taken into consideration. AlGaInAs results are also unreliable at the 85 °C, thus only 20-75 °C range should be discussed.

In this section, most of the results are not plotted. Variabilities induced by measurement imperfection yielded chaotic values that could only decrease diagram's readability. Unlike in case of Threshold current density, there was no scientifically honest way to overcome this problem.

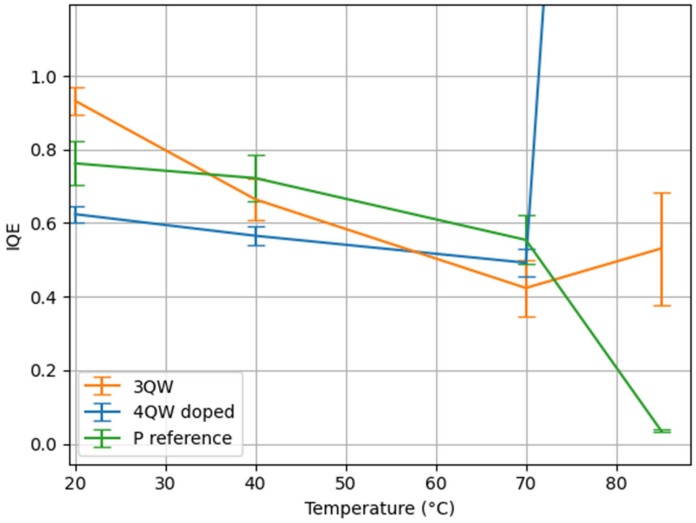

Figure 13 - Internal Quantum Efficiency as a function of the temperature.

3QW is very efficient (93%) at low temperature, however the performance decays very rapidly. The doped 4QW layerstack displays much lower efficiency at 20 °C (62 %) but its performance is robust against the temperature change. Choi investigated Broad Area Lasers and presented AlGaInAs layerstack with four 1% strained quantum wells, that operated with the IQE of 0.75 at 20 °C [38]. It is however difficult to compare, because the only 4QW layerstack that allows for straightforward IQE determination has doped SCH. On the other hand, it means that our InGaAsP layerstack displayed comparable (0.76) efficiency at 20 °C to the AlGaInAs one reported by Choi. Given that in our case, the other metrics (eg. J_{tr},

η_{WP}, or yield) display superiority of all AlGaInAs layerstacks over the InGaAsP one, we can assume that our 4QW device may be on par with the one of Choi.

Table 5 displays the T_1 of the layerstacks.

Layerstack	T_1 (K) (range: 20 to 70 °C)
3QW	63
4QW doped	210
P reference	156

Table 5 - T1 of investigated layerstacks

InGaAsP layerstack performs very well, compared to one reported by Tandon (101K), however different structure makes comparison difficult [42].

2.3.5 – Internal Loss

Below, on Figure 14 I show the numbers resulting from my measurements. Because of the reasons outlined in the section 2.3.4, in this section I will only discuss the results from the 3QW, 4QW doped, and InGaAsP layerstacks. AlGaInAs layerstacks display abrupt increase of loss at 85 °C. This can be attributed to long exposure to air, as can be noticed from the Table 4. The loss of InGaAsP reference lasers at 85 °C is unphysically low. This is most likely due to extremely poor performance of InGaAsP lasers at that temperature, which resulted in LI curves that couldn't be processed correctly and resulted in wildly varying slope efficiency results.

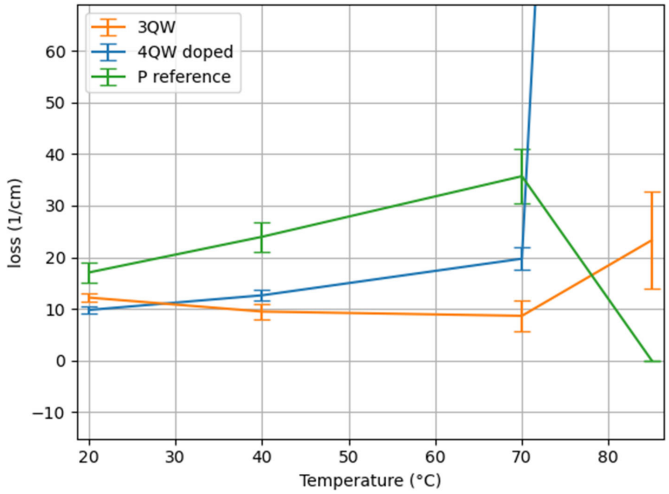

Figure 14 - Internal loss as a function of temperature.

The most reliable datapoints on this plot come from the measurements for temperatures below 85°C. Both AlGaInAs layertacks are less lossy than the P reference, which makes sense, since better electron trapping within the quantum wells means less electrons leaking into the SCH, in turn decreasing the free carrier losses.

While InGaAsP and 4QW doped follow a predictable loss increase with the temperature, one can notice that the 3QW samples displayed loss decrease over the 20-70 °C range. This anomaly surprises, since the datapoints were of high quality, and fitting avoided the unphysical IQE results. Explaining this would be very difficult, however there are two hypotheses:

- Measurement with 5 µs pulse causes all the results to be entirely unreliable and unphysical for all the layerstacks and all temperature ranges.
- Swietlik et al. observed such anomalous loss decrease and used simulations to tentatively attribute the anomaly to the decrease in the ballistic transport through the wells. At high temperature carriers cannot ballistically pass through the quantum wells, therefore there's less carriers in the p-side SCH that would contribute to the loss [102]. Kisin et al. proposed a model in which amount of ballistically overshooting electrons decrease exponentially with the distance, which would explain why this phenomenon is important in the laser with the smallest amount of quantum wells [103]

2.3.6 – Power Penalty

To calculate the power penalty, I used LI curves from the 1 mm-long devices, operating at the maximum current (5 A, corresponding to 10 kA/cm^2). It was impossible to use all the LI curves because very often mode hopping caused the optical power at 5A to be extremely low and unrepresentative of the device's performance, therefore I used only the LI curves used to determine the J_{tr} (i.e., top and bottom 30 percentiles rejected). Power values used to calculate the penalty are averages for each layerstack at each temperature.

Figure 15 shows the resulting power penalties. InGaAsP layerstack performs quite well at 40 °C, it is also the worst performer at all the other temperatures, especially at 85 °C. This matches the findings of previous sections.

Performance of all the other layerstacks is quite similar, although there are two remarkable outliers: the 3QW layerstack and the GRINSCH layerstack. 3QW layerstack displays the largest power penalty of all the AlGaInAs layerstacks. This confirms findings of section 2.3.5 – Internal Loss where it displayed the largest drop of IQE. The GRINSCH layerstack performs remarkably well at 40 °C and 70 °C.

Another interesting fact is that "4QW doped" layerstack performs un-remarkably at 40 °C, while it becomes the best layerstack at all the higher temperatures. This reveals large potential of this type of layerstack, considering it displayed un-impressive T_0 and unreliable results in terms of IQE and loss at 85 °C.

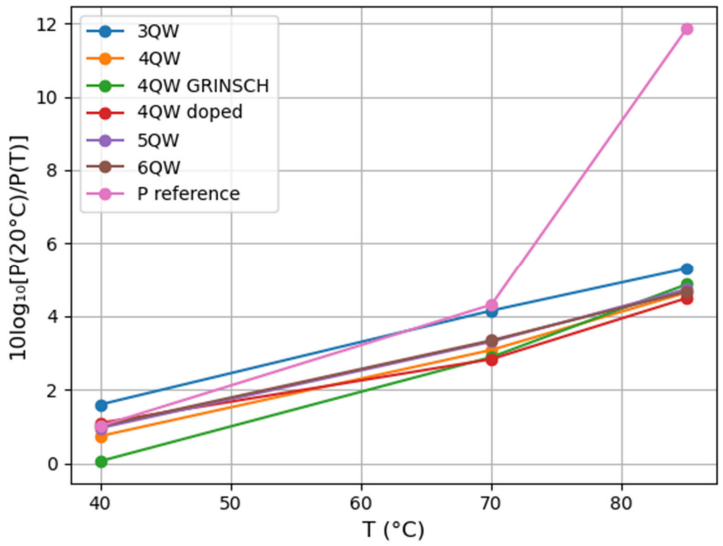

Figure 15 - Power Penalty as a function of temperature

2.3.7 – Absolute power

To study the absolute power output, I averaged the output of 1 mm long Broad Area Lasers that were used in 2.3.3 – Threshold Current Density at Transparency. It is important to remember that this data rejects top and bottom 30 percentiles to avoid anomalous read-outs.

Figure 16 displays how maximum power (from one facet) depends on the temperature and layerstack.

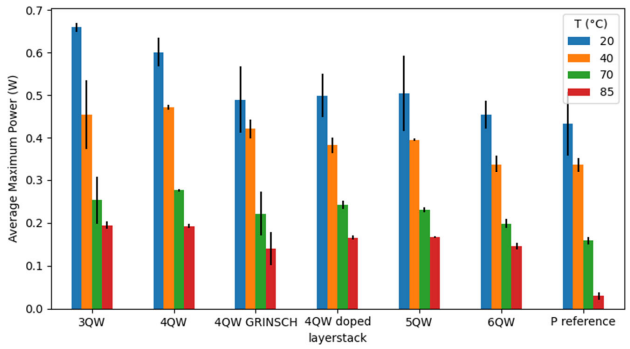

Figure 16 - Average maximum power, depending on layerstack and temperature. Error bars correspond to standard deviations.

One can see, that there's not much difference between 3QW and 4QW layerstacks. Both of them achieve highest power output of all the layerstacks, across all the temperatures.

One can clearly notice, that introduction of GRINSCH or doping into 4QW layerstack decreases the power output, however, just as shown in 2.3.6 – Power Penalty, both modified SCHs display slower decline with temperature. It is interesting, since both modified layerstacks should achieve higher output powers due to their superior electron confinement. Elenkrig reported that higher series resistance caused by the heterointerfaces limits the maximum output power [104]. Considering that in 2.3.2 – Maximum Wall-Plug Efficiency it was shown that devices with modified SCH have slightly worse η_{WPmax} than the default 4QW version, and since η_{WPmax} and maximum output power both depend on the series resistance, this indeed might be the issue. This hypothesis gains even more reliability, considering that growing a modified layerstack is indeed more difficult and might introduce unwanted heterointerfaces.

Another power-limiting factor, according to Botez et al., might be the confinement factor of the layerstack [105]. Because of SMART photonic's platform's requirements, width of the SCH has to be fixed, independent on the SCH's modification, and the resultant confinement factor's change.

For 5QW and 6QW layerstack, slight maximum power decrease is observed, compared to 4QW layerstacks.

All of the AlGaInAs layerstacks display higher maximum output powers at all temperatures, compared to the InGaAsP reference.

2.4 - Conclusions

To make conscious choices about final layerstack design for SMART photonics platform, it is necessary to concisely, qualitatively summarize the results.

3QW	η_{WPmax}	Best of all layerstacks
	J_{tr}	Best of all layerstacks
	T_0	Best of all layerstacks
	IQE	No good comparison
	T_1	Poor
	Power	Best of all layerstacks
	Power Penalty	Worst of all layerstacks
4QW	η_{WPmax}	Better than counterparts with modified SCH
	J_{tr}	worse than counterparts with modified SCH
	T_0	Unremarkable
	IQE	Unknown
	T_1	Unknown
	Power	Better than counterparts with modified SCH
	Power Penalty	Slightly worse than counterparts with modified SCH
4QW doped	η_{WPmax}	Slightly worse than 4QW
	J_{tr}	Better than 4QW
	T_0	Best of all 4QW layerstacks
	IQE	difficult to compare
	T_1	High, difficult to compare
	Power	Slightly worse than 4QW
	Power Penalty	Usually best (except at 40 °C)
4QW GRINSCH	η_{WPmax}	Slightly worse than 4QW
	J_{tr}	Better than 4QW
	T_0	Unremarkable
	IQE	Unknown
	T_1	Unknown
	Power	Slightly worse than 4QW
	Power Penalty	Unremarkable
5QW	η_{WPmax}	Unremarkable
	J_{tr}	High
	T_0	Unremarkable
	IQE	Unknown
	T_1	Unknown
	Power	Low
	Power Penalty	Unremarkable
6QW	η_{WPmax}	Worst
	J_{tr}	Worst

	T_0	Unremarkable
	IQE	Unknown
	T_1	Unknown
	Power	Worst
	Power Penalty	Unremarkable

Table 6 - Summary of research findings

Findings displayed in Table 6 suggest that using more than 4 quantum wells in the layerstack is not needed. Introduction of the SCH modifications seem to offer clear performance improvements, however one must bear in mind the trade-offs in terms of maximum power output. Those trade-offs seem to be more of a manufacturing and design issue, considering that in the bulk of literature, introduction of such modifications is generally beneficial.

There are several more conclusions:

- AlGaInAs MQW lasers are usually needed in telecommunications, where other parameters, such as K-factor, or small signal modulation bandwith play important role [73], [85]. Investigation of such parameters is necessary, so SMART photonics can offer better gain medium for their customers.
- While AlGaInAs degradation caused by oxidation is a legitimate concern, I only noticed significant performance degradation in case of devices that spent more than one month exposed to air. This means that while avoiding oxygen is very important, it is not an urgent issue to tackle.
- Improvement of SMART Photonics measurement setup is needed to avoid gain-current nonlinearities that make it impossible to determine the IQE or loss. Utilized SMU should be able to generate pulses shorter than 500 ns (preferably 100 or 200 ns)

Chapter 3 – Experiment and result discussion – AlGaInAs composition and properties

In this thesis I will use the following convention to refer to composition and strain of the AlGaInAs:

- AlGaInAs should be read as $Al_xGa_yIn_zAs$ with z=1-x-y
- x, y, and z are also called atomic fractions or Al fraction, Ga fraction and In fraction
- Strain is called compressive for $\varepsilon < 0$ and tensile for $\varepsilon > 0$
- Strain is calculated the following way: $\varepsilon = \frac{a_{InP} - a_{AlGaInAs}}{a_{AlGaInAs}}$

This part of my thesis is partially based on work done by Nick de Louw during his external internship project for master degree, done at TUe [106]. I was one of supervisors of his work. His report is confidential, and there's no full text source on the internet.

3.1 – Determining composition of the alloy

There are multiple ways to quantitatively determine the stoichiometric composition of a semiconductor, however for industrial use, requirement of scalability and cost limitation make us determine the grown alloy's composition by calculating it using the settings of the MOVPE reactor used for quaternary's growth. For example, to calculate the flux of gallium (φ_{Ga}) into the reactor, the following formula is used:

$$\varphi_{Ga} = \frac{Q_{H_2} \cdot P_{vap,Ga}}{P_{bubbler,Ga} - P_{vap,Ga}} \quad 8$$

Where Q_{H_2} is hydrogen flow through TMGa bubbler, $P_{vap,Ga}$ is compound's vapor pressure, and $P_{bubbler,Ga}$ is pressure within TMGa bubbler. Analogous calculation can be applied to other elements, with result multiplied by 2 for the TMAl, because said molecule is a dimer.

Composition of the actual alloy is then determined by normalizing given precursor flux to the sum of all precursor fluxes.

In order to validate this method we compared its results to the ones obtained by the means of Inductively Coupled Plasma Optical Emission Spectroscopy (ICP-OES), outsourced to the Eurofins company. ICP-OES is known to be a very precise method, confirmed to work very well (down to 1% of accuracy in good conditions) for the semiconductors [107].

Data of ICP-OES have been obtained using the following procedure:

1. Selective etch of AlGaInAs using a mixture of water, hydrogen peroxide, and sulphuric acid
2. Sending samples of resulting solution to Eurofins, along with a sample of etchant, for calibration
3. Since the etchant has finite selectivity, there's a chance of contamination with In coming from InP substrate. To account for that, we also measure the amount of P in each samples, since amount of contaminant In has 1:1 ratio with P.
4. To calculate the atomic fractions of each element, we convert from resulting ICP-OES concentrations (mmol/l) into atomic fractions by normalizing each result to As concentration.

Figure X shows the relation between results obtained with those two methods for 5 wafers of different compositions. It is important to note that measuring more wafers with ICP-OES would be very expensive and time consuming.

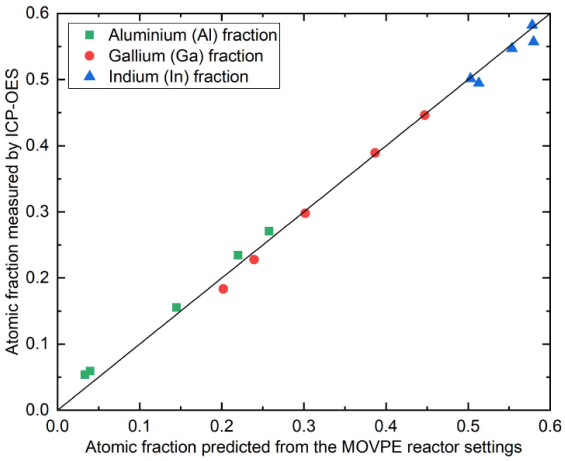

Figure 17 - Validation of MOVPE settings method, using ICP-OES method

There's a clear linear relationship between both results, with the linear regression's slope being XXXX and the correlation coefficient of XXXX. The deviations from the straight line are the strongest for the low Al fractions (up to 38% away from the reference value), however any valid statistical analysis is impossible due to limited amount of samples. Using ICP-OES lets us assume 1:1 fidelity of MOVPE/ICP-OES conversion, but one must remember about the discovered limitations.

3.2 – Quality of measurements

Measurement of the alloy's bandgap have been carried-out with a RPM2000 photoluminescence mapper. In this work we define each wafer's PL wavelength as an average of all measurements taken within 2 cm radius from the wafer's center. To know the homogeneity of each deposition, we calculate the standard deviation of all the datapoints within same region of PL map. The largest standard deviation is 5.79 nm. In the data collection process we took care to eliminate all the results coming from the "interface band-bending trap" emission, which might distort data [108], [109].

Knowing the homogeneity of each wafer, we proceed to learn about the wafer-wafer reproducibility of the results. To do that, we compile the Table 7, which shows several groups of wafers having identical growth conditions, along with corresponding information about PL measurement.

Al (x)	Ga (y)	Quantity of such samples (n_i)	Average PL wavelength (nm)	Standard deviation (nm) (σ_i)
0.036463	0.399308	6	1525.941853	2.946729
0.141529	0.296918	5	1281.001032	10.405485
0.144861	0.301656	4	1268.028674	6.783796
0.219529	0.202252	2	1147.481957	0.674887
0.237936	0.204206	4	1098.103986	5.206925

Table 7 - Samples used for wafer-wafer reproducibility study

To calculate the standard deviation originating from the production and measurement differences between different wafers, we employ the pooled standard deviation formula:

$$\sigma = \sqrt{\frac{\sum_i (n_i - 1)\sigma_i^2}{\sum_i (n_i - 1)}} = 6.6nm \qquad 9$$

Where n_i is the number of samples in given subset, σ_i^2 is the variance of given subset, and σ is the pooled standard deviation. Such approach is valid, since the data coming from table X (displayed as a histogram on figure Y) subjected to Pearson-D'Agostino normality test, resulted in p=0.48, meaning that the dataset is normal, and pooled standard deviation formula applies to it.

Those results mean that wafer-wafer reproducibility is only slightly worse than a single-wafer homogeneity, and that we can treat all the samples with the same statistical weight.

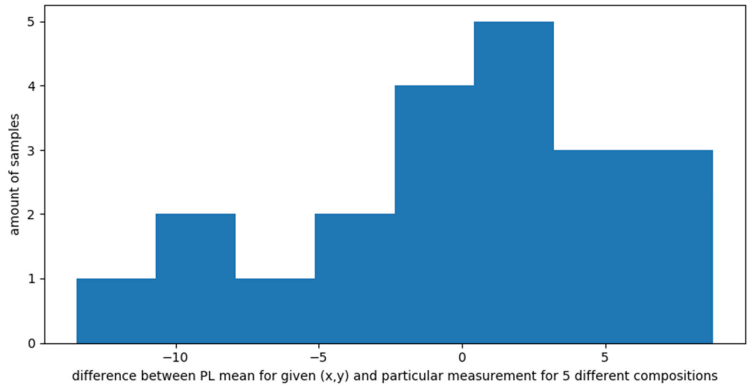

Figure 18 - wafer-wafer reproducibility study outcome

3.3 – Determining the bandgap of AlGaInAs

Appendix A – Rejected 4QW GRINSCH datapoints

4QW AlGaInAs layerstack with GRINSCH shown quite anomalous, highly scattered behaviour that couldn't be explained by my investigation.

Results coming from non-modified data are shown on fig AX

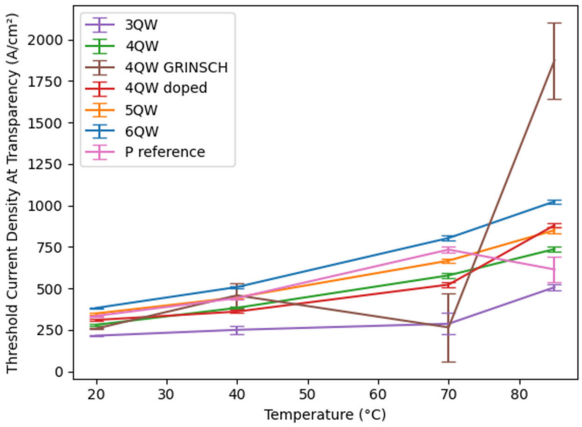

GRINSCH layerstack is performing poorly at 40 °C, anomalously well at 70 °C, and extremely poorly at 85 °C. To understand the source of this behavior one must investigate raw data.

Threshold current density as a function of Inverse Cavity Length at 40 °C is shown on figure AX. For each length, top and bottom 30 percentiles were removed. One can see, that nonlinearity described in section "Pitfalls of linear models" does not occur, however the 1.5 mm cavity displays exceptionally scattered behavior. This might be caused by some technical imperfection of the measurement. With

longest and shortest cavity removed the outliers cause the fitting line to shift the intercept (J_{tr}) towards higher values.

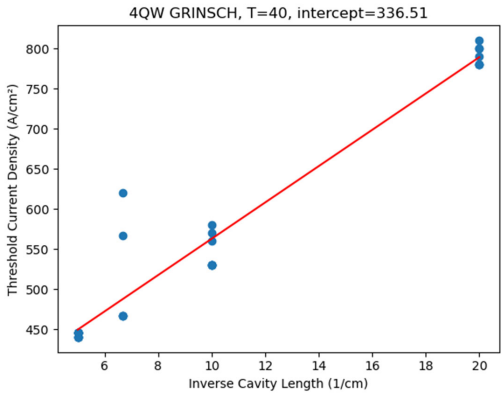

AX

At 85 °C the 1.5 mm cavity laser also displays extremely scattered outlier behavior, however without linear trend.

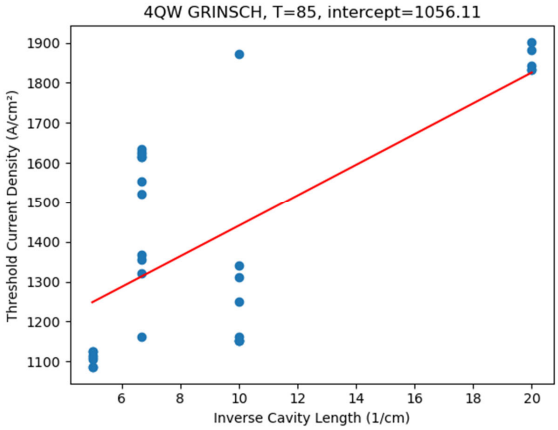

At 70 °C one can see that all datapoints display clear linear trend without suspicious nonlinearities, however medium-length cavities display very scattered behaviour, which also might be a sign of technical issues during the measurement.

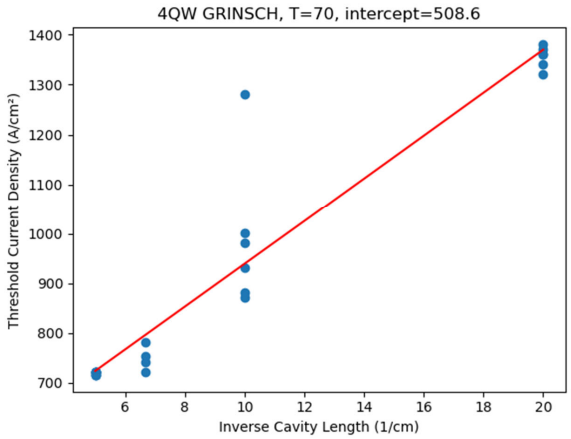

Justified with above explanation, the following action was taken:

40	Use of all datapoints except for the ones with 1.5 mm cavity (6.666 1/cm)
70	Use of all datapoints.
85	Use of all datapoints, acknowledging their unreliability, not using them for any judgement.

[1] P. E. Haggerty, 'Integrated electronics—A perspective', *Proc. IEEE*, vol. 52, no. 12, pp. 1400–1405, 1964, doi: 10.1109/PROC.1964.3422.

[2] M. A. Rafiq, C. Li, and B. Cheng, 'Remembering John Bardeen: inventor of transistor', *J. Semicond.*, vol. 40, no. 2, p. 020301, Feb. 2019, doi: 10.1088/1674-4926/40/2/020301.

[3] G. E. Moore, 'Cramming More Components onto Integrated Circuits', *PROCEEDINGS OF THE IEEE*, vol. 86, no. 1, p. 4, 1998.

[4] P. E. Ceruzzi, *A history of modern computing*, 2nd ed. London, Eng. ; Cambridge, Mass: MIT Press, 2003.

[5] L. R. Berlin, 'Robert Noyce and Fairchild Semiconductor, 1957–1968', *Bus. Hist. Rev.*, vol. 75, no. 1, pp. 63–101, 2001, doi: 10.2307/3116557.

[6] 'The Nobel Prize in Physics 2000', *NobelPrize.org*. https://www.nobelprize.org/prizes/physics/2000/press-release/ (accessed Jul. 25, 2022).
[7] M. Krasnodębski, 'Throwing light on photonics: The genealogy of a technological paradigm', *Centaurus*, vol. 60, no. 1–2, pp. 3–24, Feb. 2018, doi: 10.1111/1600-0498.12172.
[8] S. E. Miller, 'Integrated Optics: An Introduction', *Bell System Technical Journal*, vol. 48, no. 7, pp. 2059–2069, Sep. 1969, doi: 10.1002/j.1538-7305.1969.tb01165.x.
[9] D. D'Agostino, *Capability extensions to the COBRA generic photonic integration platform*. Technische Universiteit Eindhoven, 2015.
[10] G. Lifante, *Integrated Photonics: Fundamentals: Lifante/Integrated Photonics*. Chichester, UK: John Wiley & Sons, Ltd, 2003. doi: 10.1002/0470861401.
[11] W.-P. Huang, X. Li, C.-Q. Xu, X. Hong, C. Xu, and W. Liang, 'Optical Transceivers for Fiber-to-the-Premises Applications: System Requirements and Enabling Technologies', *J. Lightwave Technol.*, vol. 25, no. 1, pp. 11–27, Jan. 2007, doi: 10.1109/JLT.2006.888482.
[12] C. Minkenberg, R. Krishnaswamy, A. Zilkie, and D. Nelson, 'Co-packaged datacenter optics: Opportunities and challenges', *IET Optoelectronics*, vol. 15, no. 2, pp. 77–91, Apr. 2021, doi: 10.1049/ote2.12020.
[13] R. Osellame and R. Martinez, 'Integrating optical sensing into lab-on-a-chip systems', *SPIE Newsroom*, 2009, doi: 10.1117/2.1200905.1597.
[14] M. Sohbati and C. Toumazou, 'Personalized Microchips for Health Care', *IEEE Potentials*, vol. 34, no. 2, pp. 33–37, Mar. 2015, doi: 10.1109/MPOT.2014.2358695.
[15] L. Kwon, K. D. Long, Y. Wan, H. Yu, and B. T. Cunningham, 'Medical diagnostics with mobile devices: Comparison of intrinsic and extrinsic sensing', *Biotechnology Advances*, vol. 34, no. 3, pp. 291–304, May 2016, doi: 10.1016/j.biotechadv.2016.02.010.
[16] A. B. González-Guerrero, J. Maldonado, S. Herranz, and L. M. Lechuga, 'Trends in photonic lab-on-chip interferometric biosensors for point-of-care diagnostics', *Anal. Methods*, vol. 8, no. 48, pp. 8380–8394, 2016, doi: 10.1039/C6AY02972H.
[17] Anne M.G. Kwak, Ed., 'Unleashing the power of PIC TECHNOLOGY ROADMAP 2021 - 2025'. JePPIX - the Joint European Platform for Photonic Integrated Components and Circuits, Mar. 08, 2021.
[18] P. Sibson *et al.*, 'Chip-based quantum key distribution', *Nat Commun*, vol. 8, no. 1, p. 13984, Apr. 2017, doi: 10.1038/ncomms13984.
[19] 'PHOTONICS APPLIED: COMMUNICATIONS: Optical technologies scale the datacenter', *Laser Focus World*, Dec. 01, 2012. https://www.laserfocusworld.com/lasers-sources/article/16549513/photonics-applied-communications-optical-technologies-scale-the-datacenter (accessed Nov. 10, 2021).
[20] *COMMUNICATION FROM THE COMMISSION TO THE EUROPEAN PARLIAMENT, THE EUROPEAN COUNCIL, THE COUNCIL, THE EUROPEAN ECONOMIC AND SOCIAL COMMITTEE AND THE COMMITTEE OF THE REGIONS A New Industrial Strategy for Europe*. 2020. Accessed: Jul. 25, 2022. [Online]. Available: https://eur-lex.europa.eu/legal-content/EN/TXT/PDF/?uri=CELEX:52020DC0102&from=EN
[21] M. Smit, K. Williams, and J. van der Tol, 'Past, present, and future of InP-based photonic integration', *APL Photonics*, vol. 4, no. 5, p. 050901, May 2019, doi: 10.1063/1.5087862.
[22] K. J. Soda, 'Keys To Successful Vlsi Realization Through Mosis (How To Get Three Computers To Cooperate And Remain Sane)', in *1998 Annual Conference Proceedings*, Seattle, Washington, Jun. 1998, p. 3.386.1-3.386.10. doi: 10.18260/1-2--7255.
[23] M. K. Smit, R. Baets, and M. Wale, 'InP-based Photonic Integration: Learning from CMOS', p. 2, 2009.
[24] M. Smit *et al.*, 'An introduction to InP-based generic integration technology', *Semicond. Sci. Technol.*, vol. 29, no. 8, p. 083001, Jun. 2014, doi: 10.1088/0268-1242/29/8/083001.

[25] 'John Tyndall Award Winners - IEEE Photonics Society'. https://www.photonicssociety.org/awards/john-tyndall-award/john-tyndall-award-winners (accessed Jul. 25, 2022).
[26] 'Home', *Jeppix*. https://www.jeppix.eu/ (accessed Jul. 27, 2022).
[27] epixfabe, 'About', *ePIXfab-European Silicon Photonics Alliance*. https://epixfab.eu/about-epixfab/ (accessed Jul. 27, 2022).
[28] R. G. Broeke, 'doctorandus in de natuurkunde, geboren te Maarssen.', p. 159.
[29] J. J. Bregenzer, 'Integrated polarisation rotators', p. 212.
[30] G. P. Agrawal and N. K. Dutta, *Semiconductor Lasers.* New York, NY: Springer, 2013. Accessed: Nov. 18, 2020. [Online]. Available: https://public.ebookcentral.proquest.com/choice/publicfullrecord.aspx?p=5575465
[31] I. Hayashi, M. B. Panish, and P. W. Foy, 'JUNCTION LASERS WHICH OPERATE CONTINUOUSLY AT ROOM TEMPERATURE', *APPLIED PHYSICS LETTERS*, vol. 17, no. 3, p. 4, 1970.
[32] P. K. Basu, B. Mukhopadhyay, and R. Basu, 'Semiconductor Laser Theory', p. 540.
[33] I. Camps, M. Sanchez, and J. C. Gonzalez, 'Efficiencies in multiquantum well lasers', *Semicond. Sci. Technol.*, vol. 17, no. 9, pp. 1013–1022, Sep. 2002, doi: 10.1088/0268-1242/17/9/320.
[34] D. Labukhin and X. Li, 'Polarization Insensitive Asymmetric Ridge Waveguide Design for Semiconductor Optical Amplifiers and Super Luminescent Light-Emitting Diodes', *IEEE J. Quantum Electron.*, vol. 42, no. 11, pp. 1137–1143, Nov. 2006, doi: 10.1109/JQE.2006.882875.
[35] S. Wang *et al.*, 'MOVPE growth of grade-strained bulk InGaAs/InP for broad-band optoelectronic device applications', *Journal of Crystal Growth*, vol. 260, no. 3–4, pp. 464–468, Jan. 2004, doi: 10.1016/j.jcrysgro.2003.09.003.
[36] I. Ladany, 'The influence of stripe width on the threshold current of double-heterojunction lasers', *Journal of Applied Physics*, vol. 48, no. 5, pp. 1935–1940, May 1977, doi: 10.1063/1.323897.
[37] S. Arafin and L. A. Coldren, 'Advanced InP Photonic Integrated Circuits for Communication and Sensing', *IEEE J. Select. Topics Quantum Electron.*, vol. 24, no. 1, pp. 1–12, Jan. 2018, doi: 10.1109/JSTQE.2017.2754583.
[38] W.-Y. Choi, 'MBE-Grown Long Wavelength InGaAlAs/InP Laser Diodes', p. 116.
[39] S. O. Slipchenko, A. V. Lyutetski, Y. A. Ryaboshtan, E. G. Golikova, and I. S. Tarasov, 'Low-Threshold-Current 1.2–1.5 mm Laser Diodes Based on AlInGaAs/InP Heterostructures', vol. 29, no. 2, p. 4, 2003.
[40] M. T. Camargo Silva, J. P. Sih, T. M. Chou, J. K. Kirk, G. A. Evans, and J. K. Butler, '1.3 µm strained MQW AlGaInAs and InGaAsP ridge-waveguide lasers-a comparative study', in *1999 SBMO/IEEE MTT-S International Microwave and Optoelectronics Conference*, Rio de Janeiro, Brazil, 1999, vol. 1, pp. 10–12. doi: 10.1109/IMOC.1999.867027.
[41] Tawee Tanbun-Ek *et al.*, 'High performance buried heterostructure 1.55 µm wavelength AlGaInAs/InP multiple quantum well lasers grown entirely by MOVPE technique', in *Conference Proceedings. 1998 International Conference on Indium Phosphide and Related Materials (Cat. No.98CH36129)*, Tsukuba, Japan, 1998, pp. 702–705. doi: 10.1109/ICIPRM.1998.712736.
[42] A. Tandon, D. P. Bour, Y. L. Chang, C. K. Lin, S. W. Corzine, and M. R. Tan, 'Low-threshold, high-T 0 and high-efficiency 1300nm and 1500nm lasers with AlInGaAs active region grown by MOCVD', presented at the Integrated Optoelectronic Devices 2004, San Jose, CA, United States, Jun. 2004, p. 206. doi: 10.1117/12.540319.
[43] R. A. G. dos Santos *et al.*, 'Datacenter Thermal Monitoring Without Blind Spots: FBG-Based Quasi-Distributed Sensing', *IEEE Sensors J.*, vol. 21, no. 8, pp. 9869–9876, Apr. 2021, doi: 10.1109/JSEN.2021.3058513.

[44] C.-E. Zah *et al.*, 'High-Performance Uncooled 1.3-pm AlxGayIn1-Ix:- As/InP Strained-Layer Quantum-Well Lasers for Subscriber Loop Applications', *IEEE JOURNAL OF QUANTUM ELECTRONICS*, vol. 30, no. 2, p. 13, 1994.
[45] S. R. Selmic *et al.*, 'Design and Characterization of 1.3- m AlGaInAs–InP Multiple-Quantum-Well Lasers', *IEEE JOURNAL ON SELECTED TOPICS IN QUANTUM ELECTRONICS*, vol. 7, no. 2, p. 10, 2001.
[46] G. Lin and C. P. Lee, 'Comparison of 1300 nm quantum well lasers using different material systems', p. 10.
[47] H. Temkin, K. Alavi, W. R. Wagner, T. P. Pearsall, and A. Y. Cho, '1.5–1.6-μm Ga $_{0.47}$ In $_{0.53}$ As/Al $_{0.48}$ In $_{0.52}$ As multiquantum well lasers grown by molecular beam epitaxy', *Appl. Phys. Lett.*, vol. 42, no. 10, pp. 845–847, May 1983, doi: 10.1063/1.93786.
[48] R. Gessner, M. Druminski, and M. Beschorner, 'GaInAs/AlGaInAs DH and MQW lasers with 1.5–1.7 μm lasing wavelengths grown by atmospheric pressure MOVPE', *Electron. Lett.*, vol. 25, no. 8, p. 516, 1989, doi: 10.1049/el:19890353.
[49] M. Allovon and M. Quillec, 'Interest in AlGaInAs on InP for optoelectronic applications', p. 5.
[50] J. Minch, S. H. Park, T. Keating, and S. L. Chuang, 'Theory and Experiment of In Ga As P and In Ga Al As Long-Wavelength Strained Quantum-Well Lasers', *IEEE JOURNAL OF QUANTUM ELECTRONICS*, vol. 35, no. 5, p. 13, 1999.
[51] L. A. Coldren, S. W. Corzine, and M. Mashanovitch, *Diode lasers and photonic integrated circuits*, 2nd ed. Hoboken, N.J: Wiley, 2012.
[52] P. G. Eliseev, B. N. Sverdlov, I. Ismailov, and N. Shokhudzhaev, 'Influence of anisotropic deformation on the radiative characteristics of GaInAsP/InP injection lasers. I. Lasing threshold, polarization, and watt-ampere characteristic', *Sov. J. Quantum Electron.*, vol. 16, no. 8, pp. 1046–1050, Aug. 1986, doi: 10.1070/QE1986v016n08ABEH007236.
[53] E. P. O'Reilly and A. R. Adams, 'Band-structure engineering in strained semiconductor lasers', *IEEE J. Quantum Electron.*, vol. 30, no. 2, pp. 366–379, Feb. 1994, doi: 10.1109/3.283784.
[54] C. E. Zah *et al.*, 'Low threshold 1.5 μm tensile-strained single quantum well lasers', *Electron. Lett.*, vol. 27, no. 16, p. 1414, 1991, doi: 10.1049/el:19910887.
[55] A. R. Adams, 'Strained-Layer Quantum-Well Lasers', *IEEE J. Select. Topics Quantum Electron.*, vol. 17, no. 5, pp. 1364–1373, Sep. 2011, doi: 10.1109/JSTQE.2011.2108995.
[56] Y. Zhao, J. Huang, Y. Sun, S. Yu, K. Li, and J. Dong, 'Influence of growth conditions on the quality of strained InAlGaAs/AlGaAs quantum wells grown by MOCVD', *Appl. Phys. A*, vol. 125, no. 2, p. 117, Feb. 2019, doi: 10.1007/s00339-019-2411-5.
[57] M. Ogasawara, H. Sugiura, M. Mitsuhara, M. Yamamoto, and M. Nakao, 'Influence of net strain, strain type, and temperature on the critical thickness of In(Ga)AsP-strained multi quantum wells', *Journal of Applied Physics*, vol. 84, no. 9, pp. 4775–4780, Nov. 1998, doi: 10.1063/1.368719.
[58] Y.-K. Kuo, S.-H. Yen, and M.-W. Yao, 'Optimization study on active layers and optical performance for 1.3-μm AlGaInAs and InGaNAs semiconductor lasers', presented at the Integrated Optoelectronic Devices 2006, San Jose, CA, Feb. 2006, p. 611526. doi: 10.1117/12.645196.
[59] V. B. Yekta and H. Kaatuzian, 'Design considerations to improve high temperature characteristics of 1.3 μm AlGaInAs-InP uncooled multiple quantum well lasers: Strain in barriers', *Optik*, vol. 122, no. 6, pp. 514–519, Mar. 2011, doi: 10.1016/j.ijleo.2010.03.016.
[60] S. Seki, '1.3- m InP-Based Quantum-Well Lasers with n-Doped Separate Confinement Heterostructure Layers for High-Temperature Operation', *IEEE PHOTONICS TECHNOLOGY LETTERS*, vol. 10, no. 2, p. 3, 1998.
[61] H. Wada, K. Takemasa, T. Munakata, M. Kobayashi, and T. Kamijoh, 'Effects of well number on temperature characteristics in 1.3-μm AlGaInAs-InP quantum-well lasers', *IEEE J. Select. Topics Quantum Electron.*, vol. 5, no. 3, pp. 420–427, Jun. 1999, doi: 10.1109/2944.788400.

[62] T. Ishikawa *et al.*, 'Well-Thickness Dependence of High-Temperature Characteristics in 1.3- m AlGaInAs–InP Strained-Multiple-Quantum-Well Lasers', p. 3.
[63] J. C. L. Yong, J. M. Rorison, and I. H. White, '1.3-µm quantum-well InGaAsP, AlGaInAs, and InGaAsN laser material gain: a theoretical study', *IEEE J. Quantum Electron.*, vol. 38, no. 12, pp. 1553–1564, Dec. 2002, doi: 10.1109/JQE.2002.805100.
[64] D. A. Veselov *et al.*, 'On the problem of internal optical loss and current leakage in laser heterostructures based on AlGaInAs/InP solid solutions', *Semiconductors*, vol. 50, no. 9, pp. 1225–1230, Sep. 2016, doi: 10.1134/S1063782616090244.
[65] N. A. Gun'ko, A. S. Polkovnikov, and G. G. Zegrya, 'A numerical calculation of auger recombination coefficients for InGaAsP/InP quantum well heterostructures', *Semiconductors*, vol. 34, no. 4, pp. 448–452, Apr. 2000, doi: 10.1134/1.1188006.
[66] M. I. Dyakonov and V. Yu. Kachorovskii, 'Nonthreshold Auger recombination in quantum wells', *Phys. Rev. B*, vol. 49, no. 24, pp. 17130–17138, Jun. 1994, doi: 10.1103/PhysRevB.49.17130.
[67] R. F. Kazarinov and M. R. Pinto, 'Carrier transport in laser heterostructures', *IEEE J. Quantum Electron.*, vol. 30, no. 1, pp. 49–53, Jan. 1994, doi: 10.1109/3.272061.
[68] R. F. Kazarinov and G. L. Belenky, 'Novel Design of AlGaInAs-InP Lasers Operating at 1.3 pm', p. 4.
[69] K. Takemasa, T. Munakata, M. Kobayashi, H. Wada, and T. Kamijoh, 'High Temperature Operation of AlGaInAs Ridge Waveguide Lasers with a p-AlInAs Electron Stopper Layer', *Jpn. J. Appl. Phys.*, vol. 38, no. Part 1, No. 2B, pp. 1230–1233, Feb. 1999, doi: 10.1143/JJAP.38.1230.
[70] B.-T. Liou, S.-H. Yen, M.-W. Yao, M.-L. Chen, Y.-K. Kuo, and S.-H. Chang, 'Numerical study for 1.55-µm AlGaInAs/InP semiconductor lasers', presented at the Optics East 2006, Boston, MA, Oct. 2006, p. 636814. doi: 10.1117/12.685959.
[71] M. Irikawa, H. Shimizu, I. Fukushima, K. Nishikata, and Y. Hirayama, 'Strained GaInAs-AlGaInAs 1.5-µm-wavelength multiquantum-well lasers loaded with GaInAs-AlInAs multiquantum barriers at the p-side optical confinement layer', *IEEE J. Select. Topics Quantum Electron.*, vol. 1, no. 2, pp. 285–292, Jun. 1995, doi: 10.1109/2944.401207.
[72] N. Ohnoki, G. Okazaki, F. Koyama, and K. Iga, 'Record high characteristic temperature (To = 122 K) of 1.55 [micro sign]m strain-compensated AlGaInAs/AlGaInAs MQW lasers with AlAs/AlInAs multiquantum barrier', *Electron. Lett.*, vol. 35, no. 1, p. 51, 1999, doi: 10.1049/el:19990031.
[73] T. Fukushima, H. Shimizu, K. Nishikata, Y. Hirayama, and M. Irikawa, 'Carrier confinement by multiple quantum barriers in 1.55 µm strained GaInAs/AlGaInAs quantum well lasers', *Appl. Phys. Lett.*, vol. 66, no. 16, pp. 2025–2027, Apr. 1995, doi: 10.1063/1.113680.
[74] J.-W. Pan, K.-G. Chau, J.-I. Chyi, Y.-K. Tu, and J.-W. Liaw, 'Suppression of electron and hole leakage in 1.3 µm AlGaInAs/InP quantum well lasers using multiquantum barrier', *Appl. Phys. Lett.*, vol. 72, no. 17, pp. 2090–2092, Apr. 1998, doi: 10.1063/1.121285.
[75] Y. S. Yong, H. Y. Wong, and H. K. Yow, 'Novel Separate Confinement Heterostructure Design for Long-Wavelength Lasers', *IEEE Electron Device Lett.*, vol. 32, no. 7, pp. 925–927, Jul. 2011, doi: 10.1109/LED.2011.2147275.
[76] Y. S. Yong, H. Y. Wong, H. K. Yow, and M. Sorel, 'Systematic study on the confinement structure design of 1.5-µm InGaAlAs/InP multiple-quantum-well lasers', *Laser Phys.*, vol. 20, no. 4, pp. 811–815, Apr. 2010, doi: 10.1134/S1054660X10070376.
[77] Y. S. Yong, H. Y. Wong, H. K. Yow, and M. Sorel, 'Separate confinement heterostructure design for InGaAlAs/InP multiple-quantum-well lasers: critical analysis and proposal of novel design', presented at the Photonics North 2010, Niagara Falls, Canada, Jun. 2010, p. 77501Y. doi: 10.1117/12.873038.
[78] N. A. Volkov *et al.*, 'Semiconductor AlGaInAs/InP lasers (λ = 1450 – 1500 nm) with a strongly asymmetric waveguide', *Quantum Electron.*, vol. 51, no. 2, pp. 133–136, Feb. 2021, doi: 10.1070/QEL17480.

[79] B. S. Ryvkin and E. A. Avrutin, 'Effect of carrier loss through waveguide layer recombination on the internal quantum efficiency in large-optical-cavity laser diodes', *Journal of Applied Physics*, vol. 97, no. 11, p. 113106, Jun. 2005, doi: 10.1063/1.1929087.
[80] A. A. Marmalyuk *et al.*, 'AlGaInAs/InP semiconductor lasers with an increased electron barrier', *Quantum Electron.*, vol. 49, no. 6, pp. 519–521, Jun. 2019, doi: 10.1070/QEL17032.
[81] A. A. Marmalyuk *et al.*, 'Effect of the waveguide layer thickness on output characteristics of semiconductor lasers with emission wavelength from 1500 to 1600 nm', *Quantum Electron.*, vol. 48, no. 3, pp. 197–200, Mar. 2018, doi: 10.1070/QEL16545.
[82] C. K. Williams, T. H. Glisson, J. R. Hauser, and M. A. Littlejohn, 'ENERGY BANDGAP AND LATTICE CONSTANT CONTOURS OF Ill-V QUATERNARY ALLOYS OF THE FORM', p. 8.
[83] C. G. Van de Walle, 'Band lineups and deformation potentials in the model-solid theory', *Phys. Rev. B*, vol. 39, no. 3, pp. 1871–1883, Jan. 1989, doi: 10.1103/PhysRevB.39.1871.
[84] I. Vurgaftman, J. R. Meyer, and L. R. Ram-Mohan, 'Band parameters for III–V compound semiconductors and their alloys', *Journal of Applied Physics*, vol. 89, no. 11, pp. 5815–5875, Jun. 2001, doi: 10.1063/1.1368156.
[85] R. Bhat *et al.*, 'High-performance 1.3 µm AlGaInAs/InP strained quantum well lasers grown by organometallic chemical vapor deposition', *Journal of Crystal Growth*, vol. 145, no. 1–4, pp. 858–865, Dec. 1994, doi: 10.1016/0022-0248(94)91154-1.
[86] M. Zyskowski, S. Kleijn, F. J. Diaz-Otero, and L. Augustin, 'AlInGaAs MQW laser layerstacks for the InP generic integration platform', p. 4.
[87] C. Harder, Kam Lau, and A. Yariv, 'Bistability and pulsations in semiconductor lasers with inhomogeneous current injection', *IEEE J. Quantum Electron.*, vol. 18, no. 9, pp. 1351–1361, Sep. 1982, doi: 10.1109/JQE.1982.1071711.
[88] C. Shieh, R. Engelmann, J. Mantz, K. Alavi, and C. Shu, 'Cavity length dependence of threshold current for quantum well lasers', *Appl. Phys. Lett.*, vol. 54, no. 12, pp. 1089–1091, Mar. 1989, doi: 10.1063/1.100766.
[89] G. W. Taylor, 'A new theoretical approach for the quantum well semiconductor laser', *Progress in Quantum Electronics*, vol. 16, no. 2, pp. 73–133, Jan. 1992, doi: 10.1016/0079-6727(92)90001-C.
[90] J. Z. Wilcox, G. L. Peterson, S. Ou, J. J. Yang, M. Jansen, and D. Schechter, 'Gain- and threshold-current dependence for multiple-quantum-well lasers', *Journal of Applied Physics*, vol. 64, no. 11, pp. 6564–6567, Dec. 1988, doi: 10.1063/1.342028.
[91] Y. Chen *et al.*, 'Review on the Progress of AlGaN-based Ultraviolet Light-Emitting Diodes', *Fundamental Research*, vol. 1, no. 6, pp. 717–734, Nov. 2021, doi: 10.1016/j.fmre.2021.11.005.
[92] J. Piprek, P. Abraham, and J. E. Bowers, 'Cavity length effects on internal loss and quantum efficiency of multiquantum-well lasers', *IEEE J. Select. Topics Quantum Electron.*, vol. 5, no. 3, pp. 643–647, Jun. 1999, doi: 10.1109/2944.788430.
[93] H. Yoshida *et al.*, 'Gain characteristics of gain-guided II–VI laser diodes', *Appl. Phys. Lett.*, vol. 69, no. 25, pp. 3893–3895, Dec. 1996, doi: 10.1063/1.117561.
[94] G. T. Liu, A. Stintz, E. A. Pease, T. C. Newell, K. J. Malloy, and L. F. Lester, '1.58-µm lattice-matched and strained digital alloy AlGaInAs-InP multiple-quantum-well lasers', *IEEE Photon. Technol. Lett.*, vol. 12, no. 1, pp. 4–6, Jan. 2000, doi: 10.1109/68.817428.
[95] S. A. Sayid *et al.*, 'Thermal Characteristics of 1.55-μm InGaAlAs Quantum Well Buried Heterostructure Lasers', *IEEE J. Quantum Electron.*, vol. 46, no. 5, pp. 700–705, May 2010, doi: 10.1109/JQE.2009.2039117.
[96] J. Gilor, I. Samid, and D. Fekete, 'Threshold current density reduction of strained AlInGaAs quantum-well laser', *IEEE J. Quantum Electron.*, vol. 40, no. 10, pp. 1355–1364, Oct. 2004, doi: 10.1109/JQE.2004.834561.

[97] M. J. Mondry, Z. M. Chuang, M. G. Peters, and L. A. Coldren, 'Low threshold current density 1.5 µm (In,Ga,Al)As quantum well lasers grown by MBE', *Electron. Lett.*, vol. 28, no. 15, p. 1471, 1992, doi: 10.1049/el:19920936.
[98] T.C. Newell and P.M. Varangis, 'High-power AlGaInAs strained multiquantum well lasers operating at 1.52 µm', *Electron. Lett.*, vol. 36, no. 11, p. 955, 2000, doi: 10.1049/el:20000717.
[99] J. Aaviksoo', C. Gourdon, R. Grousson', P. Lavallard', and R. Planel', 'PHOTOLUMINESCENCE QUANTUM YIELD IN GaAs/AlAs SUPERLATTICES', p. 5.
[100] W. J. Fritz, L. B. Bauer, and C. S. Miller, 'ANALYSIS OF ALUMINUM GALLIUM ARSENIDE LASER DIODES FAILING DUE TO NONRADIATIVE REGIONS BEHIND THE FACETS', p. 6.
[101] D. Botez *et al.*, '66% CW wallplug efficiency from Al-free 0.98 [micro sign]m-emitting diode lasers', *Electron. Lett.*, vol. 32, no. 21, p. 2012, 1996, doi: 10.1049/el:19961300.
[102] T. Świetlik *et al.*, 'Anomalous temperature characteristics of single wide quantum well InGaN laser diode', *Appl. Phys. Lett.*, vol. 88, no. 7, p. 071121, Feb. 2006, doi: 10.1063/1.2177368.
[103] M. V. Kisin and H. S. El-Ghoroury, 'Injection characteristics of polar and nonpolar multiple-QW structures and active region ballistic overshoot', *Phys. Status Solidi C*, vol. 8, no. 7–8, pp. 2264–2266, Jul. 2011, doi: 10.1002/pssc.201000891.
[104] B. B. Elenkrig, S. Smetona, J. G. Simmons, B. Takasaki, J. D. Evans, and T. Makino, 'Series resistance and its effect on the maximum output power of 1.5 µm strained-layer multiple-quantum-well ridge waveguide InGaAsP lasers', *J. Appl. Phys.*, vol. 87, no. 1, p. 5, 2014.
[105] D. Botez, 'Design considerations and analytical approximations for high continuous-wave power, broad-waveguide diode lasers', *Appl. Phys. Lett.*, vol. 74, no. 21, pp. 3102–3104, May 1999, doi: 10.1063/1.124075.
[106] Nick de Louw, 'Investigating the InAlGaAs composition relationships with the reactor settings and the material properties', TU Eindhoven, Eindhoven, Jun. 2021.
[107] C. Morrison, H. Sun, Y. Yao, R. A. Loomis, and W. E. Buhro, 'Methods for the ICP-OES Analysis of Semiconductor Materials', *Chem. Mater.*, vol. 32, no. 5, pp. 1760–1768, Mar. 2020, doi: 10.1021/acs.chemmater.0c00255.
[108] O. J. Pitts, W. Benyon, and A. J. SpringThorpe, 'Modeling and process control of MOCVD growth of InAlGaAs MQW structures on InP', *Journal of Crystal Growth*, vol. 393, pp. 81–84, May 2014, doi: 10.1016/j.jcrysgro.2013.10.019.
[109] M. Sacilotti, F. Motisuke, L. Horiuchi, R. Landers, L. Cardoso, and B. Waidman, 'Growth and characterization of type-II/type-I AlGaInAs/InP interlaces', p. 7.

European Doctorate in Indium Phosphide
PIC Fabrication Techonology

Universidade Vigo

Peter Eoin Forde

Doctoral Thesis

Design and characterisation of a fully integrated Indium Phosphide transmitter for Satellite Optical Communications

Supervisor:

Dr. Francisco Javier Díaz Otero

Year: 2022

“Mención internacional”

I. Abstract

There is a growing demand for compact, high throughput optical satellite communications terminals, due to ever-increasing usage of CubeSats and NanoSats with tight volume and mass constraints, as well as increasing demands on the RF spectrum as a communications channel. In this work, a fully integrated InP photonic coherent transmitter has been designed and simulated, with the intent of providing a solution to this technology gap. In addition, radiation testing has been performed on an integrated laser on the same InP platform to gain some insight into the robustness of this technology in the radiation environment. It has been determined that the proposed design, even in the most demanding radiation environment of low Earth orbit, will be capable of establishing a ~0.3gbps downlink, at a range of 550km, to a COTS ground station.

II. Acknowledgments

Throughout my fellowship work and the writing of my thesis I have received great support and advice from many people.

I would first like to thank my supervisor, Francisco Diaz-Otero, who not only had the experience and expertise to advise and guide my learning over the past years of this project, but also allowed me a great deal of freedom in defining the topic and scope of my exploration of integrated photonics for space applications. On top of that he worked tirelessly to help arrange connections necessary to perform the radiation testing of my chips.

I would also like to thank my colleagues at the University of Vigo, Andrea Volpini, Damiano Massella, Marcin Zyskowski, and David Álvarez Outerelo, for their wonderful collaboration and many interesting conversations, which I'm sure positively impacted all our respective works.

In addition, I would like to thank Ronald Broeke, Katarzyna Lawniczuk and Valentina Moskalenko, who each taught me a great deal while I worked with them at Bright Photonics in the early days of this project. Your patience and guidance are greatly appreciated.

Finally, I would like to thank all those I worked alongside at SMART Photonics, in particular Steven Grijseels and Paul Tiebot, who supervised my projects there.

III. Dedication

I dedicate this thesis to my Nana, Carmel McManamon, who always supported me in my educational pursuits, and always went out of her way to make sure I always had plenty of books to read. She is greatly missed.

I dedicate it to my partner Çağıl, who has supported and encouraged me in so many ways both in the pursuit of this PhD and in our lives outside of it. I love and cherish you so much.

This thesis is dedicated to my parents and family, thank you for your unconditional love and support.

IV. In this Thesis

The chapters of this thesis are laid out as follows:

- **Chapter 2:** The state of the art for photonics as well as communication systems for nano satellites is detailed.
- **Chapter 3:** In this chapter the link budget calculations and design considerations they need are demonstrated, along with a suggested ground station telescope setup for use in conjunction with the transmitter system.
- **Chapter 4:** Here the transmitter chip design is shown, along with simulated outputs used to refine the link capability estimates from chapter 3.
- **Chapter 5:** The designs for the transmitter chip are explained.
- **Chapter 6:** Results for transmitter and test chip measurements. As well as the results for irradiated test chips.
- **Chapter 7:** Conclusions and possible further work.

V. Contents

VI. Table of Figures

1. Introduction

In this section we will introduce integrated photonics technology and some of its history and current potential. We also introduce the topic of small satellites and their place in the growing sector, while highlighting their communications need and how integrated photonics might play a role.

Much of modern technological advances rely heavily on the rapid development of integrated electronic chips which began in the 1970s. For 40 years the component density and performance of integrated electronic circuits has been doubling every 2 years, driven by component optimisation, improved lithography techniques and better materials (1). However, it is becoming clear that the device size component of this advancement is reaching a hard limit, with lithography approaching atomic dimensions.

Around the same time as this explosion of electronic circuit development the idea of an integrated circuit that utilised photons in place of electrons as the signal carriers of the device was postulated (2). Photonic Integrated Chips (PICs) can be thought of as the optical analogue of integrated electronic circuits. Active photonic chips can integrate laser sources as well as amplifiers, modulators, and other optical functions onto a single device, allowing for comparatively large equipment and functions to be greatly reduced in volume and power requirements. They have the potential to have great impacts on certain technology fields such as telecoms, medical, and aerospace. However, there are some challenges that must be overcome if PIC technology is to experience a similar boom as ICs did in the 70s and onwards.

The first challenge is the achievable density of component building blocks (BBs) that can be fabricated on chips. This is partially due to having to maintain a minimum separation between waveguides and BBs to avoid crosstalk and interference. The higher the density of BBs on the chip the more electrical connections are needed to drive them, this can also cause cross talk issues as well as create difficulties managing the temperature of the chip and the effects this has on BB performance. Additionally, the market for PICs is lacking in standardisation, especially when compared to ICs. There are a multitude of bespoke platforms and materials being developed for singular applications, as well as multiple foundries striving to develop a generic platform. This has an overall effect of increased costs as for specific applications to derive best results one often needs to develop unique building blocks or layer stacks, which involves a change to the entire fabrication process in some cases. The fact that there are multiple material platforms being developed for PICs only increases this fragmentation further, though it does allow for some more niche applications to be developed. However, the generic integration platform foundries working on

developing standardised BBs for their respective technology really is the key to opening PICs to wider markets, expanding production, and reducing chip costs.

Despite this, PICs show promise for great utility, especially in the telecoms field. As an example, when data centres are expanded, newer and larger centres are built next to existing datacentres. These must be connected using very fast, high throughput links so that they can function as one larger datacentre. Integrated products exist to address this growing need, with 10gbps transceiver products already on the market. Such transceivers are also key enabling technologies for establishing 5G networks. Low power consumption is an additional advantage of integrated photonics in both scenarios. Photonic sensors are also showing promise in a variety of areas. PICs have been developed which utilise the changing group index along an optical fibre to monitor the strain experienced by helicopter rotor blades in real time, this can potentially increase the service lifetime of parts as the user can understand much better the stress the blades have experienced over the course of their use, rather than all blades being replaced automatically after a certain lifetime usability estimate has expired. Sensors have also been developed for metrology and bio sensing applications.

Meanwhile, in the space sector, Nanosats and CubeSats in particular are being utilised for an ever-greater fraction of both scientific and commercial space missions (3). CubeSats are composed of multiple 10cm cubic modules that are restricted to 1.33kg mass per module. There are several factors contributing to the growth of the CubeSat industry: low cost of deployment (18), standardised components reduce cost by enabling compatible COTS (commercial off the shelf) subsystems such as power supply, command and data handling, communications, ADCS, propulsion and communication. RF communication is the main stay for orbital satellite communications, with CubeSats and Nanosats tending to use lower frequency bands as less power is required. The increasing number of satellites in LEO, driven in part by the growth of the small sat industry, has led to these bands becoming crowded, and it can be challenging to acquire licenses. One solution to this is to utilise optical communications, it is possible a PIC could be a part of that solution. NASA has several optical communications programs underway, envisaging various high data throughput link scenarios:

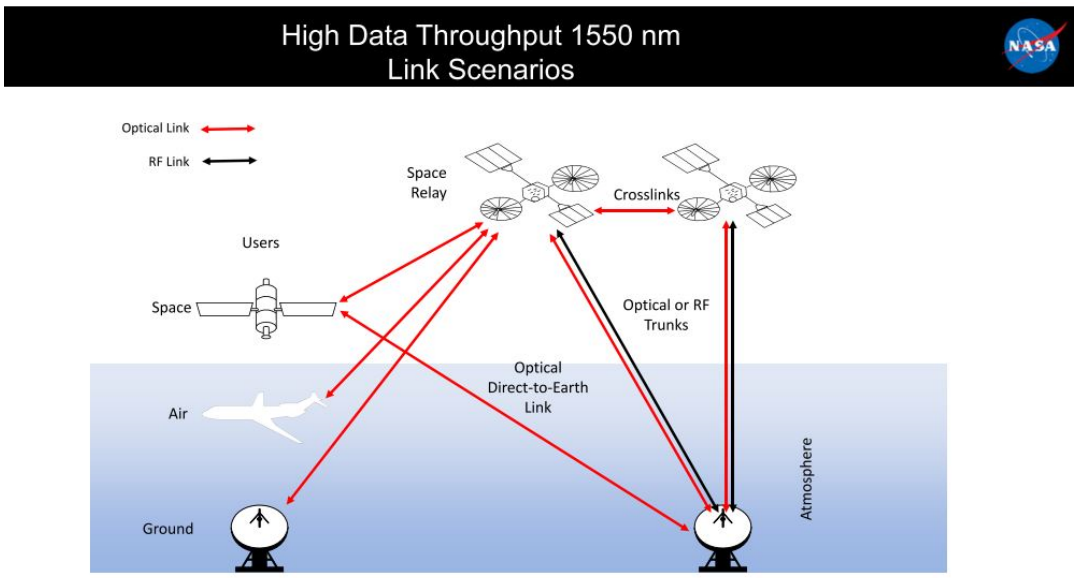

FIGURE 1: HIGH DATA THROUGHPUT LINK SCENARIOS (21)

These cover intersatellite optical links, where pointing accuracy is more critical, to satellite to ground links, and even proposing links enabling data transfer between aircraft and satellites. The idea would not be for optical links to replace RF communications links entirely, rather to create additional information channels for additional services and internet of things.

1.1. State of the Art:

1.1.1. Small Satellites and Optical Communications Overview:

As the goal of this thesis is to develop an integrated optical communication system for small satellites, we will begin this section with an overview on small satellites, and related communication techniques. The needs of the sector and what potential solutions have been offered, as well as drawbacks, will be reviewed, before discussing integrated photonics technology and how it could potentially deliver a solution.

CubeSats being typically launched alongside other larger missions to various LEO orbits (17). CubeSats can also be launched from the ISS as it is regularly sent supplies or has crew rotated. For this reason, an LEO orbit of 400km will be considered in this thesis.

RF communication is the main stay for orbital satellite comms, with SmallSats tending to use lower frequency bands as less power is required. The increasing number of satellites in LEO, driven in part by the growth of the small sat industry, has led to these bands becoming crowded, and challenging to acquire licenses (20). One solution to this is to utilise optical communications. In addition, CubeSats can now be equipped with more advanced payloads which can generate large volumes of data. A multispectral imager on a CubeSat is limited to

only 63 seconds of data acquisition as its S-Band link consumes so much power it can only be run for 10 minutes each orbit (16). This further highlights the need for low power, high data rate links.

There are a multitude of optical communication systems designed for small satellites. To maximise atmospheric transmission, most operate in a 1550nm wavelength regime. Crabb et al (3) designed a master oscillator power amplifier-based transmitter for CubeSats, with a downlink speed of 500Mbps and has a 300mW output power (3). They also point out that it was challenging to make this system compact enough to fit into the volume constraints of a CubeSat. The Micius Coherent Laser Communication Demonstration, meanwhile, is a small (635kg) satellite used to demonstrate an optical link capable of 5.12Gbps from LEO. The larger size of the satellite, while still classified as small, allows it to make use of higher power (1W) lasers and more complex modulation formats to achieve this high-speed downlink (7). A Japanese team designed RISESAT which is an example of a small sat utilising optical downlinks. Its optical payload, VSOTA, can operate at 980nm or 1550nm and can deliver up to 540 mW of power, enabling link rates of up to 100kbps from a transmitter subsystem of less than 1kg, and requires less than 10W to operate (17). As another example, the Aerospace Corporation has been developing a 1.5U CubeSat as an optical communications demonstrator. The design goal is to achieve a 5Mbps link across 900km. Their transmitter is a 10 W optical system utilising OOK modulation at 1064nm. While it can likely achieve this link goal, it also requires nearly 60W of power for operation, which would pose a challenge for many CubeSats power systems. A lower power solution would be more useful for CubeSat missions (17).

When designing a system for space craft it is of course important to consider the radiation environment it will experience. This effect is largely dependent on the orbit selected. SPENVIS (SPace ENVironment Information System) is an ESA programme for visualising space environment effects from various models. For example, one can calculate that for a 45-degree inclination orbit at 400km altitude, with 5mm Al shielding, a device would expect a dose of 100 Si (krad) per year. In general, single event effects, like bit flips, are less well studied in the CubeSat domain, yet these effects risks can be mitigated with power cycling, watchdog timers, and resets.

Looking at optical communications literature more generally, in the past few decades it has been explored for fast, short ranged (less than 5km) terrestrial data links. These links are quite susceptible to bad weather conditions, but adaptive optics in the ground station/receiver can mitigate this (8). The following table summarises the transmitters described earlier:

Satellite /Transmitter Name	Transmitter Wavelength	Data rate	Transmitter Power	Required Power	Satellite/ Transmitter Volume	Transmitter Mass

RISESAT	1550/980nm	100kbps	540mW/80mW	<10W	50cm x 50cm x 50cm (Sat)	<1kg
AeroCube-OCSD	1064	>5Mbps	10W	~60W	10cm x 10cm x 15cm (Sat)	<2kg
PERSEUS-LP-LE-C-LR	1535-1560	500Mbps	300mW	Unknown	10cm x 10cm cm 3cm (transmitter)	0.15kg
MOCT	1520-1580nm	2.48Mbps	500mW	4W	Undefined, Nanosat compatible	Undefined

TABLE 1: SUMMARY OF OPTICAL TRANSMITTERS

1.1.2. Overview of Integrated Photonics Platforms and foundries:

As this project was undertaken using a generic platform, here some details on three foundries and their technology will be described. These are Fraunhofer HHI (Heinrich Hertz Institute) SMART Photonics, and TriPleX.

1.1.2.1. HHI:

HHI is a foundry in Berlin that fabricates InP (Indium Phosphide). As it is a direct band gap semiconductor stimulated emission is possible and therefore this platform enables integration of active components such as lasers. In their layer stack (Figure (2)) four quaternary alloy (InGaAsP(Q)) are used. The concentration of elements in this material is used to control the bandgap and refractive index of the material to guide light in the chip. In this setup only the upper quaternary layer is used as a core guiding layer, the lower layers enable more efficient coupling(18A) with SSCs (spot size converters).

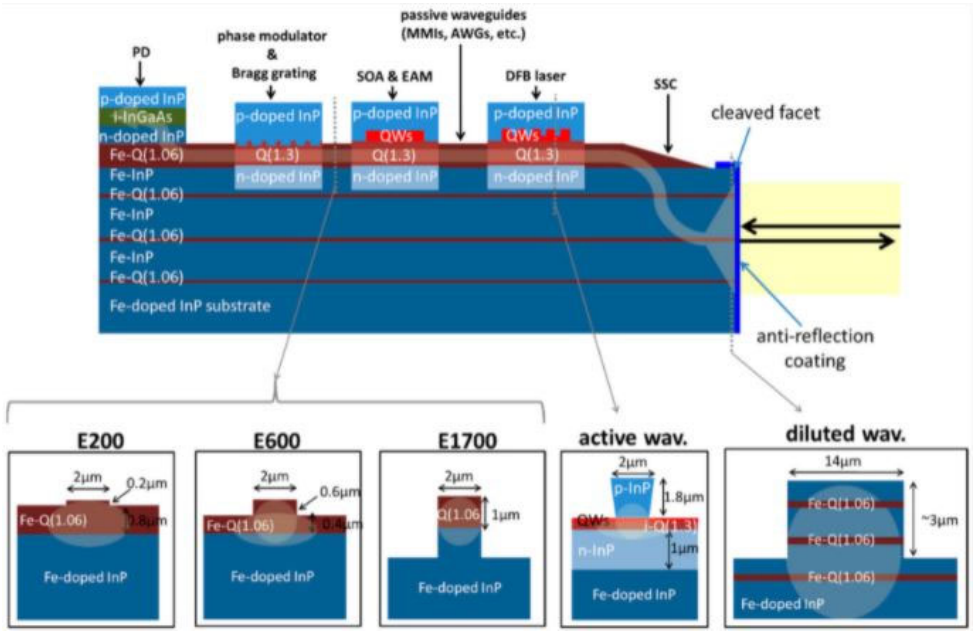

FIGURE 2: EPITAXIAL LAYERS ALONGSIDE THE PROPAGATION DIRECTION (4)

Active components are based on an 8 multi-quantum well (MQW) layer. Below the MQW there is a quaternary bulk layer acting as the core guiding layer for regions where the MQWs

are removed (4). For DFB lasers, gratings are patterned using electron beam lithography and reactive ion etching and allows designers to choose any C-band wavelength for the laser. Vertical couplers can be integrated using gratings also in the Q1.3 quaternary layer (4). The different waveguide types also allow designers to make their own bends, MMIs and AWGs as they desire. The platform supports Semiconductor Optical Amplifiers (SOAs), Distributed feedback (DFB) and distributed Bragg-Reflector (DBR) lasers, Polarization splitters and rotators, phase shifters, photodetectors, and balanced detectors (4).

1.1.2.2. TriPleX

On the TriPleX platform, layers of stoichiometric silicon oxide and silicon nitride are deposited on a silicon wafer. These materials do not allow for direct integration of active component, as silicon is an indirect semiconductor, meaning stimulated emission is improbable to occur unlike in InP. TriPleX offers four types of waveguides:

Boxshell consists of an SiO_2 core is buried in Si_3N_4. Its symmetrical shape reduces its polarization dependence is greatly reduces, making it useful for telecoms applications. It also is available both in low and high index contrast variants. It has a low propagation loss of 0.2dB/cm in the high contrast version, and 0.06dB/cm in the low contrast variant (5).

Single Strip: The mode is weakly confined in a single strip of Si_3N_4. The main purpose of this configuration is to achieve the lowest possible propagation loss. As there is such low confinement there is no optical scattering on sidewalls, resulting in losses as low as 0.007dB/cm. However, with such low confinement large turning radii are needed. So, there is another waveguide configuration to enable these necessary tight turns to allow for greater component density on chip (5).

Symmetric/Asymmetric Double Stripe Layout: Useful in components that need tight bends and enables low loss coupling from the chip to optical fibres. It consists of two strips of Si_3N_4, one placed on top of the other. In the symmetric case they are the same size and are separated by 500nm vertically, in the asymmetric case this distance is reduced to 100nm, and the upper waveguides thickness can be changed to control the minimum radii of curvature required for bends (5). Between bends and straight sections, the waveguide can be tapered to match the single strip version with very low loss (5).

The platform also supports SSCs, splitters/couplers, and thermally controlled phase modulators (5).

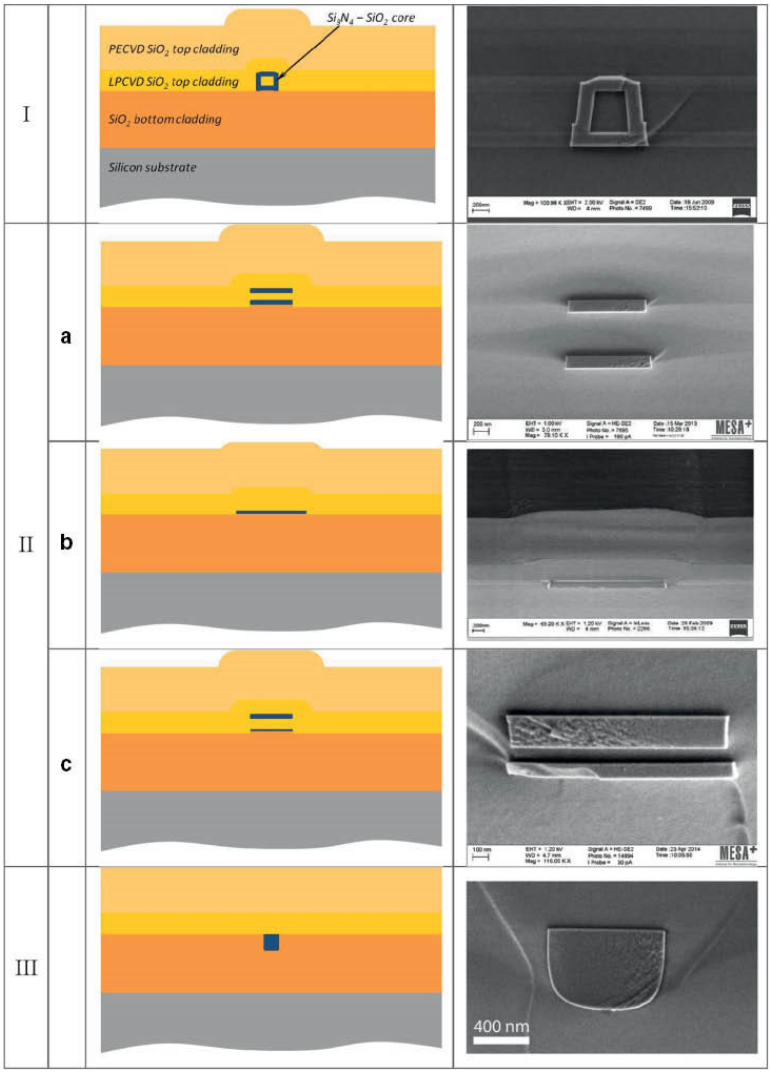

FIGURE 3: WAVEGUIDES IN THE TRIPLEX LAYER STACK (5)

1.1.2.3. SMART Photonics

The SMART Photonics platform is InP based, like HHI, and so has much the same strengths in integrating active components. Their building blocks are also designed to operate in the C-band.

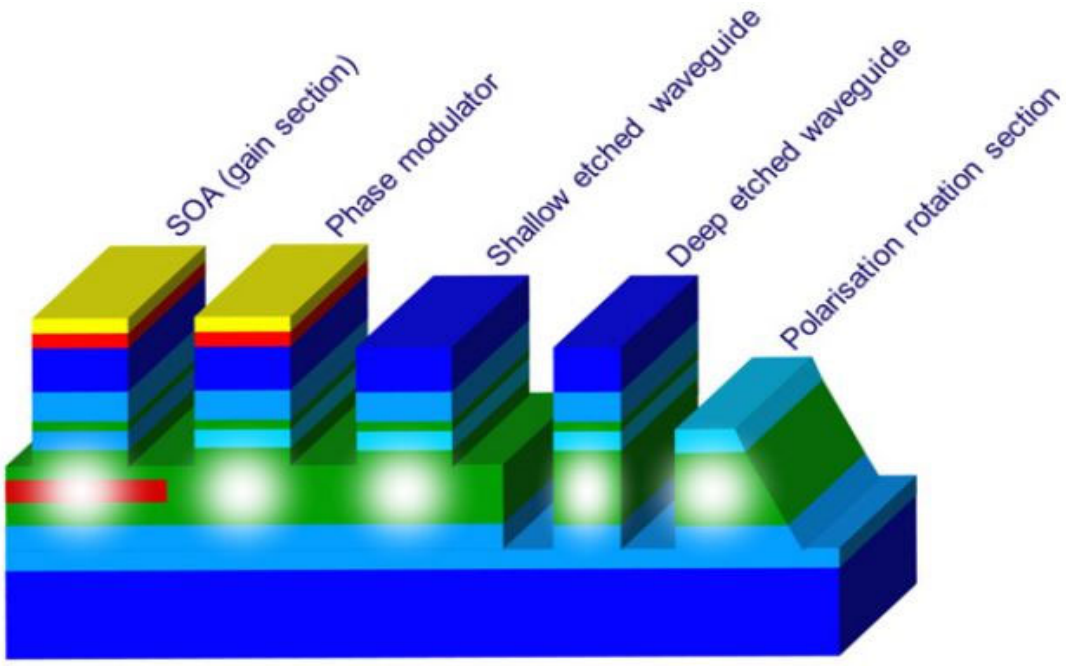

FIGURE 4: SMART PHOTONICS LAYER STACK (6)

The fabrication process is as follows, onto a substrate, different layers of InP, InGaAsP and InGaAs are deposited. In figure (4) the green layer is composed of the quaternary allow InGaAsP, and the ratio of the different elements controls the bandgap and refractive index of the alloy to control light propagation on the chip. Red layers are also composed of this allow, but with a different bandgap, and are used for light generation in the active elements (6). The top layer provides a buffer between the core layer and the metal connections to reduce loss. Yellow layers are for electrical connections and are composed of InGaAs (6).

There is a trade off in designing the layer stack to best accommodate both active and passive building blocks. One of these trade-offs is the doping concentration in the cladding layers, which can improve electrical connections and active component performance, but increases losses when present in passive components (6).

On figure (4) some components are shown. First is the SOA, where the mode is confined to the green core layer and the device is pumped by the cladding layers. The red layer enables stimulated emission as described earlier. For the phase modulator, a reverse bias is applied generating an electro optical effect which effects the phase of the light.

There are two kinds of waveguides on this platform: deep and shallow, deep has greater confinement but also greater losses, while shallow is less confined but has less loss, so a designer must carefully choose which to use in their chip designs. The PDK will also has photodetectors and will soon also provide polarisation converter building block.

	HHI	TriPleX	SMART
Waveguide Loss	2 dB/cm	0.1 dB/cm	3 dB/cm
Spotsize Loss	2 dB/cm	0.5 dB/cm	x
Bending Radius	250µm	150µm	100 µm
SOA Gain	40dB/cm	Not Supported	30dB/cm
PD 3dB bandwidth	45Ghz	x	30Ghz

TABLE 2: COMPARISON OF SOME BUILDING BLOCK PERFORMANCES ACROSS THE THREE NAMED FOUNDRIES.

1.1.3. Integrated photonics as an optical communication solution:

Indium phosphide (InP) is generally considered to be the most advanced substrate for creating integrated active photonics circuits. The technology has already been used for various design functions such as transmitters and transceivers and have the potential to revolutionise applications where low power, compact, high performing devices are needed, including satellite communications. SOAs have been demonstrated to achieve output power up to 0.3W, which brings the chip outputs into a power regime where establishing downlinks becomes a possibility (9). An SOAs gain and saturation output power are the main dependent variable that determines the potential output power of a PIC, and transmitter chips have been designed in InP with off chip powers of up to 14.5dBm (9).

There is also some heritage for using this technology for FSO (free space optics) links. Utilising Mach-Zender modulators, SGDBR laser, and an SOA as BBs, a transmitter was capable of achieving 3Gbps for a link distance of 180m. In this setup an EDFA was used to recover the link loss and then the signal was passed to a PIN photodiode. The designers believe higher data rates are possible if more compact modulator designs are developed. (10)

Freedom Photonics has developed coherent transmitters designed for QPSK modulation, operating in 1550nm. The Local Oscillator (LO) is in this case also a SGDBR laser, amplified by an SOA. MZM in this design are nested and utilise MMIs, with two MZMs in parallel each receiving half the laser power, and phase is adjusted in each using static phase electrodes. The average bandwidth of 3dB was determined to be 8GHz which enabled the transmitter to deliver 10Gbps data rates. However, this transmitter, receiver setup is not tested for FSO usage, so it's likely these stats would deteriorate outside of off-chip measurements.

Well-characterised high-speed electro absorption modulators (EAMs) have been reported on open access generic foundries. The redesign took the BB from 9 GHz bandwidth capability to 24 GHz for a 100-micron long component, while having a return loss of less than -10 dB (11).

Another possibility with PIC technology is to design widely tuneable transmitters, as was done by Estrella et al, who achieved 20 Gbps operation over a 20nm tuning range, using

QPSK encoding techniques. This design however requires a more complex receiver design (Estrella 12).

In summary, a wide array of InP transmitter PIC designs have been published in the literature. The majority of these offer data rates in the Gb range. With regards to establishing FSO links, it is not as developed. Most designs reviewed were only measured directly off-chip, one having a range of 100s of metres, and the longest FSO link reviewed, while being on the order of kilometres, did not depend on integrated photonic technology. However, the capabilities of the InP platform and pre-existing building blocks are sufficient to explore their utilisation for FSO links between satellites and ground stations. The question is whether these integrated technologies are capable of achieving high enough power outputs to achieve a stable link with good signal to noise performance through the atmosphere. For this application 1550nm is the obvious wavelength choice, yielding the best atmospheric transmission, and integrated lasers can operate in this wavelength regime well. SOAs may have the capability to increase transmitted power from the chips enough to satisfy an orbital link budget, and EDFA may bridge any remaining power gap if not. So not only is there a need for compact optical transmitter technology for satellites in LEO, but there is also an untapped potential for PICs to fill this gap. Furthermore, no research has been conducted to the authors' knowledge on radiation effects on the InP platform. This needs to be investigated to understand the viability of InP to operate in the space environment.

1.2. Thesis Motivation

From the previous section, it should hopefully be clear that there is a growing need for low power, compact optical communications solutions for CubeSats and NanoSats in LEO. There has been some promising work in Free Space Optics Links using integrated photonics technology, but these links are so far short ranged and not designed for the needs of satellite to ground downlinks. Such a system would need an operational range of at least 500km, and high data rates to make the most of the short windows they will be in range of a ground station each orbit. Some considerations should also be given to the type of ground station required by any solution, as a compact and relatively cheap ground station setup could yield better capabilities for the system as a whole. InP is a clear choice as a platform for such a device, as it allows for active component integration which is necessary to achieve a device without needing external optical sources, which would increase the volume and mass of the system. Since the main drawback of InP is the propagation loss, care should be taken in the design to minimise the path length of the light in the device, to maximise the

power output of the chip. There are also no studies done on the effects of the space environment on integrated photonic circuits, such as temperature, radiation, and vacuum.

This work devises an integrated photonics solution for satellite communications. This consists of a coherent transmitter integrated on HHIs InP platform. This device was packaged both for ease of measurement and creating a hypothetical full system that could be integrated into a CubeSat or NanoSat platform. Additionally, test chips were designed and fabricated on HHIs platform. These consist of test circuits for the important components in a coherent transmitter, DFB laser as the master oscillator, optical modulator, SOA, each with its own test circuit on chip. This enables some quantification of the effects of radiation on these components, which can be extrapolated to predict the transmitter chips performance in the space environment.

2. Link Budget Calculations

In this section we will describe and calculate using python the link conditions for a LEO satellite using optical comms. This will lead us to a preliminary design for a transmitter capable of establishing a satellite downlink for such a scenario.

As has been established in the literature review, there is a growing demand for optical link solutions for small satellites. The first component of the work to realise this solution using integrated photonics is to estimate a link budget for such a system, based on the Building Blocks (BBs) of foundry Process Design Kits (PDKs). However, in the initial round of calculations some generic stand-in values were used for simplicity, and then substituted for closer estimates. After this preliminary check a chip was designed and simulated in Lumerical Interconnect to determine precise estimates of a transmitter chips power output, which was then fed into the calculations set up.

A link budget comprises of a number of variables which together describe a communications link in terms of power between a transmitter and receiver. The key parameters for the link calculations are transmitted power (Ptx), link distance (R), wavelength (λ), and bit rate (Rb). On-Off Keying (OOK) is a commonly used and simple modulation scheme which will be used for the transmitter both for simplifying the design and because more complex formats require additional building blocks which would further constrain the already limited power of an integrated optical device. Under this regime the transmitter optical signal (a square wave) can be described by equation (1).

$$p_{tx}(t) = \sum 2P_{tx} b_n \cdot rect\left(\frac{t - nT_b}{T_b}\right)$$

EQUATION 1

Where Ptx is the average optical power, Ptx(t) is the instantaneous transmitter power, bn ∈ 0,1 and represents the transmitted bits, and Rb=1/Tb is the data rate. The limit on Ptx required to receive a signal result from the quantised nature of light, and for a Bit Error Rate (BER) of 10-9 a PIN photodiode requires 10000 photons per detected bit. This is lowered to 1000 points for an APD photodiode (15). The minimum required power to receive a signal can therefore be described as follows:

$$P_{req} = \frac{E_{b,req}}{T_b} = N_{ph} h f R_b$$

EQUATION 2

The common link budget () was used to calculate actual received power.

$$P_{rx} = G_{tx} L_{rx} P_{tx}$$

EQUATION 3

Gtx is the gain of the transmitter, Lrx is the path loss (which includes Rx gain). One of the most important parameters to consider in optical communications is the divergence angle θdiv. The transmitter gain is dependent on this value. From (13), a more accurate equation for deriving the necessary transmitter power for PIN and APD receivers is:

$$P_{req,PIN} = \frac{erfcinv(2P_b)\sqrt{2\sigma_{noise}^2}}{R}$$

EQUATION 4

or:

$$P_{req,APD} = \frac{erfcinv(2P_b)\sqrt{2\sigma_{noise}^2}}{RM}$$

EQUATION 5

Where erfc(x) is the complementary error function:

$$erfc(x) = \frac{1}{\pi}\int_x^\infty e^{-t^2} dt$$

EQUATION 6

σ^2_{noise} is the noise variance R is the responsivity and M is the gain (for the APD case only).

Using these equations, a python code was written to output the received power vs receiver diameter for a variety of divergence angles for both PIN and APD detectors, taking a rough output power estimate of 10mW, a link distance of 500km, and a data rate of 1Mb/s.

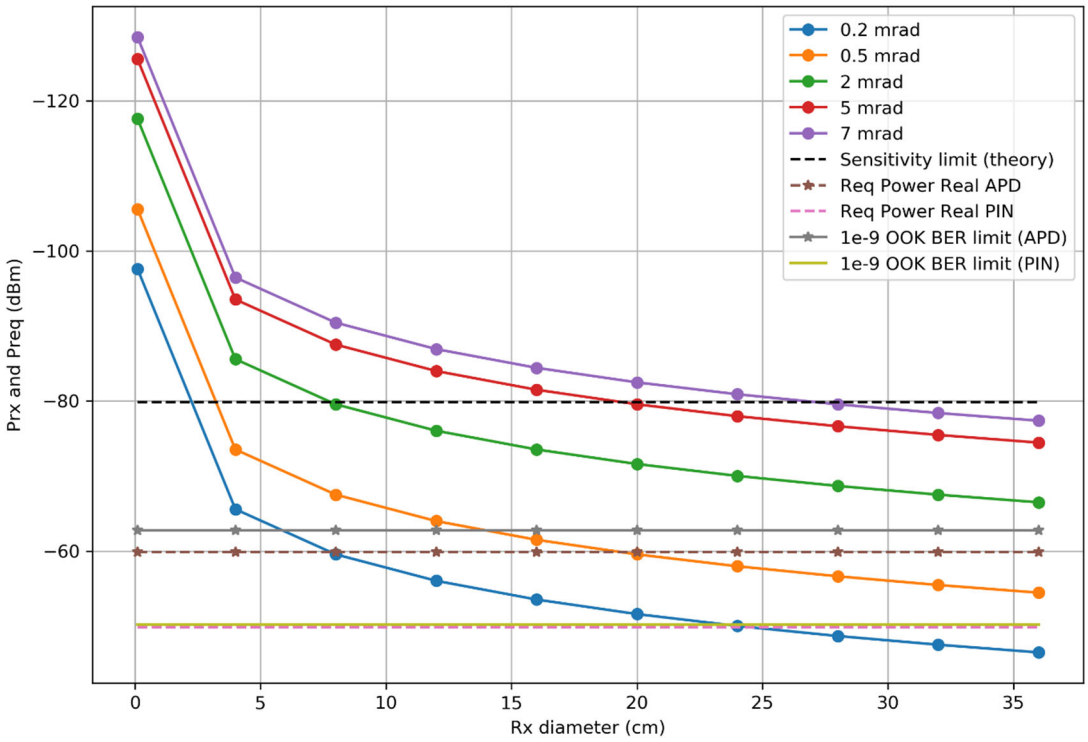

FIGURE 5: RECEIVER DIAMETER VS PREQ AND PRX, FOR A 10MW TRANSMITTER POWER, 500KM LINK DISTANCE AND 1MBPS DATA RATE

From this we can see even with a very low power transmitter (10mW) it is possible to receive a signal with a relatively compact receiver telescope, provided the beam divergence of the transmitter is less than 0.5mrad. This calculation assumed a relatively cloudless day and inputs a nominal transmission value of >99% (14). Figure (6) and (7) were generated using the ATRAN modelling software (14). Spectra for Mauna Key are shown for wavelengths between 1.4 and 1.9 microns. Different weights for the atmosphere are used to show pressure effects on the transmission, as well as different precipitable water vapour of 1.0 and 3.0mm. From both charts one can clearly recognise that for the 1.55-micron regime there is little effect on either factor on the transmission (14). Additionally, it is important to remember that only a small fraction of the link distance is in atmosphere, most occurs in the vacuum of space, so this small effect is reduced even further in terms of its impact on the link budget.

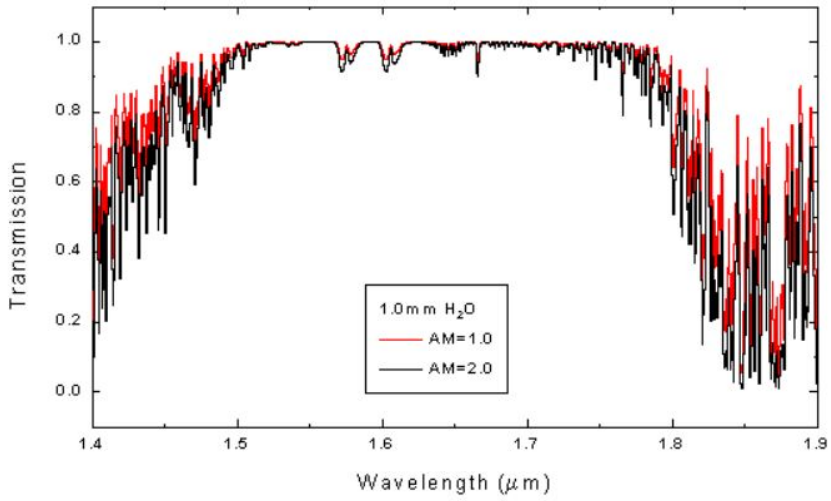

FIGURE 6: TRANSMISSION SPECTRA FOR 1.4-1.9 MICRONS, WITH VARIED ATMOSPHERIC WEIGHTING

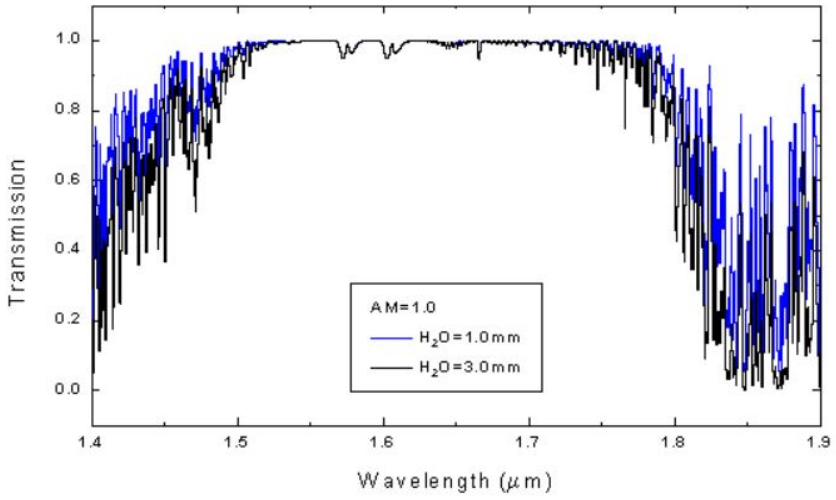

FIGURE 7: TRANSMISSION SPECTRA FOR 1.4-1.9 MICRONS, WITH VARIED WATER VAPOUR

Following this evaluation, a circuit block design was drawn up, allowing for a more accurate estimate of the output power of the chip, based on building block statistics provided by HHI. For a 21mW output power from the transmitter chip (which could be further boosted by an EDFA on-board the satellite. The output of the python code is as follows:

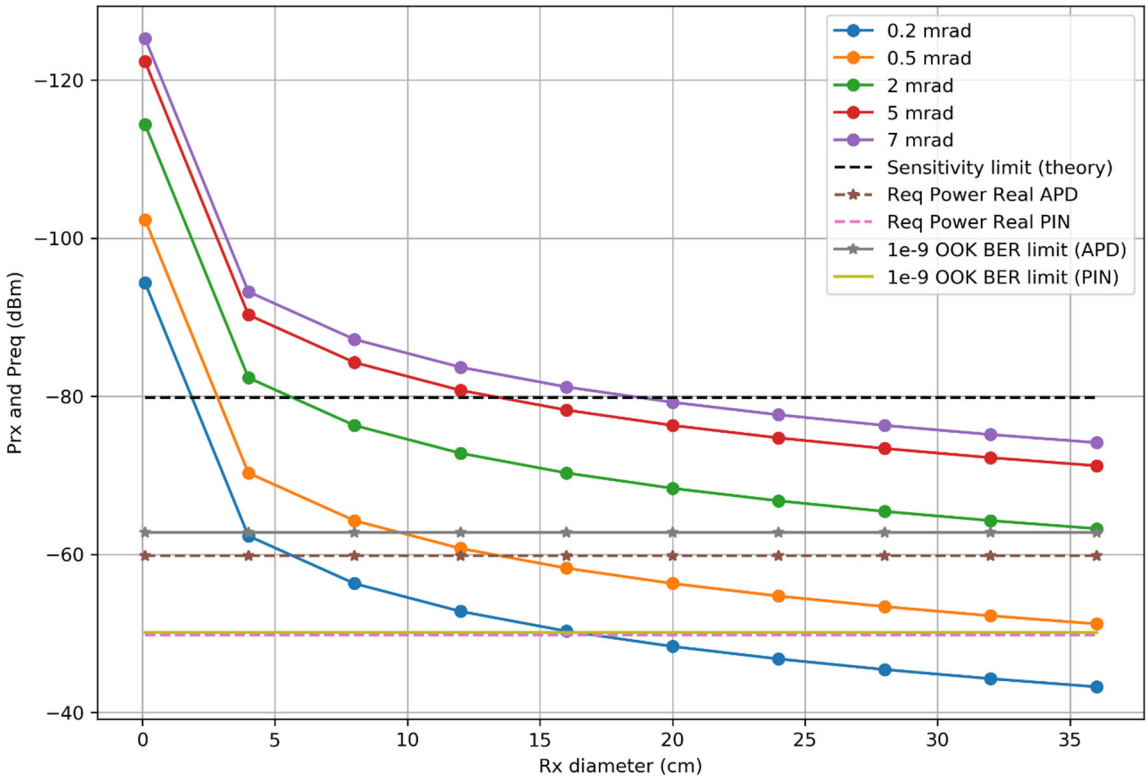

FIGURE 8: RECEIVER DIAMETER VS PREQ AND PRX, FOR A 21MW TRANSMITTER POWER, 500KM LINK DISTANCE AND 1MBPS DATA RATE

Upon seeing this output, it was realised that perhaps a higher data rate could be achieved, so the data was plotted once more for a higher data rate of 1gbps.

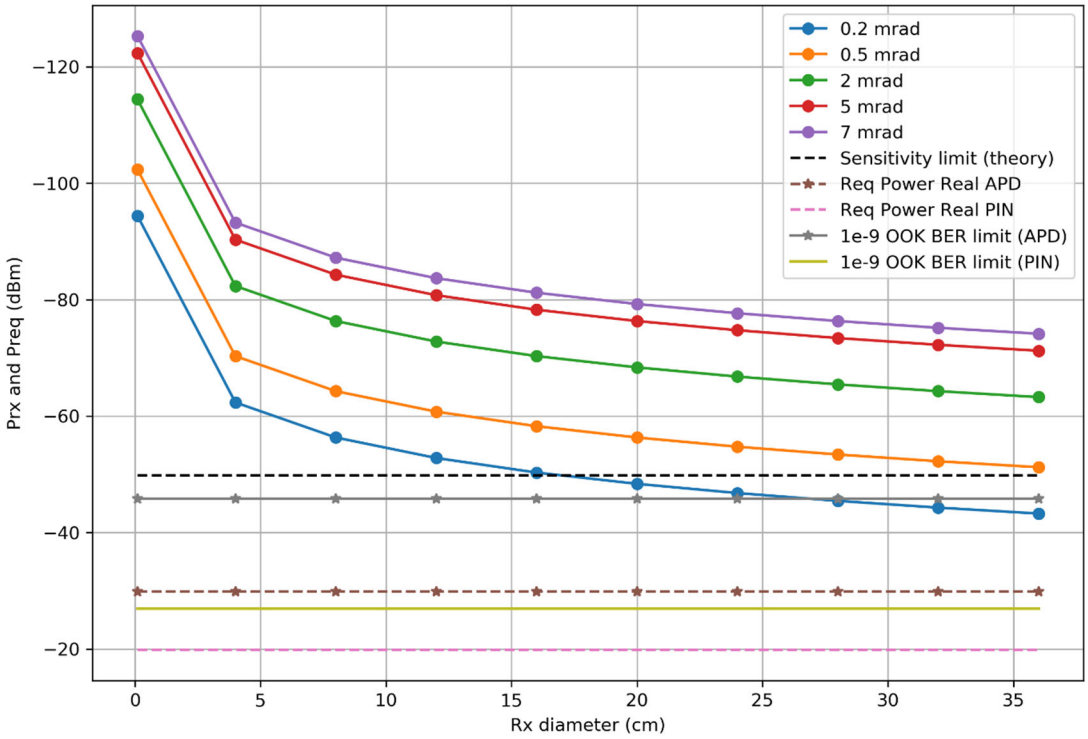

FIGURE 9: RECEIVER DIAMETER VS PREQ AND PRX, FOR A 21MW TRANSMITTER POWER, 500KM LINK DISTANCE AND 1GBPS DATA RATE

This strains the link too far, and would necessitate a larger receiver telescope, one final modification to the data set will be to include gain for a space graded EDFA which could be included in the system. iXblue's EDFA has a gain of 30dB which if used to pump the chips output signal allows the data rate to comfortably be increased to 2gbps, while also allowing

a larger link distance of up to 600km for a receiver telescope of 25cm diameter or larger.

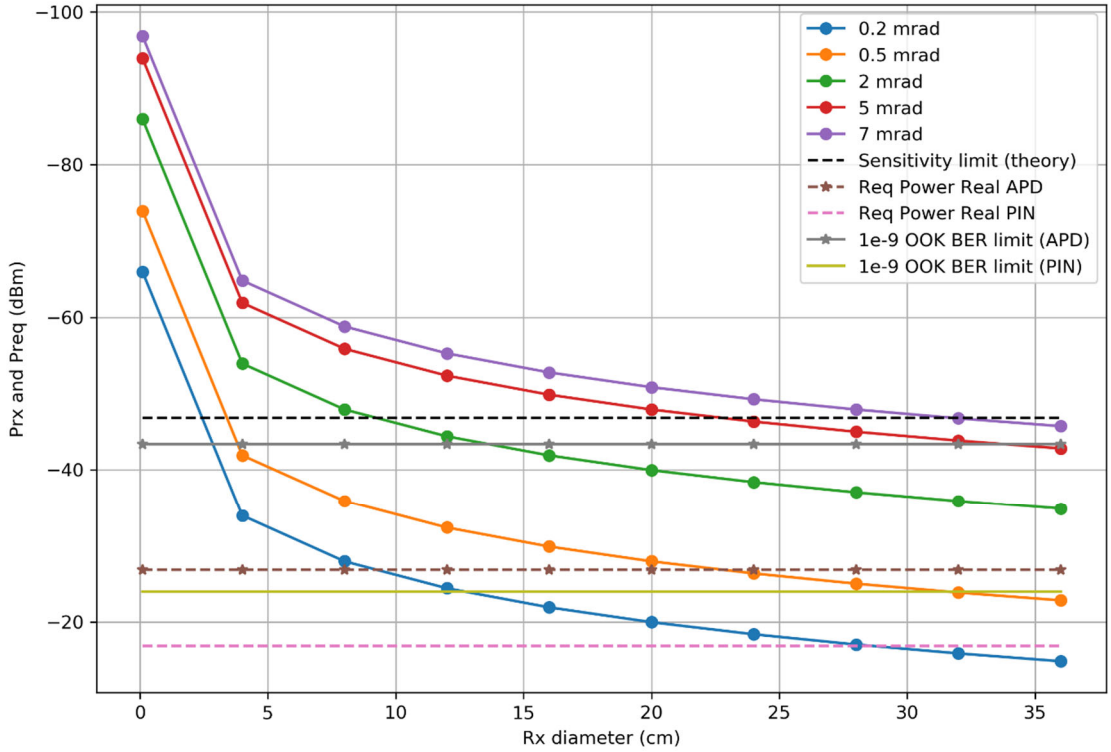

FIGURE 10 RECEIVER DIAMETER VS PREQ AND PRX, FOR A 21MW TRANSMITTER POWER, 30DB OF GAIN FROM AN EDFA 600KM LINK DISTANCE AND 2GBPS DATA RATE

Knowing the requirements of a ground station, it was established whether such a solution existed, with the idea of having a full downlink setup to be established on paper. A portable optical ground station is proposed which utilises a COTS telescope, the Celestron CPC 1100, which has an aperture diameter of 27.9cm (19). Additionally in their paper they utilise a Thorlabs APD, their ground station can be set up in approximately 30 minutes, and the telescope can track LEO satellites to within arcseconds of accuracy. On the satellite side of the system, it is important to establish the viability of the collimation required of the transmitter, the chip would be connected to fibre optics and an EDFA in the proposed system setup, then a beam collimator is needed. A cursory search reveals there are a plethora of options available, with a multitude of fibre optic collimator lenses available, many with beam divergences of 0.5mrad or even 0.2mrad.

Considering that the target mission for the transmitter is an LEO CubeSat mission, a 400km orbit is most likely. Therefore, if we take into consideration the 600km link distance we have calculated for, this will enable the link to be established from an elevation angle as

little as 55 degrees. In the following chart the orbital altitude h for our case is 400km, while the slant range p is 600km.

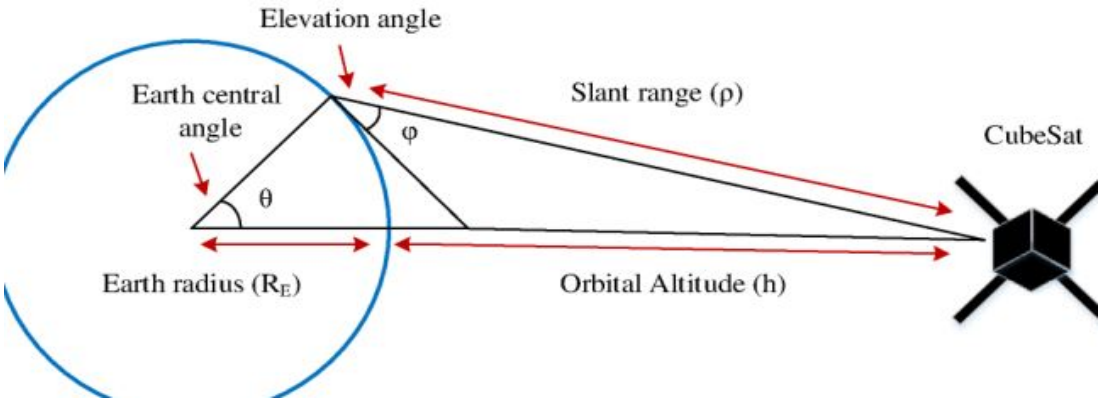

FIGURE 11: DIAGRAM ILLUSTRATING THE RELATIONSHIP BETWEEN ELEVATION ANGLE, SLANT RANGE, AND ORBITAL ALTITUDE. (18)

With all these considerations and effects in mind, we want to design an integrated chip consisting of a coherent transmitter that can form a link with a ground station in these conditions. For this task we consider using InP platform as it has active and passive elements. The HHI platform was selected due to time to fabrication, performance of the DFB laser (which is not available with the Smart Photonics PDK) and the availability of SSCs for ease of alignment with external optics.

3. Test Chip Designs

In this chapter we will detail the design of the test chips which will undergo radiation testing in order to estimate the performance of the transmitter chip under space conditions. The GDS of the chips will be shown and described, alongside performance specifications for the relevant building blocks used, for later comparison with test data before and after irradiation.

To begin, with all the considerations of the previous chapter, the system block diagram decided upon was that of figure (12). In reality there was more interplay between the designs and building blocks used, and the link budget calculations, but this was the general decided upon layout. With that decided the next task was to design the test chips for individual components on the transmitter chip.

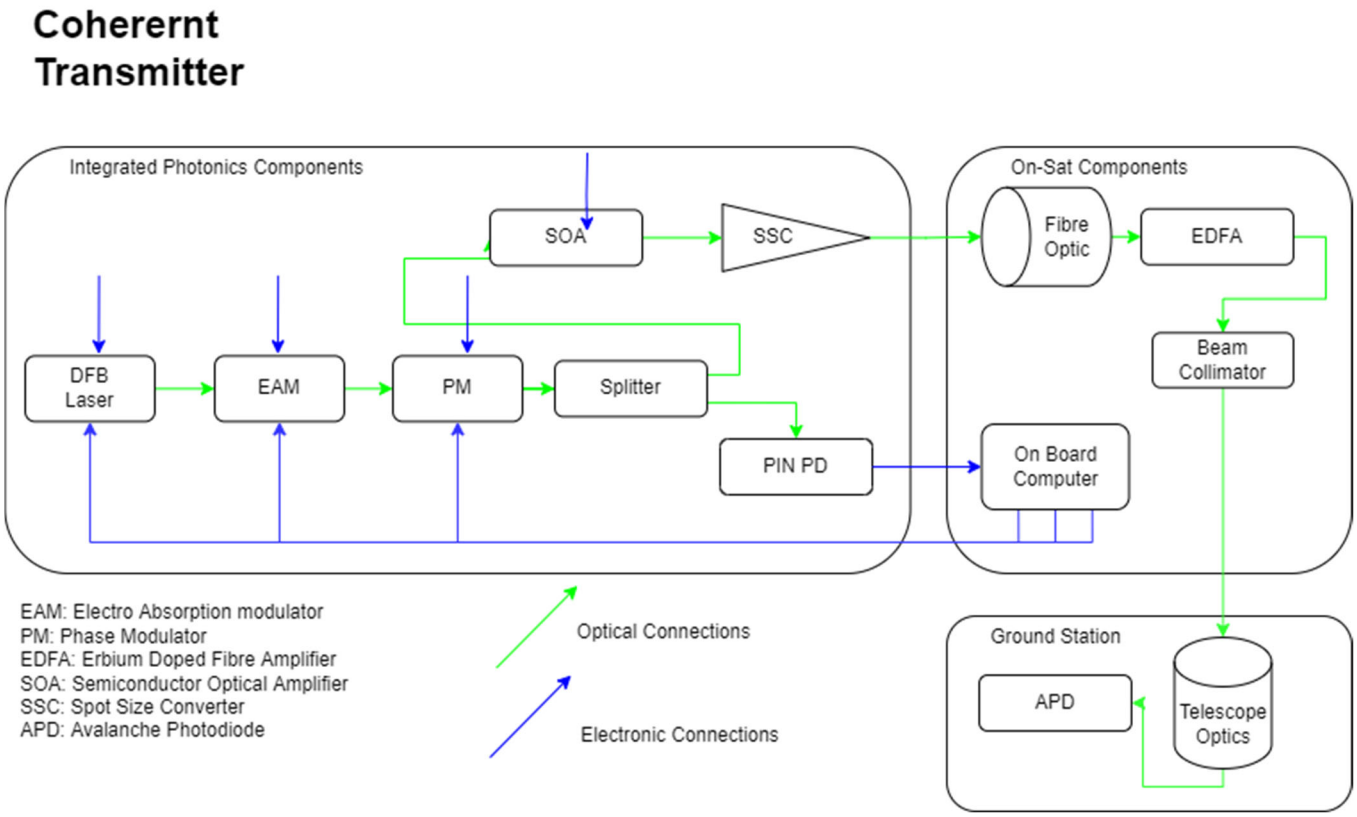

FIGURE 12:TRANSMITTER SYSTEM BLOCK DIAGRAM

To reiterate, the test chip's purpose is to allow for characterisation of the building blocks after they have been exposed to a radiation dose to simulate the effects of this aspect of the space environment on their functionality. To this end a test chip was designed to allow for each building block; DFB laser, Modulator (Mach Zender), SOA, Photodiode, to be tested individually. As a starting point the following block diagram was created:

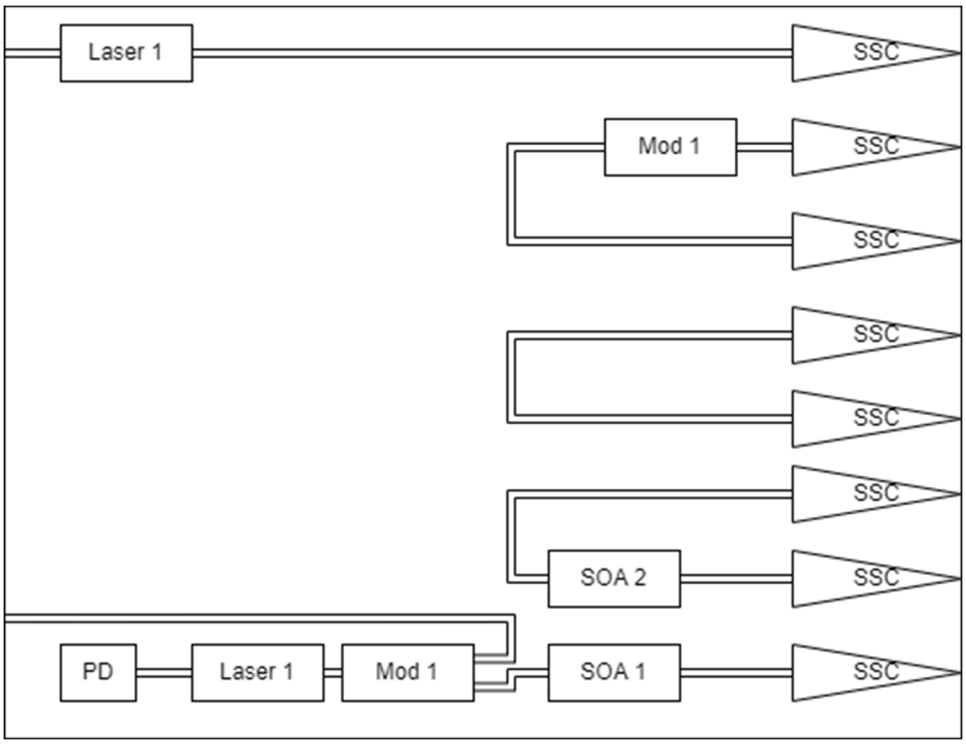

FIGURE 13: COMPONENT TEST CHIP BLOCK DIAGRAM

This design would allow for each component to be measured individually, has a central loop between two SSCs for assisting in alignment of the chip, and has a full transmitter circuit so potentially a measurement could be done of the full transmitter operation directly after irradiation. Every element used is supported by HHI. With this desired amount of tests in mind the chip layout was designed in collaboration with VLC.

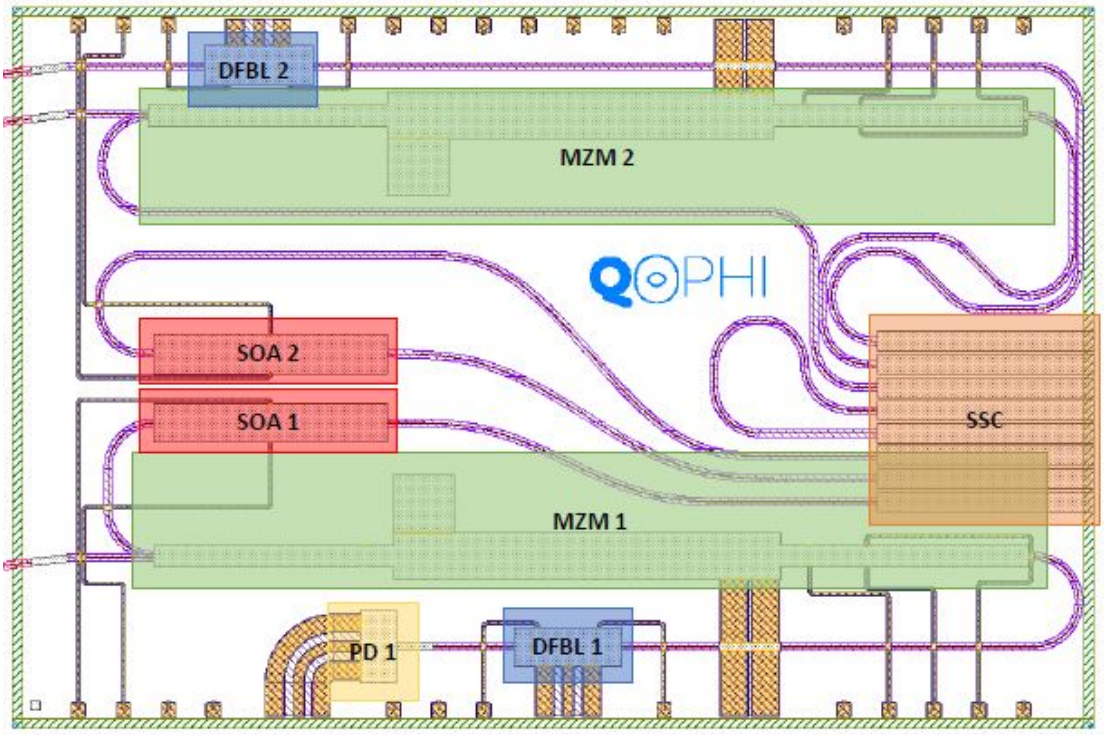

FIGURE 14. GDS OF THE TEST CHIP

In the end it was possible to fit all the desired tests into the chip. For the sake of completion, the relevant data as available from the foundry is also presented here.

DFB Laser:

Characteristics	Value	Units	Notes
Wavelength tuning range	~3	nm	
Wavelength accuracy	±5	nm	Shift applies to whole wafer
Single-sided output power	5	mW	At 150 mA bias current
Sidemode suppression ratio	50	dB	
Linewidth	~5	MHz	

TABLE 3: DFB LASER CHARACTERISTICS

Mach-Zehnder Modulator:

Characteristics	Value	Units	Notes
Electrode wave impedance	50	Ω	
Extinction ratio	>20	dB	
Vπ of individual arms	<4	V	For 16 modulator sections and bias point of -8V
F_{3dB}	>25	GHz	
Insertion loss	<6	dB	

TABLE 4: MZM CHARACTERISTICS

SOA:

Characteristics	Value	Units	Notes
Gain per length	~20	dB/mm	At 400mA/mm current
Saturation output power	~13	dBm	

TABLE 5: SOA CHARACTERISTICS

SSC:

Characteristics	Value	Units	Notes
SSMF alignment tolerance	<2	μm	At 400mA/mm current
Loss SSMF- waveguide	<2	dB	

TABLE 6: SSC CHARACTERISTICS

High-Speed PIN Photodiode:

Requirements	Value	Units	Notes
Sensitivity	~0.8	A/W	At 1550 nm
Linear regime input power	<10	dBm	
Polarization dependence	<0.8	dB	
Dark current	<10	nA	At -2V
3dB bandwidth	~45	GHz	

TABLE 7: PD CHARACTERISTICS

4. Transmitter Chip Designs

Here the designs of the transmitter chips are shown and described, along with any additional building blocks specifications. Furthermore, the packaging of the chip will be detailed, and simulation results for the transmitter in Lumerical Interconnect will be presented.

For the transmitter chip some changes were implemented into the design compared to the test chips. This includes the addition of an Electro Optical Phase Modulator (EOPM) as offered by HHI. This was to test whether more complex modulation formats could be used with the transmitter to achieve a higher data rate. While there won't be data for the radiation testing of this component it could be informative for future work in the topic. Additionally, an electro absorption modulator (EAM) was used in place of a MZM as in the test chips. This was to accommodate the large footprint of the EOPM, as the EAM is much smaller than a MZM. This would provide some insight into which modulator and hence which transmitter setup had the best performance, though it would leave open the question as to whether these components would perform on par in the space environment, this is left for future work to explore.

With that said as only 2 chips will be packaged, one thing kept in mind during the chip design was that potentially, if additional chips have good functionality, they could be radiation tested in the same manner as the first set of test chips, to this end several test structures for the new components were also included in the design, as well as a full transmitter circuit and alignment features. After the signal is modulated, but before it is boosted by the SOA, a splitter with an 80:20 splitting ratio was included. The lower powered end of the split was sent to a photodiode. The intention of this was to enable on-sat diagnostics of the transmitter system, allowing for the components operation to be managed by the on-board computer rather than relying on diagnostics from the ground station. Potentially, this could allow for different modulation formats to be chosen based on link conditions. This could increase the efficiency of transmissions, as if the link is strained a lower data rate, better SNR data modulation format like OOK could be used, while QPSK is switched to when conditions allow. Additionally, the satellite can understand if there is a fault occurring with, for example, the DFB laser, and switch to a redundant laser on chip. A future chip could be designed to take advantage of this, which has a second transmitter circuit on the same chip, without the test structures, each transmitter system therefore having a full back up built in.

With these considerations in mind the following block diagram for the circuit was drawn up, and used as a guide for the circuit layout:

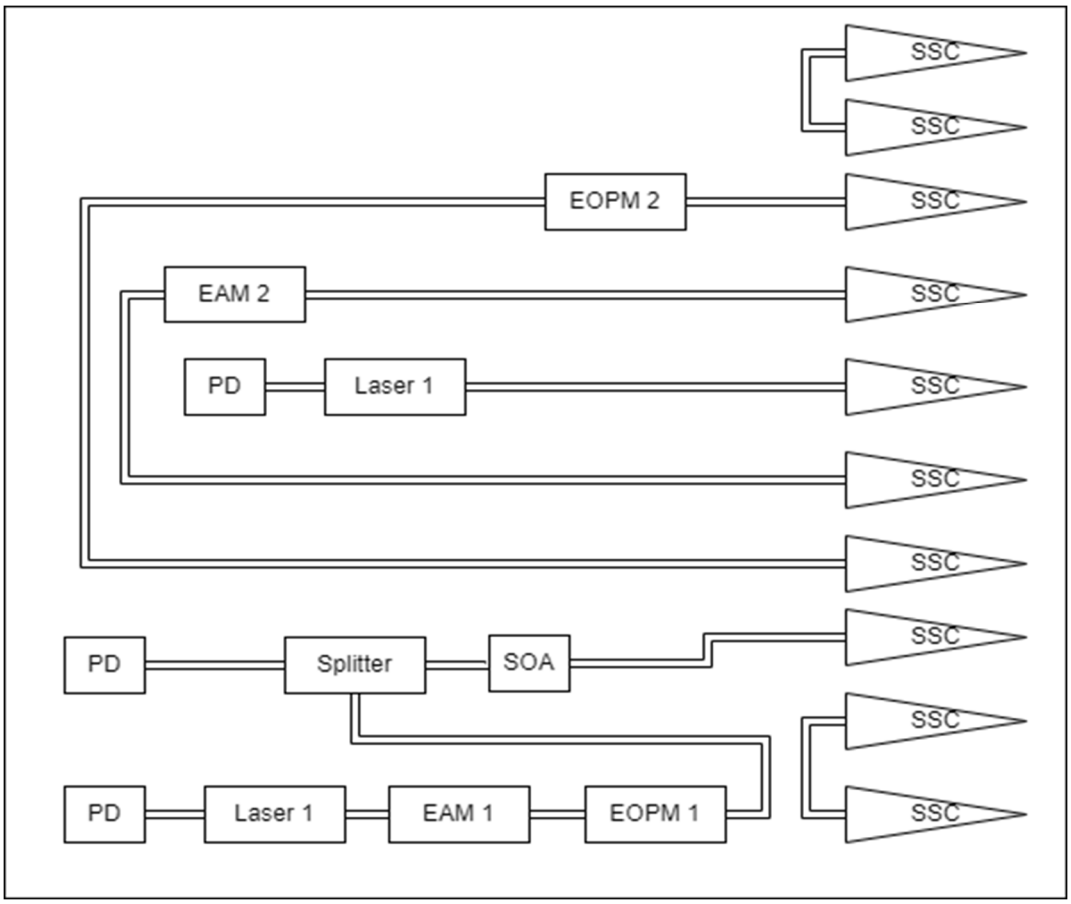

FIGURE 15: TRANSMITTER CHIP BLOCK DIAGRAM

The characteristics of the building blocks not included in the first test chips are noted here also:

EOPM:

Characteristic	Value	Units	Notes
Electrode wave impedance	50	Ω	
Termination impedance	50	Ω	
Vπ of individual arms	<8	V	For 16 modulator sections and bias point of -8V
F_{3dB}	>25	GHz	
Insertion loss	<6	dB	

TABLE 8: EOPM CHARACTERISTICS

EAM:

Characteristic			
Optical loss TE	8	dB	
Optical loss TM	4	dB	
F_{3dB}	20	GHz	
Series resistance	0.8	Ω	
Capacitance @ -2.5V	0.4	pF	
Extinction ratio	20	dB	

TABLE 9: EAM CHARACTERISTICS

Based on the block diagram (14), the layout was designed as follows in collaboration with VLC, implementing all desired features.

For the assembly of this chip, the 12 DC and 8 RF connections were wire bonded to a high-speed electrical carrier, and the optical fibre pig tailing of the 10 optical ports were performed by VLC. The electrical carrier was designed on a ceramic substrate for high frequency signals, allowing up to 20Ghz operation for the RF ports controlling the EAM and therefore the signal modulation. For thermal control a bond-pad for a thermistor was placed close to the PIC, peltier-cell and thermistor will be connected to spare pin-connectors on the PCB. Fujikura PM1550 fibre optic cables were chosen for the fibre array. They are single mode fibres with larger than -20dB crosstalk. The PCB provides the mechanical support on top of which to die-attach face-up the PIC using a thermal conductive epoxy. This solution enhances the mechanical robustness of the optical fibres, and it can allow to use an embedded Peltier cell for temperature stabilization.

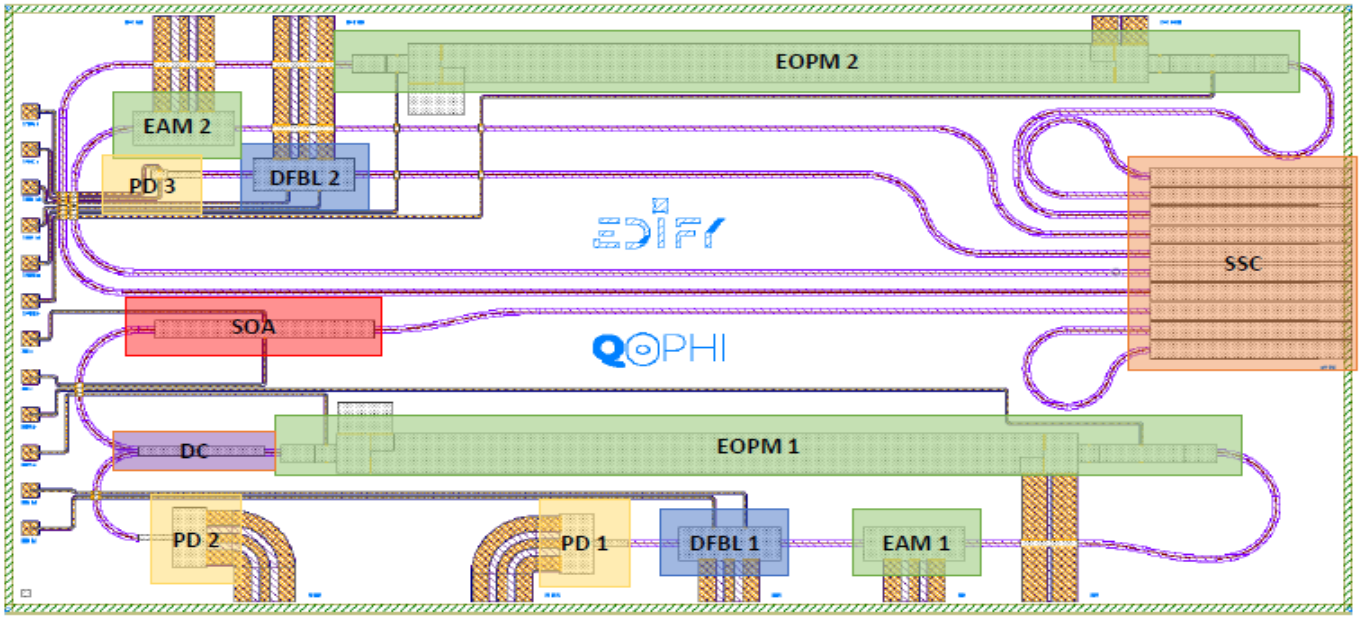

FIGURE 16: TRANSMITTER CHIP GDS

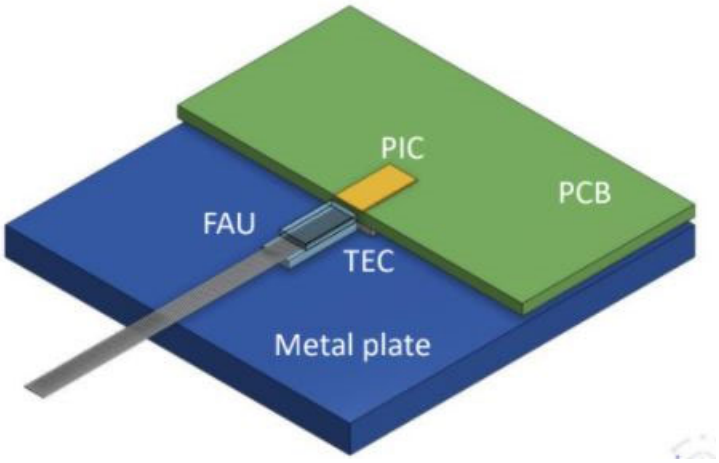

FIGURE 17: ILLUSTRATION OF THE PIC ASSEMBLY

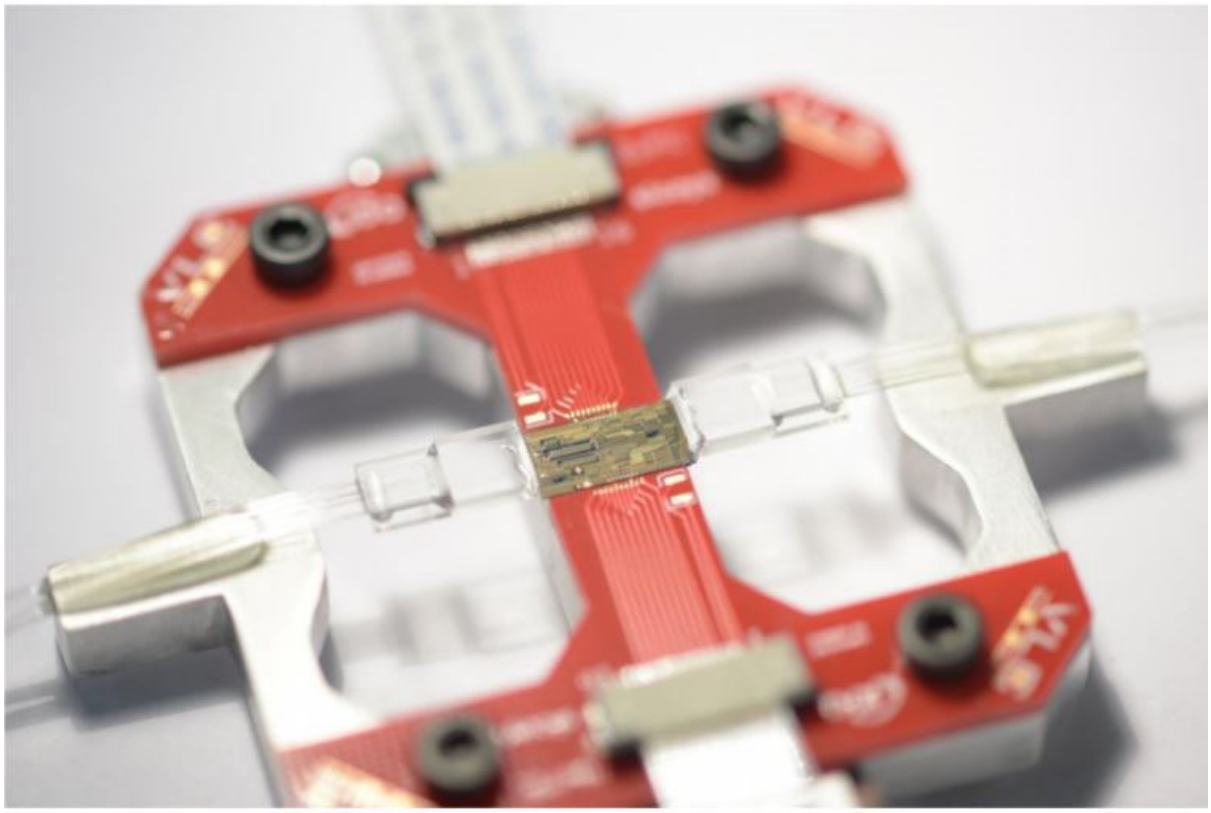

FIGURE 18: FINAL (STAND IN) ASSEMBLY OF THE TRANSMITTER CHIP, READY FOR TESTING.

Before proceeding to the measurement results of the test and transmitter chips, some data from simulations of the transmitter chip in Lumerical Interconnect will be presented and discussed below.

Insert Diagram here listing all the points I measure in the circuit simulation:

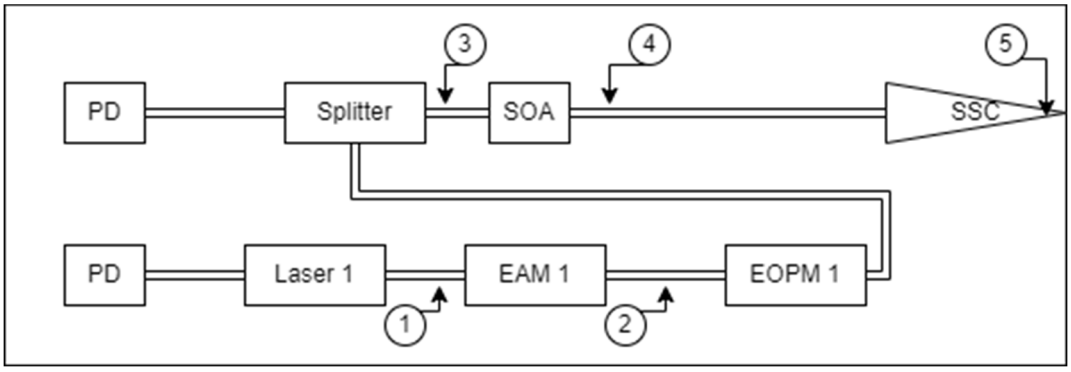

FIGURE 19: DIAGRAM ILLUSTRATING THE MEASUREMENT POINTS USED FOR PRODUCING THE FOLLOWING GRAPHS IN INTERCONNECT

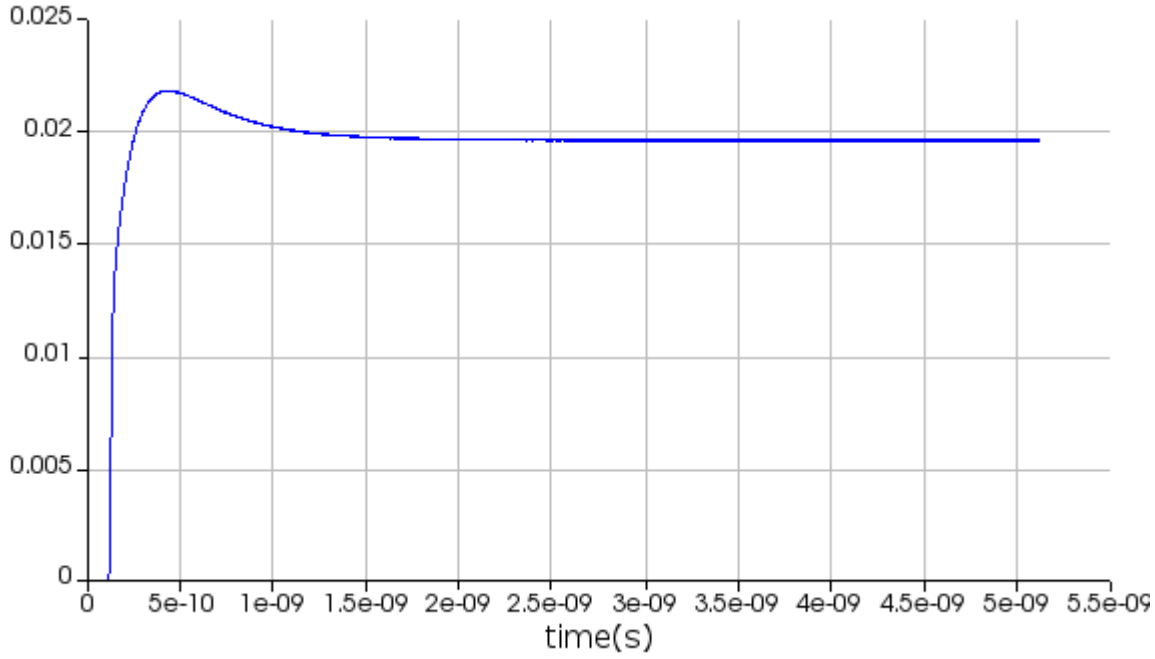

FIGURE 20: LOCATION 1, SHOWING THE POWER OUTPUT OF THE DFB LASER FROM ONE SIDE.

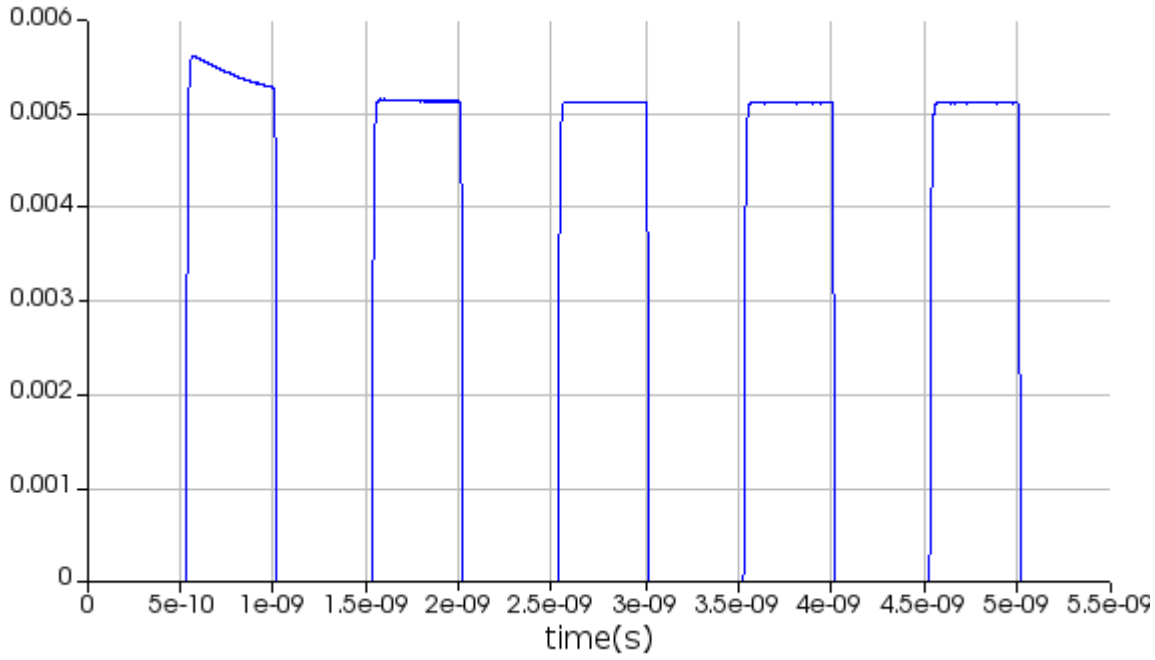

FIGURE 21: LOCATION 2, SHOWING THE POWER OUTPUT AFTER THE EAM.

The EAM here is being powered by a PBRS driven applied voltage switching between -4 and 0 Volts. At this setting the EAM is able to absorb all the light when fully powered, creating sharp square waveforms for encoding the signal.

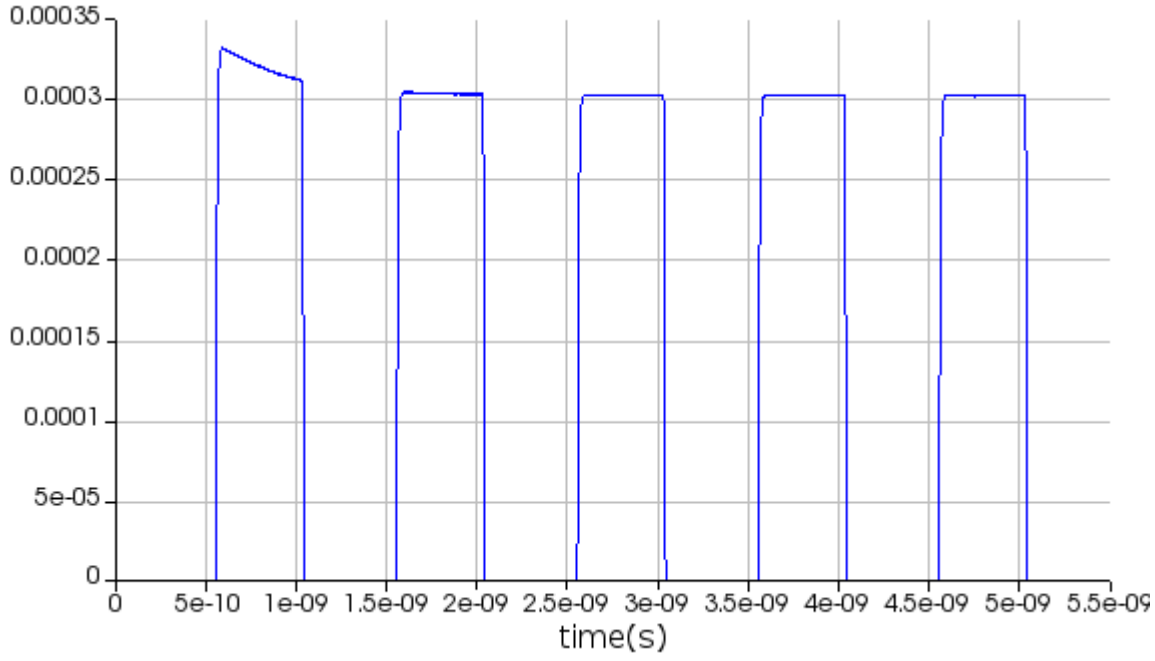

FIGURE 22: LOCATION 3, SHOWING THE POWER AFTER THE SPLITTER

The only noticeable difference being from propagation loss, insertion loss and the 80:20 split the splitter performs as mentioned in the design description.

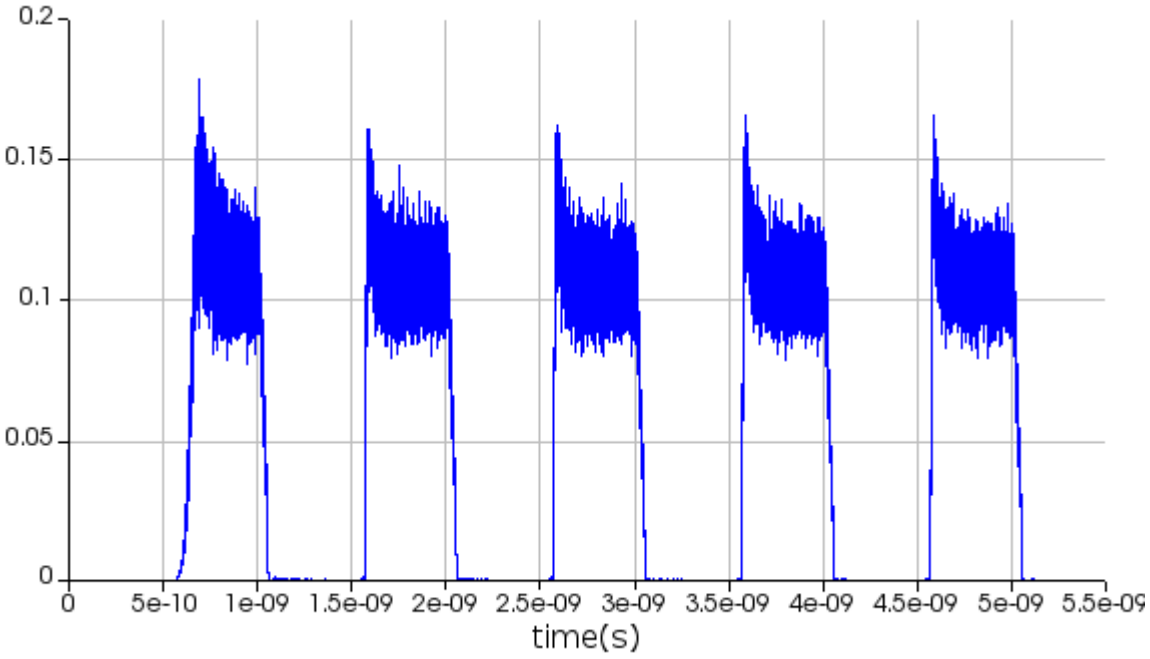

FIGURE 23: LOCATION 4, SHOWING THE OPTICAL POWER AFTER THE SOA

The SOA was driven by the same PBRS as the EAM, as if left in its on state it pumped low noise levels in the system too much for the 0 and 1 bits to be distinguishable.

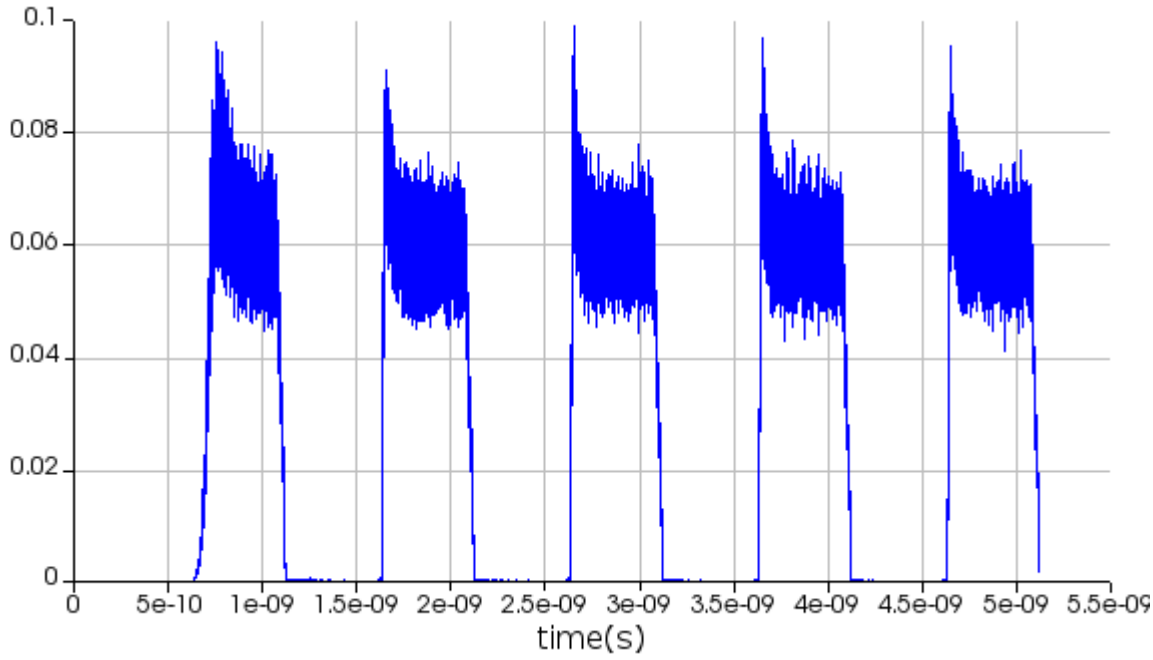

FIGURE 24: LOCATION 5, SHOWING THE POWER OUTPUT FROM THE SSC AT THE END OF THE CIRCUIT.

Again, this change just accounts for propagation losses in the waveguide as well as some loss from the SSC BB itself.

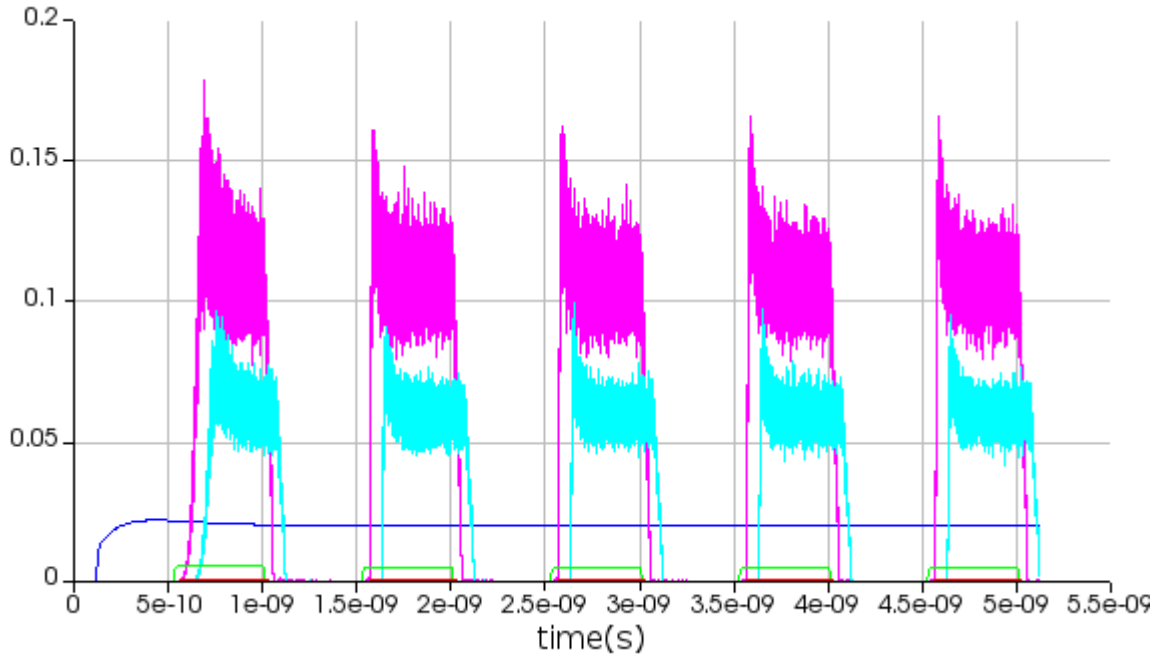

FIGURE 25: SUMMARY OF THE PREVIOUS CHARTS FOR EASE OF VIEWING HOW THE POWER CHANGES THROUGHOUT THE CIRCUIT.

5. Component Chip and Transmitter Chip Characterisation results and packaging description

The aim of the characterisation testing was to determine the functionality of key optical and electrical features to determine which of the chips show the best performance, since only 2 of the 6 chips transmitter chips will be packaged, and only some of the component chips will be sent to be irradiated, for best results they should of course be the ones with best performance.

5.1. Transmitter Chip Characterisation

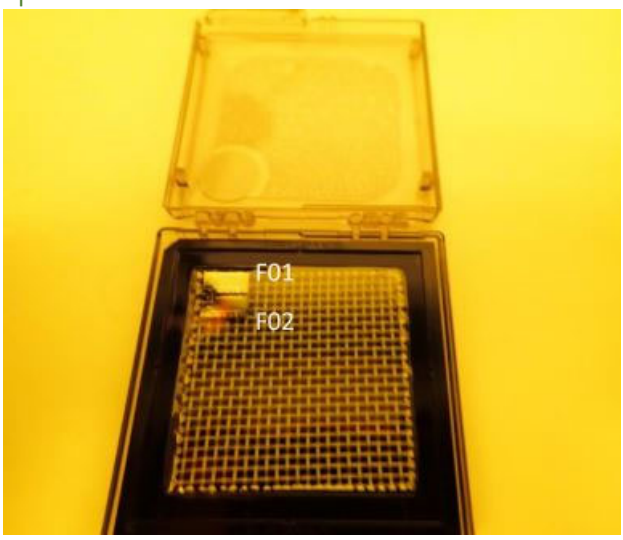

FIGURE 26: TWO OF THE TRANSMITTER CHIPS AS THEY ARRIVED FROM HHI

The characterisation testing can be broken down into two groups, electrical screening, and optical measurements. The electrical screening consisted of acquiring V-I curves of the 6 heaters on chip: sweep current and measure voltage, and V-I curves of the RF connections (of which there are 8 on chip) at continuous operation. The optical measurements consisted of: OSA Spectra of one alignment loop. Calculation of coupling losses using a broadband source (1530-1590nm), and OSA spectra of internal sources (DFB Laser or SOA) while sweeping the bias. Table (10) summarises the main characterisation parameters as used in these tests:

Parameters	Values
Wavelength range	1530 nm – 1590 nm (SOA and loop) 1545 nm – 1555 nm (DFBL)
Resolution	0.02 nm
Polarisation control	No
Optical source	Broadband source
Thermal stabilisation	25 degrees C

Input/output	One side
Coupling method	SSMF, SSM Fibre Array
Fibre array pitch	127 µm
Electrical pad pitch	250 µm (DC), 130 µm (RF)
DC electrical pad size	100 µm x 100 µm
Simultaneous DC measurements	1
Simultaneous RF measurements	1

TABLE 10: SUMMARY OF MAIN CHARACTERISATION PARAMETERS FOR TESTING

The setup for the electrical screening is shown below. The RF probe is located in north and south facets and DC probe in left facet. A 20 x 250 µm pitch DC multicontact probe and 130 µm pitch GSG RF probe was used.

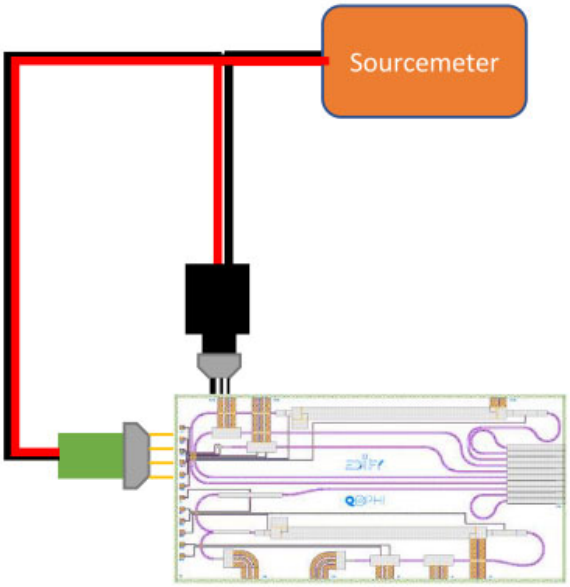

FIGURE 27: SETUP FOR ELECTRICAL SCREENING

For the electro-optical response tests for the SOA and DFB laser the following setup was used. The probe was located in the north facet, a 20 x 250 µm pitch DC multicontact probe and a 130 µm pitch GSG RF probe were used once again. Output light was coupled to a standard single-mode fibre (SSMF) and the spectrum was captured with an Optical Spectrum Analyser (OSA).

The results will be organised by the type of test.:

- **Test 1.1:** Electrical screening of DC pads
- **Test 1.2:** Electrical screening of RF pads
- **Test 2:** Coupling losses (measurements of the loops)
- **Test 3:** DFBL, SOA measurements

In each section, the results of the measured chips will be compared to determine the best performance in each case. In the electrical screening the results will be compared component by component. The same naming conventions have been used to describe the components as in the gds image presented in Figure (16).

Test 1.1:

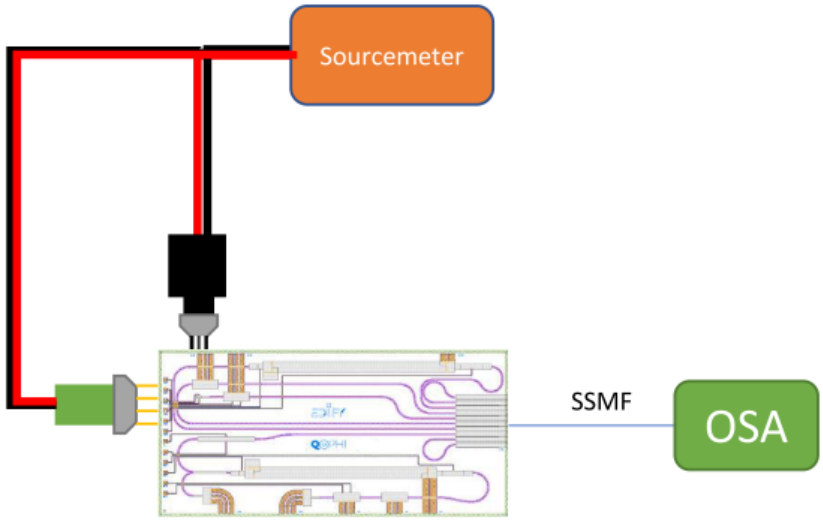

FIGURE 28: TEST 1 SETUP

To test the DFB pads a current sweep between 0 and 160mA was performed. All the pads obtained similar responses, except for the DFB laser 1 on the F05 chip, which seems to have become inoperable during testing.

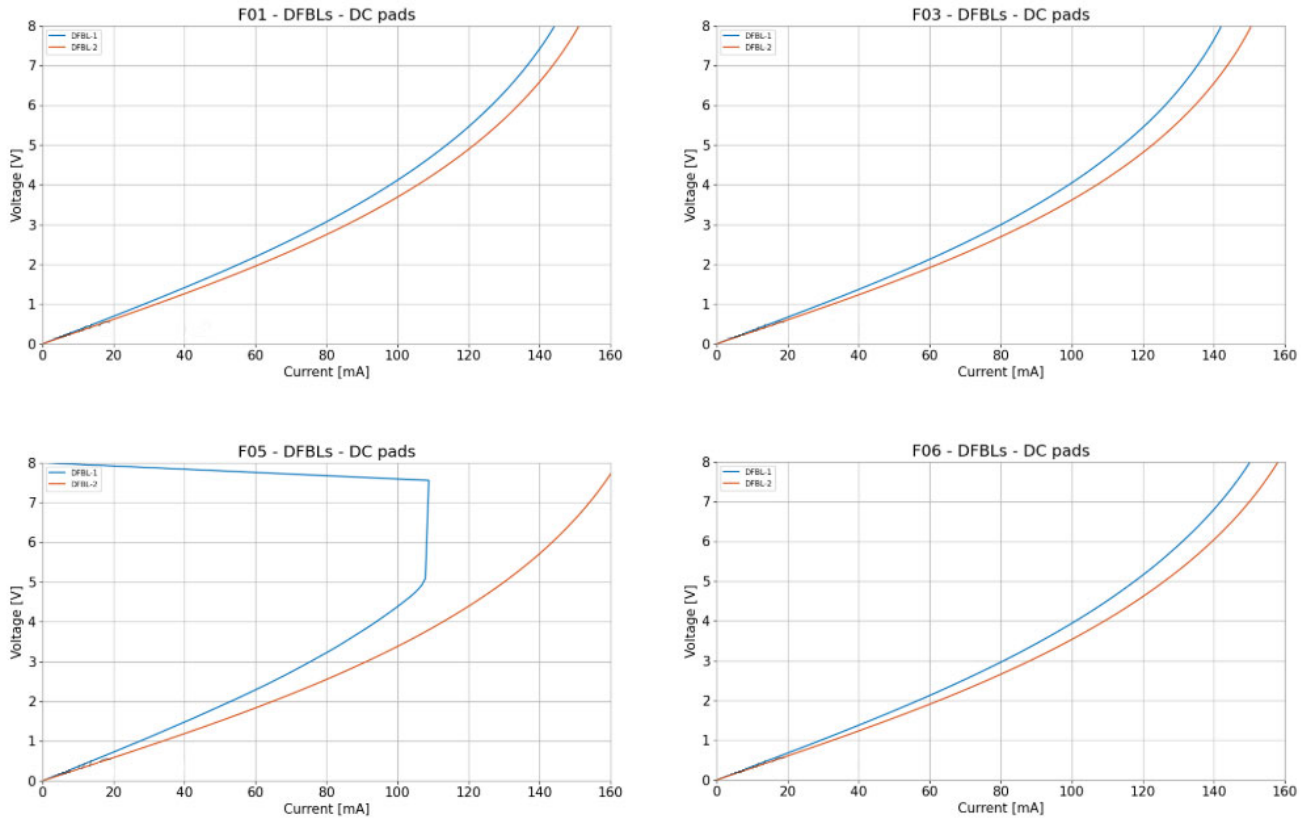

FIGURE 29: DFB PAD CURRENT SWEEP RESULTS

To test the EOPMs pads, in accordance with HHI#23s design manual, a voltage sweep between 0 to -5V was performed.

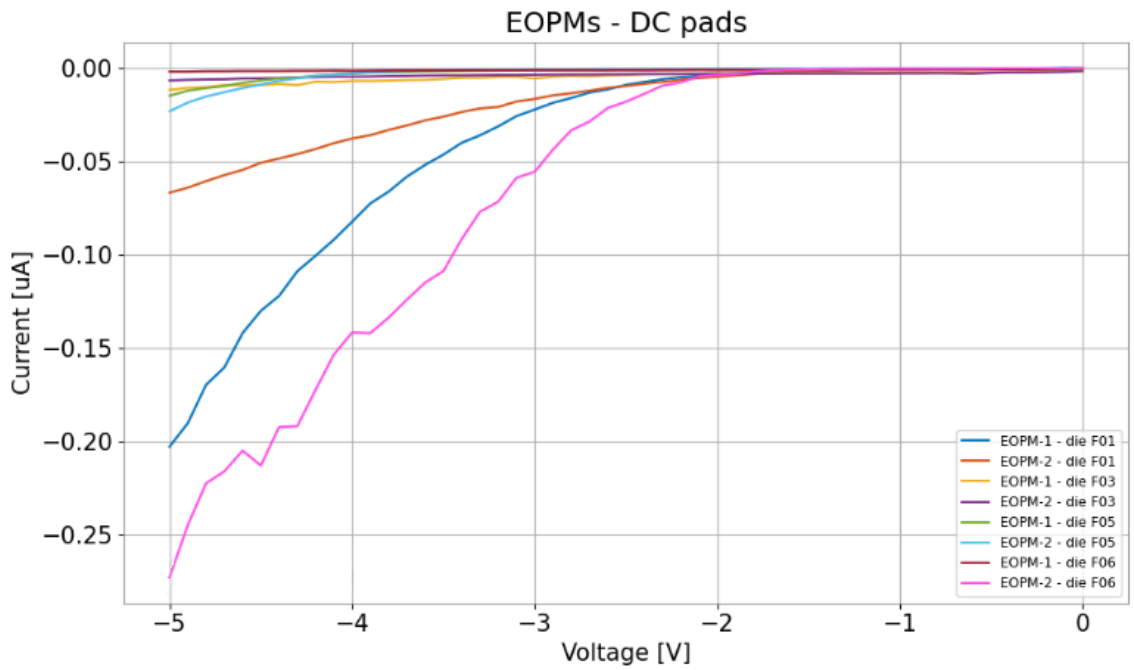

FIGURE 30: EOPM DC PADS VOLTAGE SWEEP

In order to better compare and evaluate the performances of the EOPMs, tables were generated with the current values measured at -2V and -5V.

	Dark current at -2V			
Elements	Chip F01	Chip F03	Chip F05	Chip F06
EOPM 1	-3.4 nA	-2.8 nA	-1.1 nA	-1.1 nA
EOPM 2	-4.8 nA	-3.6 nA	-0.5 nA	-3.6 nA

TABLE 11

	Dark current at -5V			
Elements	Chip F01	Chip F03	Chip F05	Chip F06
EOPM 1	-200 nA	-11 nA	-15 nA	-2 nA
EOPM 2	-65 nA	-6.7 nA	-23 nA	-273 nA

TABLE 12

When biased at -2V all the components measured had a dark current below -10nA. However, when biased at -5V, EOPM 1 of chip F01 and EOPM 2 of chip F06 had overly high dark currents. To test the PD pads, as the HHI manual describes, a voltage sweep from 0 to -5V was performed. The results for Photodiode 3 when biased at -2V are summarised in the table below:

	PD-3 dark current summary			
Elements	Chip F01	Chip F03	Chip F05	Chip F06
PD-3 at -2V	-13 nA	-3.6 nA	-1.2 uA	-3.5 nA

PD-3 at -5V	-30 nA	-11 nA	-62 uA	-9.4 nA

TABLE 13

In this case, at a -2V bias the currents are generally around -10nA, indicating good operation, however chip F05s PD pad has a much too high dark current, indicating it's not functioning correctly. For the other chips, when bias increased to -5V the values remain on the order of nano Amps.

The full voltage sweep results for PD-3 are shown in figure (31), followed by a zoomed in chart in figure (32).

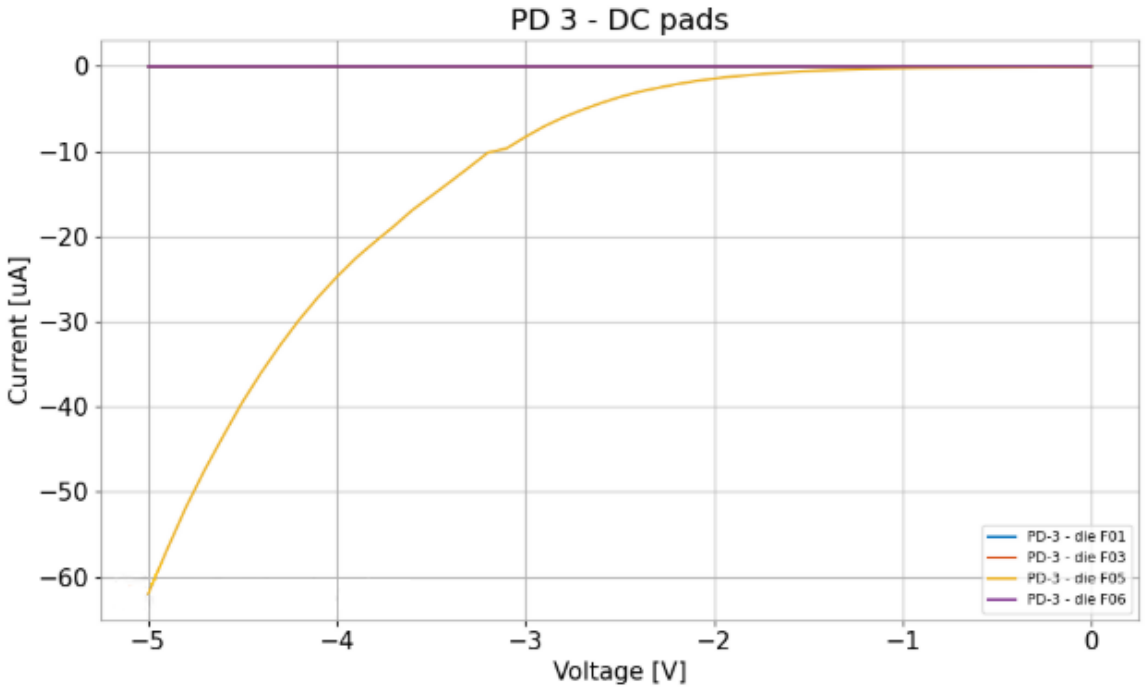

FIGURE 31: PD3 DC PADS VOLTAGE SWEEP

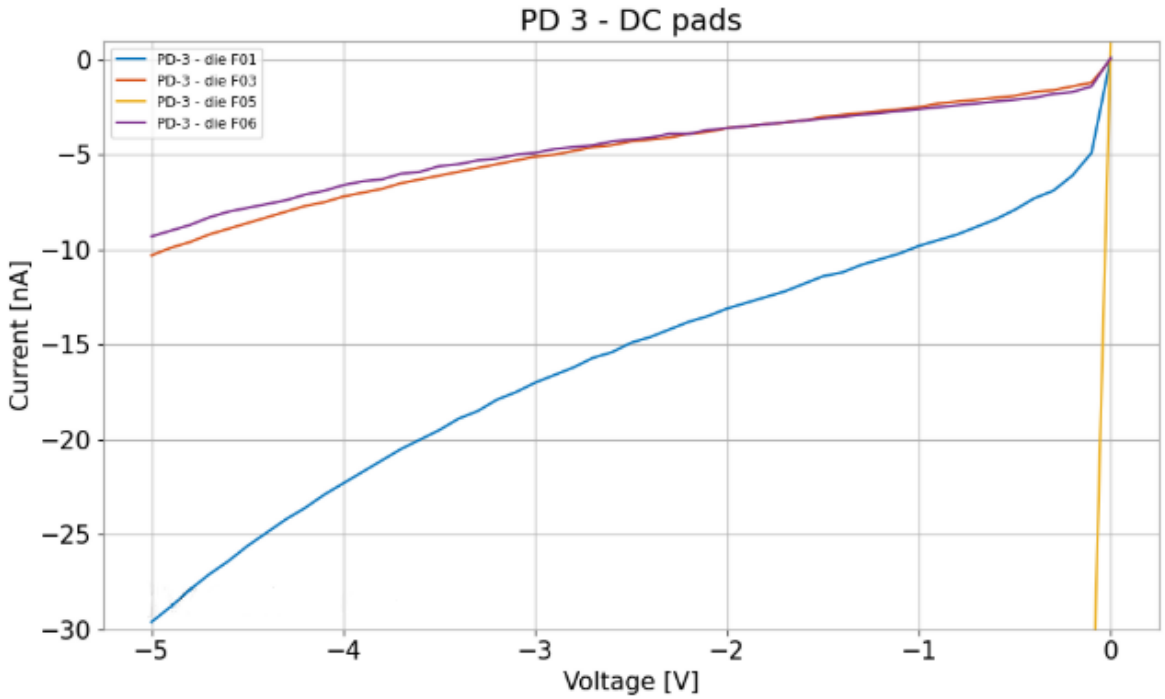

FIGURE 32: PD3 DC PADS VOLTAGE SWEEP (ZOOMED)

In line with the design manual instructions, to test the SOA pads a current sweep from 0 to 150mA was conducted. The results are displayed in figure (33).

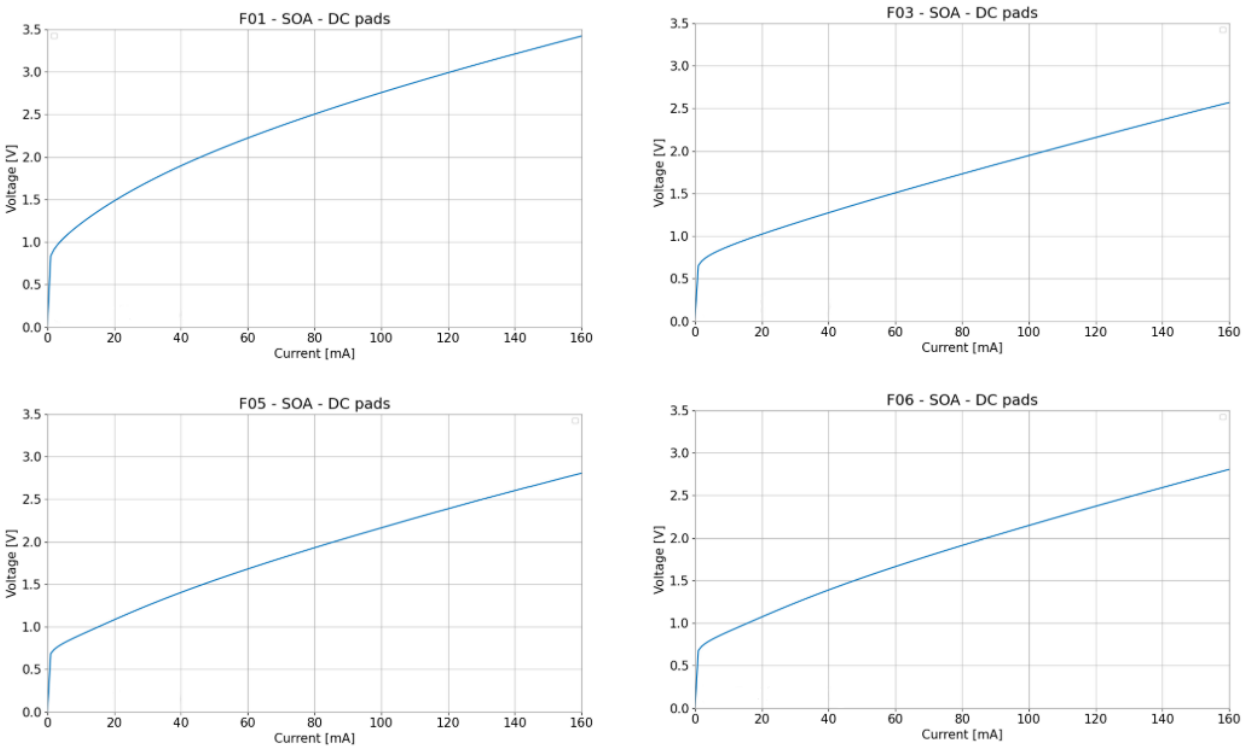

FIGURE 33: F01, F03, F05 AND F06 SOA DC PAD CURRENT SWEEPS

We see from this a general p-n junction is obtained, indicating all the pads work well.

Test 1.2:

To test the DFB lasers RF pads, a current sweep was performed from 0 to 160mA. All seem to perform well, showing a typical p-n junction curve.

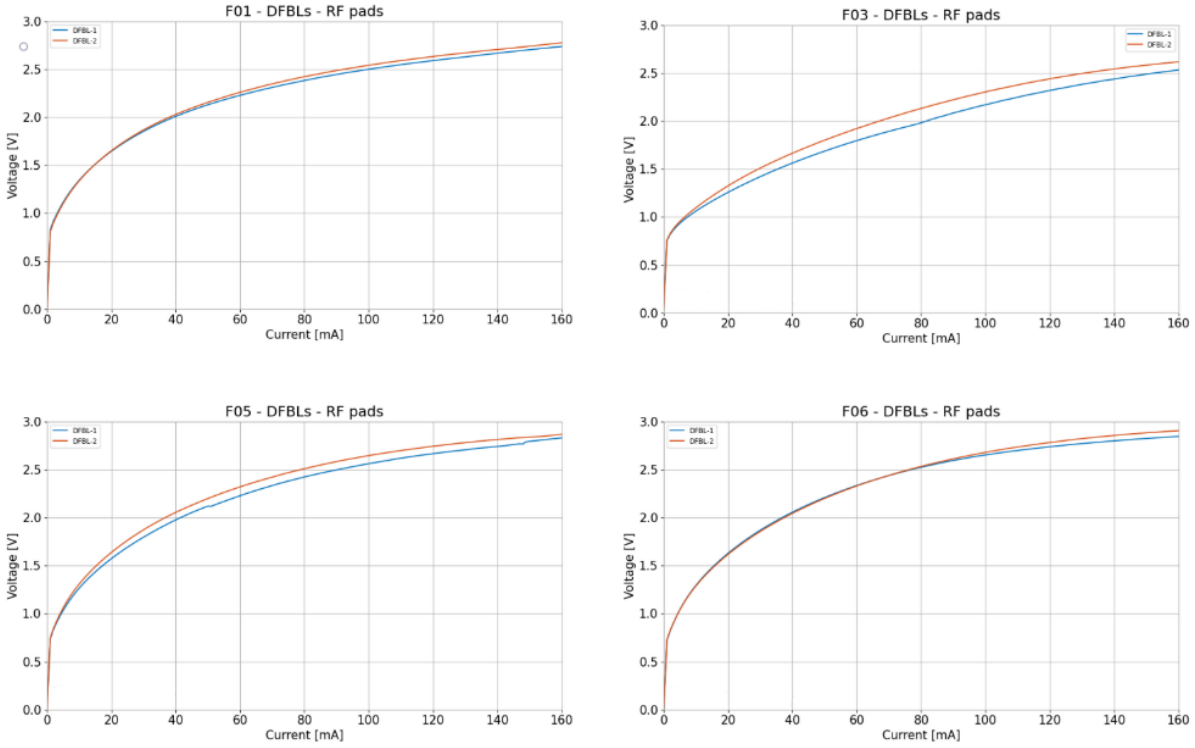

FIGURE 34: F01, F03, F05 AND F06 DFB LASER RF PAD CURRENT SWEEPS

To test the EAMs RF pads, a voltage sweep from 0 to -5V was performed.

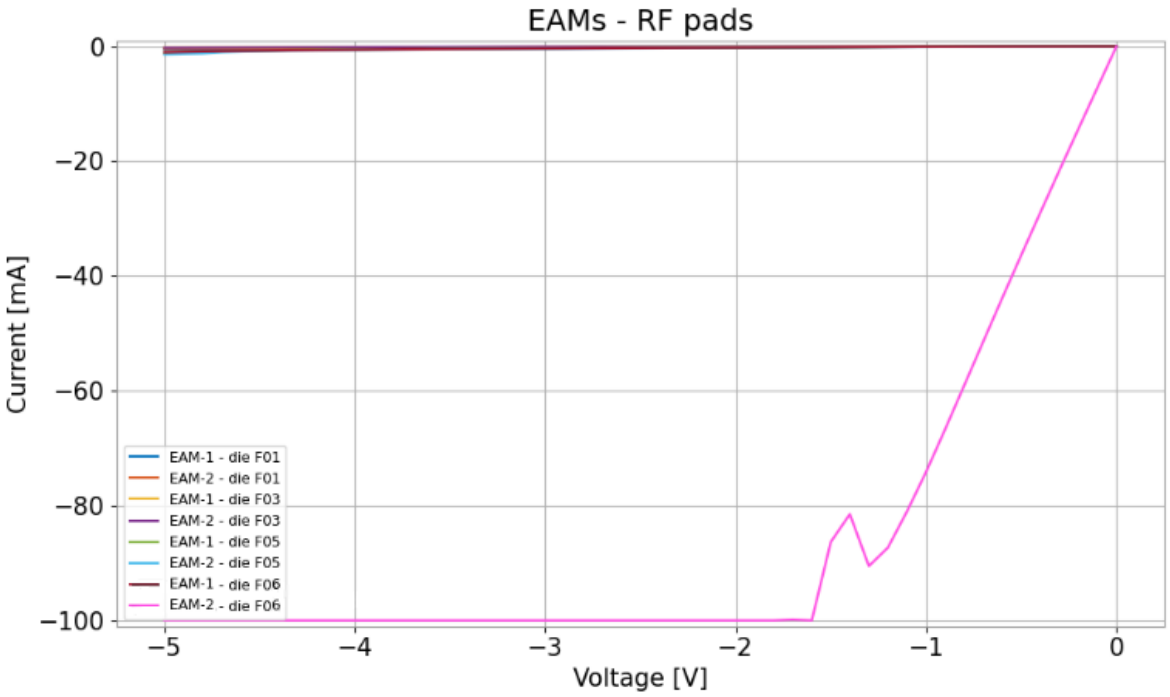

FIGURE 35: EAM RF PAD VOLTAGE SWEEPS

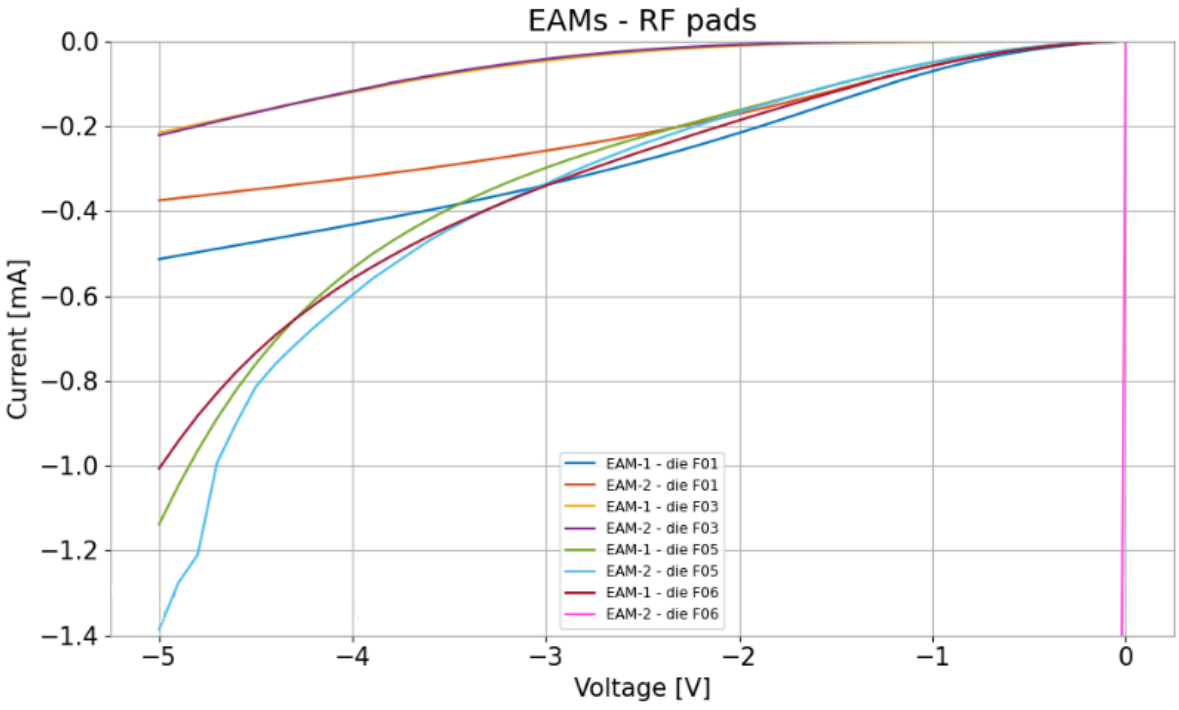

FIGURE 36: EAM RF PAD VOLTAGE SWEEPS (ZOOMED)

In order to better evaluate and compare the performance of the EAMs, a summary table with current values measured at -2V and -5V has been prepared.

	PD-3 dark current summary at -2V			
Elements	Chip F01	Chip F03	Chip F05	Chip F06
EAM 1	- 0.21 mA	- 11.1 uA	- 0.15 mA	- 0.15 mA
EAM 2	-0.17 mA	-8.4 uA	-0.16 mA	-100 mA

TABLE 14

	PD-3 dark current summary at -5V			
Elements	Chip F01	Chip F03	Chip F05	Chip F06
EAM 1	- 0.52 mA	- 11.8 uA	- 0.17 mA	- 1 mA
EAM 2	-0.37 mA	-9.15 uA	-0.18 mA	-100 mA

TABLE 15

In general, the measured dark currents in these components are in the order of tenths of a mA. The exception is die F03, they're on the order of a uA.

Similarly, for the EOPMs, voltage sweeps from 0 to -5V were performed. In general, this produced a resistor-like response, but it seems EAM1 on chip F05 is not working correctly.

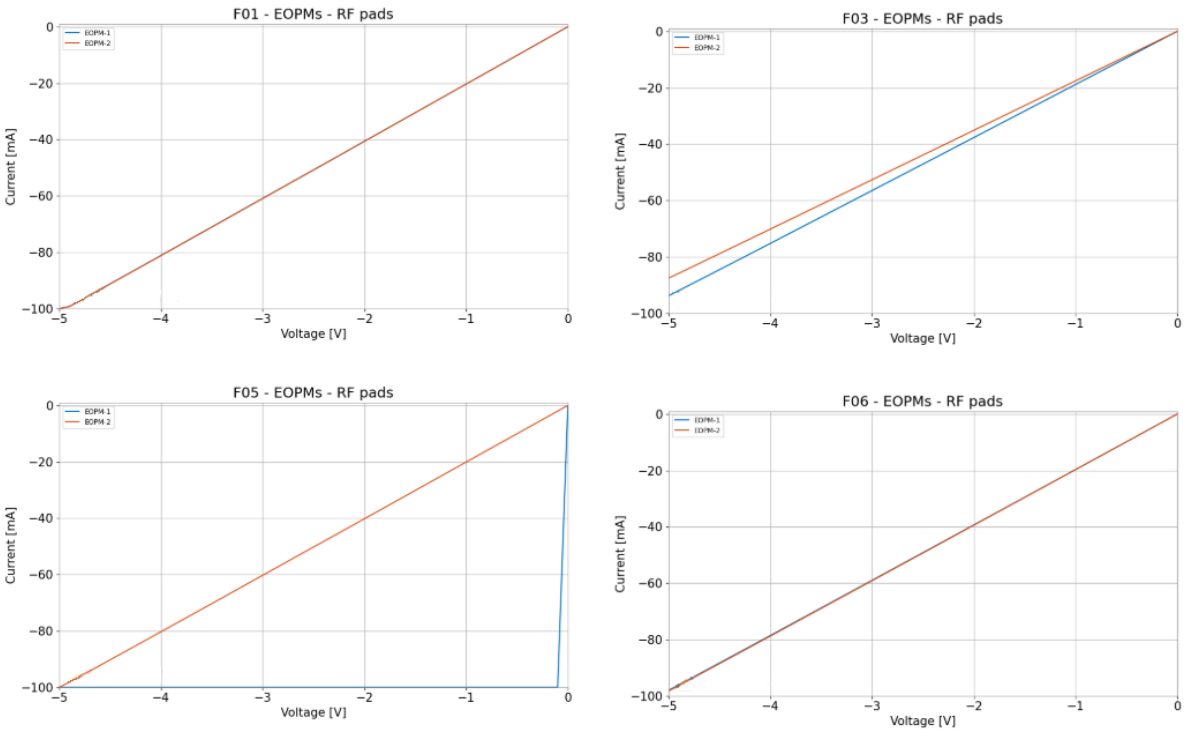

FIGURE 37: F01, F03, FO6 AND F06 VOLTAGE SWEEPS FOR EOPM RF PADS

Finally, the PD RF pads were electrically screened by performing a voltage sweep from 0 to -5V.

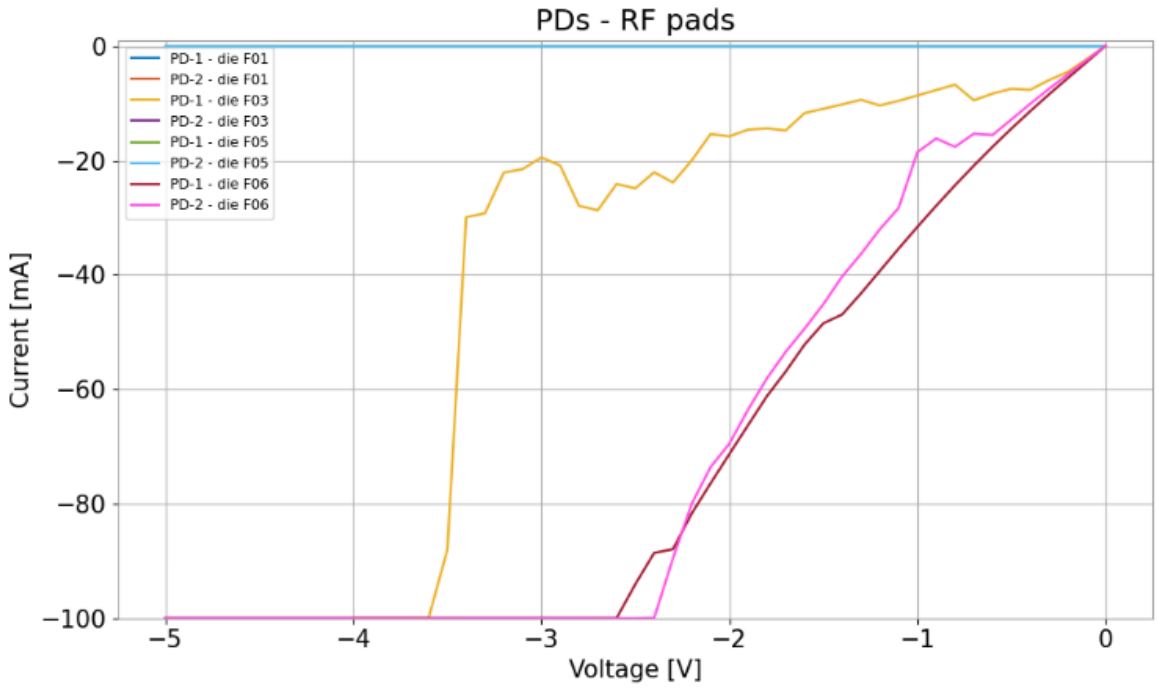

FIGURE 38: PD RF PAD VOLTAGE SWEEPS

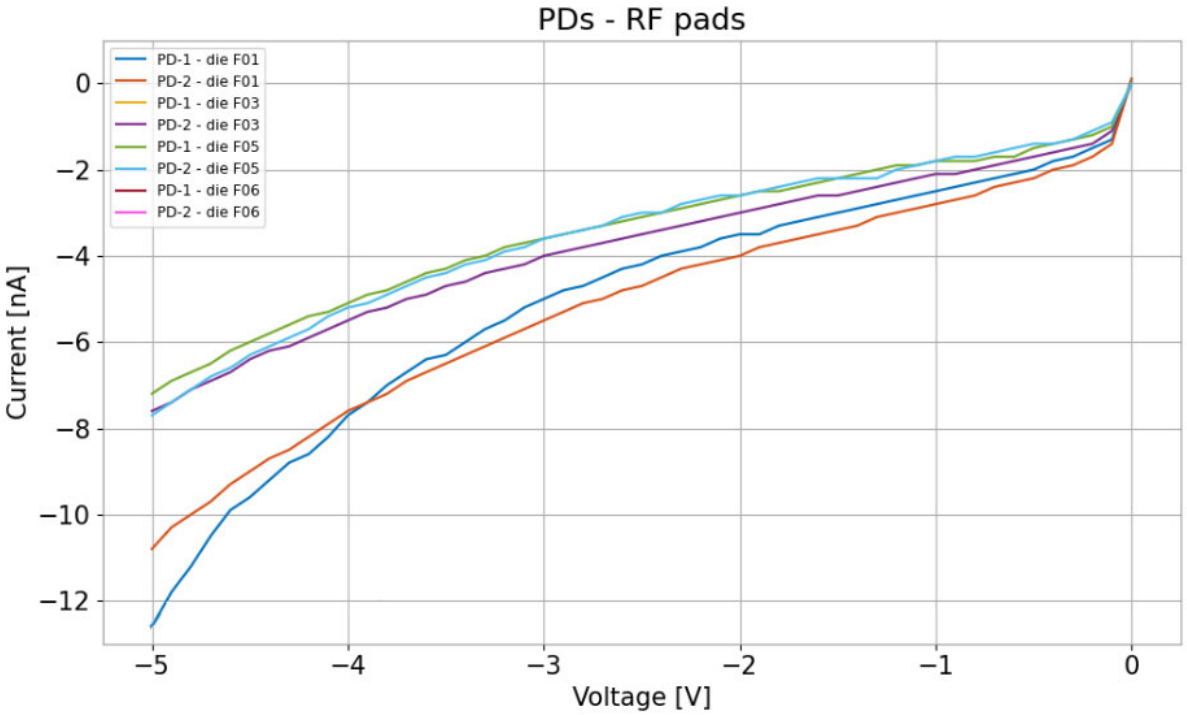

FIGURE 39: PD RF PAD VOLTAGE SWEEPS (ZOOMED)

Once again, in order to better assess the performance, summary tables have been prepared for the current values measured at -2V and -5V.

	PD dark current summary at -2V			
Elements	Chip F01	Chip F03	Chip F05	Chip F06
PD 1	-3.4 nA	-16 mA	-2.6 nA	-31 mA
PD 2	-4 nA	-3 nA	-2.6 nA	-20 mA

TABLE 16

	PD dark current summary at -5V			
Elements	Chip F01	Chip F03	Chip F05	Chip F06
PD 1	-13 nA	-100 mA	-7.2 nA	-100 mA
PD 2	-11 nA	-7.6 nA	-7.8 nA	-100 mA

TABLE 17

We can see that for a -2V bias the currents are generally below -10 nA. However, PD1 on chip F03 and the two PDs on die F06 have a current above -10 mA (at -2V bias) so it appears they are not working correctly.

Test 2: Coupling losses – Loops test

In general, in each chip one loops performs best, and across chips this is generally about 4 to 5 dB of coupling losses per facet. However, for F06 the losses are somewhat higher, between 5 and 7 dB per facet.

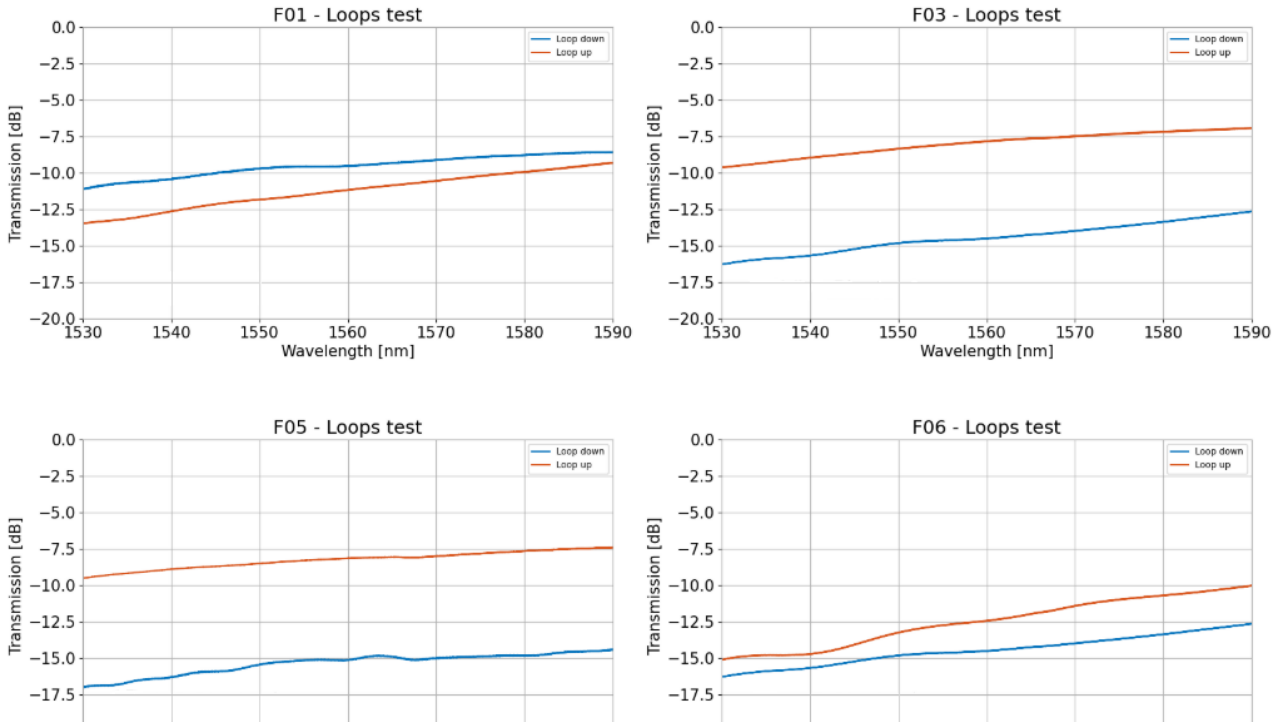

FIGURE 40: COUPLING LOSS TESTS FOR F01, F03, F05 AND F06

Test 3:

To test the SOAs active performance a current sweep from 0 to 160 mA was performed. The emission lines of the lasers at different currents are shown, one can see that the best emission range is when the SOA is powered between 80 and 160 mA. Many lines are also observed for each applied current due to internal reflections.

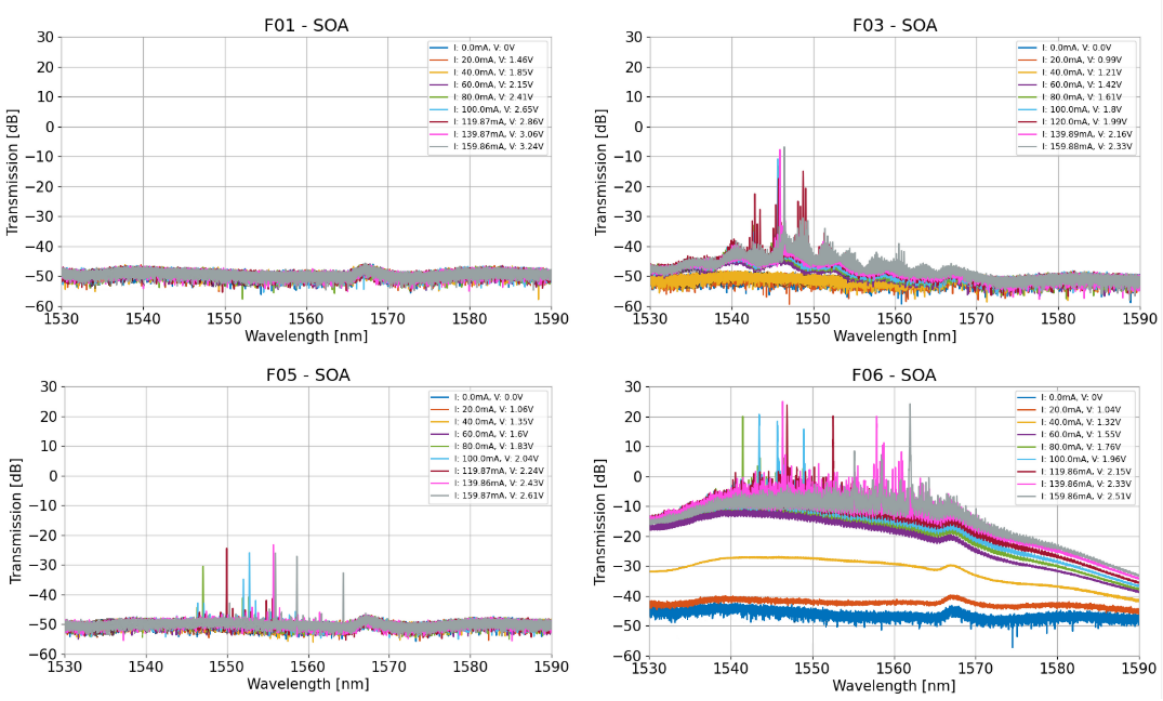

FIGURE 41: OPTICAL OUTPUT FOR ALL TESTED CHIPS SOAS, WHEN SWEPT FROM 0 TO 160MA

To summarise these charts, charts showing the optical power were also generated. These show that only chip F06 seems to work well. The SOA in chip F01 doesn't function at all.

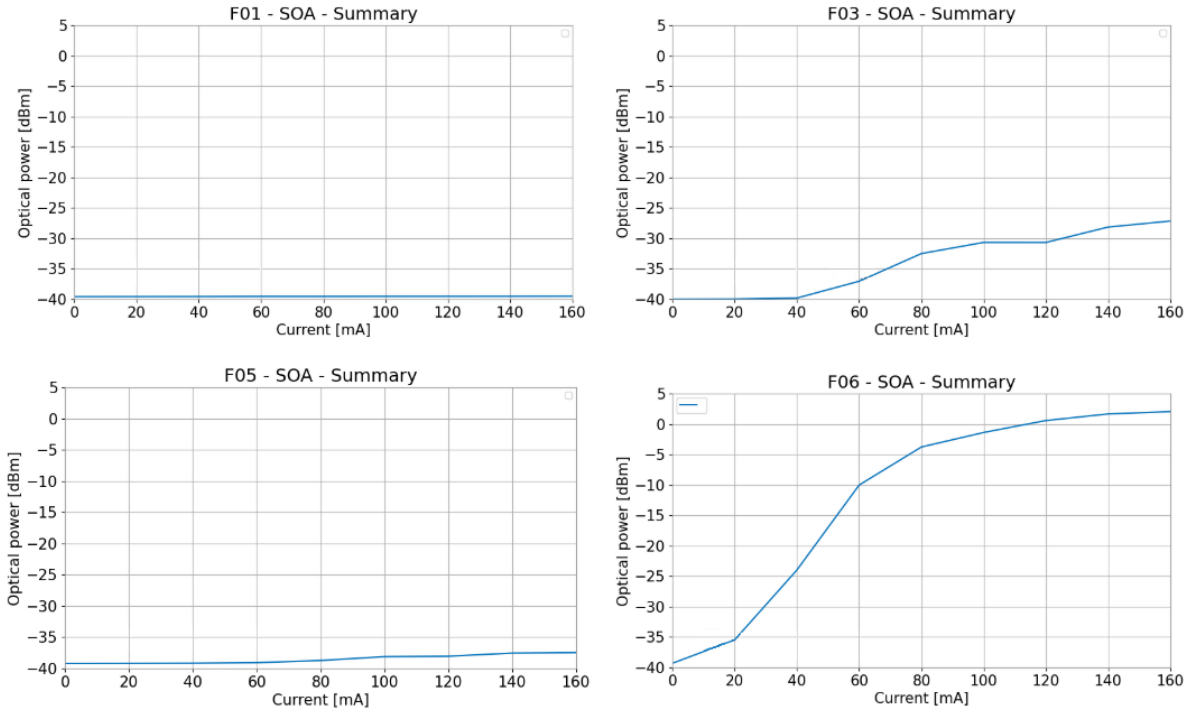

FIGURE 42: SUMMARY OF FIGURE 40S CHARTS, CLARIFYING THE PERFORMANCE OF THE SOAS

Finally, the DFB laser was tested by performing a current sweep from 0 to 160mA in increments of 20mA. The emission lines of the lasers at different currents are shown, the best emission range occurs when the DFB is powered between 60 and 140mA.

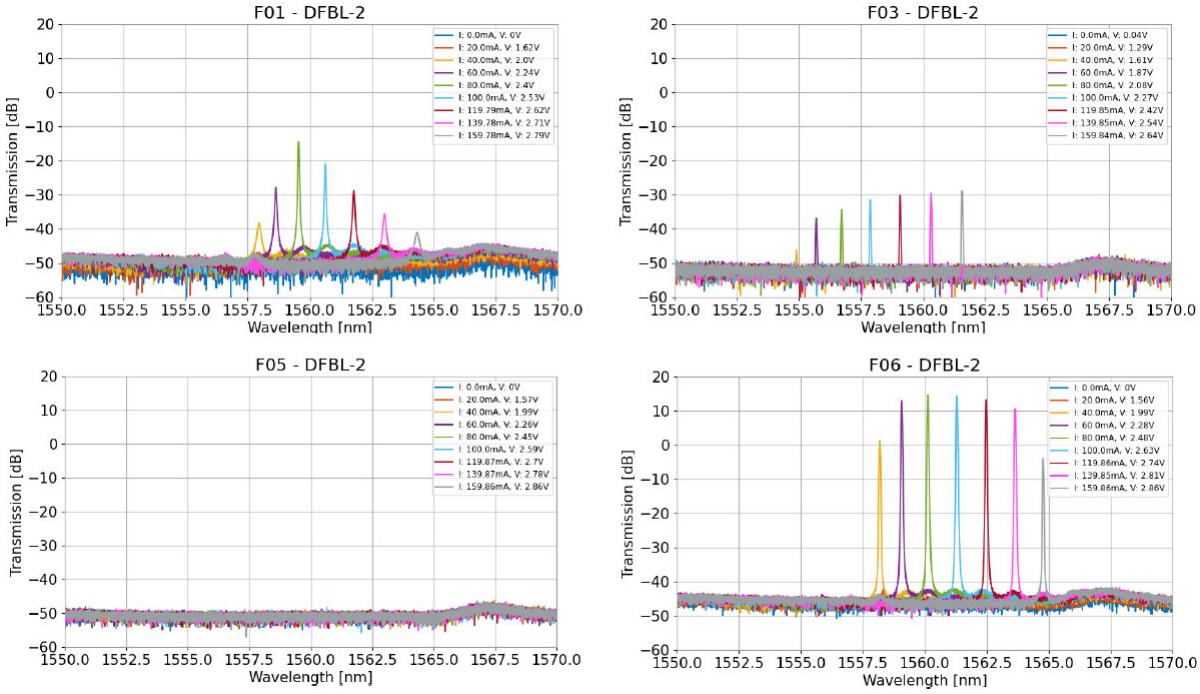

FIGURE 43: CURRENT SWEEPS FOR THE 4 CHIPS DFB LASER, SHOWING OPTICAL OUTPUT

As before, there follows a set of summary charts to better compare the performance of the lasers. Only chip F06 appears to function correctly.

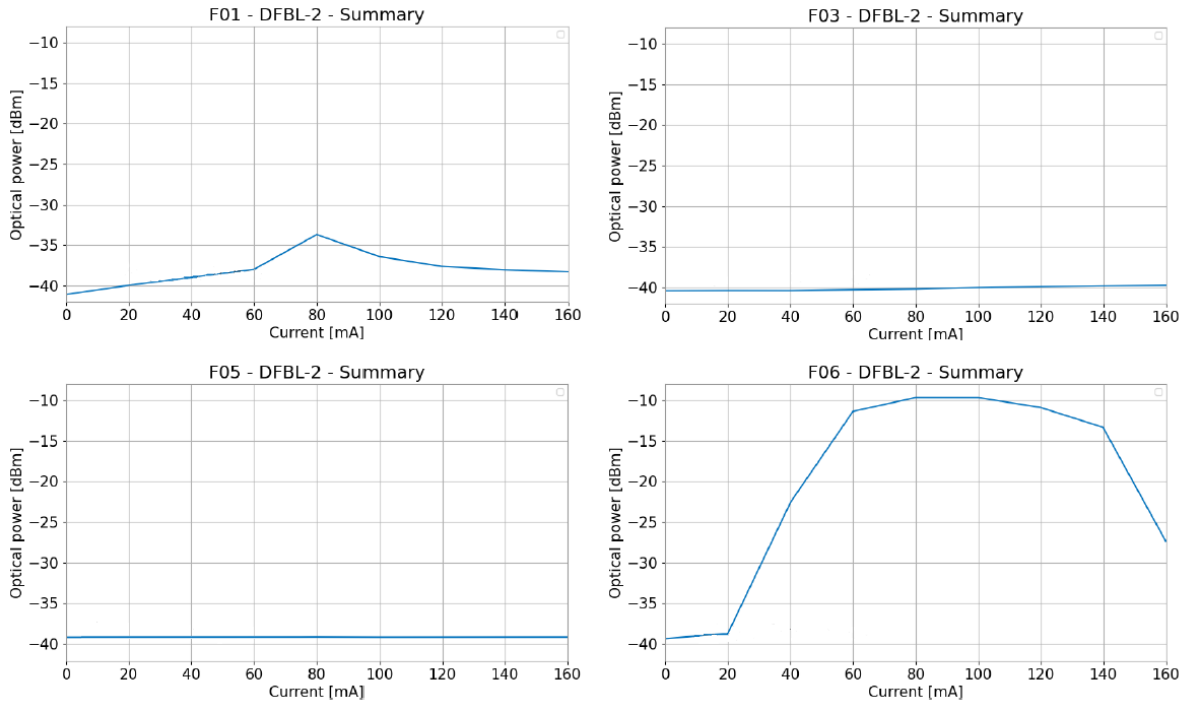

FIGURE 44: SUMMARY OF LASER PERFORMANCE

To better summarise the outcomes of all this testing, some tables have been prepared to identify which chips have the overall best performance. From this evaluation 2 chips will be chosen to be packaged.

		Electrical Screening Summary			
	Elements	Die F01	Die F03	Die F05	Die F06
RF Pads	DFBL 1	✓	✓	✓	✓
	DFBL 2	✓	✓	✓	✓
	EAM 1	✓	✓	✓	✓
	EAM 2	✓	✓	✓	Fails
	EOPM 1	✓	✓	Fails	✓
	EOPM 2	✓	✓	✓	✓
	PD 1	✓	Fails	✓	Fails
	PD 2	✓	✓	✓	Fails

DC Pads	DFBL 1	✓	✓	Fails	
	DFBL 2	✓	✓	✓	✓
	EOPM 1	✓	✓	✓	✓
	EOPM 2	✓	✓	✓	Poor
	PD 3	✓	✓	✓	
	SOA	✓	✓	✓	✓
	Total Poor	0	0	0	1
	Total Fails	0	1	2	3
	Total	0	1	2	4

TABLE 18: ELECTRICAL SCREENING SUMMARY

The F05 and F06 chips have performed the worst in electrical screening, in both at least two components were not working. Chip F03 has a malfunctioning component. Chip F01 is the best of the lot, electrically.

		Optical Tests Summary			
	Elements	Die F01	Die F03	Die F05	Die F06
Loops tests	Loop up	✓	✓	✓	Poor
	Loop down	✓	Poor	Poor	Poor
Active Test	SOA	Fails	Poor	Poor	✓
	DFB 2	Poor	Poor	Fails	✓
	Total poor	1	3	2	2
	Total Fail	1	0	1	0
	Total	2	3	3	2

TABLE 19: OPTICAL TESTS SUMMARY

Some of the loops flagged as poor have a few dB extra losses, but this does not necessarily affect the performance of the chip. As we can see, chips F01, F03 and F05 have the worst performance in active testing. The F01 chip stands out as its SOA does not work and the DFB laser has low power level performance. The F06 chip, however, performs perfectly in these tests.

From these tests we can conclude the following. The F01 and F03 chips perform well in electrical screening tests, while the other chips fail in some components. However, in the SOA and DFB laser tests, the F06 chip is the only one which functions correctly across testing. Additionally, while the F03 die, while not perfect in optical tests, does show that

both its SOA and DFB laser work to some degree. Therefore, the F03 and F06 chips were selected for assembly.

5.2. Component Chip Characterisation

As for the transmitter chip, the testing in this section is divided into electrical screening and optical measurements as follows:

- **Test 1.1:** Current sweep of the 8 heaters, measuring the voltage
- **Test 1.2:** Electrical screening of 5 RF pads
- **Test 2:** Coupling losses (measurements of the loops)
- **Test 3:** Measuring spectra of internal sources: DFBL and SOA

Setup 1: The following setup was used for the electrical screening, with the probe located either at the north or south facets. A 20 x 250 µm pitch DC multicontact probe and 130 µm pitch GSG RF probe were used.

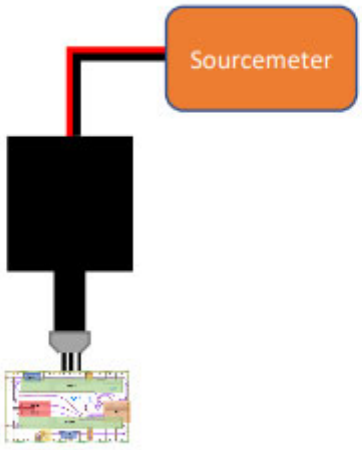

FIGURE 45: SETUP 1

Setup 2: The following setup was used for measuring the coupling losses using the internal loop. An 8 channel 127-micron pitch SSMF array was used. The light source was a broadband source (1530 nm – 1590 nm), and the returning light was measured with an OSA.

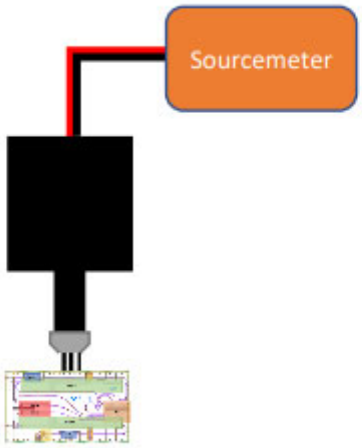

FIGURE 46: SETUP 2

Setup 3: Finally, here follows the setup for measuring the electro-optical response of the active components. The probe was located at the north facet in order to probe DFB2 and SOA2.

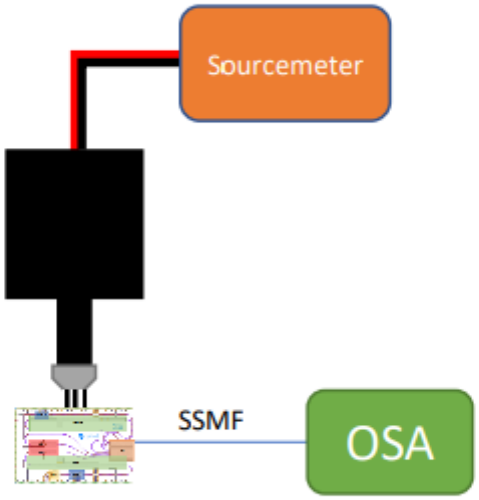

FIGURE 47: SETUP 3

Test 1.1:

The VI curves of the SOAs seem correct. The series resistance is slightly higher in SOA2 of die F01.

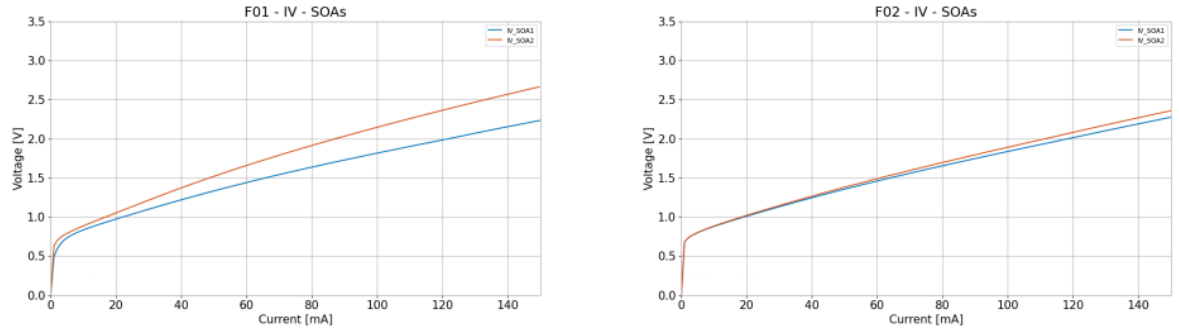

FIGURE 48: VI CURVES OF THE SOAS

The VI curves of the DFBL DC pads show that the resistance of the heater is extremely high, in the order of MΩ.

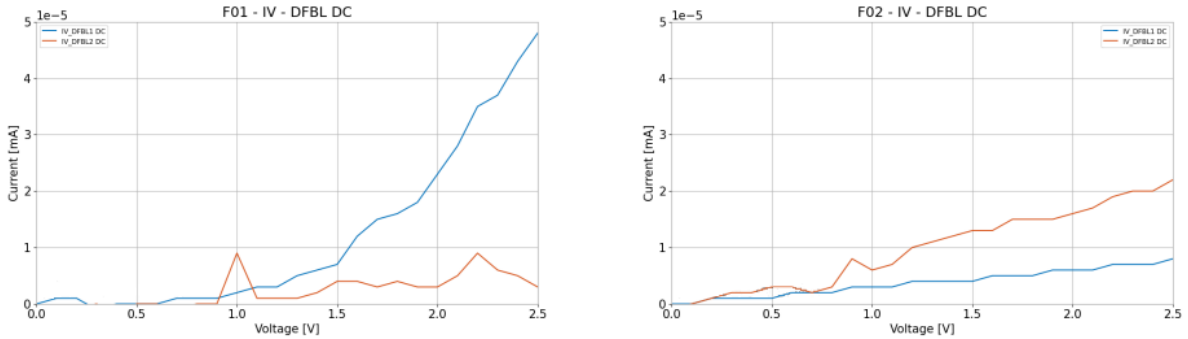

FIGURE 49: VI CURVES OF THE DFB LASERS

The VI curves in the MZM DC pads were measured between p1-n and p2-n contacts in each modulator. The resistances of MZM1 DC pads for die F01 are lower than the rest, being this resistance 1 kΩ. The resistance of MZM2 DC pads for die F01 is 30 kΩ. For die F02, MZM1 DC pads have a resistance of 13 kΩ and in MZM2 DC pads the resistance is 67 kΩ.

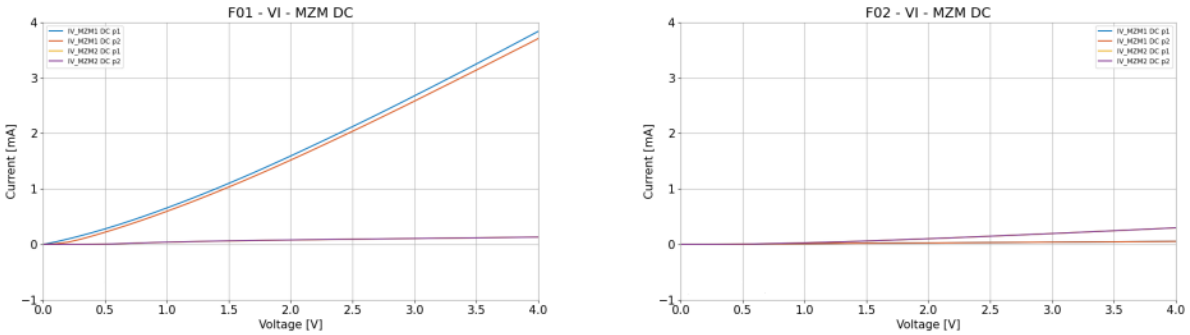

FIGURE 50: VI CURVES OF THE MZMS

Test 1.2:

The PDs were reverse biased in order to obtain the dark currents. The dark current of PD in F01 die is 12 nA at 2V and in die F02 is 9 nA at 2V.

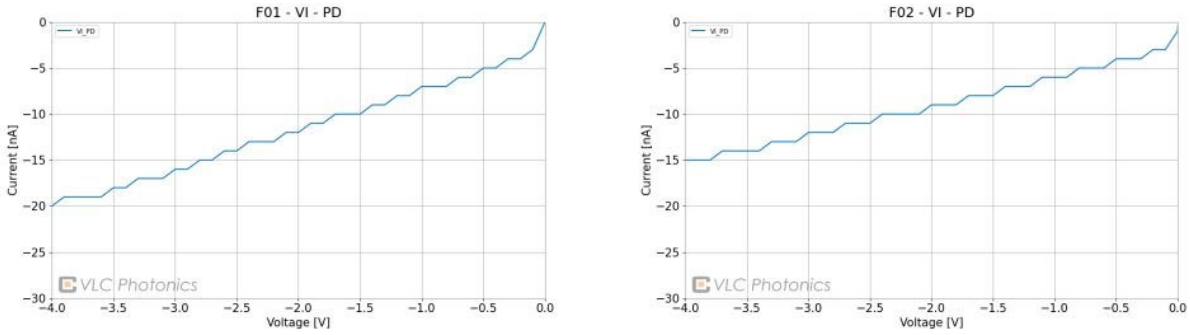

FIGURE 51: VI CURVES OF THE PDS

The VI curves of the DFBL RF pads present a series resistance which decreases (slope of the VI curve) when the current applied increases. The VI curve of DFBL1 RF of die F01 is distorted for currents above ~130 mA. In the die F02 the VI curves are homogeneous.

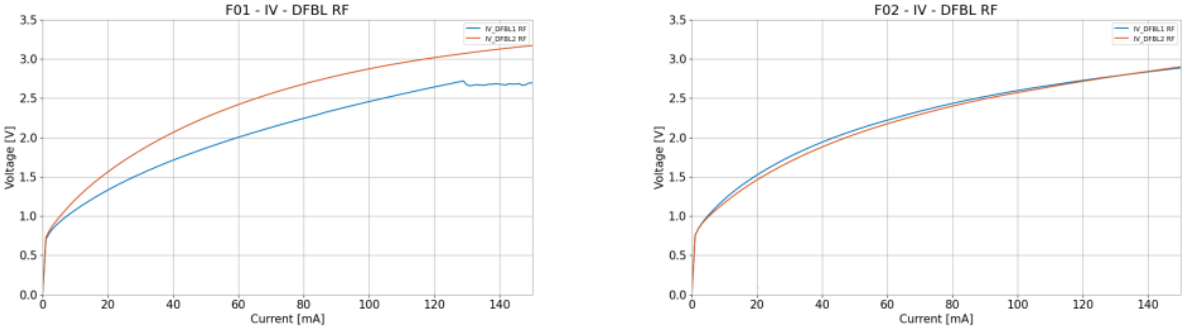

FIGURE 52: DFBL RF PADS VI CURVES

The VI curves in the MZM RF pads are very homogeneous between MZM1 and MZM2 in both dies. The resistance is around 52 Ω.

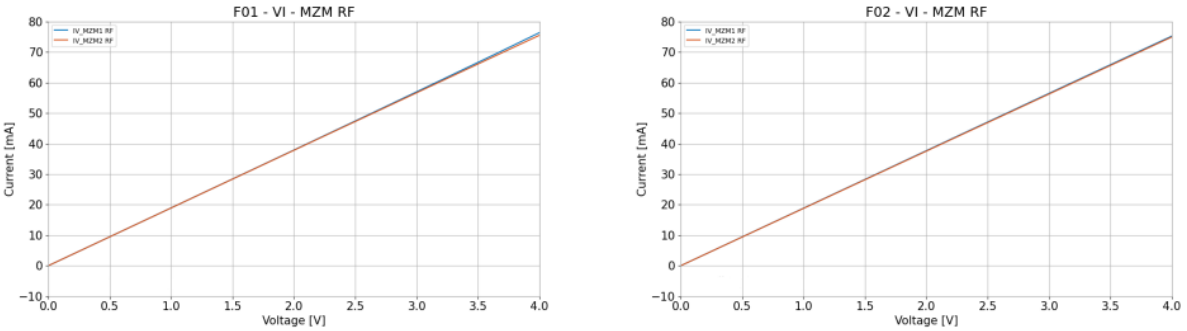

FIGURE 53: MZM RF PADS VI CURVES

Test 2:

The optical spectra of the alignment loops in transmission are shown in the graphs below. A fibre array of SMF with a pitch of 127 µm has been used. The IL is 7 dB at 1550 nm (3.5 dB/facet) for die F01 and 5.4 dB (2.7 dB/facet) for die F02. In the IL the coupling losses of the facet and the tolerances of the fibre array are included.

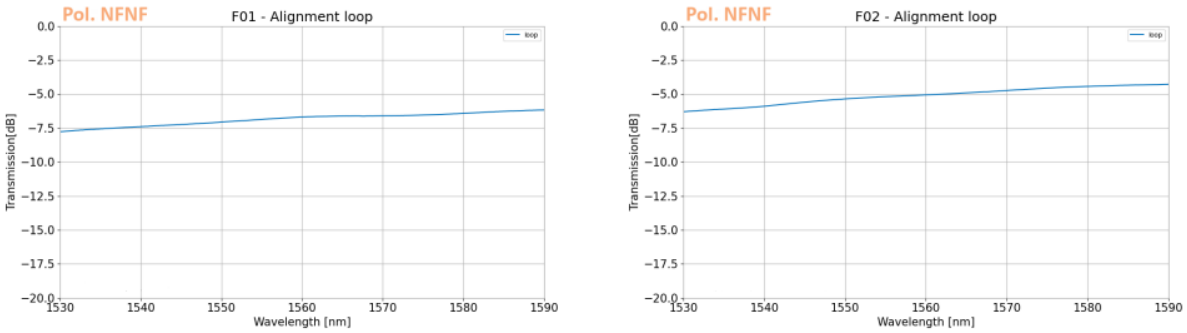

FIGURE 54: ALIGNMENT LOOP TRANSMISSION FOR F01 AND F02

Test 3:

Die F01: The optical spectrum of the DFBL2 output has been measured for each current step of 10mA between 0 mA and 150 mA. The spectra of the DFBL2 are deformed for some currents. The power evolution seems correct. The threshold current is 17 mA for die F01. The maximum power measured is -1.2 dBm at 100 mA. The 3.5 dB IL of the PIC facet must be considered.

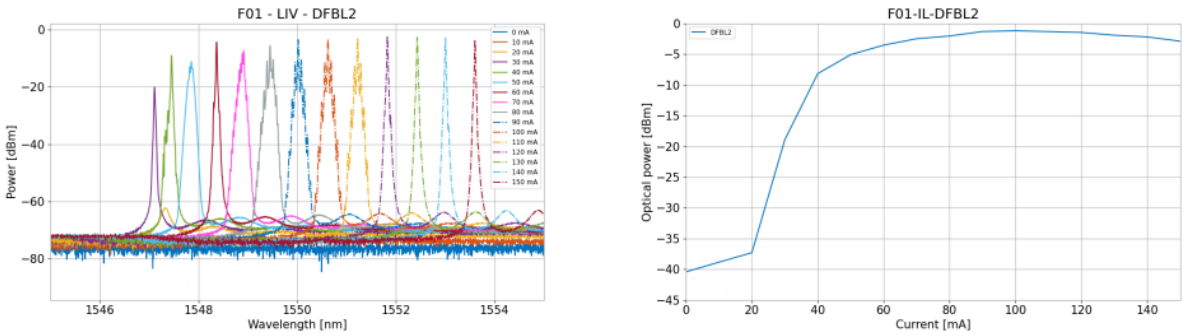

FIGURE 55: OPTICAL SPECTRUM OF THE F01 DFBL2 OUTPUT, IN CURRENT STEPS OF 10MA

Die F02: The optical spectrum of the DFBL2 output has been measured for each current step of 10 mA between 0 mA and 150 mA. The power evolution shows a strange behaviour, the power is decreasing very early. Some of the spectra is deformed for some currents. The threshold current 65 mA for die F02. The maximum power measured is -20.8 dBm at 80 mA. The 2.7 dB IL of the PIC facet must be taken into account.

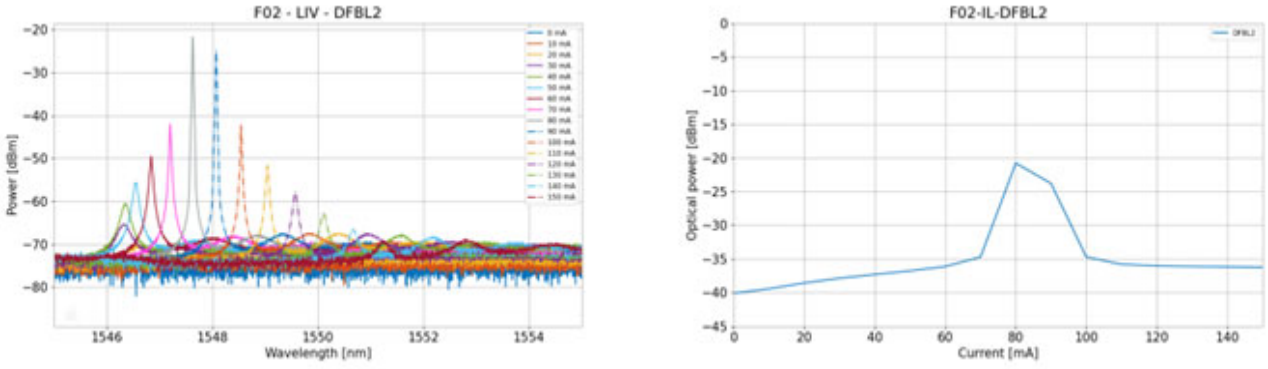

FIGURE 56: OPTICAL SPECTRUM OF THE F02 DFBL2 OUTPUT, IN CURRENT STEPS OF 10MA

In figures (54) to (55) the optical spectrum of the SOA2, outputs 1 and 2, are shown for each current step of 10 mA between 0 mA and 150 mA. The spectra present lasing lines due probably to the cavity formed of the facets at each side of the SOA2. This converts the structure into a laser. The output power vs applied current graphs are also included:

- Maximum output power of -3.8 dBm (out1) and -3.3 dBm (out2) for die F01 is reached at 150 mA. The 3.5 dB IL of the PIC facet must be considered.
- Maximum output power of 0.8 dBm (out1) and -0.6 dBm (out2) for die F02 is reached at 150 mA. The 2.7 dB IL of the PIC facet must be considered.

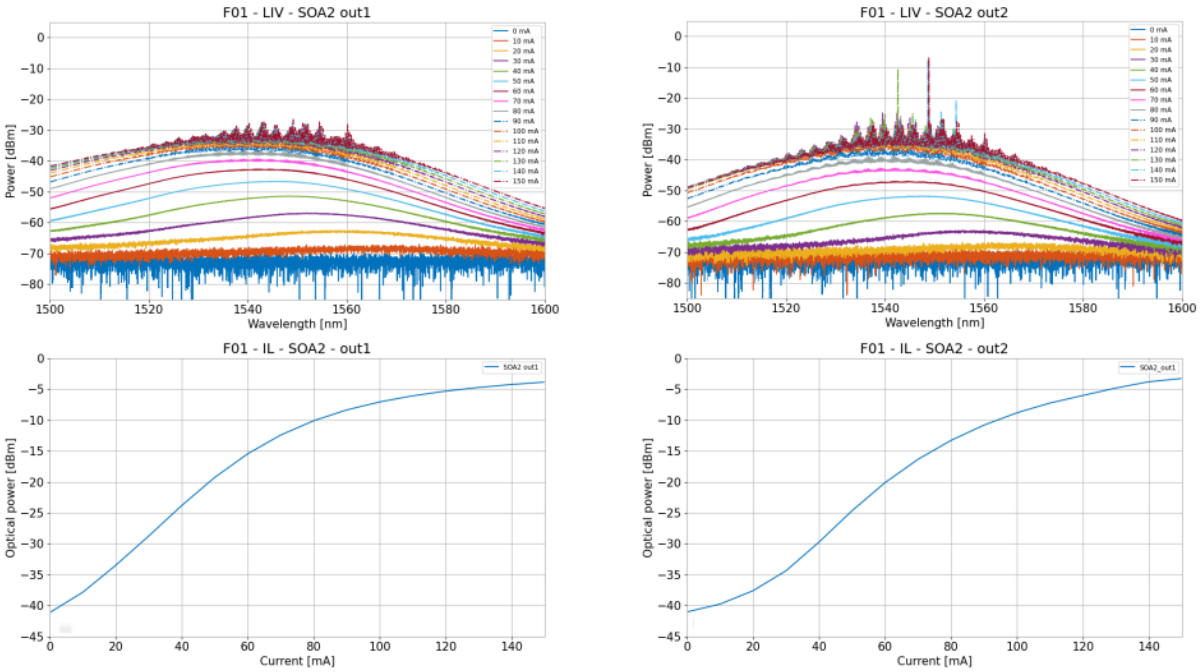

FIGURE 57: SOA2 OPTICAL OUTPUTS F01

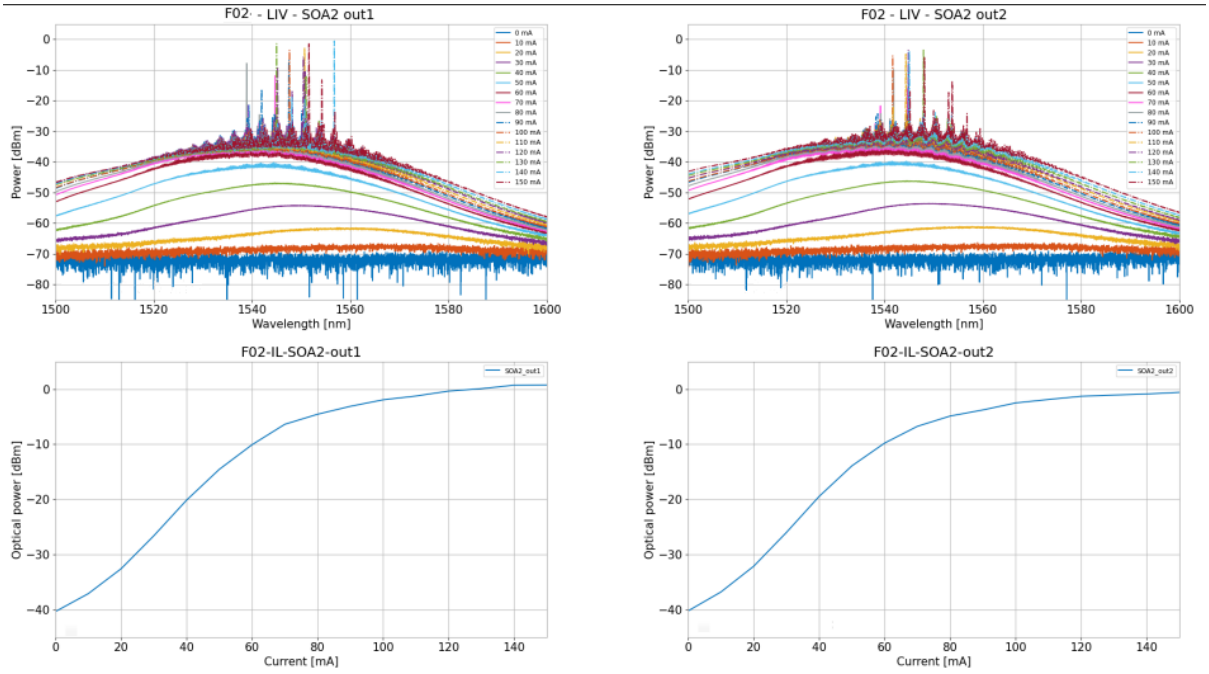

FIGURE 58: SOA2 OPTICAL OUTPUTS F02

Summary:

Test 1:

Regarding the VI curves from the electrical screening, the responses of the DFBLs seem to have some issues:

- The resistance of the heaters is extremely high, in the order of MΩ, meaning that there is a problem is the electrical conductivity.
- The shape of the VI curves of the RF bias pads the series resistance is decreasing all over the injected current range. One of the DBFL present a distorted VI curve above 130 mA.

The rest of the electrical responses seem correct.

- The values of IL of the facet to SSMF coupling are correct but the response is not flat in the wavelength range measured.

Test 2:

The internal losses measured on the internal loops are 7dB for chip F01 at 1550nm, and 5.4dB for chip F02.

Test 3:

Concerning the Electro-optical response of the DFBLs, there are again some issues:

- In one DFBL the spectrum is distorted for some currents, although the power evolution seems right.
- In another DFBL, the threshold current is too high and the power decreases quite early.

The electro-optical response of the SOAs seem to be correct.

6. Additional DBR Test Chip Description and Radiation Testing Results

In this chapter the radiation experiment(s) conducted at Alter Technology are described, along with some additional chips which were used to supplement the data available for this work.

Due to some delays in fabrication, some previously fabricated chips with some DBR lasers were sent to Alter to undergo radiation testing, as it was not yet known if the component chips would be ready in time for these tests to be performed on them. This was due to them having some metallisation errors which made wire bonding them difficult.

The GDS of the DBR chip follows below. One can see that the chip contains features that when tested will yield generally useful data, such as how SOAs perform after irradiation. Since all the active components to be tested in the chips fabricated for this project (DBR lasers, SOAs) are based on an SOA, it was hoped we could extrapolate some good estimations of performances for the other chips under similar conditions. Additionally, when the component chip is radiation tested, it will allow for comparison between the HHI and Smart Photonics platforms in terms of radiation hardness of their active components. As the DBR laser chips were fabricated by Smart photonics.

6.1. DBR Laser Chips description and screening test results

The chips in question are very simple, consisting of a DBR laser and one or two photodiodes at the laser outputs for measurements.

FIGURE 59: BREAKDOWN OF THE DBR LASERS CONSTITUENT COMPONENTS

FIGURE 60: PACKAGING OF THE CHIP SHOWING THE ELECTRICAL CONNECTIONS

Figure (59) shows the overview of the PIC. The DBR laser is composed of the following sections, Rear, SOA (active region of the laser), Phase shifter (PS) and Front. The photodetector (PD) can be biased to detect light emitted by the SOA. 8 such dies were packaged on 4 PCBs, an example packaged chip is shown below:

A brief summary of the electrical and optical screening tests performed on the chips is shown below, this information was used to determine which chips to be sent to be

irradiated based on getting the most data from the tests from maximising operational components to test.

Die	Bottom			Top		
	SOA	PD1	PD2	SOA	PD1	PD2
H1a	X	X	✓	✓	✓	✓
H1b	✓	✓	X	✓	✓	✓
H2a	X	X	-	✓	✓	-
H2b	X	X	-	✓	X	-
H1c	X	✓	X	X	X	✓
H1d	X	X	✓	✓	✓	✓
H2c	X	X	-	X	X	-
H2c	X	-	-	✓	-	-

TABLE 20: ELECTRICAL SCREENING TESTS OF THE DIES

Laser	Light Emission	Output Power Level	Lasing Peak
H1a-Bottom	X	X	X
H1a-Top	✓	**High**	✓
H1b-Bottom	✓	Low	✓
H1b-Top	✓	Low	✓
H2a-Bottom	X	X	X
H2a-Top	✓	Low	X
H2b-Bottom	X	X	X
H2b-Top	✓	**High**	✓
H1c-Bottom	X	X	X
H1c-Top	X	X	X
H1d-Bottom	X	X	X
H1d-Top	✓	**High**	✓
H2c-Bottom	X	X	X
H2c-Top	X	X	X
H2d-Bottom	X	X	X
H2d-Top	✓	Medium	x

TABLE 21: OPTICAL SCREENING TESTS OF THE DIES

8 of the dies from the HHI foundry were packaged on 4 PCBs. According to the above results, 3 lasers are feasible for radiation experiments: H1a-Top, H2b-Top and H1d-Top.

6.2. Radiation Test Results of the DBR Laser Chips

In this section the performance for some of the DBR laser chips after radiation testing is described and compared to the performance of the same chips prior to irradiation. In this way an estimate can be made about the performance of the transmitter device, though further testing of the device itself will provide better insight once the packaging has been completed.

First, we will show results for the H1B chip before and after irradiation.

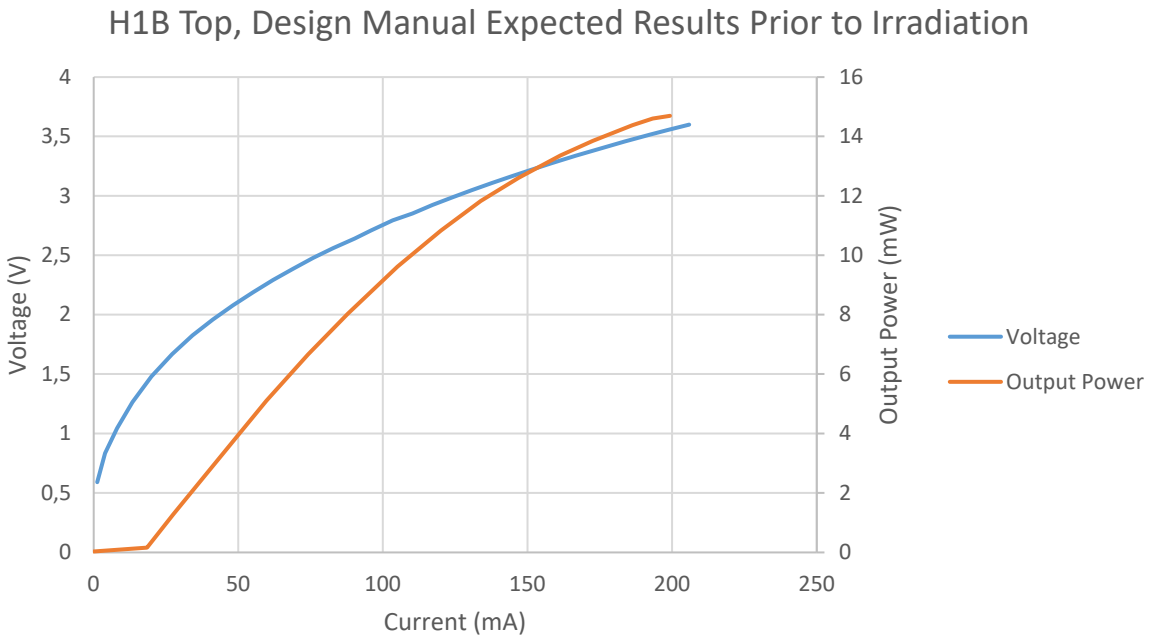

FIGURE 61: H1B TOP, DESIGN MANUAL EXPECTED RESULTS PRIOR TO IRRADIATION

From the external measurements before irradiation, we can see the laser is performing normally, with a standard V-I curve demonstrated.

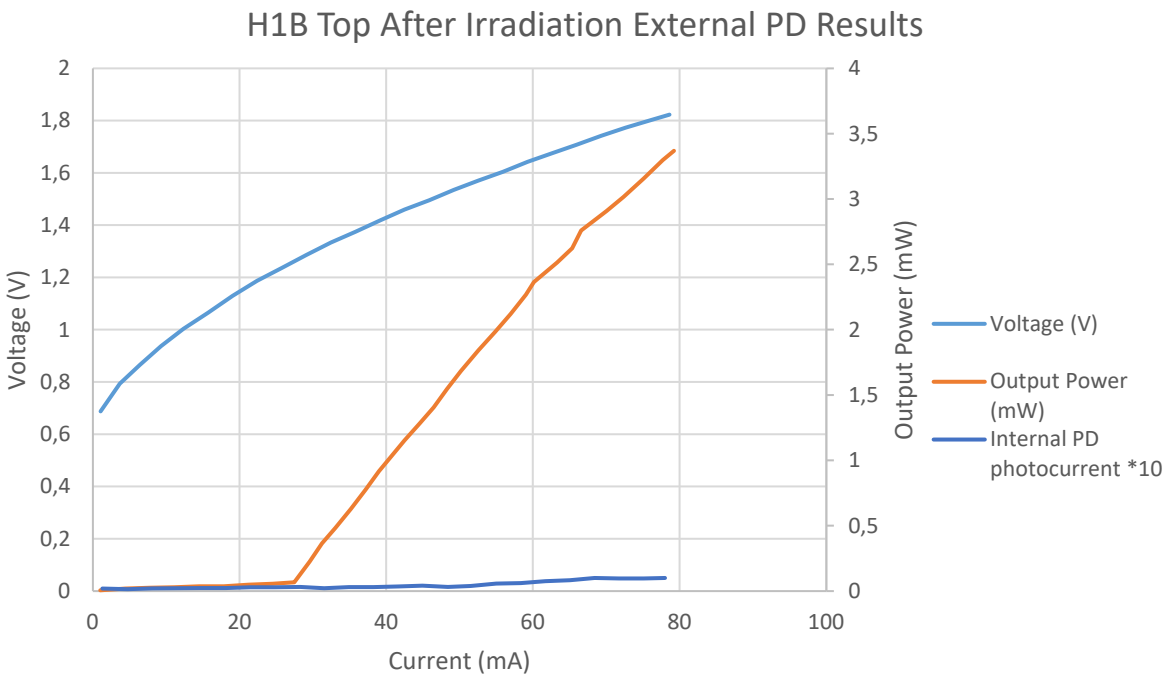

FIGURE 62: H1B TOP AFTER IRRADIATION EXTERNAL PD RESULTS

When we then compare this to the results for the irradiated chip, we can see that at just under 80mA current the chip now produces between 3mW and 3.5mW of power, compared to approximately 8mW of power prior to the radiation dose. Not all chips show the same response despite equal dosage. As an example, here follows the results for the chip whose performance was most impacted by the radiation dosage (Figures 62 & 63)

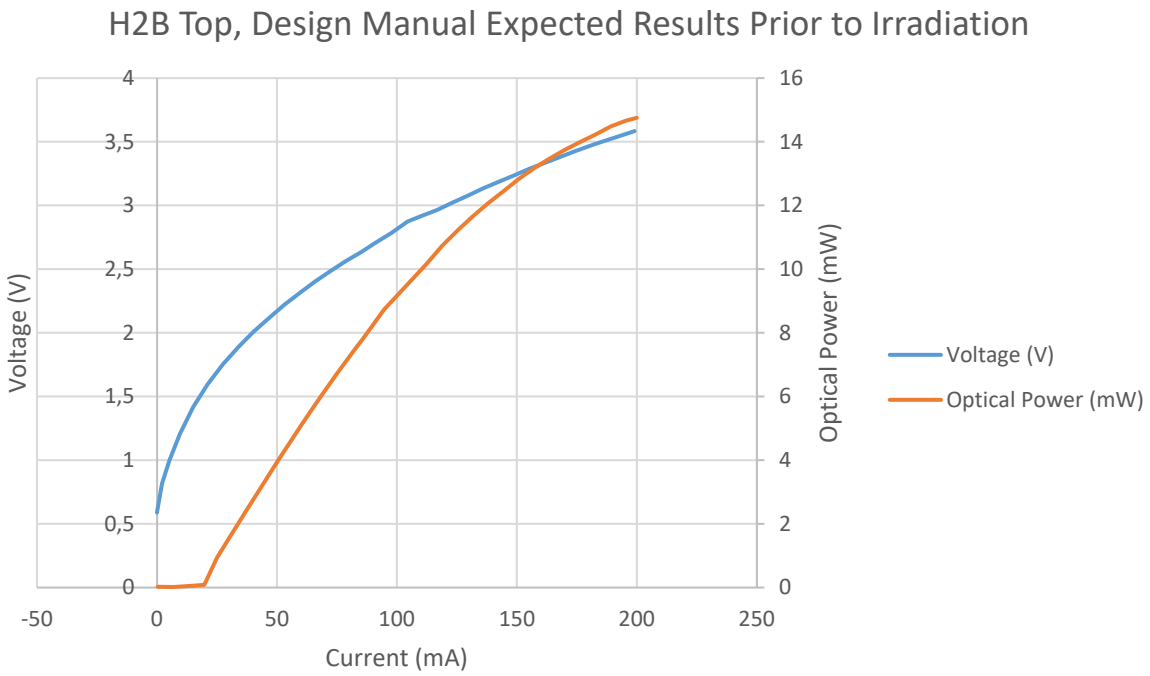

FIGURE 63: H2B TOP, DESIGN MANUAL EXPECTED RESULTS PRIOR TO IRRADIATION

As for H1B, the voltage-current curve is normal prior to irradiation.

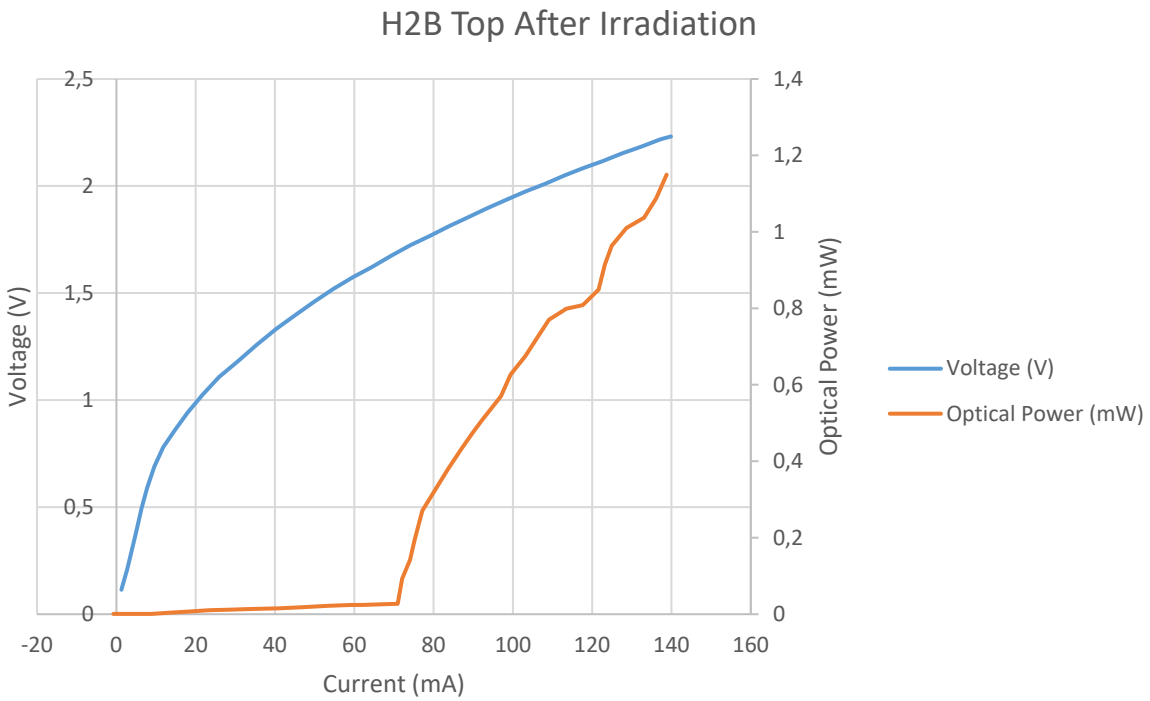

FIGURE 64: H2B TOP AFTER IRRADIATION

After the radiation dosage was complete, the lasers performance is dramatically changed. The optical power only begins to rise once current is above 60mA, while before irradiation it was climbing once current exceeded 25mA. The optical power curve is much less smooth, and at 140mA current it achieves about 10% of its pre/irradiation power (~1.1mW compared to ~11mW). The performances of the other chips are generally closer to that of H1B Top.

Additionally, the centre wavelength of the laser was not found to have shifted from the nominal wavelength in the design manual (Figure64&65). The threshold current of the laser was consistent with the design manual for 4/5 chips, with H2B Top being the exception, requiring a 70mA for its operational threshold to be reached.

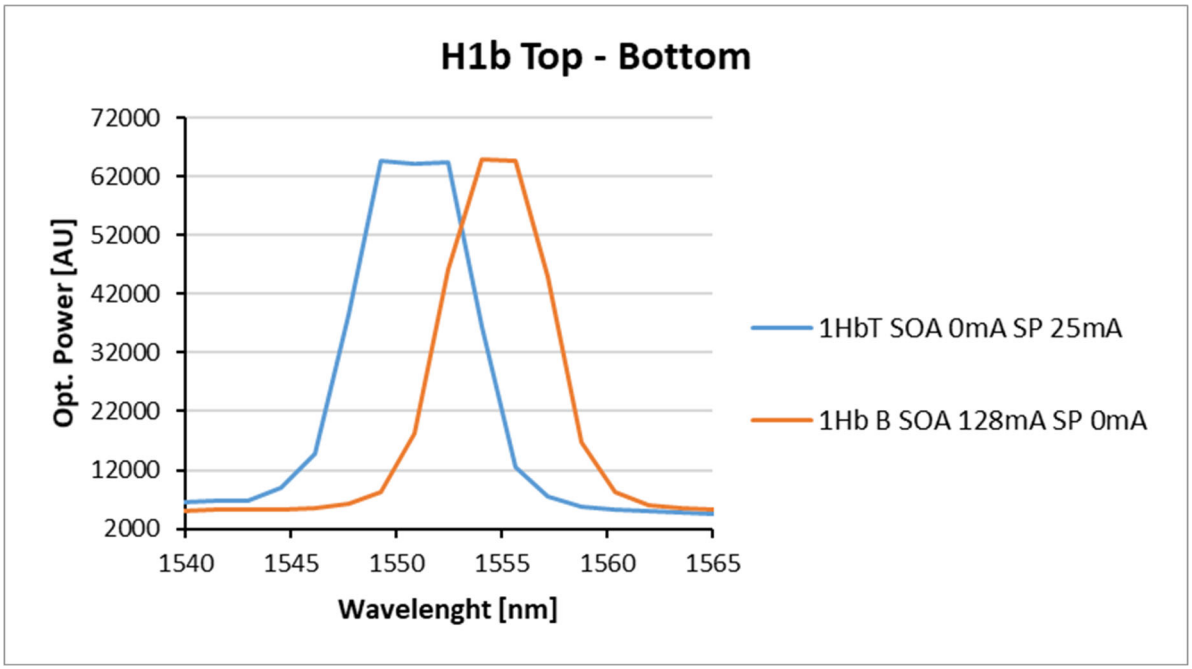

FIGURE 65: CENTRE WAVELENGTH OF H1B TOP AND BOTTOM

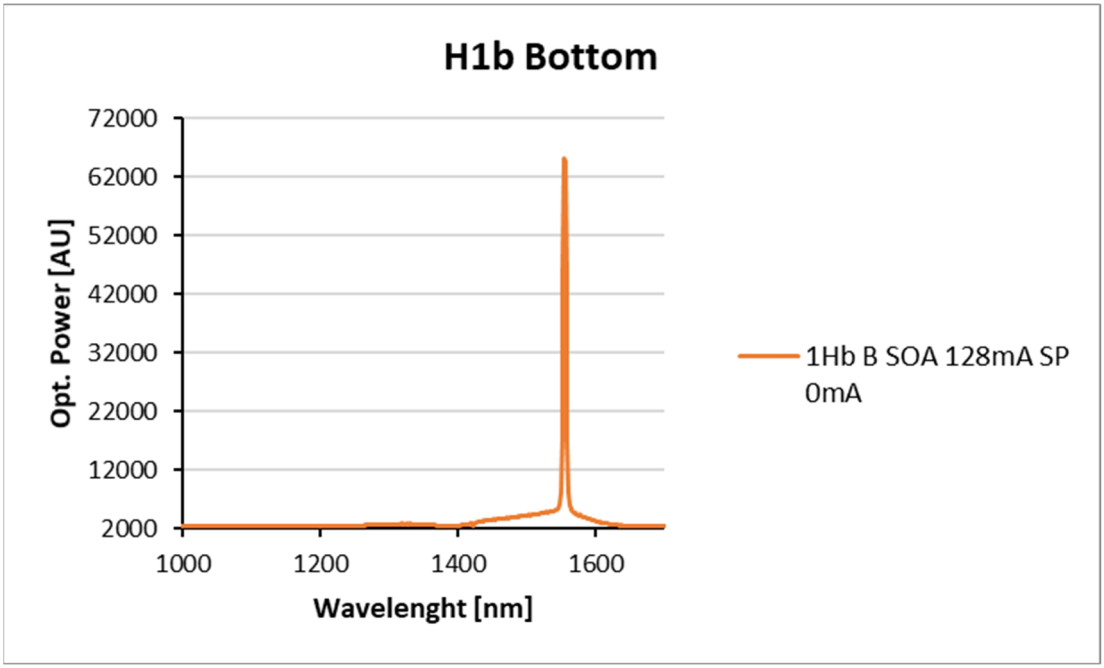

FIGURE 66: H1B BOTTOM SOA CENTRE WAVELENGTH

Thus, it appears that the main result is a loss of power in the active laser component following irradiation, the implications of this performance drop for the transmitter design is extrapolated. Since the DBR laser essentially consists of an SOA and 2 sets of gratings, it can be assumed that the SOA in the transmitter circuit will also function, if to a reduced amplification capacity. The passives can be assumed to function also, while for the DFB laser, the main question is whether its low index contrast, low reflectivity gratings in its design will be more adversely affected by radiation than the DBRs high contrast, highly reflective gratings. For the purposes of this work, as the components chip has not been measured after radiation testing, we will assume that the difference in architecture results in minimal change under radiation conditions.

Using the same calculations as in chapter 3, it became clear that the data rate would have to be significantly reduced, even when using an on-satellite EDFA. The results show that if the signal is reduced to less than 0.33Gbps, the signal can still be received by the proposed ground station, from a range of up to 500km.

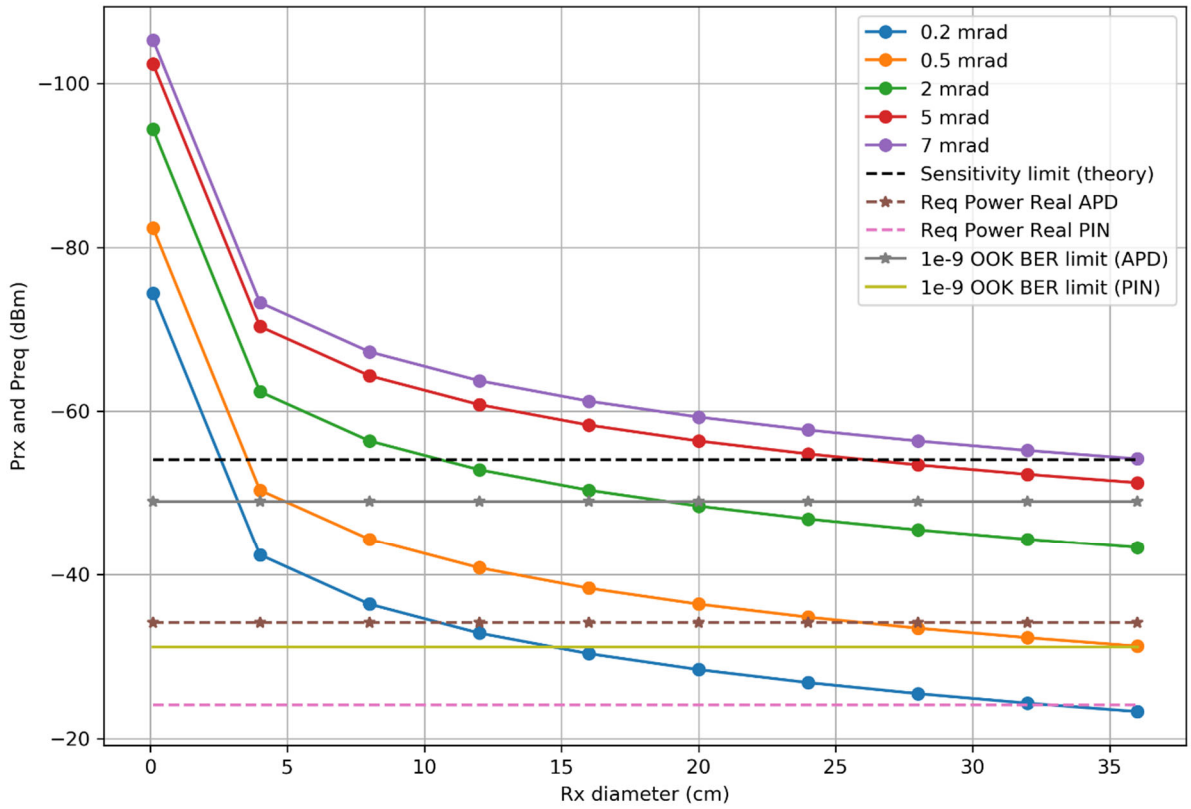

FIGURE 67: REQUIRED RECEIVER DIAMETER FOR THE PROPOSED TRANSMITTER UNDER SPACE CONDITIONS

6.3. Radiation Dosage

The chips were dosed with both proton and gamma radiation. The total ionising dose (TID) for proton radiation was 1.5×10^{11} p^{+}/cm^{2}, while the TID of gamma radiation was 105.88krad, with a total dose rate (Td) was 225rad(Si)/hour.

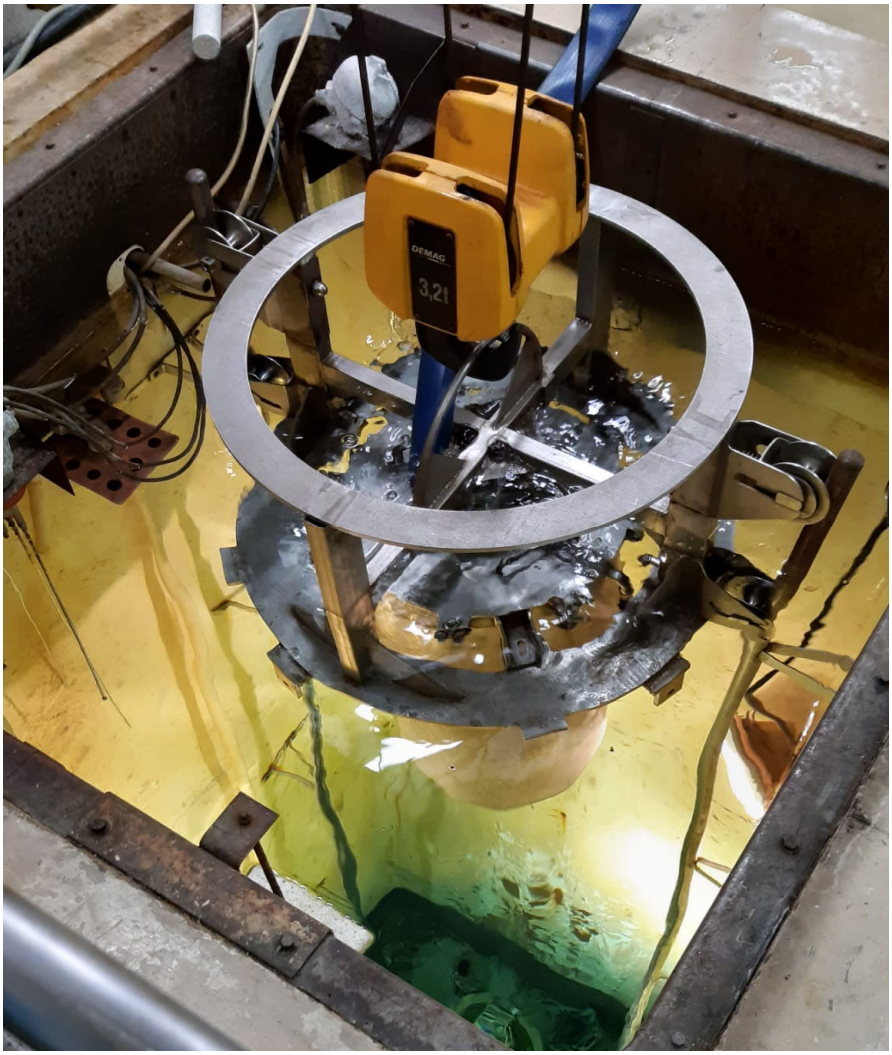

FIGURE 68: GAMMA IRRADIATION SETUP, COURTESY OF ALTER TECHNOLOGY.

7. Conclusions

A coherent transmitter has been designed on an integrated InP platform. While packaging is yet to be completed, there will be useful future experiments to be conducted using the packaged devices. The results from the DBR chips radiation testing indicate that at the very least, the threshold currents and centre wavelength of the transmitter device should be unaffected (in most cases), while the output of the transmitter is expected to be reduced. However, it is not known at what rate this degradation occurs. It will be important to follow up this work with measurements of different radiation doses, so that the devices performance over time in the space environment can be better understood. It may well be that early in the mission lifetime of the device, it will be able to provide close to its designed data rate performance, while nearing mission end it will deteriorate rapidly. It could also

deteriorate steadily over time, but it is important to understand how this deterioration progresses for better mission planning. Alternatively, these results can be seen as an incentive to conduct further tests on rad-shielded PICs, to understand how well these negative effects can be guarded against.

There is good evidence that the proposed integrated transmitter design would be capable of establishing satellite downlinks from LEO, capable of 0.3Gbps even at end of mission lifetime, whilst initially being capable of establishing a 2Gbps link with the proposed COTS ground station. This is reinforced considering the chips received a dose of 105.88krad, which when compared to results from SPENVIS corresponds to a 10-year long mission in a very high inclination orbit. For shorter missions at lower inclinations this dose can be reduced by more than 90% for orbital inclinations of less than 28 degrees. More than likely an orbit of about 45-60 degrees would be most useful, but it depends greatly on the intended mission of the satellite the transmitter is installed on. Nonetheless, this reinforces further the need to measure InP chips at various other radiation doses to better understand at what rate the performance degrades for different radiation exposures.

8. Further Work

As mentioned in the conclusions, this work leads to several avenues for future research. Firstly, the component chips, once packaging is completed, should be irradiated to fully confirm the functionality and performance of all the necessary components for the coherent transmitter chip. Secondly, it would be extremely useful to measure the components chip repeatedly with increasing radiation doses. This would allow for a better understanding of how the full transmitter device will perform across the lifetime of a mission in LEO. Additionally, it would be useful to perform radiation testing at full mission dosage on both of the packaged transmitter chips, having added some radiation shielding to one of them, to get a better understanding of the trade-offs between adding shielding mass and volume vs improved transmitter performance, hopefully being able to maintain the compact nature of the packaged transmitter such that it conforms to CubeSat volume constraints.

9. References

(1) Thompson, S.E. & Parthasarathy, S., 2006. Moore's law: the future of Si microelectronics. *Materials Today*, 9(6), pp.20–25. Available at: http://dx.doi.org/10.1016/s1369-7021(06)71539-5.

(2) Miller, S.E., 1969. Integrated Optics: An Introduction. *Bell System Technical Journal*, 48(7), pp.2059–2069. Available at: http://dx.doi.org/10.1002/j.1538-7305.1969.tb01165.x.

(3) Crabb, J. et al., 2019. Laser transmitter for CubeSat-class applications. In H. Hemmati & D. M. Boroson, eds. *Free-Space Laser Communications XXXI*. SPIE. Available at: http://dx.doi.org/10.1117/12.2506967.

(4) Soares, F.M. et al., 2019. InP-Based Foundry PICs for Optical Interconnects. *Applied Sciences*, 9(8), p.1588. Available at: http://dx.doi.org/10.3390/app9081588.

(5) Wörhoff, K. et al., 2015. TriPleX: a versatile dielectric photonic platform. *Advanced Optical Technologies*, 4(2). Available at: http://dx.doi.org/10.1515/aot-2015-0016.

(6) Smit, M. et al., 2014. An introduction to InP-based generic integration technology. *Semiconductor Science and Technology*, 29(8), p.083001. Available at: http://dx.doi.org/10.1088/0268-1242/29/8/083001.

(7) Barnwell, N. et al., 2018. The Miniature Optical Communication Transceiver—A Compact, Power-Efficient Lasercom System for Deep Space Nanosatellites. *Aerospace*, 6(1), p.2. Available at: http://dx.doi.org/10.3390/aerospace6010002.

(8) Zeller, J. & Manzur, T., 2012. Free-space optical communication at 1.55 μm and 4.85 μm and optical correlation through the evaporation layer. In *Unattended Ground, Sea, and Air Sensor Technologies and Applications XIV*. SPIE. Available at: http://dx.doi.org/10.1117/12.924732.

(9) Zhao, H. et al., 2019. High-Power Indium Phosphide Photonic Integrated Circuits. *IEEE Journal of Selected Topics in Quantum Electronics*, 25(6), pp.1–10. Available at: http://dx.doi.org/10.1109/jstqe.2019.2908788.

(10) Zhao, H. et al., 2018. Indium Phosphide Photonic Integrated Circuits for Free Space Optical Links. *IEEE Journal of Selected Topics in Quantum Electronics*, 24(6), pp.1–6. Available at: http://dx.doi.org/10.1109/jstqe.2018.2866677.

(11) Trajkovic, M. et al., 2019. Increasing the Speed of an InP-Based Integration Platform by Introducing High Speed Electroabsorption Modulators. *IEEE Journal of Selected Topics in Quantum Electronics*, 25(5), pp.1–8. Available at: http://dx.doi.org/10.1109/jstqe.2019.2913727.

(12) Estrella, S.B. et al., 2013. First Monolithic Widely Tunable Photonic Coherent Transmitter in InP. *IEEE Photonics Technology Letters*, 25(7), pp.641–643. Available at: http://dx.doi.org/10.1109/lpt.2013.2245886.

(13) Zlata Gibalina, Vladimir Fadeev. Optical Inter-Satellite Link in Comparison with RF case in CubeSat system. *Zhurnal Radioelektroniki - Journal of Radio Electronics*. 2017. No. 10. Available at http://jre.cplire.ru/jre/oct17/6/text.pdf

(14) Chiboucas, K. (2022) 'Gemini Observatory Telescopes and Sites', The Sites, 5 April. Available at: https://www.gemini.edu/observing/telescopes-and-sites/sites#Transmission (Accessed: 28/04/2022)

(15) Stewart D. Personick, "Optical Detectors and Receivers," J. Lightwave Technol. **26**, 1005-1020 (2008)

(16) S. Tsitas and J. Kingston, “6U CubeSat design for Earth observation with 6.5 m GSD, five spectral bands and 14Mbps downlink,” Aeronaut. J. 114(1161), 689-697 (2010).

(17) Kingsbury, Ryan. (2015). Optical communications for small satellites.

(18) Saeed, N. et al., 2020. CubeSat Communications: Recent Advances and Future Challenges. *IEEE Communications Surveys & Tutorials*, 22(3), pp.1839–1862. Available at: http://dx.doi.org/10.1109/comst.2020.2990499.

(19) K. Riesing, H. Yoon and K. Cahoy, "A portable optical ground station for low-earth orbit satellite communications," 2017 IEEE International Conference on Space Optical Systems and Applications (ICSOS), 2017, pp. 108-114, doi: 10.1109/ICSOS.2017.8357219.

(20) Clements, E. et al., 2016. Nanosatellite optical downlink experiment: design, simulation, and prototyping. *Optical Engineering*, 55(11), p.111610. Available at: http://dx.doi.org/10.1117/1.oe.55.11.111610.

(21) Edwards, B, 2019. NASA’s Optical Communications Programs. Available at: https://ntrs.nasa.gov/api/citations/20190025298/downloads/20190025298.pdf (Accessed: 28/05/2022)